# Fabrication and Analysis of

# Injection Molded Plastic Microneedle Arrays

A Thesis
Presented to
The Academic Faculty

By

Jordan David Hamilton

Submitted in Partial Fulfillment
of the Requirements
for the Degree of

Master of Science in Mechanical Engineering

Georgia Institute of Technology

Fall 2010

“It is a capital mistake to theorize before you have all the evidence.

It biases the judgement.”

*A Study in Scarlet* (1888), Chapter 3

Sir Arthur Conan Doyle

## ACKNOWLEDGMENTS

I would like to thank the many people that helped and supported me during my time at Georgia Tech. First and most importantly, I would like to thank my advisor, Dr. Colton for providing guidance and support during my research and for helping me to complete my thesis while working away from Georgia Tech. I would also like to thank Dr. Prausnitz and Dr. Ku for serving on my thesis committee.

Additionally, I would like to express my gratitude to the National Collegiate Inventors and Innovators Alliance for helping, in part, to fund this project. I want to express thanks to all of the support staff at Georgia Tech. A special thanks goes to John Graham and the folks in the machine shop for assisting me with the fabrication of numerous parts.

Finally, I want to express my sincere appreciation to all of my friends and family, who gave me support and encouragement during my time at Georgia Tech. I am especially thankful to my parents and my fiancée Jessica for their love and support

## TABLE OF CONTENTS

## LIST OF TABLES

## LIST OF FIGURES

## SUMMARY

This thesis describes the fabrication of plastic microneedle devices, their fabrication by injection molding, and analysis of the penetration mechanics. Injection molding is an economical mass-production technique that may encourage widespread adoption of microneedles for drug delivery.

Four polymers were injection molded into hexagonal and square patterns of between 91 and 100 needles per array. The patterns and geometries were chosen to study the effect of needle spacing and array design on penetration force. Two needle spacings of approximately 1 mm and 1.5 mm were employed for both patterns. Molded parts showed tip radii below 15 microns, heights of 600 to 750 microns, and an included angle of approximately 30 degrees.

An economic analysis performed of the injection molded polymer devices showed that they can be manufactured for approximately $0.10 - $0.179 per part, which should be low enough to gain market acceptance. The added benefits of low pain perception, improved drug delivery for certain treatments, and the possibly of being recyclable make injection molded micro-needle devices a desirable alternative to silicon or metal micro-needles.

Penetration tests were performed with plastic micro-needle arrays and arrays of steel needles of the same spacings and patterns. Silicone rubber with mechanical properties similar to human skin was used as a skin simulant. The results showed that the micro-needles penetrated skin to depths between 120 and 185 microns depending on pattern, spacing, tip radius and needle length. This depth is sufficient to deliver drug

therapies, but not so far that they stimulate the nerve endings present beyond 130 microns inside the dermis layer in human skin.

An analytical model was developed to estimate the effects of various micro-needle and skin characteristics on penetration force. The model was based on literature sources and derived from test results. The model accounted for coefficient of friction, tip radius, tip angle, and needle spacing, as well as the skin mimic's mechanical properties such as elastic modulus, mode I fracture toughness, and puncture fracture toughness. A Monte Carlo simulation technique was used to correct for errors in needle length and testing angle. Comparison of the experiments to the model showed good agreement.

# Chapter 1

## Introduction

Primary healthcare today often consists of therapeutic drug delivery for the treatment of many conditions. Medicinal and gene treatments can be delivered to the body in a number of different ways, the most common of which are oral and transdermal methods. Oral drug delivery, though painless, can often take hours to effectively circulate drugs through the body. Transdermal delivery through the use of hypodermic needles is fast and effective and prevents the degradation of drug molecules that is associated with oral drug therapy. The drawbacks with drug delivery using hypodermic needles are the associated pain and patient stigma, required training for effective drug delivery, and problems associated with continuous delivery (Martanto, 2005).

Transdermal drug delivery patches are effective for certain types of molecules and offer certain positive benefits over other drug delivery systems. The first transdermal patch was approved in 1979 to deliver scopolamine for the treatment of motion sickness (Segal, 1991). Since then a number of different treatments have been developed to administer drugs via transdermal patch delivery systems, including clonidine, fentanyl, lidocaine, nicotine, nitroglycerin, oestradiol, oxybutinin, scopolamine, and testosterone (Prausnitz, Mitragotri & Langer, 2004). Transdermal patches currently have uses that include chronic pain management, treatment of drug withdrawal symptoms, and administration of various hormones. Although drug delivery works well for certain drugs with favorable properties for diffusion into skin, many other drug are simply too large

and too hydrophilic to be readily absorbed through human skin (McAllister, 2000, p. 6). Such limitations have led to a number of novel methods of drug delivery which includes intentional skin abrasion and removal of the top-most layer of skin, microjet-infusion, electrically based drug delivery enhancement (iontophoresis), and microneedle patch technology (Kumar & Philip, 2007).

Microneedle drug delivery patches offer attractive benefits over other drug delivery technologies. Microneedle drug delivery involves the creation of superficial physical pathways through the stratum corneum, the top layer of hard skin cells that normally prevents drug infusion through the skin (Cormier et al., 2004). Drugs of larger molecular weights then can be absorbed through the skin and carried into the bloodstream via capillaries in the skin (Kumar & Philip, 2007). Microneedles offer the advantage of being relatively painless as compared to traditional hypodermic needles because the lengths of the needles are insufficient to reach nerve endings located deeper in the skin tissue. Studies have shown that microfabricated needle arrays cause a pain sensation that is statistically indistinguishable from a smooth piece of silicon (McAllister, 2000, p. 11). Another possible advantage to microneedle drug delivery is the ability to allow a more controlled release of drugs into the body. This can be achieved by using a micro-pump between a drug reservoir and microneedle patch or by controlling the rate of diffusion into the body by managing drug concentration (Reed & Lye, 2004). *In vivo* insulin administration using metal microneedles has been demonstrated to lower blood glucose levels by as much as 80% in diabetic rats (Martanto, 2005, p. 81).

Although there are a number of distinct advantages to employing microneedles over other drug delivery technologies, certain barriers impede large-scale

commercialization efforts. Current manufacturing methods involve a few complex or slow methods for making microneedle patches. Costs for current microneedle technology may be a major impediment to mass marketing and usage of microneedles. This is because current microneedles are made primarily through the use of silicon-based processing techniques used in the microelectronics industry (Chandrasekaran & Frazier, 2003; Izumi & Aoyagi, 2007; Mo et al., 2007). While silicon processing technology is well documented and easily controlled, it is relatively expensive, slow, and creates silicon and glass structures that are mechanically brittle, and has unproven safety when used in the body (Mo et al., 2007). Another method of creating microneedles uses a hybrid process of photochemical etching and mechanical forming to create the desired microstructures (Cormier et al., 2004). This method includes many that are found in microelectronics processing and can be expensive and slow. However, metal microneedles do offer the advantage of being biocompatible and mechanically strong (Park, Yoon, Choi, Prausnitz & Allen, 2007). Finally, a method for creating polymer microneedle arrays was developed that utilizes a master microneedle array that was created using a microlens UV exposure technique. This master is used to create a polydimethylsiloxane (PDMS) mold. The mold is used to create polymer microneedle arrays with the same geometry as the master part. This method offers the advantage of being able to utilize a wide range of polymers and inexpensively create microneedle arrays. However, the cycle time for such a process is currently too slow to be economical and the PDMS molds can become degraded after repeated use (Park et al., 2007).

## Objective

This thesis explores a method of manufacturing micro-needle arrays through the use of injection molding and materials selection. Injection molding is believed to be a more economical method of producing microneedle arrays compared to typical silicon micro-fabrication methods and other methods currently being employed. Plastic microneedles also have an advantage in being easily disposable and possibly bio-degradable depending on the material used. This work is intended to show that injection molded micro-needle patches can be made to withstand the force of skin penetration and seeks to optimize needle spacing. This thesis presents results and conclusions of manufacturing, testing, simulation, and analysis of plastic injection molded micro-needle arrays.

## Thesis Outline

Chapter 2 discusses the background of this thesis and the technologies that currently exist for transdermal drug delivery. Skin properties, pain perception with microneedles, and current microneedle fabrication techniques are discussed.

Chapter 3 discusses the market potential and commercial viability of injection molded microneedles. This is accomplished by providing an in-depth cost analysis of manufacturing injection molded microneedles, exploring potential markets and uses of microneedles, and discussing the potential regulatory process for bringing a product to market.

Chapter 4 discusses the production of injection molded microneedle devices. The fabrication of the mold and microneedle features is outlined, as well as aspects of polymer selection and injection molding.

Chapter 5 discusses the testing performed to evaluate the performance of certain aspects of microneedles. This includes creating and testing devices to evaluate needle spacing of a microneedle device. The experimental apparatus and testing procedures for polymer microneedles in a silicone rubber skin simulant are discussed. Fabricated microneedles are evaluated for tip radius and height.

Chapter 6 presents the results of physical testing. These tests include results for needle spacing apparatus tests and polymer microneedle tests.

Chapter 7 interprets the results of physical testing. Needle spacing and various stages of penetration are analyzed to create a basic model. Aspects of tip radius, angle, and spacing are analyzed.

Chapter 8 presents an overall summary, conclusions of work performed, and recommendations for future work.

# Chapter 2

## Background

This chapter discusses the background of the project and the technologies that currently exist for transdermal drug delivery. Skin properties, pain perception with microneedles, and current microneedle fabrication techniques also are described.

## Skin Properties

Skin is the largest organ in the human body and is essential to survival because of its many functions. Skin must prevent harmful bacteria and chemicals from entering the body and also must avert water loss from the body. The skin is composed of several layers including the stratum corneum, living epidermis, dermis, and subcutaneous fat layer (Subramanyan, Misra, Mukherjee & Ananthapadmanabhan, 2007). Figure **2.1** shows a basic anatomy of each skin layer and the approximate thickness of each layer.

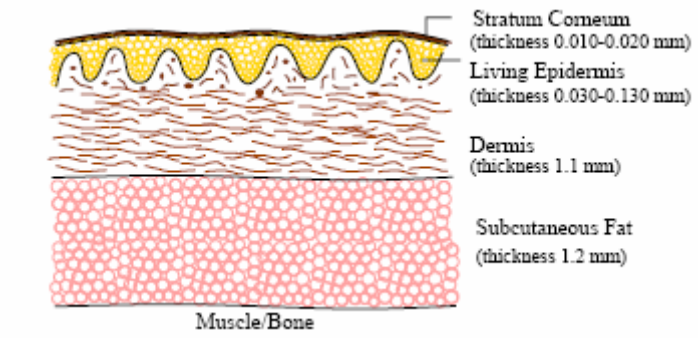


Figure **2.1**: Schematic of skin anatomy showing each layer of skin (Hendriks, Brokken, Oomens, Baaijens & Horsten, n.d.).

The top layer of skin called the stratum corneum is the body's main barrier to the outside environment. The stratum corneum is composed of non-living cells that are formed by the underlying living epidermis. The stratum corneum tends to be stronger and stiffer than the other skin layers (Subramanyan et al., 2007). The elastic modulus of the stratum corneum skin layer is estimated to be between ~6 and 2000 MPa depending on hydration, person, location, and other factors (Roxhed, Gasser, Griss, Holzapfel & Stemme, 2007). Figure **2.2** shows experimentally derived values for stratum corneum strength at three humidity levels.

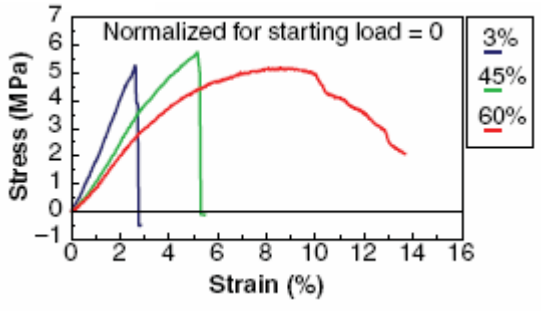


Figure **2.2**: Tensile strength of stratum corneum for various humidity levels (Subramanyan et al., 2007).

The next skin layer is called the living epidermis. Its role is to actively rebuild and repair the stratum corneum layer. The epidermis has no nerve or vascular network and relies on diffusion through the interstitial layer from the underlying dermis to provide nutrients (Wijaya Martanto, 2005, p. 5). The living epidermis is approximately 30 to 130 microns thick and has an elastic modulus of approximately 16 MPa (Busillo, 2008, p. 26).

The dermis layer is of great interest to the study of microneedles because this is where the first nerve cells are located. The dermis layer is approximately 1 to 2 mm thick

and contains many of the vital structures including nerve endings, blood vessels, and hair follicles (Subramanyan et al., 2007).

## Pain Perception with Microneedles

The perception of pain is expected to be minimal using microneedles as compared to using hypodermic needles. This is due to the minimal depth that microneedles penetrate into the skin as well as the diameter of individual needles. One study that attempted to quantify pain of hypodermic needle penetration into skin found that speed and angle of penetration do not make a statistical difference in pain perception. The only factor found to influence pain level was the needle diameter (Egekvist, Bjerring, & Arendt-Nielsen, 1999). This suggests that needle diameter has a direct effect on pain perception and smaller needles will be felt less than larger needles.

Studies have shown that microneedle insertion lacks the perception of pain. One such study sought to confirm the hypothesis that microneedles caused minimal pain sensation compared to traditional hypodermic needles. The study compared a 26-gauge hypodermic needle, a 400-needle microneedle array, and a smooth section of silicon in a blind study of 12 participants. The study confirmed with 95% confidence that microneedle sensation is virtually imperceptible and equal to that of smooth silicon, while the hypodermic needles inflicted a higher level of pain (Kaushik et al., 2001).

The lack of pain associated with a microneedle device is a great advantage over traditional injections that use hypodermic needles for drug delivery. Painful injections can deter some patients from seeking treatment due to a fear of needles. Approximately

10% of diabetic insulin users suffer from needle phobia that has been related to poor glycemic control which can result in negative long term side-effects (Egekvist *et al*., 1999, p. 42). Pain association with drug delivery transcends being just a matter of comfort and becomes medically pertinent for a patient's health and quality of life.

## Drug Delivery Methods

Several drug delivery methods have been studied using microneedle technologies. All of these methods share the goal of pain-free transdermal delivery of various drug therapies. A microneedle patch has the potential to provide controlled release of drug therapies as opposed to the peak and trough of drug concentrations resulting from conventional drug delivery methods (Moh *et al.*, 2009, p. 151). The drug delivery methods currently undergoing study include reservoir delivery through hollow tip microneedles, dissolving microneedles, microneedle skin pre-treatment with subsequent topical drug application, and coated microneedles.

Hollow tip microneedles have proved popular in academic research but have drawbacks that hinder the possibility of their clinical usage. Several groups and companies have explored the use of hollow tip microneedles through which the drug therapy is delivered into the skin (Khanna, Luongo, Strom, and Bhansali, 2010; McAllister, 2000; Moh *et al*., 2009). One disadvantage of a hollow tip microneedle delivery system is that all tips must penetrate into the skin for the fluid reservoir to be effective. If all needles on a device do not penetrate simultaneously, delivery of the drug therapy cannot be assured due to fluid leakage from the needles that have not penetrated

the skin. Another problem is that the narrow hollow passageways can become clogged with skin tissue and similarly hinder drug delivery. Nonetheless, hollow microneedles remain a widely studied topic due to the attractiveness of controlled release of drug therapies over longer time periods than other technologies.

Dissolving microneedle devices present another technology with obvious benefits. The efficacy of dissolving microneedles was demonstrated by Lee *et al*. In his study, proteins were encapsulated into a biocompatible polymer microneedle though the use of a novel centrifugal molding process. The microneedles were then successfully inserted into cadaver skin where results showed that the needle tips were almost completely dissolved within 15 minutes (Lee, Park and Prausnitz, 2008). Such a technology offers the advantage of having no medical waste after their application and does not require separate storage or reconstitution of the desired drug therapy. Drawbacks of this method may include the limited types of therapies that can be administered using such a method as well as the cost to produce the microneedle devices.

Microneedle skin pretreatment is another method that some research groups and companies have sought to employ for delivery of transdermal drug therapies. The idea behind this category of microneedle drug delivery is that piercing the skin and creating pathways through the stratum corneum will allow for more effective absorption of drug therapies into the body than untreated skin (Yan, Warner, Zhang, Sharma, and Gale, 2010). One advantage of skin pretreatment over other microneedle treatment options is the separation of the skin barrier penetration from the drug delivery. This allows the microneedle geometry to be optimized for mechanical penetration without regard for diffusion of the drug therapy into the body. There are two major disadvantages of this

method. First, delivery of treatments must be separated into two separate processes. This takes more time and allows for more error in effective drug delivery. Because of the separation of skin penetration from drug delivery, time-released treatments would not be feasible. Second, as Yan *et al.* explains, "Microneedle pretreatment would not be feasible for transdermal drug delivery if the skin recovers its barrier properties too quickly, resulting in a narrow window for drug delivery" (Yan *et al*., 2010, p. 11). This may preclude using certain high molecular weight drug therapies if the skin recovers too quickly from pretreatment. Other uses for skin pretreatment include its use for improving the effectiveness of topical anesthetic (Li *et al*., 2010).

Coated microneedle therapy is the final method being studied for drug delivery. This method involves fabrication of solid microneedle devices and subsequent coating of a particular drug onto the needle tips. Coated microneedles are popularly studied by university groups and companies due to their feasibility in delivering drug therapies. One advantage to coated microneedles is that, unlike skin pretreatment, skin penetration and drug delivery occurs in one step. This allows for the development of microneedle patches that can release their drug payload over time. Unlike dissolving microneedles that can use only specific biocompatible materials, coated microneedles could conceivably be fabricated from any material, provided the drug coating can be made to adhere to the needles.

The delivery of influenza vaccine via coated microneedles is an area of research interest that has garnered much attention. One group has successfully proven the efficacy of vaccine administration using coated microneedles. This was achieved by a creating a small microneedle array from laser cut stainless steel and manually dip coating the array

into a solution containing the inactivated flu virus. The solution was developed for its biocompatibility so that it could be dissolved in the skin within a few minutes. Results showed that the microneedle administered flu vaccine was effective in producing a strong antibody response and effective protection against infection (Koutsonanos et al., 2009; Zhu et al., 2009). The demonstrated value of coated microneedle drug delivery can be extrapolated to other microneedle shapes and materials. The methods demonstrated for transdermal vaccine delivery may enable the future use of lower cost injection molded polymer microneedle devices in the future.

## Microneedle Fabrication Techniques

As discussed briefly in Chapter 1, there are many techniques for producing microneedles that have been explored to date. These methods include many processes and techniques that come directly from microelectronics and MEMS fabrication industries. Other techniques include various polymer molding techniques that are used for repeated replication. These fabrication methods normally employ high-tech methods of producing structures that can be expensive due to the time involved and the high cost of materials and equipment. The goal of each fabrication method is to produce high quality sub-micron tips that are sharp and mechanically strong enough to resist the stress of skin penetration.

**Silicon Micro-fabrication**

Silicon fabrication methods have been widely employed in the fabrication of microneedles. The microelectronics industry has mastered these manufacturing techniques to mass produce computer chips. A number of useful microelectromechanical systems (MEMS) devices that include everyday products like accelerometers, printer components, and light projection equipment all employ silicon fabrication methods in their manufacture. This fabrication method is flexible in that it can be used to create a variety of structures and shapes and can create both hollow and solid microneedles.

The basis of silicon micro-fabrication is photolithography. Photolithography is a process that involves using light-sensitive materials to selectively add and remove material from a silicon substrate. Many processes begin with a silicon wafer that is covered with an oxide layer. The wafer is coated with a photo-sensitive resist material that is cured. The wafer is exposed to a high intensity UV light that contains a pattern. The transferred pattern area can be removed or retained, depending on the type of photoresist. The wafer is etched, normally with acid, and the remaining pattern areas are protected from the etchant to create desired structures. Various processing methods can be utilized to create the desired structures and must take into account crystal planes that etch at different rates (Madou, 2002).

Many research groups that focus on microneedles have fabricated them using silicon micro-fabrication processes. One group has attempted to overcome certain fabrication limits by using deep reactive ion etching (DRIE), for high aspect ratio

structures, in combination with a dicing saw for tip shaping. Figure **2.3** shows an example of the structures that were created using this method.

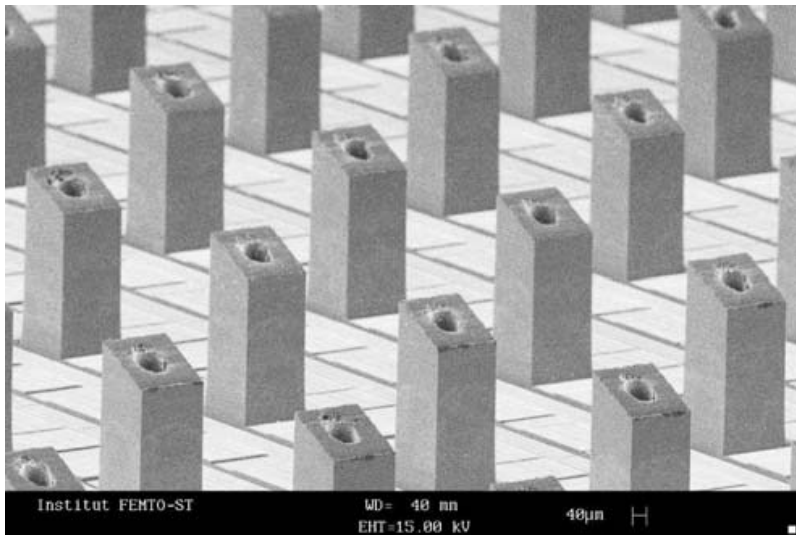


Figure **2.3**: Square shaped microneedle array created using DRIE and dicing saw (Shikida, Hasada, & Sato, 2006)

Other problems that exist with silicon microneedles are their brittle nature and their tendency to break easily. The silicon tips can break off in the skin upon insertion and cause infections. One solution to this problem was to create a silicon main structure with a biodegradable porous silicon tip (Chen, Wei, Tay, Wong & Iliescu, 2008). This solves one problem with silicon micro-fabrication, but does not overcome the high cost of producing such structures.

**Metallic Miconeedles**

Metallic microneedles have been demonstrated in two different forms. In one form the microneedles are created by first creating a polymer mold using laser micromachining. The mold is then coated with a conductive seed layer and

electrodeposited with metal such as nickel, nickel-iron, or gold. The microneedle array is released from the mold using a wet etching process (Davis, Martanto, Allen & Prausnitz, 2005). Figure **2.4** shows an array of microneedles created using the aforementioned process. This process does have the advantage of being less expensive than other methods due to the use of mylar for the mold instead of the more expensive silicon and does not require as much expensive equipment.

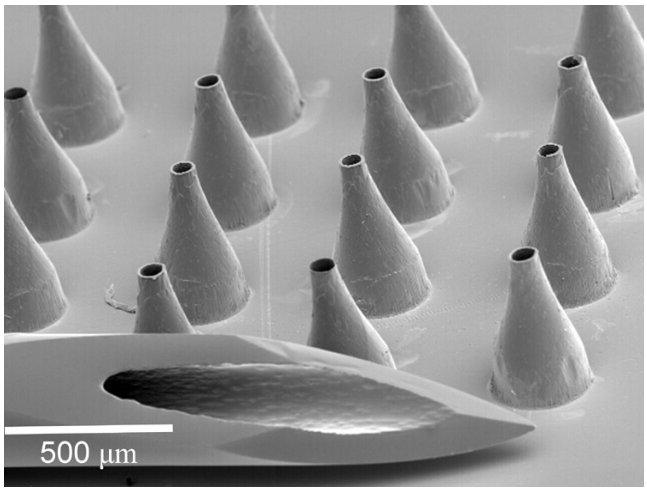


Figure **2.4**: Array of hollow electrodeposited metallic microneedles next to a 27-ga hypodermic needle (Davis et al., 2005, p. 912).

Another method for creating metallic microneedles involves shaping titanium to create a sharp, solid microneedle array. Manufacturing for this type of array is performed by coating a thin sheet of titanium with a photoresist. The photoresist is exposed and developed to create the desired pattern. The titanium is selectively etched so that the microprojections can be released on all but one side. Finally, the projections are bent at 90 degrees to create a pattern of out-of-plane solid microneedles. Figure **2.5** shows an SEM micrograph of such a microneedle array. An array like this has been tested in

limited animal studies with several medications and immunizations (Martanto, 2005; Matriano et al., 2002).

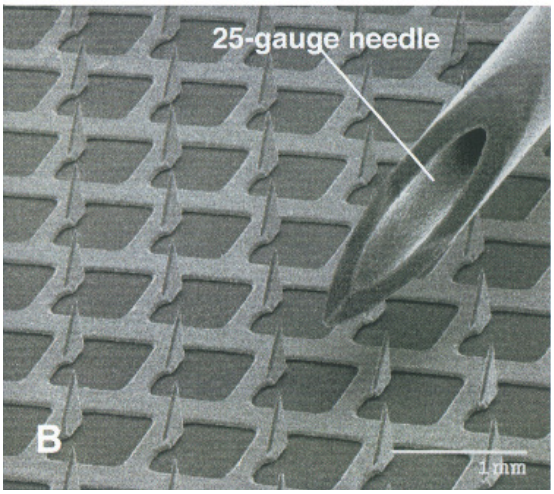


Figure **2.5**: Array of titanium microprojections shown next to a 25-ga hypodermic needle for comparison (Matriano et al., 2002, p. 64).

Metallic microneedles offer certain distinct advantages over certain competing microneedles that have been researched for various reasons. Metals such as titanium and stainless steel have long been employed for clinical uses due to their biocompatibility. Their mechanical strength also lends itself well to application in microneedle applications. However, the methods of manufacture continue to be cost prohibitive compared to hypodermic needles.

## LIGA

LIGA is a German acronym that stands for LIthographie, Galvanik, and Abformung. In English this translates to lithography, galvanizing (electroplating), and molding. In this process high aspect ratio structures, like microneedles, can be produced

with high quality results. The process is recognized as the most expensive micro-fabrication process due to its need to employ synchrotron radiation for resist development. Once a structure has been created using LIGA, the idea is to reuse a metallic mold created by the process to repeatedly create replica structures to a master (Madou, 2002). Figure **2.6** shows one such array of hollow microneedles created using a LIGA process.

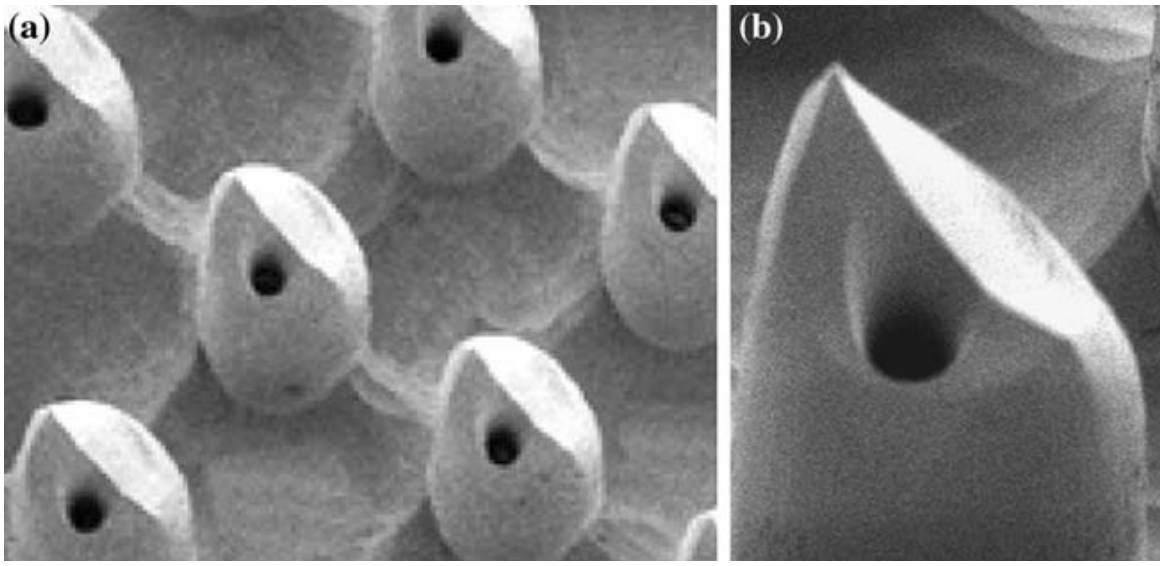


Figure **2.6**: SEM micrographs of structures created using LIGA process (Khumpuang, Horade, Fujioka & Sugiyama, 2007).

**Polymer Molding**

Several techniques have been studied for the creation of microneedles using polymer molding techniques. These techniques have taken the form of PDMS molding, laser fabrication, and injection molding.

PDMS molding has been extensively studied by one research group that uses more traditional silicon micro-fabrication methods to create the master structures. These eventually are used to create polydimethyl siloxane (PDMS) molds which can be filled with various polymers to create replicate parts. Several advantages exist with this method including relatively low material and process costs and the ability to utilize biocompatible polymers (Park, Allen & Prausnitz, 2005). Figure **2.7** shows SEM micrographs of microneedle arrays that were created using micro replication molding of polymers.

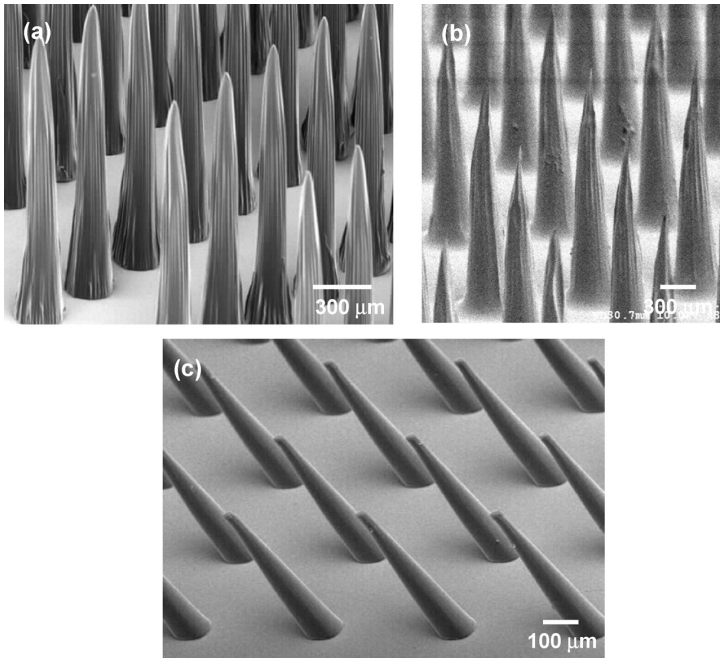


Figure **2.7**: SEM micrographs of biodegradable polymer microneedles of various lengths and sizes (Park, Yoon, Choi, Prausnitz & Allen, 2007, p. 908).

Laser fabrication is another method that has been employed to assist in microneedle fabrication for polymeric needles. In one example of this, a single solid needle is made using a silicon mold with a simple process similar to injection molding.

The needles are then post-processed using an excimer laser to create features on the part. Both jagged and trenched microneedles have been made using this process that uses the needles for blood sampling (Aoyagi, Izumi, Isono, Fukuda & Ogawa, 2007). Figure **2.8** shows one of the jagged needles that has been created using the laser fabrication process.

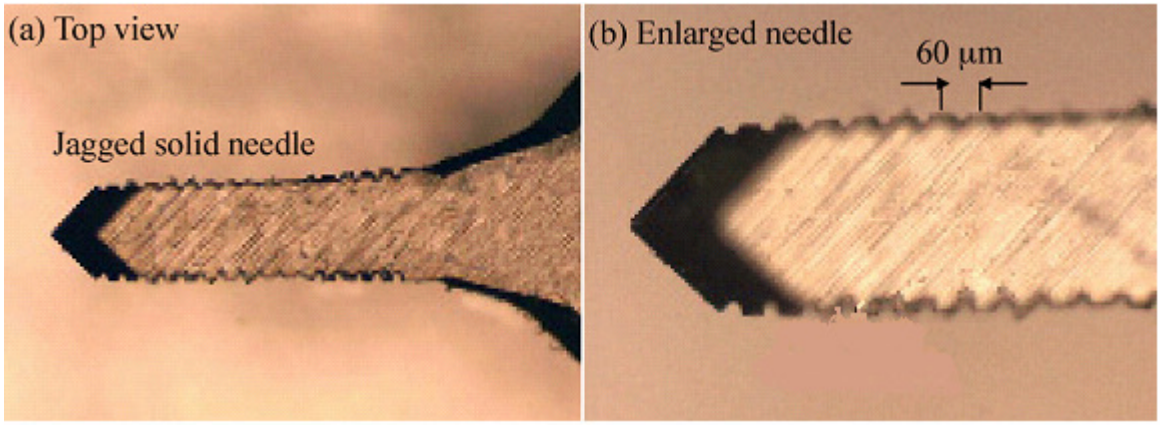


Figure **2.8**: Optical micrographs of finished microneedle parts created using a laser fabrication process (Aoyagi et al., 2007, p. 299).

Another process to create microneedles that has had limited research exposure is injection molding. Injection molding is the main focus of this research due to its cost effectiveness, repeatability, and capability to make quality parts quickly.

One research group has successfully created microneedles using an injection molding process. In their research, they created a single in-plane needle with an open channel and reservoir design (Sammoura, Kang, Heo, Jung & Lin, 2007). The in-plane nature of this design eases mold fabrication. Figure **2.9** shows the basic layout of this design that is created using injection molding.

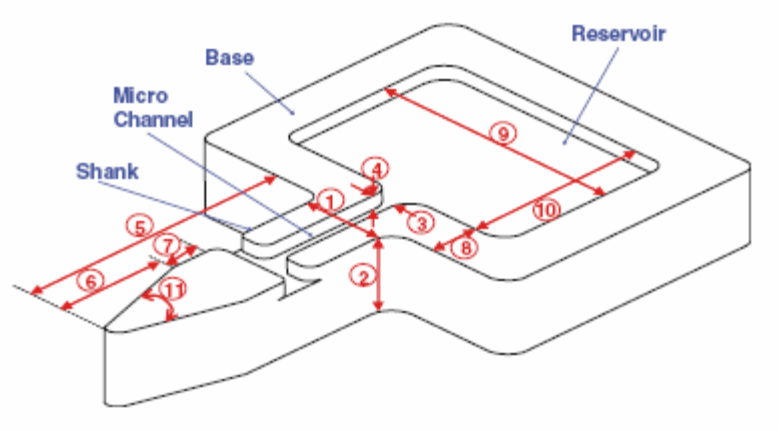


Figure **2.9**: Layout of single in-plane microneedle made by injection molding (Sammoura et al., 2007, p. 519).

The process for creating the single needle used Topas® COC from Ticona to create the desired structures. The needles were successfully fabricated using this process and were subsequently tested. Testing using chicken legs showed that the needle could successfully penetrate flesh and liquid was drawn through the microchannel (Sammoura et al., 2007). Figure **2.10** shows SEM micrographs of finished single microneedles created by injection molding.

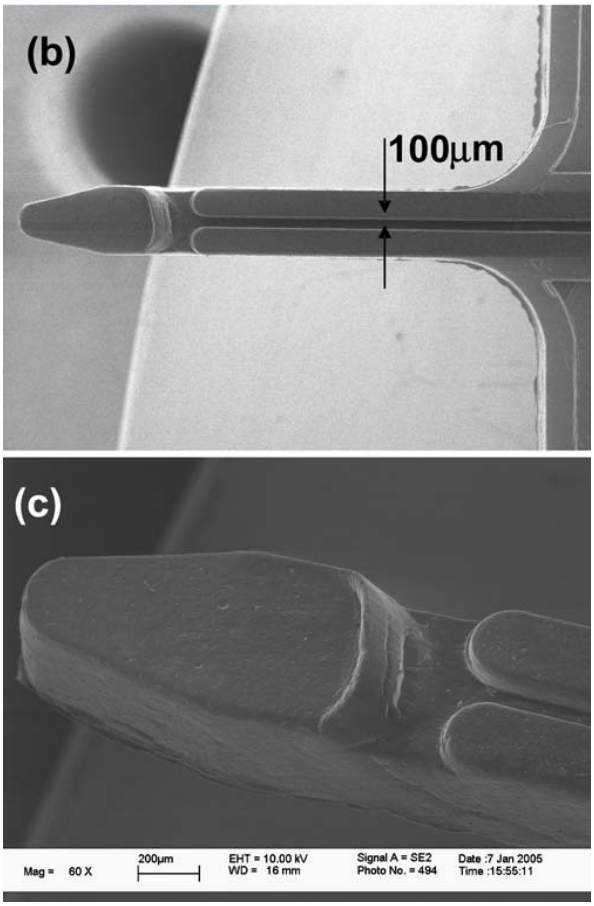


Figure **2.10**: SEM micrograph of finished microneedle structure (Sammoura et al., 2007, p. 520).

Injection molding is a good technique for creating in-plane single needle structures, but creating large arrays of needles out-of-plane needles is expected to be more difficult due to the intricacy of creating the molds for such a process. One goal of this thesis is to create out-of-plane microneedle arrays using injection molding and prove its cost-effectiveness compared to other manufacturing methods. Figure **2.11** shows representations of the four microneedle device patterns created for this project. These include microneedle patterns arranged in 1 mm square, 1.5 mm square, 1 mm hexagonal, and 1.5 mm hexagonal forms.

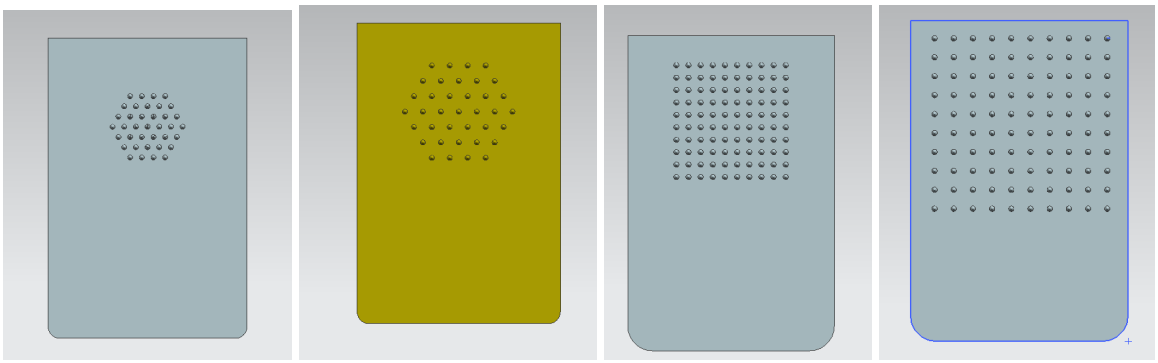

Figure **2.11**: Representations of the four microneedle device patterns created including from left 1.0 mm hexagonal, 1.5 mm hexagonal, 1.0 mm square, and 1.5 mm square.

Closer examination of one of the microneedle devices used for this project can be seen in Figure **2.12**. This shows a 1.5 mm square pattern in front and side views. These are labeled and dimensioned showing the attributes of the device. Further description of the devices, fabrication methods, and materials will be provided in later chapters.

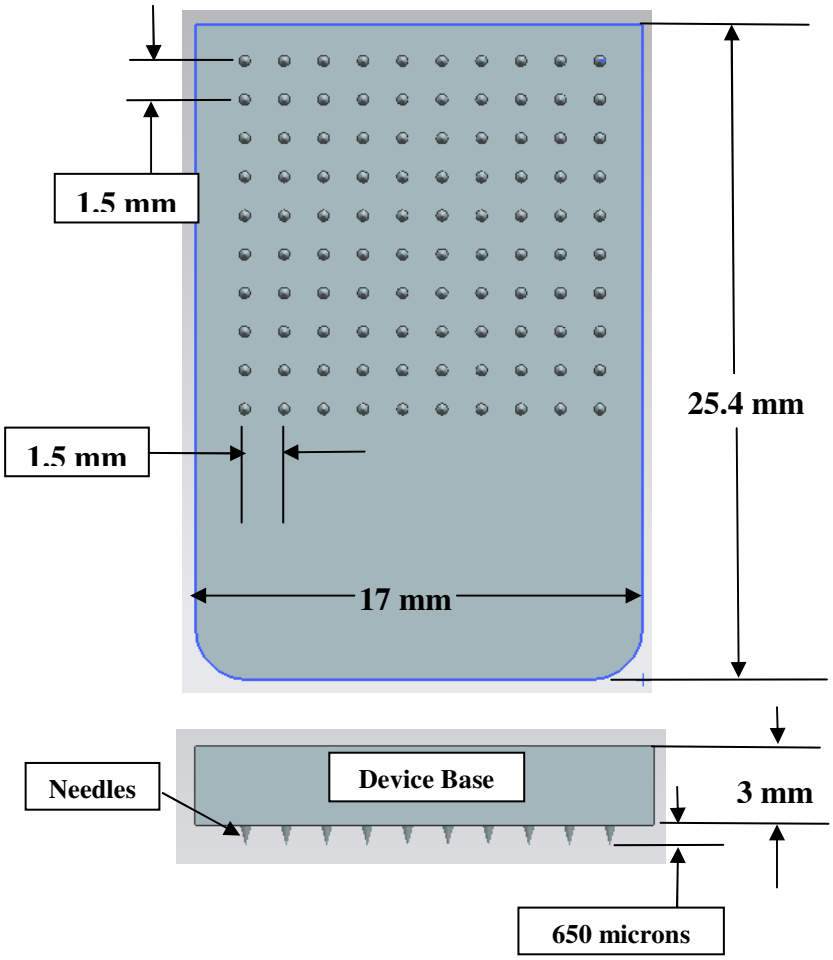


Figure **2.12**: Representation of 1.5 mm square microneedle device labeled for various device attributes and dimensions.

The background of this project and the technologies that currently exist for transdermal drug delivery have been discussed. Skin properties, pain perception with microneedles, and current microneedle fabrication techniques were also described. Chapter 3 describes aspects of marketability and part costs for polymer microneedle devices.

# Chapter 3

## Market Potential and Economics of Injection Molded Microneedle Patches

The total piece cost of a finished microneedle is an important area of discussion. The future viability of microneedles in the marketplace depends on their ability to deliver superior overall value to a customer. One microneedle researcher suggests that microneedle part costs must be below $1.00 and ideally below $0.10 to be marketable (Park, Yoon, Choi, Prausnitz & Allen, 2007). Microneedles may not need to cost less than hypodermic needles because of the added value brought to consumers by lower pain sensation, but lower part costs would result in broader market acceptance. This chapter will discuss part costs of injection molded microneedles, comparisons to other drug delivery methods, and the steps required for regulatory approval before such parts could come to market.

## Injection Molding Cost Estimation

Precise cost estimates are difficult because they include many factors that are difficult to assess. Machine size, molding cycle time, operating costs, and mold costs can be highly variable and will be estimated using techniques developed for Design for Manufacture and Assembly (DFMA). The book *Product Design for Manufacture and Assembly: Second Edition* will be used for injection molding cost estimation (Boothroyd,

Knight & Dewhurst, 2001). Actual part molding conditions developed for the manufactured microneedle parts will also be used to develop a part cost estimate.

**Mold Cost Estimate**

Mold costs can be broken into two major categories that include the cost of the mold base components and the cavity and core fabrication costs (Boothroyd *et al*., 2001, p. 359). The mold base is usually prefabricated and includes the plates, bushings, pins, and other normal parts used in all molds. The base cost is estimated as a function of the area of the mold base, $A_c$ ($cm^2$), and the combined cavity and core plate thickness, $h_p$ (cm). This is represented by Eq. **3.1** (Boothroyd *et al.*, 2001, p. 359).

$$C_b = 1000 + 0.45 A_c h_p^{0.4} \qquad \text{Eq. } \mathbf{3.1}$$

Eq. **3.1** yields a cost of $2161 when dimension from Table **3.1** is used. This mold size would be suitable for a nine cavity mold with a two plate mold. Such a mold layout would look like the one shown in Figure **3.1**. Each mold cavity would house the microneedle features.

Table **3.1**: Base mold dimensions used to calculate base mold costs.

| **Mold Base** | | |
|---|---|---|
| Mold Base Area ($cm^2$) | Mold Base Thk (cm) | Cost ($) |
| 610 | 5 | $2,161 |

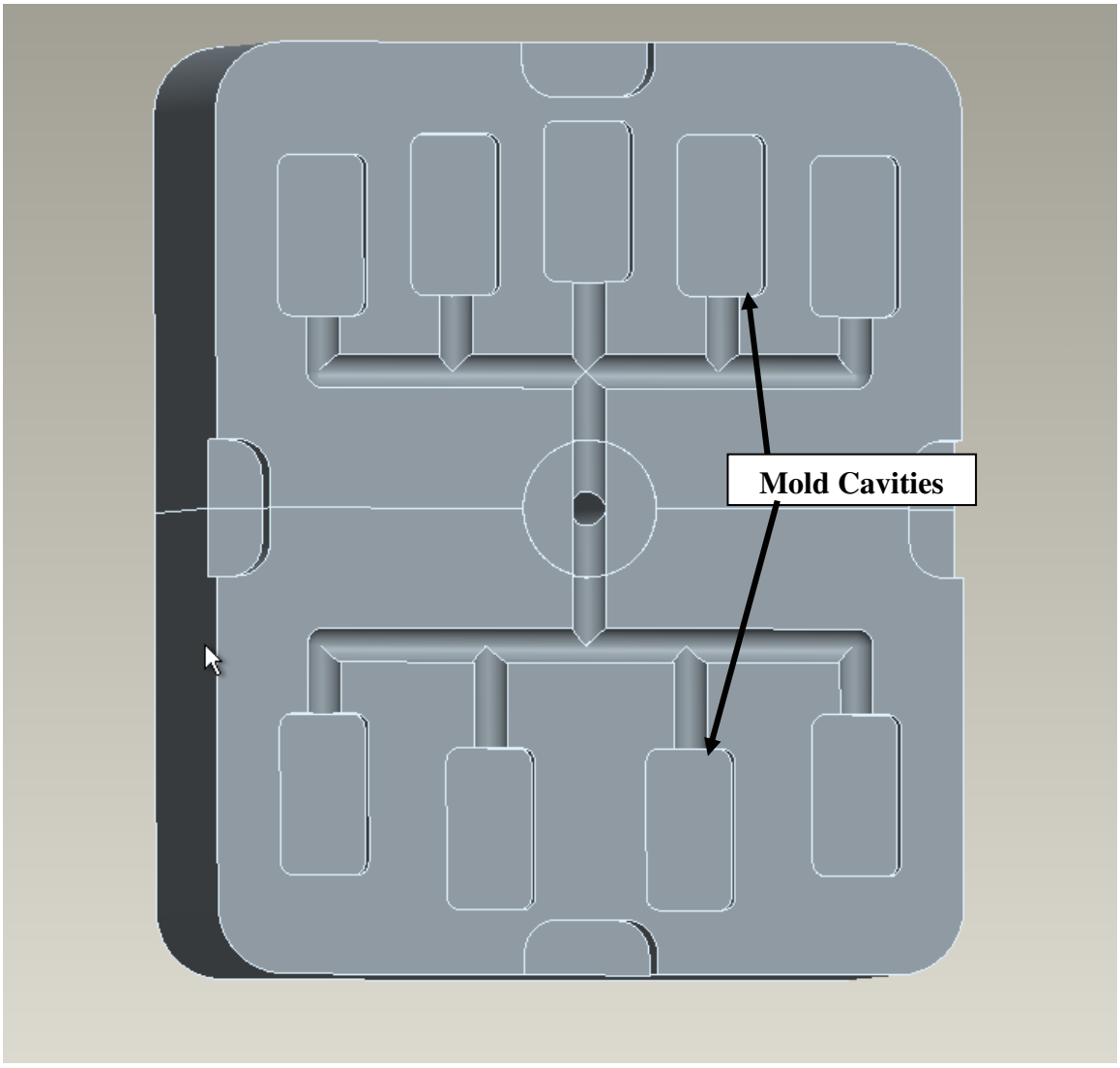


Figure **3.1**: Representation of a two plate, nine cavity mold layout.

The other major cost associated with mold fabrication is the cost to make the cavity and core. Fabrication of the cavity and core for the microneedle parts involves creating tools, drilling, micro-forging, milling operations, ejector plate and pin customization, and any cooling or electrical systems that may be incorporated. The representation shown in Figure **3.2** displays a complete listing of parts used in injection molds.

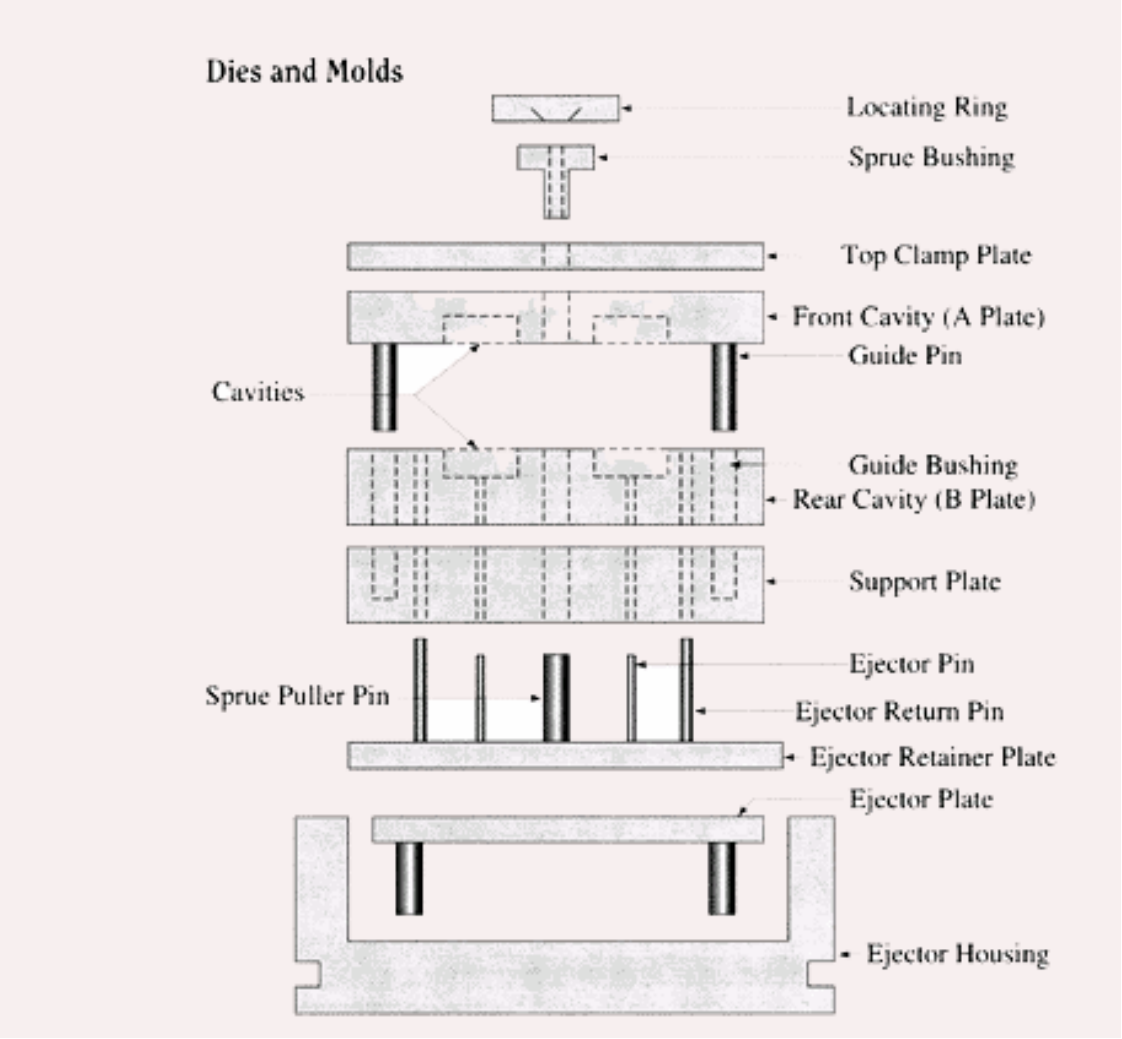


Figure **3.2**: Diagram of parts used in polymer injection molds (Strong, 1996).

There are two ejector pins used for each part cavity. The cost estimate for ejector pins includes the number of pins and estimates 2.5 hours for each pin (Boothroyd *et al.*, 2001, p. 362). This results in 45 hours of machining time being required for a nine cavity mold.

The next constituent mold cost deals with part complexity and how it relates to machining time. Approximating the number of machining hours based on complexity requires some judgment regarding particular appearance, tolerance levels, and geometric

complexity concepts that are difficult to assess. The estimate generated for the number of machining hours for the cavities and cores will be a combination of guidelines set forth by the book *Product Design for Manufacture and Assembly*, as well as knowledge from experience gained while machining the microneedle molds.

The geometric complexity of the mold is estimated by Eq. **3.2** (Boothroyd *et al.*, 2001, p. 362).

$$M_x = 5.83\left(X_i + X_o\right)^{1.27} \qquad \text{Eq. } \mathbf{3.2}$$

This equation gives the number of machining hours in terms of inner and outer part surface complexity. Each of these complexity assignments ($X_i$ and $X_o$) is given a value that is accounted for by Eq. **3.3** (Boothroyd *et al.*, 2001, pp. 363 - 364).

$$X_i = 0.1N_{spi} \text{ and } X_o = 0.1N_{spo} \qquad \text{Eq. } \mathbf{3.3}$$

The values for $N_{sp}$ are simply the number of surfaces on the inside (i) and outside (o) of the part. For the microneedle molds, the number of inside surface is equal to zero because the parts are solid and have no core. The only outside features to be counted are the microneedle features, as the other features will be accounted for in a later equation. Additionally, identical part features are reduced by a power index of 0.7 to account for time savings. The microneedle features are machined twice using different tools and techniques. There are 1800 duplicate outside features; Eq. **3.2** is then filled in with the required values and shown in Eq. **3.4**. This suggests that 245 hours will be required to machine the microneedle features.

$$X_o = 0.1\left(1800\right)^{0.7} = 19 \;;\; M_x = 5.83(19)^{1.27} = 245\,hours \qquad \text{Eq. } \mathbf{3.4}$$

To machine the basic mold shape, excluding the microneedle features, Eq. **3.5** can be used (Boothroyd *et al*., 2001, p. 364).

$$M_{po} = 5 + 0.085\left(A_p\right)^{1.2} = 5 + 0.085\left(45.9\right)^{1.2} \approx 13\,hours \qquad \text{Eq. } \mathbf{3.5}$$

Summing the machining time for ejector pins, microneedle features, and simple part shape features results in a base estimate of 303 manufacturing hours. Other considerations include the need for higher quality surface finish and tighter dimensional tolerance. These other factors add additional manufacturing time as a percentage of the sub-totaled core and cavity costs. Table **3.2** uses the methods described by Boothroyd and estimates total mold costs at $19,735 using $40 per hour for mold manufacturing (Boothroyd *et al*., 2001, pp. 365-369). A mold of this type could be expected to last approximately 500,000 shots based on the materials used and the complexity of the mold features.

Table **3.2**: Constituent and total costs for purchasing and machining injection molds.

| | Description | Hours | Cost |
|---|---|---|---|
| **Base Mold Components** | Plates, Bushings, Pins, etc. | --- | $2,161 |
| **Core & Cavity Manufacturing** | Ejector Pins | 45 | $1,800 |
| | Geometric Complexity | 245 | $9,800 |
| | Basic Mold Shape | 13 | $520 |
| | Sub-Total | 303 | $12,120 |
| **Additional Factors** | Finish - Opaque high gloss (25%) | 75.75 | $3,030 |
| | Tolerance - +/- 0.05 mm (20%) | 60.6 | $2,424 |
| | **Overall Total** | 439.35 | $19,735 |

**Material Cost Estimate**

Material costs per part will depend on part volume, runner and sprue volume, and material cost. Several materials have been explored for this project and will be examined in this section. Table **3.3** shows the volume attributed to each part including the part itself, the runner, and the portion of the sprue for a nine cavity mold.

Table **3.3**: Volume of plastic needed for each part including the microneedle part, runner, and sprue.

| Part Volume ($cm^3$) | Runner Volume ($cm^3$) | Sprue Volume ($cm^3$) | Total/part ($cm^3$) |
|---|---|---|---|
| 1.53 | 0.12 | 0.52 | 2.17 |

Next, the volume information is combined with information about each that was used. Table **3.4** shows part cost for each of seven materials (Peterson, 2009). The material cost is highly dependent on the type of material used and ranges from less than one penny for commodity polymer like polystyrene, to nearly $0.08 per part for an engineering plastic such as liquid crystal polymer.

Table **3.4**: Material cost for each part based on cost per pound and density.

| Material | Density (g/cm^2) | Mass per Part (g) | Cost ($/lb Approx) | Part Cost ($) |
|---|---|---|---|---|
| **Polystyrene** | 1.04 | 2.26 | $1.12 | $0.006 |
| **LCP Vectra A130** | 1.62 | 3.52 | $10.17 | $0.079 |
| **COC 8007x10** | 1.02 | 2.22 | $7.55 | $0.037 |
| **COC 5013s04** | 1.02 | 2.22 | $6.70 | $0.033 |
| **Makrolon 2207 PC** | 1.20 | 2.61 | $4.88 | $0.028 |
| **IXEF 1022** | 1.64 | 3.56 | $9.50 | $0.075 |

**Processing Cost Estimate**

Processing costs are directly related to the amount of processing time required for each part. Processing time includes injection time, hold time, cooling time, and ejection time. Although each type of polymer is different, the processing time is approximately 60 seconds for all grades used as measured during the injection molding of 100-needle solid microneedle devices. This cost estimate includes the machine costs, machine operator's salary, and associated overhead costs. The processing rate is highly dependent on the clamp force and can be represented by Eq. **3.6** (Boothroyd *et al*., 2001, p. 371). The equation is based on machine rates, represented by $k_1$ and $m_1$, and clamp force in kN, represented by F.

$$C_r\,(\$/hr) = k_1 + m_1 F \qquad \text{Eq. } \mathbf{3.6}$$

Using Eq. **3.6** and determining the clamp force and using \$25/hr for $k_1$ and \$0.0091/hr for $m_1$ yields the results shown in Table **3.5.** Processing cost per microneedle patch in its current form is estimated to be \$0.055. The injection pressure is determined to be approximately 1100 kg-cm$^2$ based the average injection pressures specified by the manufacturers of the polymers used. This is reasonable based on the specifications available from Sumitomo for current generation injection molding machines that have maximum injection pressures of 1700 – 2800 kg-cm$^2$ (Sumitomo, 2009). Based on this injection pressure and projected part area, the required clamping force is determined to be 61.15 Tons; this is a reasonable clamping force for the 75-ton Sumitomo injection molding machine.

Table **3.5**: Estimated processing cost per part using Eq. 3.6.

| Injection Pressure (kg-cm^2) | Proj Area (m^2) | Clamp Force (Tons) | Cost ($/hr) | Cost per Part ($) |
|---|---|---|---|---|
| 1100 | 0.00504 | 61.15 | $29.95 | $0.055 |

**Total Part Cost Estimate**

Adding together each of the constituent costs will yield the estimated cost per part shown in Table **3.6**. The part cost is shown to be between $0.10 and $0.179 per microneedle array.

Table **3.6**: Total cost per microneedle part and constituent costs.

| Description | Total Cost | Part Cost |
|---|---|---|
| **Mold (500,000 shot life)** | $19,735 | $0.039 |
| **Material** | $1.12 - $10.79 per lb | $0.006 - $0.079 |
| **Operations** | $29.95 per hr | $0.055 |
| **Total** | --- | $0.10 - $0.179 |

This estimate is based on a number of factors and actual costs can be highly variable. Polymer prices can vary based on petroleum costs to the manufacturer and bulk price discounts offered to customers that order large amounts. Processing costs can vary based on several factors. The processing cost includes both machine and manpower costs. The associated salary and benefit costs are highly dependant on the market rates of the country where the parts are manufactured. Mold costs are also highly variable depending on the manufacturing location and expertise of the mold maker. The cost estimate is designed to give a rough idea of manufacturing costs to determine the marketability of such a product.

The estimated cost of a single microneedle patch is competitive compared to other technologies available for drug delivery. As previously mentioned, a cost below $1.00, and ideally below $0.10, is a prerequisite for marketability. The estimated cost for producing microneedles with injection molding makes it possible for the technology to be commercially viable. Hypodermic needle and hub without the syringe cost between $0.09 and $0.23, depending on needle length and gauge (Allegro Medical Supplies, Inc., 2009). Most other microneedle manufacturing technologies are highly dependant on silicon manufacturing techniques, which are generally very expensive due to the equipment, materials, and processing steps involved. The estimated cost for an injection molded microneedle patch may allow it to compete against other technologies in the commercial marketplace.

## Potential Market Size

The market potential for an injection molded microneedle patch is very large. A number of medications and drug therapies could be delivered via microneedles rather than via hypodermic needles or oral drug delivery. The effect of a pain-free method of drug delivery also has the potential to increase the regularity of prescribed medication use amongst patients.

The global market for syringes in 2002 was estimated to be worth approximately $3.6 billion with an expected growth around 5% annually (Dorlands Directories, 1999). In developing countries, approximately 16 billion injections are given each year. Of these, about 5% account for vaccinations while the remainder account for curative

medicine, blood transfusions, and other care (WHO Press Office, 2002). Plastic microneedles have the potential to capture at least some portion of this market. Microneedles have the demonstrated ability to offer painless delivery of certain types of medicines that would normally be delivered via traditional hypodermic needle or via the gastrointestinal tract. Studies have shown that microfabricated needle arrays cause a pain sensation which is statistically indistinguishable from a smooth piece of silicon (McAllister, 2000, p. 130). The market for similar devices, transdermal patches such as those used to deliver nicotine, nitroglycerine, and birth control was estimated at $1.4 billion in 1997, displaying a great interest in simple, pain-free drug delivery technology (McAllister, 2000, p. 11).

Certain therapies have been identified which may be equally or more effective when administered using microneedles. These include insulin for diabetes, erythropoietin for anemia, calcitonin for osteoporosis, and Heparin in its use as an anticoagulant (McAllister, 2000, p. 57). *In vivo* insulin administration using metal microneedles has been demonstrated to lower blood glucose levels by as much as 80% in diabetic rats (Martanto, 2005, p. 81). Plastic microneedles would be expected to have the same effect. The U.S. Centers for Disease Control and Prevention estimate there are approximately 20.6 million diabetics in the United States alone with an additional 54 million people showing signs of pre-diabetes. Of the 14 million Americans diagnosed with diabetes, approximately 28% are estimated to use insulin to help control their diabetes (Centers for Disease Control and Prevention, 2007). Such insulin users could benefit from a pain-free method of injection. Table **3.7** shows selected medications and treatments that have potential for use in conjunction with microneedle arrays. The table shows a huge

potential market for microneedle devices based only on the selected treatments. Plastic microneedle devices have the potential to offer an inexpensive, highly effective, and pain-free method of drug delivery with a great market outlook.

Table **3.7**: **Needle and market size for selected medications**

| Medical Name | Trade Name(s) | Therapeutic Use | Approx. Drug Market Value | Est. Current Number of Users | Est. Potential Number of Users | Annual Needle Usage Potential |
|---|---|---|---|---|---|---|
| Insulin | Humulin<br>Lantus<br>Humalog | Diabetes | $4.4 billion | 4 million (US) | 120 million (Worldwide) | 43 billion |
| Erythropoietin | Arenesp<br>Procrit<br>Epogen, etc. | Anemia | $11.5 billion | Unknown | 3.4 million (US) | 530 million |
| Calcitonin | Miacalcin | Osteoporosis | $300 million | Unknown | 10 million (US)<br>42 million (Worldwide) | 3.7 billion (US) |
| Heparin | Lovenox<br>Clexane | Anticoagulant | $3.1 billion | Unknown | Unknown | Unknown |

Other therapies that may be considered for administration by microneedles include certain vaccines. The forecasted US vaccine market for 2007 is estimated to be worth more than $2.8 billion (Datamonitor, 2002). Around 58% of the vaccine market is represented by pediatric vaccines which are administered to approximately 4 million children annually (Centers for Disease Control and Prevention, 2007). Some of this vaccine administration market could be also captured by plastic microneedle devices.

Overall, there exists a large market for plastic microneedles. Given their advantages over traditional hypodermic needles and microneedles manufactured with MEMS techniques, plastic injection molded microneedles have the potential to capture a significant portion of the drug delivery market.

## Regulatory Approval

FDA approval would be required before commercially marketing a plastic microneedle device. Approval could be accomplished in one of two ways. The easier and faster method would be through the 510(k) approval process. This method involves submitting evidence of substantial equivalence with another currently marketed and Food and Drug Administration (FDA) approved device. This submission must be received by the FDA at least 90 days prior to the start of commercial distribution. According to the FDA, "Substantial equivalence is established with respect to: intended use, design, energy used or delivered, materials, performance, safety, effectiveness, labeling, biocompatibility, standards, and other applicable characteristics" (Food and Drug Administration, 2003).

Although there are no known microneedle arrays or patches currently on the U.S. market, several companies are actively working on functioning designs using integrated circuit fabrication techniques. These devices would be expected to receive approval and could act as a predicate device for approval of the proposed plastic microneedles. A material such as liquid-crystal polymer which has already received a USP Class VI rating could be used for the proposed product. It is also worth noting that some of the polymers used in this project have grades available with USP Class VI ratings. These polymers are currently used in surgical devices and have the highest rating available from USP for tissue contact.

A full FDA Premarket Approval of a Class III medical device would be required if substantial equivalence cannot be established prior to launching the product. This

process involves a number of steps and requires information such as safety and effectiveness data, nonclinical data, clinical data, and other information to document the device's acceptability (FDA, 2003).

This chapter has discussed the market potential and commercial viability of injection molded microneedles. A cost analysis of manufacturing injection molded microneedles was performed. Potential markets that may use polymer microneedle drug delivery devices were discussed. Finally, the regulatory approval process for bringing a product to market was outlined. Chapter 4 will describe the fabrication process for injection molding polymer microneedle devices.

# Chapter 4

## Injection Molding Solid Plastic Microneedle Devices

Many methods for successfully fabricating microneedles were discussed in Chapter 2. This chapter focuses on using injection molding to quickly create high quality microneedle patches. Injection molding offers several advantages over other methods of fabrication because it is cost effective, fast, consistent, and is an existing technology used for manufacturing many medical products. There are challenges in creating such small part features using injection molding. The largest challenge is creating negative part features in a mold that are sufficiently small to create sharp needle tips. This chapter will discuss each aspect of injection molding microneedle patches.

## Injection Molding Equipment

This project utilized a Sumitomo SG75 (Japan 1988) injection molding machine to create the desired microneedle patches. The machine is located in the high bay laboratory of the Manufacturing Research Center on Georgia Tech's Atlanta campus. The injection molding machine has a three ounce shot capacity and can be used to mold a wide variety of polymers. Figure **4.1** shows the injection molding machine.


Figure **4.1**: Sumitomo Sycap SG-75 75 Ton Injection Molding Machine

**Mold**

Custom mold parts were created for the machine so that small mold inserts could be easily replaced and changed as necessary. A set of solid model CAD renderings were created to easily modify the molds and various parts that were needed for completion of the project. Figure **4.2** shows the mold layout. This layout allows for two mold inserts to be placed in the machine at one time. Ejector pins were placed in the mold runners and in the microneedle part cavity to eject parts from the molds.

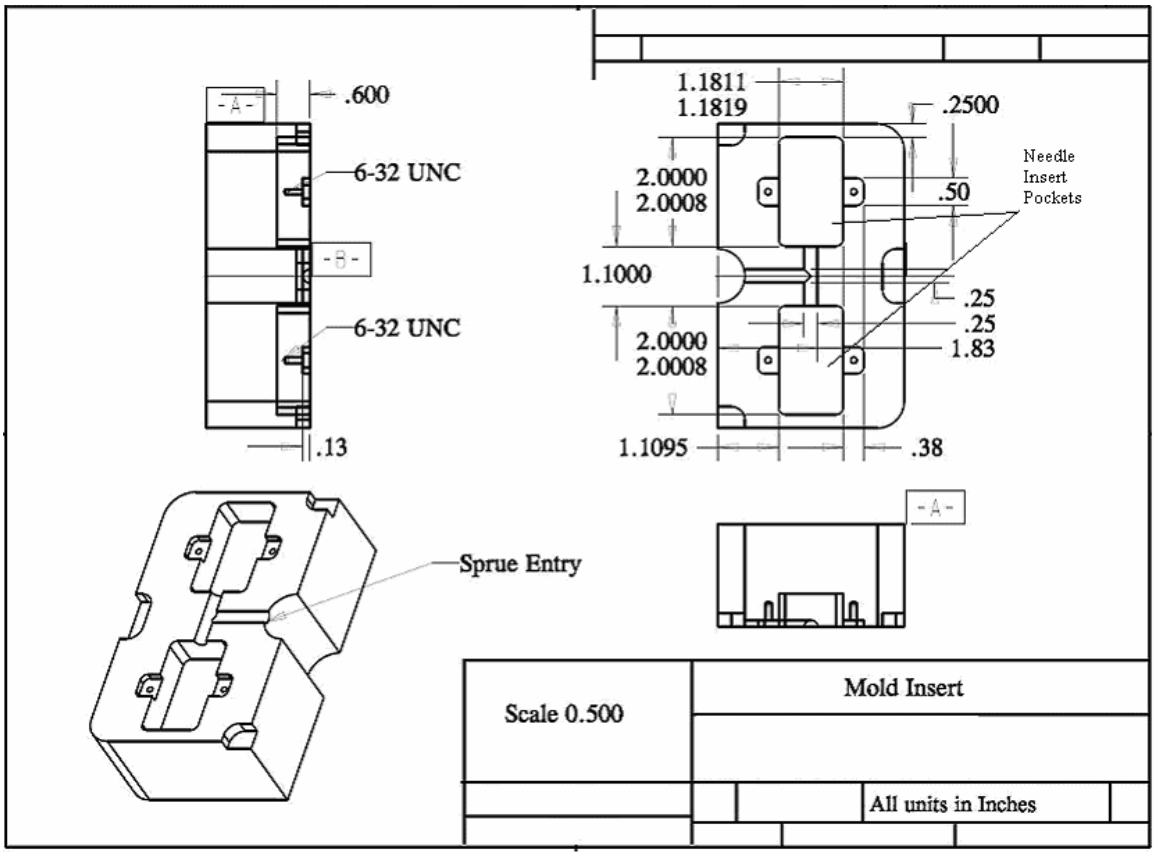


Figure **4.2**: Large mold section into which smaller inserts are placed. (Drawing courtesy of Taylor Stellman)

**Mold Inserts**

Mold inserts are small parts that contain all of the negative microneedle features and are used because they are easily modified without needing to remove and scrap a much larger part. They measure 15.24 mm deep, 30 mm wide, and 50.8 mm long. Several iterations of mold inserts were explored and modified as necessary to create the final desired part shape.

The shape of the microneedle patch evolved through the course of the project. Initially the parts were 17 mm wide, 10 mm deep, and 50.8 mm long. After parts were first made, the depth was reduced to 3 mm to correct for warpage. The part length was also reduced from the initial 30 mm to 17 mm. This reduced the amount of plastic used for each part by approximately 40%. The reduction in length also reduced the mold area contacted by the liquid polymer as it flowed into the mold; this helps prevent the polymer from freezing prematurely in the mold.

Four microneedle patterns were made to test needle spacing and its relation to the required penetration force. These spacing patterns and how they affect skin penetration will be discussed further in Chapter 6. The spacing patterns include 1.0 mm hexagonal spacing, 1.5 mm hexagonal spacing, 1.0 mm square spacing, and 1.5 mm square spacing. These patterns are shown in Figure **4.3**, Figure **4.4**, Figure **4.5**, and Figure **4.6.**

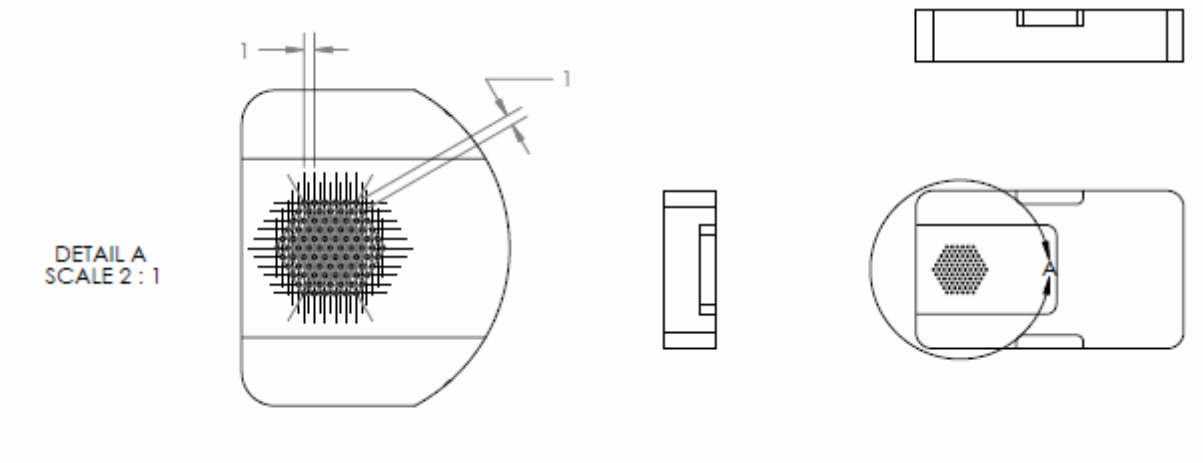


Figure **4.3** Mold with 1.0 mm hexagonal spacing pattern (dimensions in mm).

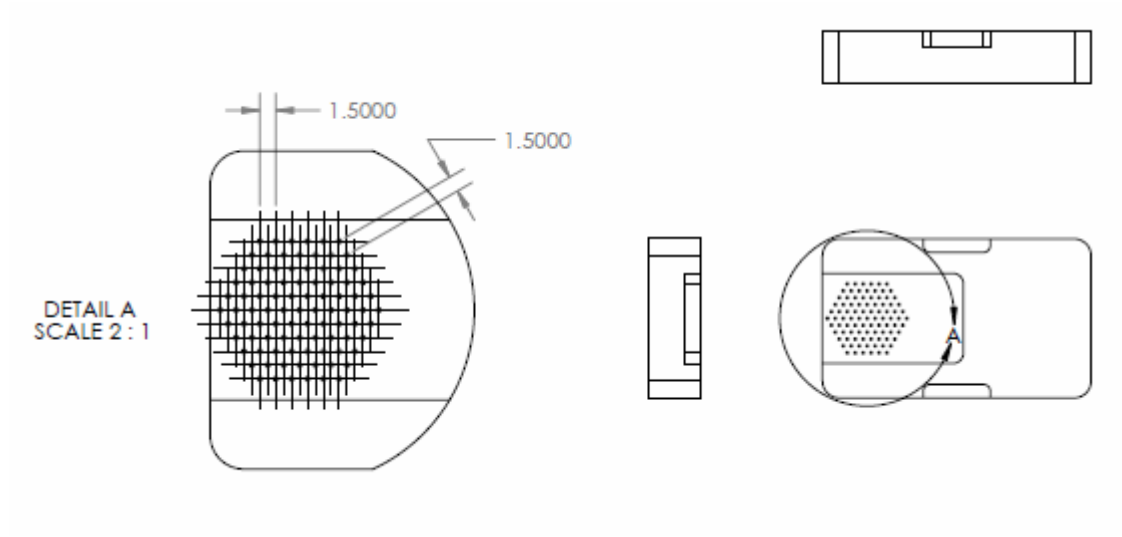


Figure **4.4**: Mold with 1.5 mm hexagonal spacing pattern (dimensions in mm).

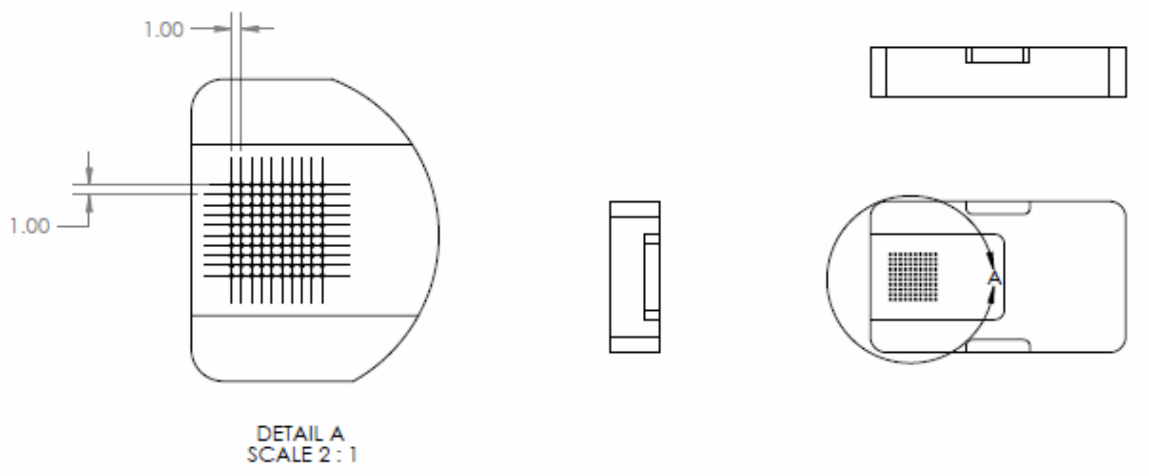


Figure **4.5**: Mold with 1.0 mm square spacing pattern (dimensions in mm).

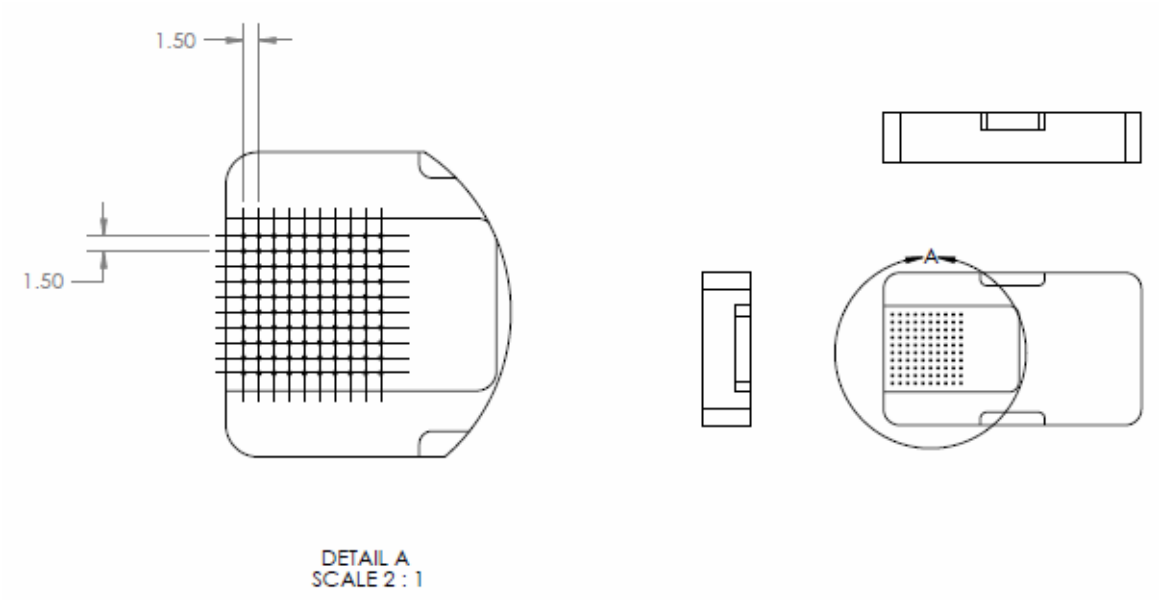


Figure **4.6**: Mold with 1.5mm square spacing pattern (dimensions in mm).

### *Mold Insert Materials*

Several materials and material combinations were explored for use as mold inserts. The first material used was AL2024-T351, which is an aircraft grade aluminum with mechanical characteristics that make it a good mold material. The first machining trials of this material showed that its hardness may have been too high when trying to machine very small tip radii. The material would quickly erode the engraving tools and was only capable of producing tip radii of about 85 microns, which is much too dull for skin penetration.

Next, experiments were conducted with a range of solder and braze materials. Silver solder, lead solder, and bronze were melted into pockets that were machined into mold inserts. The silver solder and bronze were both too hard and eroded machine tools

too quickly, much like the AL2024. The lead solder filled the mold pocket very well and could be made to a very sharp tip radius of approximately 10-15 microns. However, this type of material has two major disadvantages. The first is that the lead presents a risk of toxic exposure when injection molding devices intended to be inserted into the body. The other disadvantage is that the melting temperature of the material is approximately 300°C and melts, flows, and recrystalizes when in contact with hot molten polymers. This can be seen in Figure **4.7** .

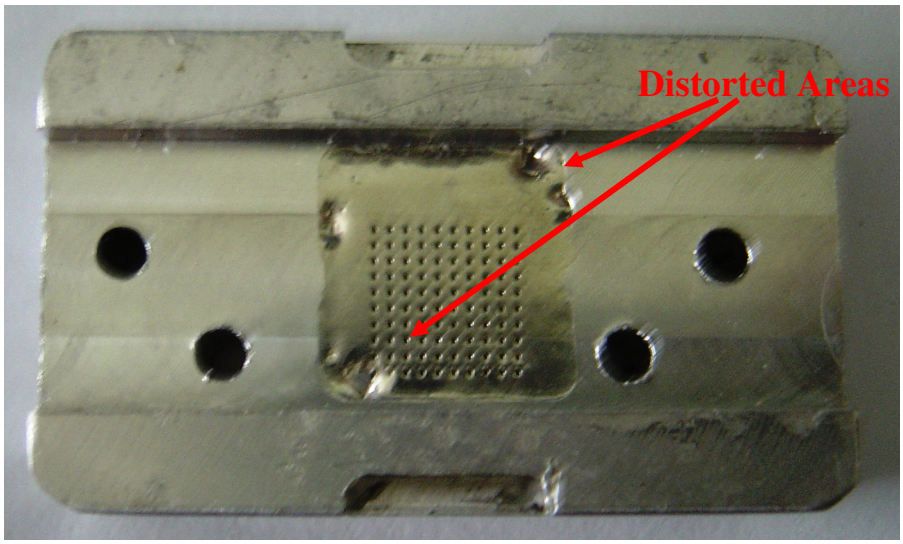


Figure **4.7**: Lead alloy mold with distorted surface after injection molding.

The final mold insert material explored was AL1100 aluminum. This grade of aluminum is commercially pure and contains no alloying agents that would increase its hardness. It was found that this material was nearly as easy to machine and forge as the lead solder, but melts at approximately 600°C and is safe to use for molding medical-grade parts. The one disadvantage of AL1100 was that its low yield strength allowed for very easy mold deformation when in contact with high pressure molten polymer. The

injection molding process quickly deformed the molds and resulted in microneedle patches that became stuck in the mold inserts and caused excessive flash. To fix this, a two part mold insert was created. A steel outer portion would bear the load of the clamping force and the forces from the high pressure polymer that tend to deform the mold. A slot was milled into this part and a smaller flat section of AL1100 was press-fit into the steel part. The microneedle cavities are contained on the aluminum portion of the mold which cannot be deformed because of the rigid steel part surrounding it. Figure **4.8** shows the final part next to an earlier AL1100 mold which has deformed sidewalls from injection molding.

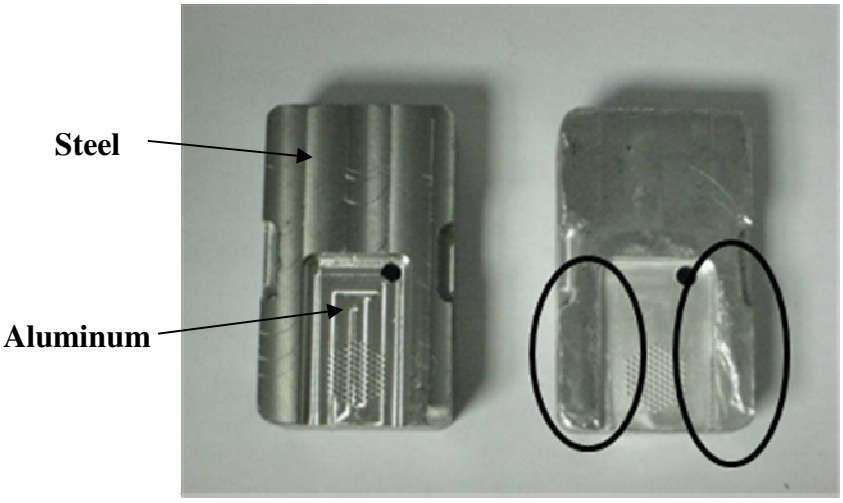


Figure **4.8**: On the left is a redesigned mold made of steel with aluminum insert, on the right is a mold made from AL1000 which easily deforms. Deformed areas are shown in ellipses.

### *Microneedle Mold Cavity Fabrication*

Many methods exist for creating the small-scale mold features desired for this project. Electro-discharge machining, or EDM, is one popular method for creating fine mold features. Sink or plunge EDM uses an electrode in the shape of the desired part, usually made from carbon or copper, to electrically vaporize mold material and create mold features. One concern with using this method which was expressed by several machining experts is that the electrode would erode too quickly to create the micron-sized features needed. Another concern with EDM is its high cost. One quote suggested it would cost in excess of $10k for each mold. Such a high cost was unreasonable when coupled with the need for at least four molds and other unknown factors regarding the progression of the final pattern and part shape.

Silicon-based fabrication technology also was considered. Such a fabrication method would take the form of a positive master being manufactured using photolithography and etching. A mold then could be made by nickel-coating the master and back-filling with epoxy to create a solid mold. This method would work well for creating high quality part features, though the process is time consuming and the molds would need to be small inserts which may not be capable of high volume production due to their fragility.

The method used to create molds for the purposes of this project uses simple manufacturing methods such as drilling and micro-forging to create high quality mold features at low cost with a high level of flexibility. A Chevalier FM-3VK (Santa Fe Springs, CA) CNC equipped milling machine in the Mechanical Engineering machine

shop was used for all machining and micro-forging operations for this project. This milling machine was found to be very accurate and could maintain true position tolerance within about 2 microns based on measurements. This made the machine very useful for keeping the engraving tool concentric with the micro-forging tool during the two phases of fabrication. Figure **4.9** shows the Chevalier CNC milling machine.


Figure **4.9**: Chevalier FM-3VK milling machine.

First, steel engraving tools are used to drill holes to a depth of 600 microns. Figure **4.10** shows a 30° steel engraving tool used for creating the initial conical shape of the desired microneedle cavities. The spindle speed for drilling these cavities is set at the machine maximum of 2800 rpm due to the small tip radius for the tool and type of aluminum being machined. Plenty of lubricant, such as Tap Magic ®, must be used to facilitate machining.

Figure **4.10**: Front and side views of 30° steel engraving tool.

Later, custom engraving tools designed to mimic the purchased tools were created using M42 tool steel due to its durability as a tool steel. These tools were made using the same technique used to create the indenters discussed below, but also include an ancillary machining operation to create the relief for chip formation. This is done using the Chevalier horizontal grinder shown in Figure **4.11**. This grinder can grind flat surfaces to a tolerance of about one micron. The grinding wheel is first dressed to ensure a flat surface. The grinder is then used to remove half of the diameter of the tool on the last 25 mm of the sharpened end. The tool is then re-sharpened to ensure a small tip radius of less than 5 microns.


Figure **4.11**: Chevalier FSG-1224 horizontal grinder used to create custom engraving tools.

A set of computer numerical control (CNC) programs were created to consistently create the mold patterns with fewer mistakes in positioning the mill. Four patterns of microneedle patches were desired, each with its own CNC program. The CNC programming allowed for x-axis and y-axis control on machine shop milling machines. The z-axis was controlled manually and a position limiter was set so that each cavity had a consistent depth. A z-axis control with the ability to control feed rate would be desirable to ensure even greater consistency between each microneedle cavity. Each CNC program was written using Prototrac software.

The second operation utilized to create the microneedle mold cavities uses indentation or micro-forging. This operation is performed after drilling and is used to greatly enhance the mold cavity sharpness. This allows for needle tip molds with radii of approximately 7-10 microns versus 50 microns, which can be obtained by drilling alone. The indenters used for this project were created using a Dumore 44-011 (Mauston, WI) precision tool post grinder set to create 30° included angle tips. Figure **4.12** shows the grinder as it is fixed on the lathe with dowel. The lathe rotates the steel dowel while the grinder removes material at a 15° angle to create the required tip. Sharp tipped indenting tools of four to five micron tip radii were readily made using this process.

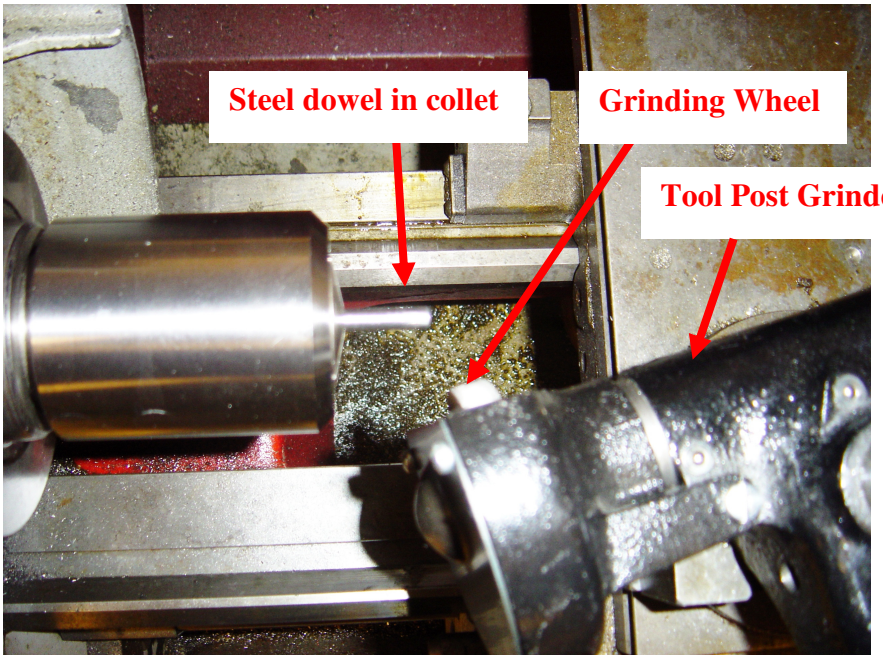


Figure **4.12**: Arrangement for creating sharp-tipped indenters using a lathe and tool post grinder.

Several materials were explored for indenters used in the micro-forging operation. The initial material was simply a case-hardened steel dowel that was readily available in

the machine shop. This material was prone to breakage and the tips would bend with little force, even when used in soft materials. Next, 52100 steel was used due to its increased durability and ability to be hardened. This material was a large improvement, but proved to be cumbersome due to the need to heat treat each indenter. Its tip was also susceptible to bending when used with harder mold materials. Finally, M42 tool steel was used with great success due its high hardness and durability. Because it was already hardened to 68 Rockwell C, it was less time consuming and more consistent than the other materials that required heat treating. These M42 indenters proved to create very sharp tip radii in both silver solder and aluminum. A conical diamond indenter also was used with good results and found to be very durable and could be used in higher grade aluminum in the future. Figure **4.13** shows four indenter that were used including annealed 52100, heat treated 52100, M42 tool steel, and a diamond tipped indenter.

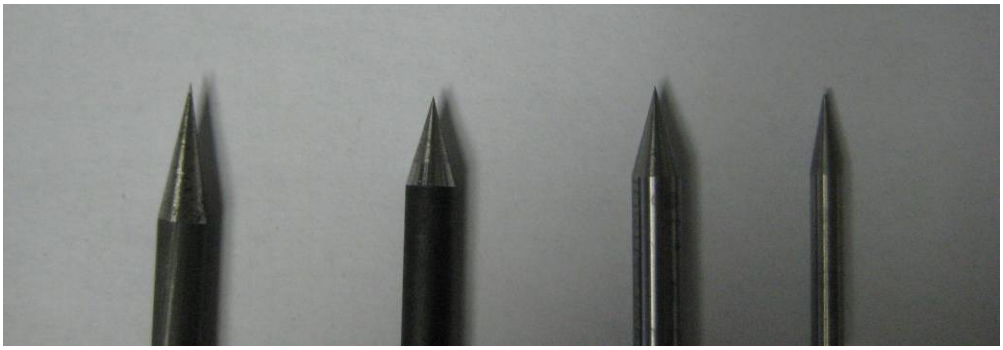

Figure **4.13**: Four indenter materials used explored in micro-forging to create sharp microneedle cavities (from left: annealed 52100, heat treated 52100, M42 tool steel, and diamond tipped indenter).

The procedure for performing the micro-forging operation is very similar to that of the drilling operation. The mold should not be unclamped from the vice in order to maintain the exact positioning used in the drilling operation. The spindle does not turn

during this operation. A Z-axis stop is set according to the desired depth create consistent microneedle cavity depth, in this case 650 microns. The same CNC program used for drilling then is cycled in order to maintain concentricity with the drilled holes.

The creation of the microneedle mold cavity features was successfully demonstrated using simple machining techniques. The process created four molds for this project in the patterns previously described. The microneedle mold cavities have tip radii as small as seven microns as measured using an optical microscope.

## Polymer Selection and Processing

A variety of polymers were selected based on their material properties. Strength, elastic modulus, and melt flow index are important factors to consider when selecting materials. Strength and elastic modulus are important for the mechanical performance of polymer microneedles. Stronger needles will be able to withstand greater forces without breaking. Melt flow index, or MFI, is related to how well a polymer flows at a certain temperature and force. A high MFI is usually desirable in injection molding because it indicates that a polymer will successfully fill a mold under a given pressure. MFI is inversely related to viscosity, although viscosity will change with applied force. Table **4.1** shows certain material properties including cost (Peterson, 2009; "Prospector - Ixef® 1022," 2010; "Prospector - Makrolon® 2207," 2010; "Prospector - Makrolon® 2458," 2010; "Prospector - Polystyrol 145 D," 2010; "Prospector - Topas® 5013S-04," 2010; "Prospector - Topas® 8007X10," 2010; "Prospector - Vectra® A130," 2010).

Unfortunately, MFI values are not available for all of the materials used for injection molding.

Table **4.1**: Polymers used for injection molding microneedles and selected material properties

| Material | Modulus (MPa) | Tensile Strength (Mpa) | MFI (g/10min) | Melt Temp (°C) | Cost ($ per lb Approx) |
|---|---|---|---|---|---|
| **Polystyrene** | 2400 | 40 | 14 | 180-280 | $1.12 |
| **Vectra A130 LCP** | 15000 | 190 | | 290 | $10.17 |
| **8007x10 COC** | 2600 | 63 | | 190-250 | $7.55 |
| **5013s04 COC** | 3200 | 46 | | 240-300 | $6.70 |
| **Makrolon 2207 PC** | 2410 | 65 | 38 | 270 | $4.88 |
| **Makrolon 2458 PC** | 2410 | 65 | 20 | 279 - 296 | $4.75 |
| **IXEF 1022 PARA** | 20000 | 255 | | 280 | $9.50 |

The liquid crystal polymer (LCP) and IXEF polymers have the best apparent mechanical properties because they are reinforced with 30% and 50% glass, respectively. The cost of polystyrene is far lower than the other polymers due to its status as a commodity material. Of the polymers listed in Table **4.1**, only polystyrene (PS), Vectra A130 LCP, Topas 8007X10 cyclic olefin copolymer (COC), and Solvay IXEF 1022 polyarylamide (PARA) were successfully injection molded. Parameters such as hold time, hold pressure, injection velocity, and shot size were adjusted for each material to optimize injection molding of each material. The specific injection molding parameters for each material is listed in Appendix 1. Attempts were made to make microneedle parts with the other materials listed in Table **4.1**, but examination showed that tip radii were larger than 30 microns and thus unacceptable for use.

Microneedle parts were successfully injection molded into the molds described earlier in the chapter. Figure **4.14** shows one of each of the four materials and each of the four patterns used for injection molding microneedle patches.

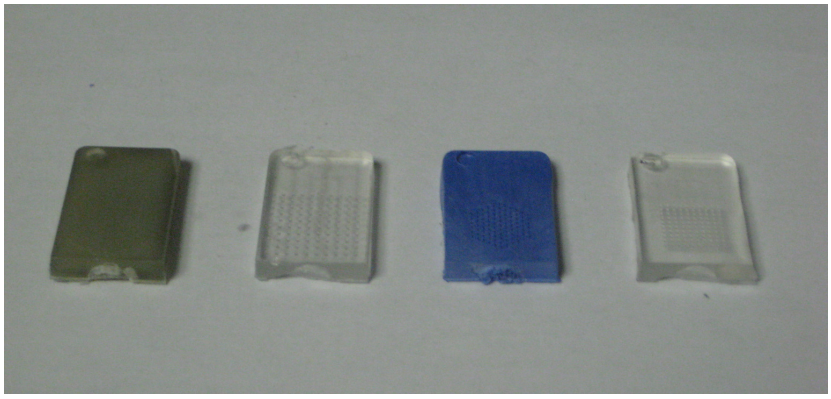

Figure **4.14**: Four materials used for injection molding (from left, IXEF, polystyrene, liquid crystal polymer, and COC).

Injection molding created microneedles with sharp tip radii ranging from 10 to 25 microns. The details of these measurements will be discussed in Chapter 5. Figure **4.15** shows a profile of a microneedle patch made from Ticona Vectra A130 LCP at 50x magnification.

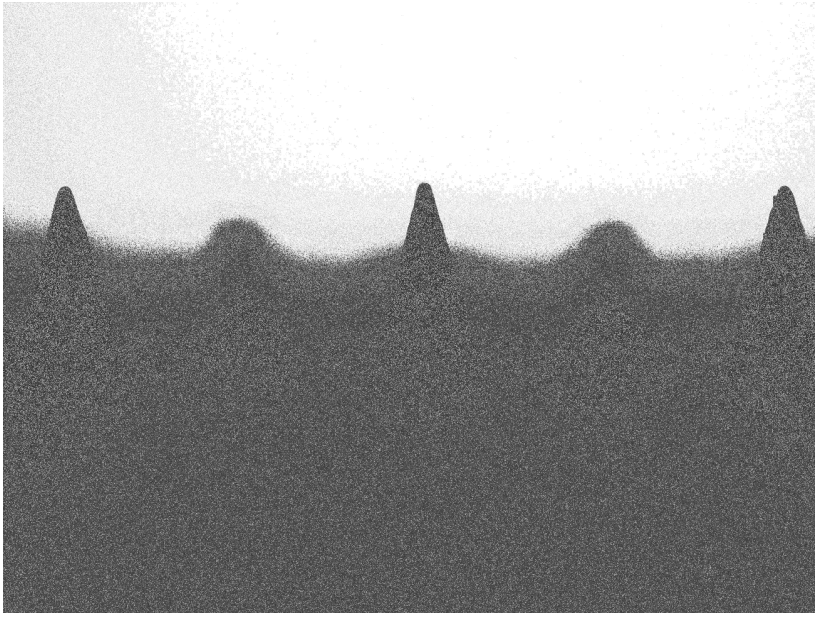

Figure **4.15**: Micrograph of LCP microneedle tips at 50x magnification.

There are several unique features related to the manufacturing of microneedle devices for this project. The demonstrated ability to injection mold out of plane polymer microneedles is the primary achievement in microneedle production. While there are several research papers and patents that suggest out of plane microneedles, no group has published their successful achievement of this goal. This project has shown that microneedles can be successfully injection molded using conventional equipment and achieve feature sizes as small as 10 microns.

Another unique feature related to microneedle fabrication was the method used to fabricate the molds. The novel use of multiple materials in conjunction with the drilling and metal forming techniques to achieve mold features in the single micron range is unique and allows for low cost mold creation. Further study of this mold fabrication technique would allow more materials to be used and may expand the techniques for creating mold features. This project successfully utilized unalloyed aluminum for the needle tip mold features and used high strength steel tools for machining and indentation.

Further study of the physics of drilling and indentation may expand the available materials that can be used with these techniques. For example, using alloyed aluminum may eliminate the need to use both steel and aluminum to create the mold structure. More involved study of the drilling and indentation process would also allow more shapes and sizes of needles to be created. Custom machine tools could be made by a custom tooling fabricator that may be able to drill tip radii sharper than the simple engraving tool used for this project.

This chapter has outlined the fabrication of injection molded plastic microneedle devices. This includes design and fabrication of the mold, creation of the microneedle

cavity features, and aspects of polymer selection and processing. Chapter 5 will discuss the testing procedures for these polymer microneedle devices.

# Chapter 5

# Test Procedures

This chapter will outline the testing procedures used for evaluating the polymer microneedle devices created by injection molding. The procedure used for measuring the tip radius and height of the microneedles is discussed. Also, the creation and testing of a needle spacing test rig will be discussed.

## Polymer Microneedle Test Procedure

There is a clear need to evaluate the performance of the injection molded microneedle devices. Basic information such as load versus displacement is required to evaluate differences in needle pattern and materials. Testing is performed on an Instron (Model # 33R4466, Norwood, MA) mechanical testing machine. The testing procedure is direct and intended to be a simple simulation of penetration into skin tissue. A testing apparatus was designed to work with the Instron mechanical testing machine. One part is a fixture that attaches to the movable portion of the Instron machine and is intended to securely hold the microneedle patch using set screws. The other part is a flat stationary aluminum base upon which the silicone rubber sits. A 500N load cell is utilized for testing all microneedle devices. Figure **5.1** shows the experimental test setup used for testing.

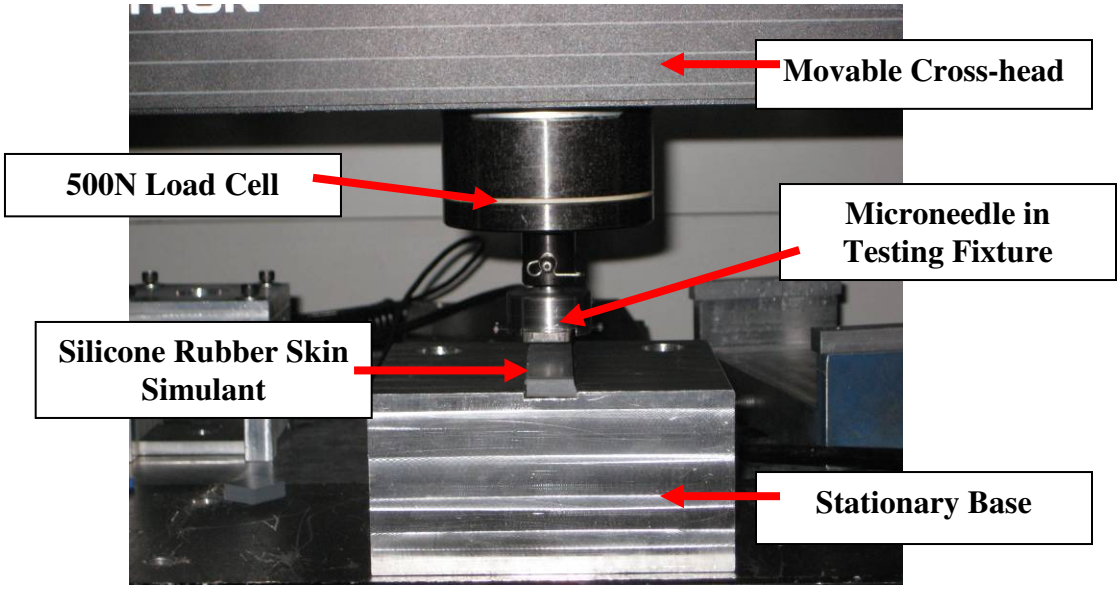


Figure **5.1**: Testing apparatus with microneedle device mounted in the Instron

Silicone rubber (McMaster-Carr Part # 5812T152) with a 50A Durometer Rating has been selected for its physical properties that are intended to simulate skin. A rubber skin simulant is used to eliminate the need to use biological samples which are more cumbersome to handle and have heterogeneous properties based on humidity, temperature, and other factors.

Testing is performed using a uniform procedure for all parts. First the part is secured in the fixture using set screws and ensuring that the back of the microneedle device is flat against the top of the fixture. All flash remaining from the injection molding process is carefully removed prior to mounting parts in the fixture with a file or rotary tool with a sanding disc. Next, an unused section of the silicone rubber skin

simulant is moved into place under the microneedle device. Finally, the test is started and the movable cross-head advances the microneedle device toward the silicone rubber at a constant rate of 6 mm per minute. A computer collects load and displacement information at a rate one data point every 10 milliseconds. The cross-head speed of 6 mm per minute is selected to yield 1000 data points per millimeter based on the computer data collection rate. Figure **5.2** shows the output of testing for Topas 8007X10 COC in 1.00 mm spaced square pattern. Data are output in comma separated value format for analysis using Microsoft Excel and other programs.

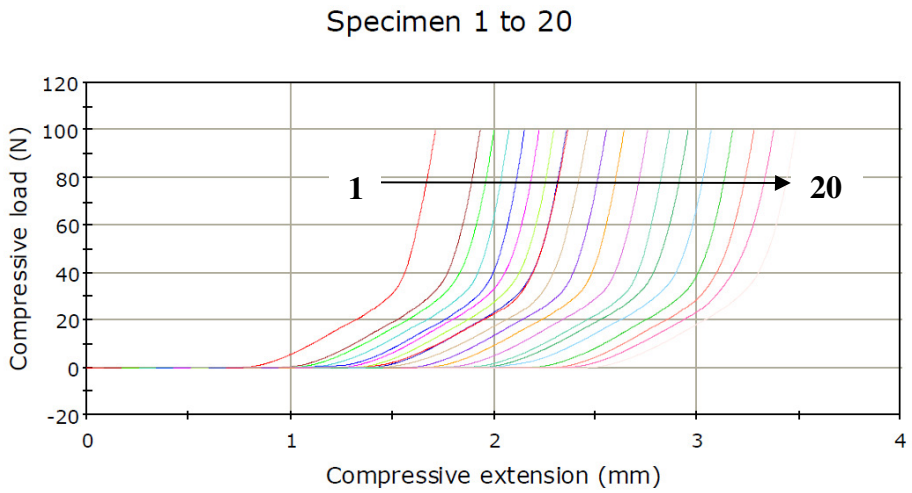


Figure **5.2**: Sample output for Instron testing. This figure shows test results of load versus extension for Topas 8007X10 COC in a 1.00 mm spaced square pattern. Each specimen is numbered 1 through 20 from left to right.

Twenty parts of each pattern and material was tested. This resulted in a total of 300 tests performed comprising four materials and four patterns. Table **5.1** shows the patterns and materials tested.

Table **5.1**: Quantity of parts tested for each pattern and material combination.

| Parts Tested | Polystyrene | Vectra A130 LCP | 8007X10 COC | IXEF1022 PARA |
|---|---|---|---|---|
| Square Pattern - 1.00 mm Spacing | 20 | 20 | 20 | 20 |
| Square Pattern - 1.50 mm Spacing | 20 | 20 | 20 | 20 |
| Hex Pattern - 1.00 mm Spacing | 20 | 20 | 20 | 20 |
| Hex Pattern - 1.50 mm Spacing | 0 | 20 | 20 | 20 |

## Polymer Microneedle Evaluation

An evaluation of injection molded microneedle devices is required for use in data analysis and for comparisons between materials and other technologies. Tip radius is of particular interest in microneedle research because it is a way to classify needle sharpness. Sharpness will be directly related to the ease of penetration for microneedles, which is in turn related to pain perception. Sharper microneedles will likely penetrate the skin with less force.

The length of the microneedles is another detail needed to perform data analysis. Length is also related to pain perception of microneedles. Longer microneedles will penetrate more deeply and interact with more pain receptors than shorter needles and will expose larger holes in the skin due to the angle of the microneedles.

These features are measured with a Leica DMRM (Wetzlar, Germany) compound microscope with magnification of 50x to 1000x. Tip radii and length of microneedles are measured by placing each on its side on the microscope's stage. The microneedle device then is moved into focus by moving the stage into position to view the needles from the side and adjusting the focus. Once in focus, the camera captures the image of the

microneedle profile. Figure **5.3** shows one such image at 100x of a Ticona Vectra A130 LCP microneedle.

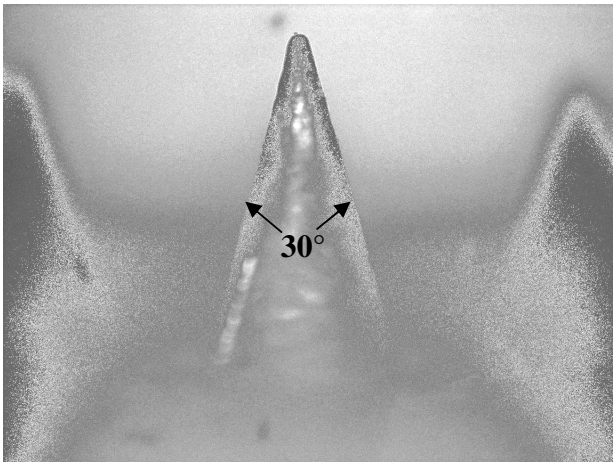


Figure **5.3**: Micrograph at 100x magnification of LCP microneedle.

The camera is calibrated so that precise measurements can be taken using the associated Leica software. Tip radius is measured by using the circle measurement tool and fitting the appropriate size to the photo. The tip radius is recorded as half of the measured diameter at the tip. The length is measured using a distance measurement from the base to the tip. Figure **5.4** shows an example of the tip radius and length measurements for a microneedle made from Topas 8007X10 COC.

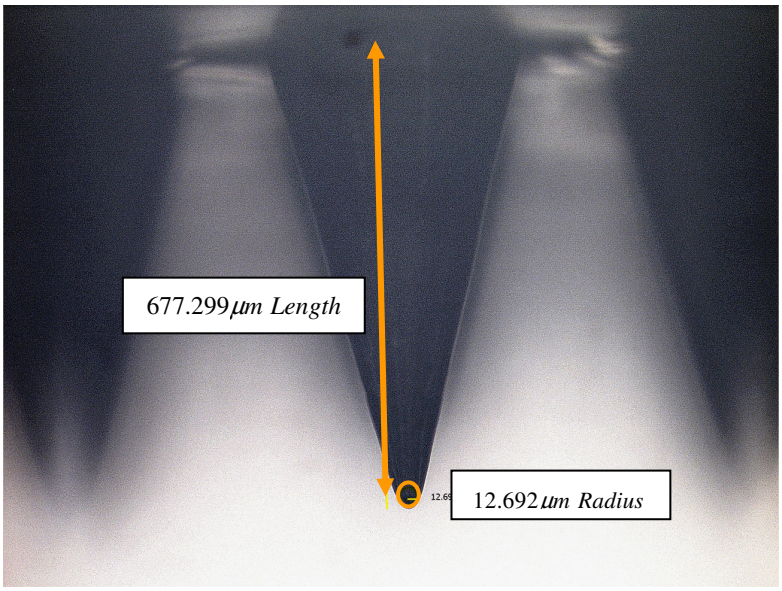


Figure **5.4**: Micrograph at 100x magnification of a Topas 8007X10 COC microneedle device. Length is approximately 677 microns and tip radius is approximately 13 microns.

A total of five measurements from each group of polymer microneedle devices are taken to get an idea of the tip radius and length for each group. While this does not provide an exact range of tip radii and lengths for each group, it does provide an idea of these parameters. Each microneedle device is scanned to gain a general idea of the variability for the part and one tip is selected and photographed. This is done to limit the amount of work required because of the 91 to 100 tips on each device and 20 devices that were to be tested from each of 15 groups.

## Microneedle Spacing Device

A simple device was created to test spacing of microneedles and how it relates to penetration force. The device allows for deeper needle penetration into the skin stimulant

to provide more data and analyze each stage of penetration separately. It also provided more uniform tips and needles heights than molded plastic parts thus providing a better foundation for analysis presented in later chapters.

A device that could be easily modified was desirable was created using simple parts. The device has a shaft that fits into the 500 N load cell attached to a square top plate. This top portion is used with seven interchangeable sets of plates. These plates contain small holes just large enough to fit 0.52 mm diameter sewing pins. The middle plate contains threaded holes for screws to adjust the distance between the plates. Four screws go through corner holes of both plates to attach them to the top plate. The pins fit into the holes of these plates to simulate steel microneedles in a fixed pattern for each set of plates. Figure **5.5** shows the spacing device with a 1.25 mm hexagonal spacing pattern.

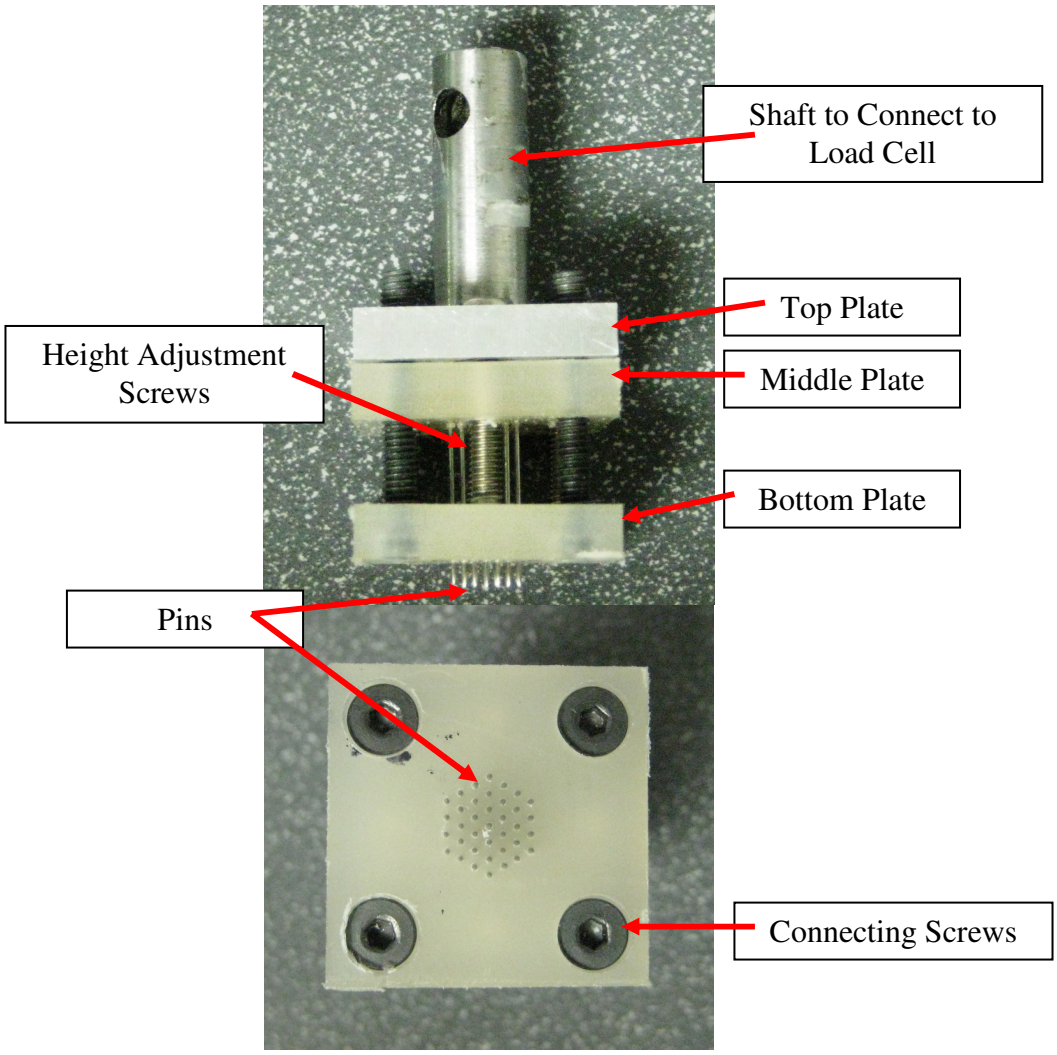


Figure **5.5**: Spacing device with 1.25 mm hexagonal spacing pattern in side view (top) and bottom view (bottom).

Six hexagonal patterns were created with spacing profiles of 0.75 mm, 1.00 mm, 1.25 mm, 1.50 mm, 2.00 mm, and 2.50 mm. One square pattern of 1.50 mm was created. The hexagonal patterns are preferred due to a pin's equal spacing from the next closest pin. Each hexagonal pattern contains 37 equally spaced pins. The square pattern contains 49 pins. Single needle tests were also performed in order to isolate the effects of each needle from the effects of the other needles in the array.

Each steel needle spacing device was tested in the same way as the polymer microneedles. Testing speed was set at 6 mm per minute. The data acquisition rate was set at one data point every 10 milliseconds. Five identical tests were conducted for each pattern using a new silicone rubber section for each test.

**Penetration Depth Testing**

A final set of tests was performed using each steel needle device to isolate actual needle penetration depth from the deflection of the skin simulant. The total displacement consists of both penetration and compression of the silicone. Separation of the material compression depth and the needle penetration depth is important to further analysis. Figure **5.6** shows an exaggerated representation of the initial deflection just prior to the start of penetration.

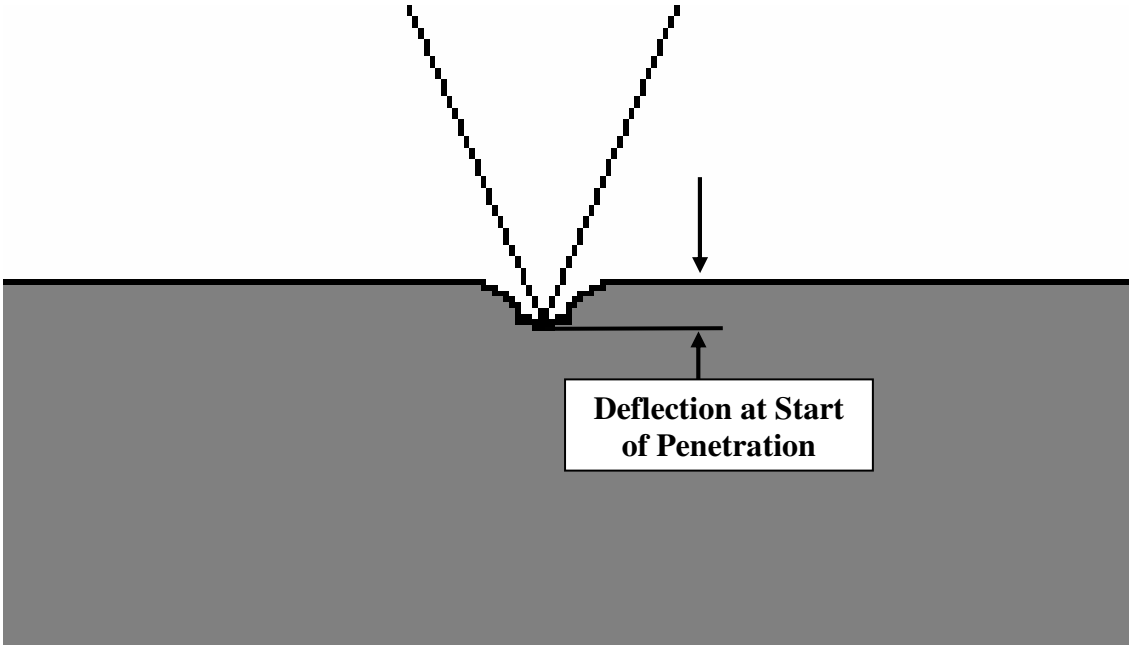


Figure **5.6**: Cross-section of solid steel needle showing skin deflection at the start of needle penetration.

This set of tests was performed by attaching a solid needle spacing device to the load cell and penetrating into the skin stimulant at a predetermined load and withdrawn until the load cell reads zero force. The procedure is as follows:

1. Attach a steel pin spacing device described earlier to the Instron mechanical testing machine.
2. Place a new section of rubber skin simulant on the stationary base.
3. Advance the cross-arm at a speed of 6 mm per minute with a data acquisition rate of one data point every 10 milliseconds to replicate the speed used in other testing. Use the Instron Bluehill software to set the Instron to stop at normalized loads of 0.28 N (experimentally determined to be the approximate load required to initiate penetration), 0.75 N, 1.75 N, 2.40 N, 2.75 N, 3.25 N,

and 4.00 N. At this lowered position, a cross-section of the steel pin and rubber will look like Figure **5.7**. Total depth is measured in this position and includes the initial penetration depth, material deflection, and penetration depth.

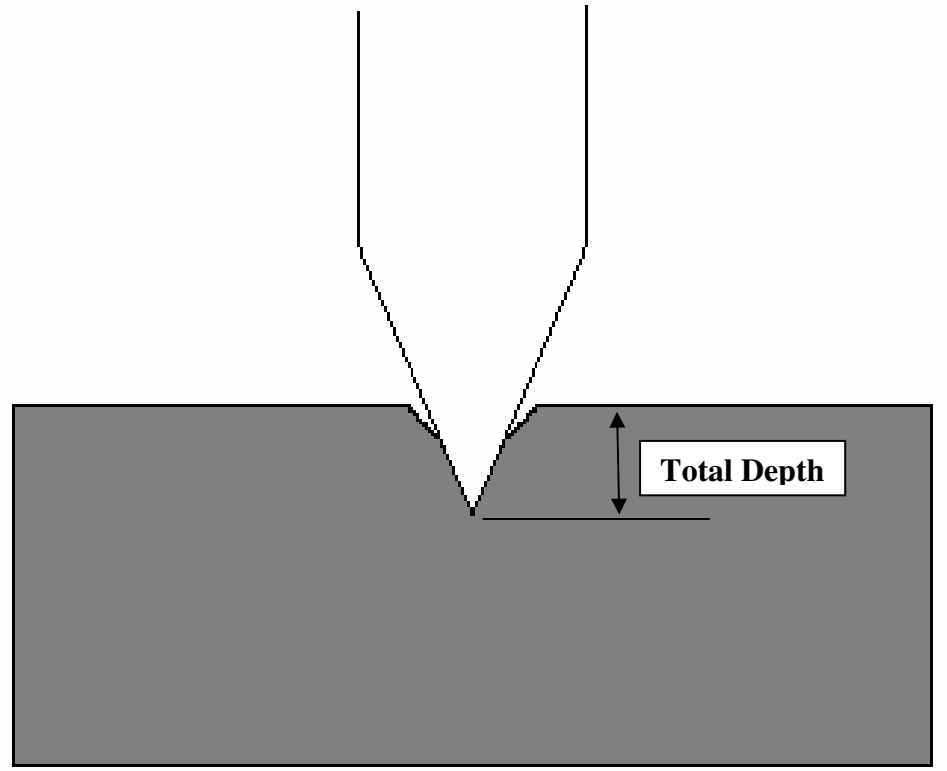


Figure **5.7**: Cross-section of solid steel needle and rubber skin simulant in loaded position.

4. Slowly reverse the direction of the cross-arm until the load reaches value of 0 N. Figure **5.8** shows a cross-section of the steel pin and rubber skin simulant after withdrawing the needle to load of 0 N. At this point, the actual depth of penetration is measured and recorded.

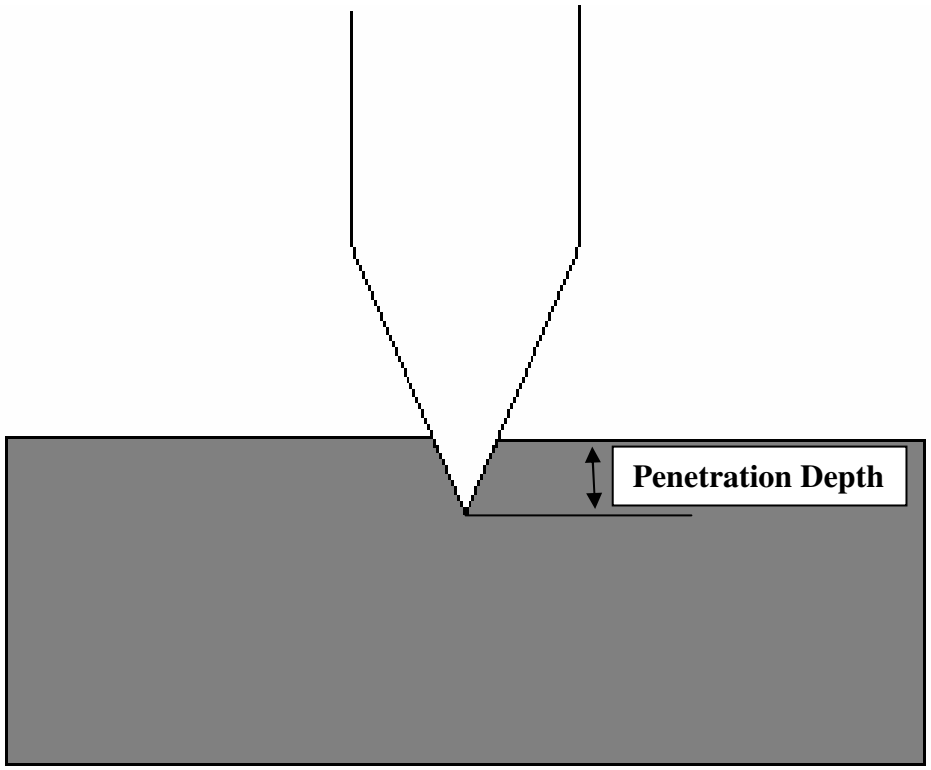


Figure **5.8**: Cross-section of solid steel needle and rubber skin simulant after withdrawing needle.

5. Repeat this procedure for each normalized load value.
6. Repeat this procedure for single steel pin tests and all steel pin spacing devices.

The displacement is recorded at zero force. By removing the load and measuring the displacement, the penetration into the rubber can be separated from the compression of the rubber for each pattern. The procedure is repeated with a new section of rubber skin simulant for each load.

**Solid Indenter Compression Testing**

Material compression by a solid surface was studied in order to further develop microneedle penetration models. The effects of a needle pattern with a theoretical zero distance between needles can be studied by examining the reaction of the rubber skin simulant to compression by solid indenters. To complete this study, six solid indenters were machined from aluminum. The indenters equal the total areas under the steel needles in each of the six steel needle patterns. Figure **5.9** shows are representation of the hexagonal needle pattern compared to the area of its corresponding solid indenter.

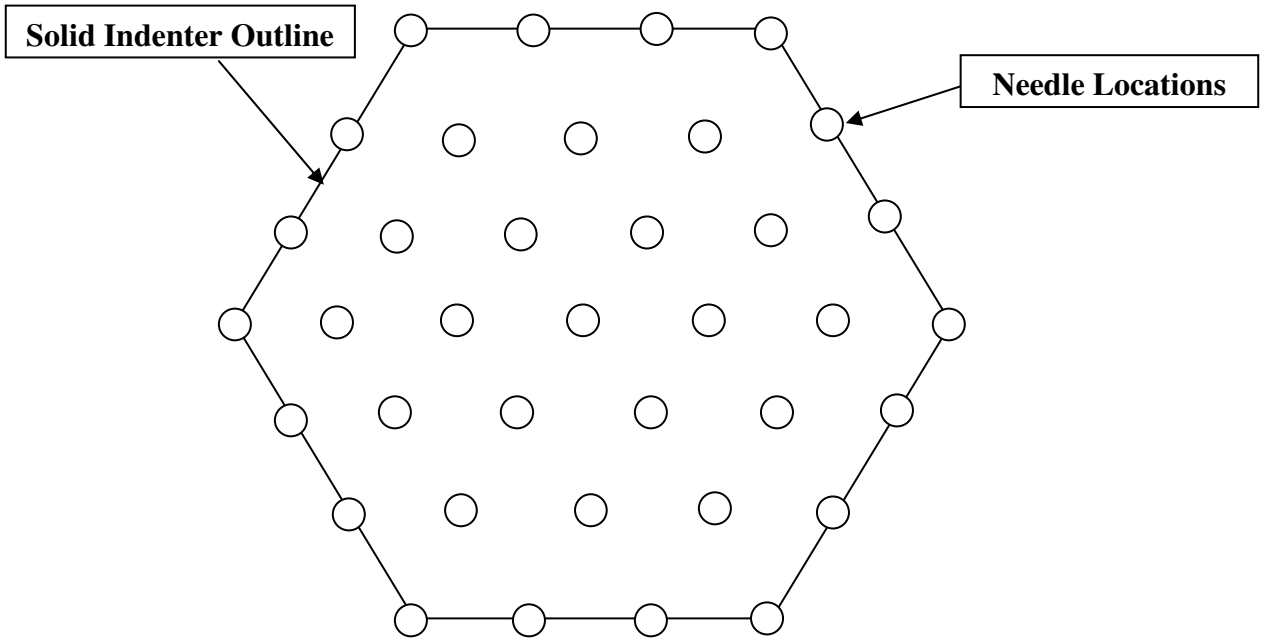


Figure **5.9**: Representation of solid indenter area compared to steel needle locations on the needle spacing device.

Each hexagonal indenter is made to attach to the top plate using four screws. The indenters are tested using the same procedure as the polymer microneedles. The results will be used to help determine mechanical properties of the rubber testing medium and

make comparisons related to the area under the needles. The data acquired will be useful in later chapters for explaining material deflection that occurs from multiple needles interacting as a single surface. Figure **5.10** shows a solid model of one of the indenters.

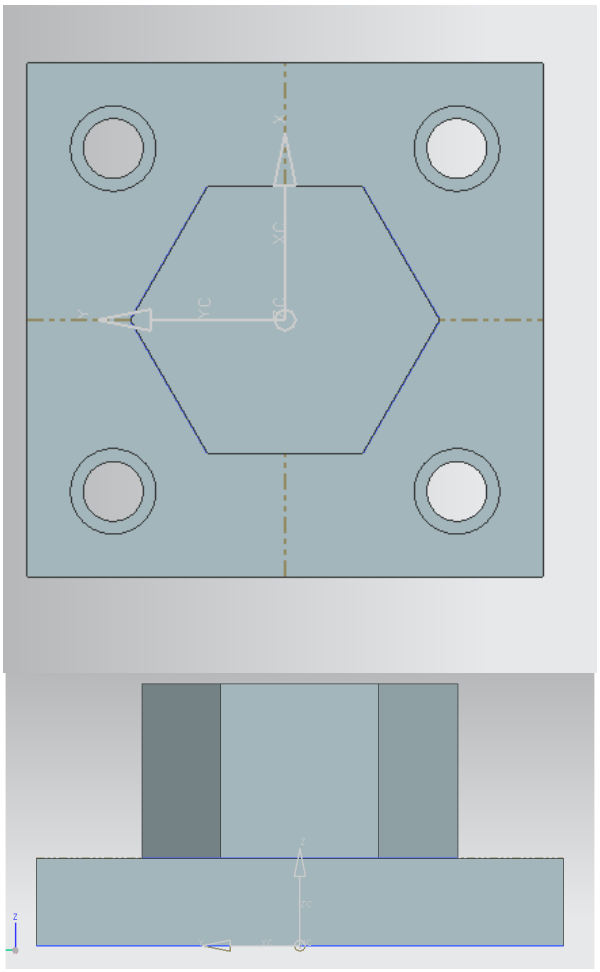

Figure **5.10**: CAD representation of solid hexagonal indenter

This chapter outlined the testing procedure used for evaluating the polymer microneedle devices created by injection molding. The creation and testing of a needle spacing device was discussed. Finally, the measurement of tip radius and length of

microneedle features was also discussed. Chapter 6 will present the results of testing the polymer microneedle devices and the microneedle spacing device.

# Chapter 6

# Penetration Testing Results

This chapter presents the results of physical testing. These tests include results for needle spacing apparatus tests, polymer microneedle tests, and tip radius and length measurements.

## Needle Geometry

Geometry measurements for the plastic microneedles and steel needles were obtained using the methods described in chapter 5. These measurements included basic information such as tip radius, length, angle, diameter, and profile shape. These parameters will be used to study the penetration characteristics of these needles.

### Steel Needles

The steel needles used for the microneedle spacing device are sewing pins with consistent geometry between needles. Figure **6.1** shows the measurement of the tip radius for the needle. The tip radius is approximately 16 microns for all measured needles.

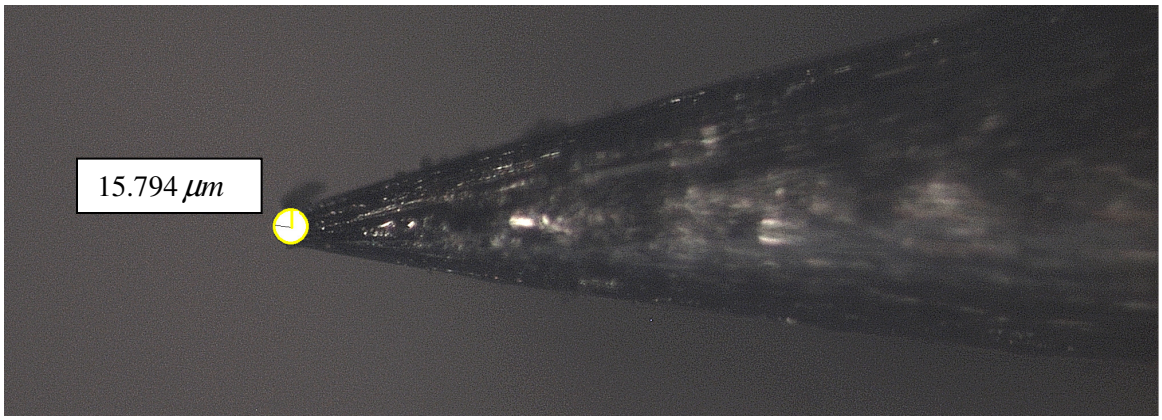


Figure **6.1**: Approximately 16 micron measured tip radius of steel needle used for microneedle spacing device.

The geometry of the needle is a transition from the small tip diameter of 32 microns to a diameter at the shaft of 520 microns. The geometry is not a simple cone on top of a cylinder, but is a more gradual blended geometry. Figure **6.2** shows the geometry of the needle from the tip to near the shaft.

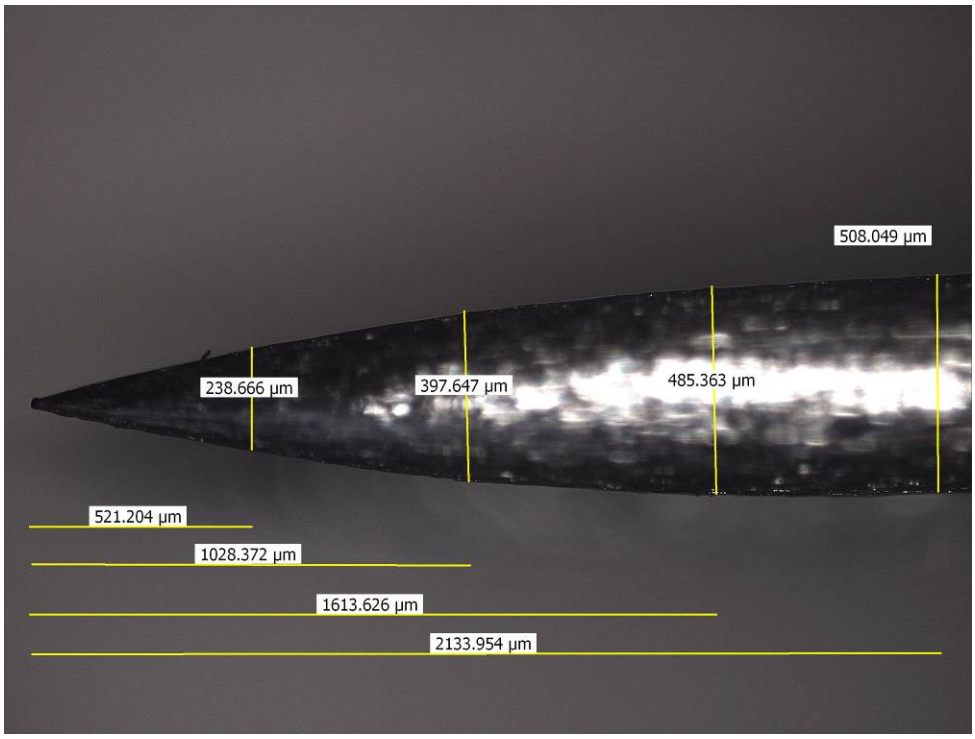


Figure **6.2**: Steel needle transition geometry.

The needle geometry can be described by using the measurements shown in Figure **6.2** to construct a regression. This will be helpful in describing needle penetration according to radius at various lengths. Figure **6.3** shows the needle transition plotted according to length.

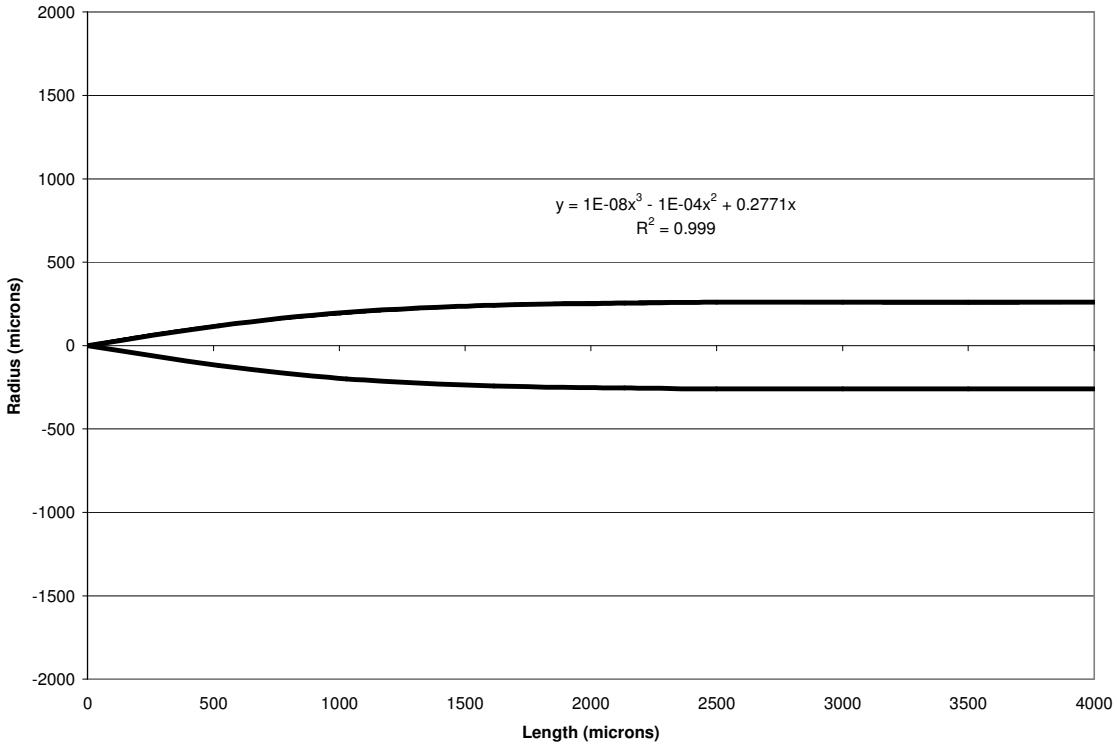


Figure **6.3**: Cross-sectional radius versus length regression for needle geometry.

A regression was fit to the shape of the needle and is shown in Eq. **6.1**. This equation describes the cross-sectional radius of the needle, y, as a function of the needle's length, x. This equation will be useful when describing penetration forces related to needle geometry.

$$y = 1\times10^{-8}x^3 - 1\times10^{-4}x^2 + 0.2771x \qquad \text{Eq. } \mathbf{6.1}$$

**Plastic Microneedles**

The plastic microneedle geometry can be described by three measurements: tip radius, length, and angle. The angle for all plastic microneedles is 30° and is very

consistent amongst all groups because all mold cavities were made using the same set of machining tools with a 30° angle. The tip radius and length vary because of the variance in the sharpness of the drilling and indenting tools throughout the process, the variability in depth of drilling and indenting operations, and the injection molding process and polymers used.

The tip radius can vary greatly due to the type of polymer being molded and the injection molding process parameters. The tip radius represents the radius of a sphere at the tip of the microneedle. The length measurement is taken from the base of the microneedle to the tip. Figure **6.4** shows a micrograph of a polystyrene microneedle at 100x magnification with a 14 micron tip radius and a length of 635 microns.

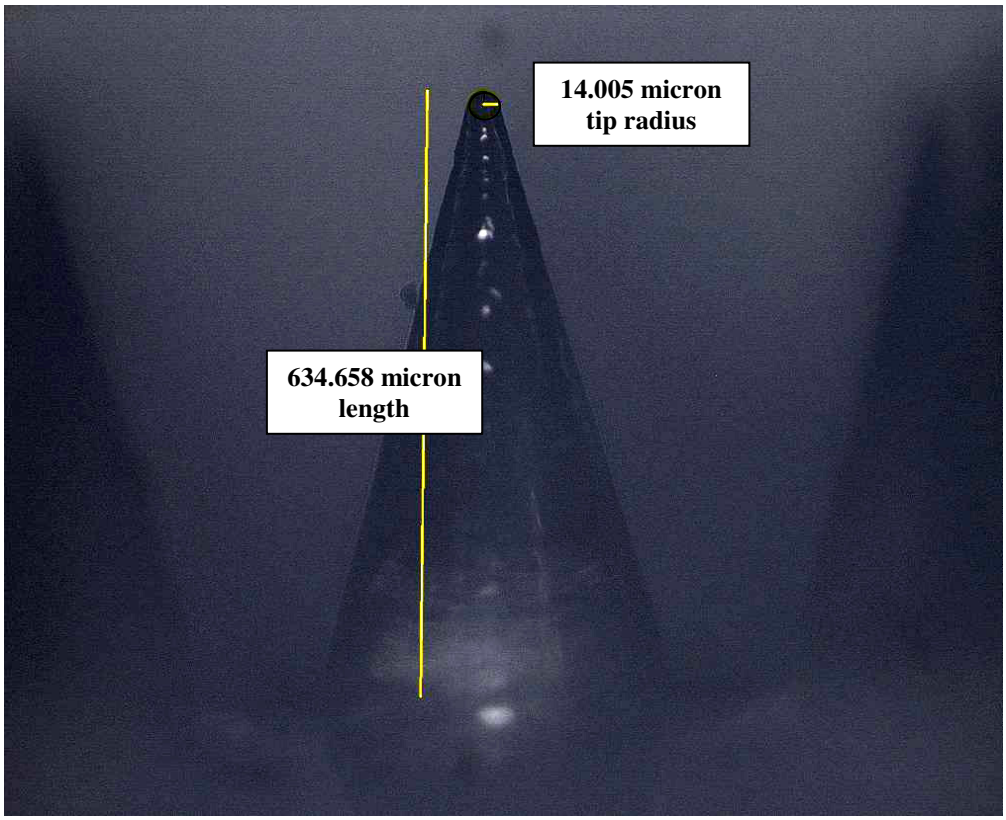


Figure **6.4**: 100x magnification of polystyrene microneedle showing tip radius and length measurements.

As discussed in chapter 5, only a limited number of individual microneedles can be measured due to their overwhelming number. Five microneedle devices were selected from each group, surveyed using the microscope, and an average tip radius and length were documented prior to testing. Table **6.1** shows the average tip radii for each group of microneedle devices in microns.

Table **6.1**: Average tip radii in microns for each group of microneedle devices

| | Vectra A130 (LCP) | IXEF 1022 (PARA) | Topas 5013-S04 (COC) | Polystyrene | Makrolon 2207 (PC) |
|---|---|---|---|---|---|
| **1.00 Sq** | 18.6 | 16.9 | 13.5 | 17.9 | N/A |
| **1.50 Sq** | 23.2 | 21.1 | 13.5 | 14.9 | 32.4 |
| **1.00 Hex** | 17.3 | 17.2 | 13.0 | 15.1 | N/A |
| **1.50 Hex** | 16.8 | 19.1 | 14.4 | N/A | N/A |

The length measurement is measured from the tip to the base of the microneedle device. Table **6.2** shows the average of length measurements for each group of microneedle devices in microns.

Table **6.2**: Average microneedle length for each group in microns.

| | Vectra A130 (LCP) | IXEF 1022 (PARA) | Topas 5013-S04 (COC) | Polystyrene | Makrolon 2207 (PC) |
|---|---|---|---|---|---|
| **1.00 Sq** | 738 | 738 | 745 | 735 | N/A |
| **1.50 Sq** | 732 | 728 | 732 | 679 | 679 |
| **1.00 Hex** | 656 | 647 | 656 | 646 | N/A |
| **1.50 Hex** | 595 | 595 | 595 | N/A | N/A |

## Microneedle Spacing Device

This section presents results from testing the microneedle spacing devices discussed in chapter 5. These devices use steel needles in single needle and multiple needle test configurations. The results for the single needle and multiple needles with various spacing patterns will be presented in this section.

### Single Needle

A set of single needle tests is helpful when trying to evaluate multiple needle arrangements. This helps in being able to determine differences in penetration force related to needle spacing as well as the various stages of penetration. Figure **6.5** shows a generalized graph of penetration force versus depth. This set of single needle tests show the needle penetrating completely through the silicone rubber used for testing. Each stage of penetration will be presented in subsequent figures.

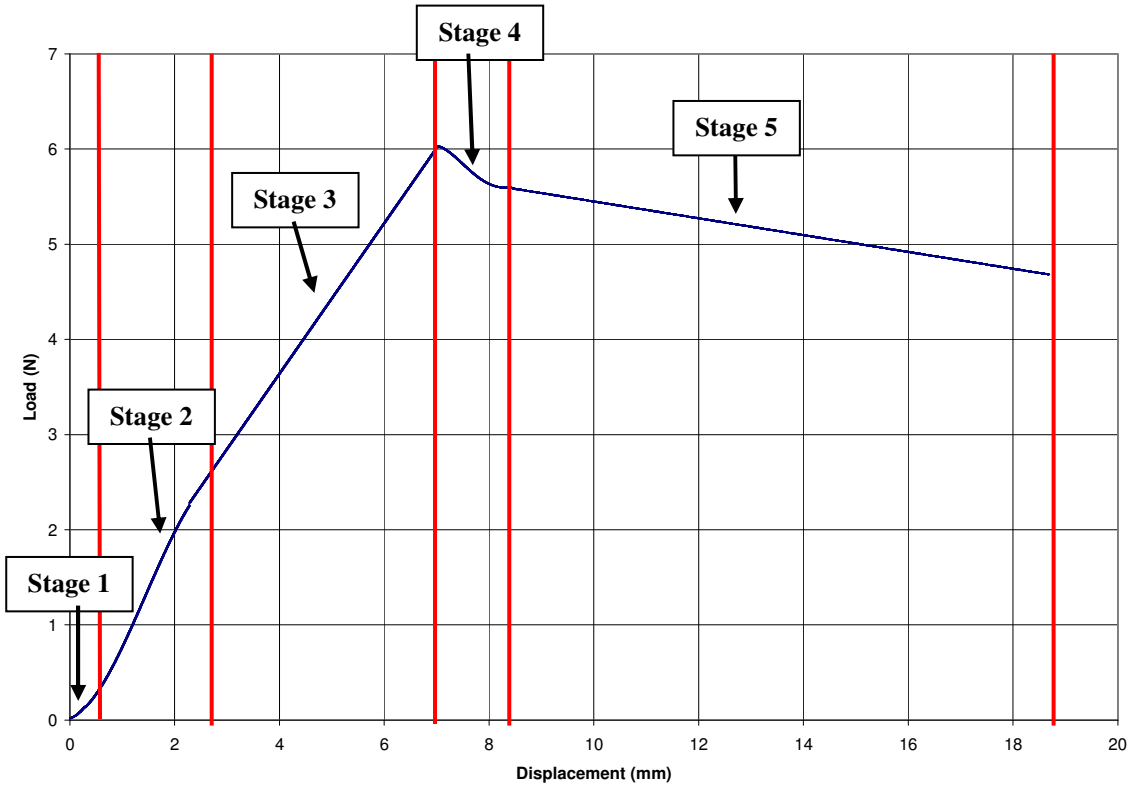


Figure **6.5**: Load versus displacement for single needle penetration with vertical lines separating each stage.

The first stage of penetration that occurs is where compression of the rubber skin simulant takes place. This stage concludes with an abrupt drop in load where fracture of the rubber occurs at the needle tip. Figure **6.6** shows the first stage of penetration for a single needle and is an enlargement of figure **6.5**.

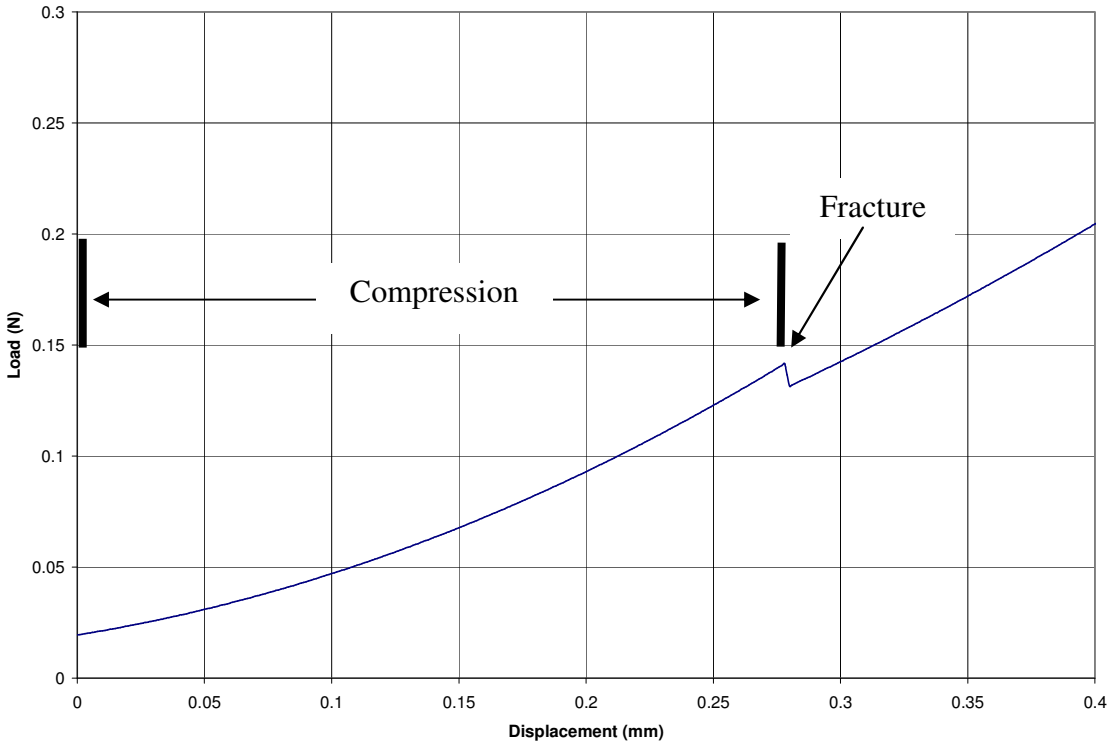


Figure **6.6**: First stage of penetration with single needle.

Figure **6.7** shows a graphical representation of the needle penetrating the rubber skin simulant. The first stage of penetration contains compression of the rubber until the needle tip just begins to penetrate.

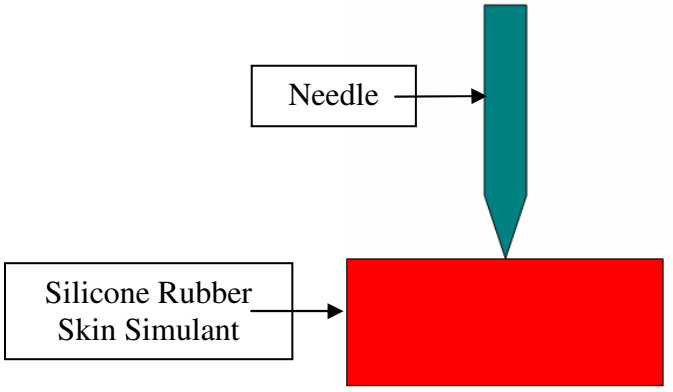


Figure **6.7**: First penetration stage where initial penetration begins.

In the next stage of penetration, the tip of the needle opens the crack that was initiated during the first stage. This stage begins with the fracture initiation and ends when the needle reaches its final diameter of approximately 520 microns. Figure **6.8** shows the second stage of penetration force increase as the needle penetrates farther into the rubber and is an enlargement of figure **6.5**.

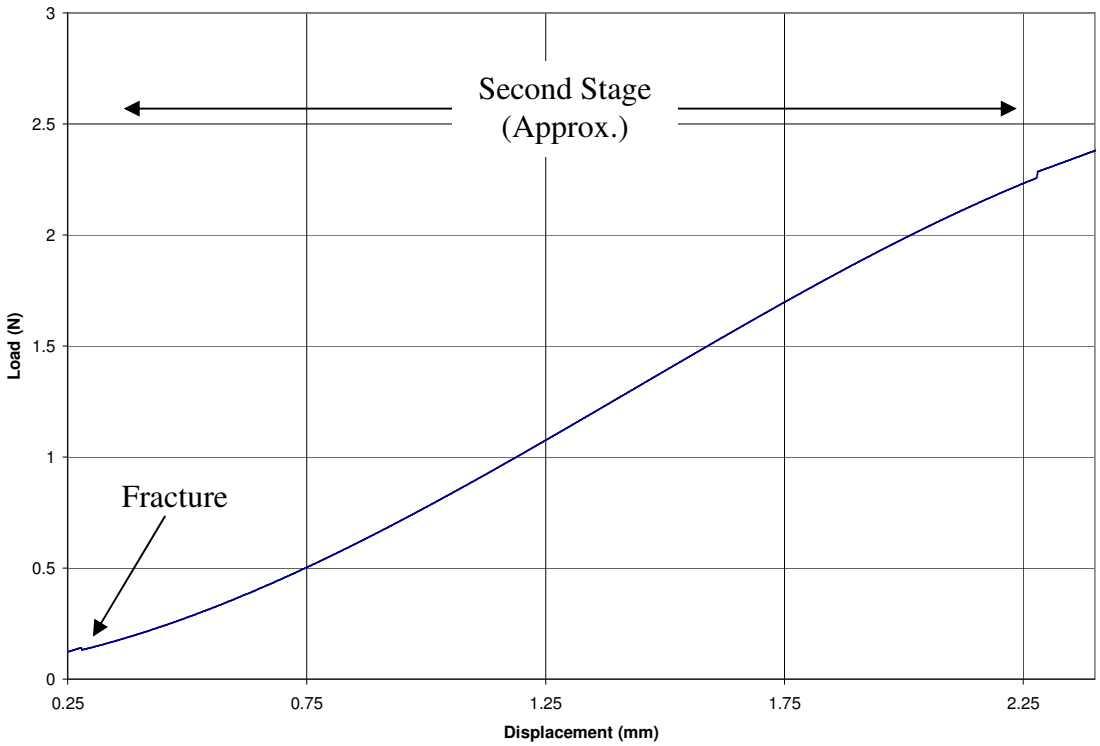


Figure **6.8**: Force versus displacement for second penetration stage.

Figure **6.9** shows a graphical representation of the second stage of penetration. Here the angled portion of the needle opens the crack to the final needle diameter.

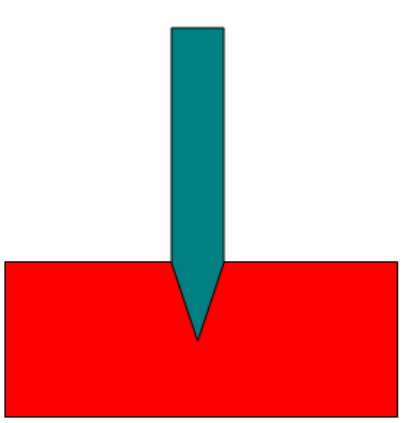

Figure **6.9**: End of second penetration stage where angled portion of needle opens crack to final needle diameter.

The third stage of penetration begins when the needle shaft enters the silicone rubber. The stage ends when the needle tip exits the other side of the silicone rubber. This stage of penetration is generally linear as more of the needle moves through the rubber. Figure **6.10** shows the third stage of penetration and is an enlargement of figure **6.5**.

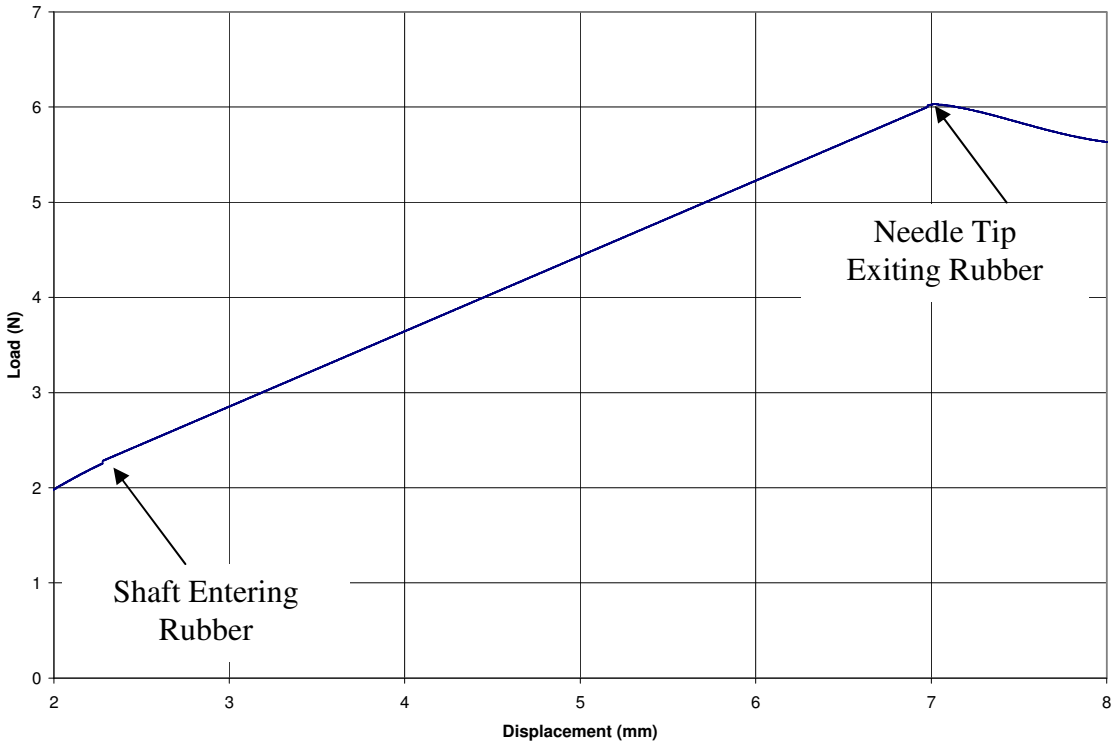


Figure **6.10**: Force versus displacement for third stage of single needle penetration.

Figure **6.11** shows a graphical representation of the end of the third stage of a single needle penetration. This stage is where the angled part of the needle begins exiting the bottom of the silicone rubber.

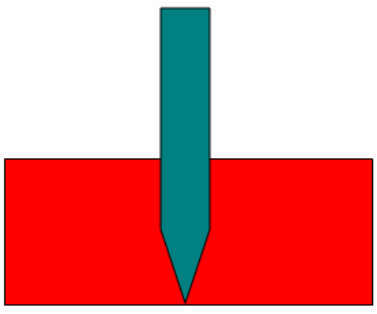

Figure **6.11**: End of third stage of single needle penetration where needle tip begins to exit rubber.

The fourth stage of penetration is a transition region following the exit of the needle tip from the rubber. The stage ends when the angled portion of the needle exits the bottom of the silicone rubber. This stage of penetration is difficult to classify due to a number of effects on force that will be discussed in Chapter 7. Figure **6.12** shows the fourth stage of needle penetration and is an enlargement of figure **6.5**.

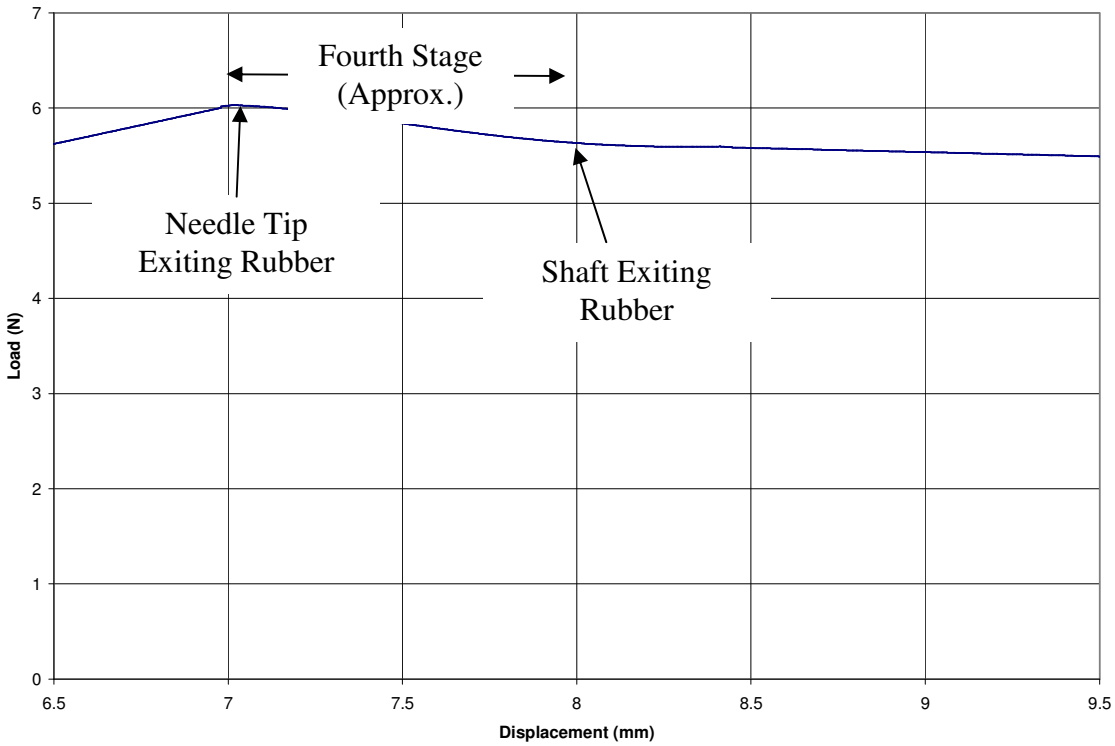


Figure **6.12**: Force versus displacement for fourth stage of single needle penetration.

Figure **6.13** shows a graphical representation of the end of the fourth stage of a single needle penetration. This stage is where the needle's shaft begins exiting the bottom of the silicone rubber.

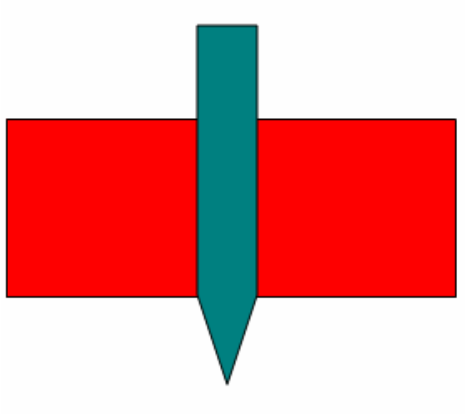

Figure **6.13**: End of fourth stage of needle penetration where shaft begins to exit bottom of rubber.

The fifth and final stage of single needle penetration happens when only the needle's shaft is sliding through the rubber skin simulant. The only force acting on the needle at this stage comes from friction between the needle and rubber. Figure **6.14** shows the fifth stage of penetration where the needle shaft is sliding through the rubber and is an enlargement of figure **6.5.**

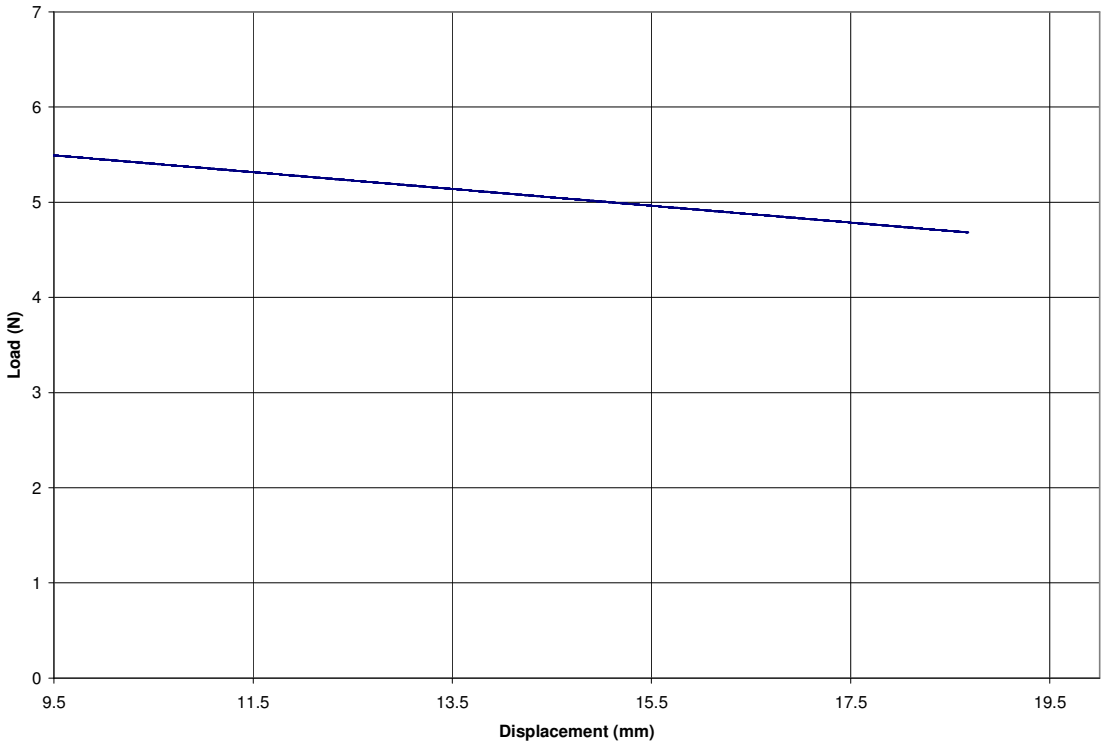


Figure **6.14**: Force versus displacement for final stage of single needle penetration.

Figure **6.15** shows a graphical representation of the final stage of a single needle penetration. In this stage the needle shaft is sliding through the silicone rubber. The decreasing load in this area is likely a result of the inside surface of the hole in the silicone rubber being smoothed by the needle shaft as it passes through. This will decrease the friction forces acting on the needle as it passes through the rubber. The decreasing slope occurred in each of the single needle tests during the fifth stage of penetration.

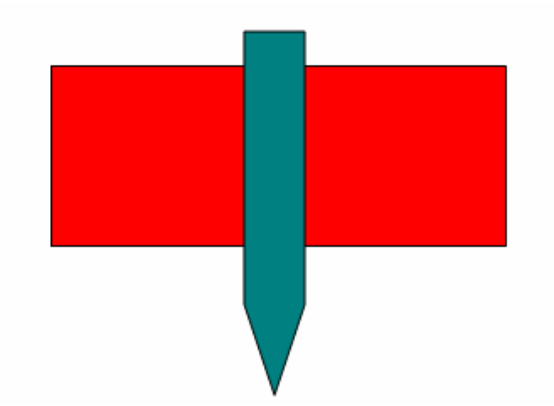

Figure **6.15**: Final stage of needle penetration where only the shaft of the needle is sliding through the rubber skin simulant.

The loads between each stage of penetration can be compared using a boxplot to graphically show variation. Figure **6.16** shows a boxplot for the loads between each of the five penetration stages for a single needle and the final load. Boxplots are a graphical method for displaying numerical data sets and show spread, skew, and outliers that exist in data populations. This information will be useful for later analyzing differences with each group of multiple needle patterns.

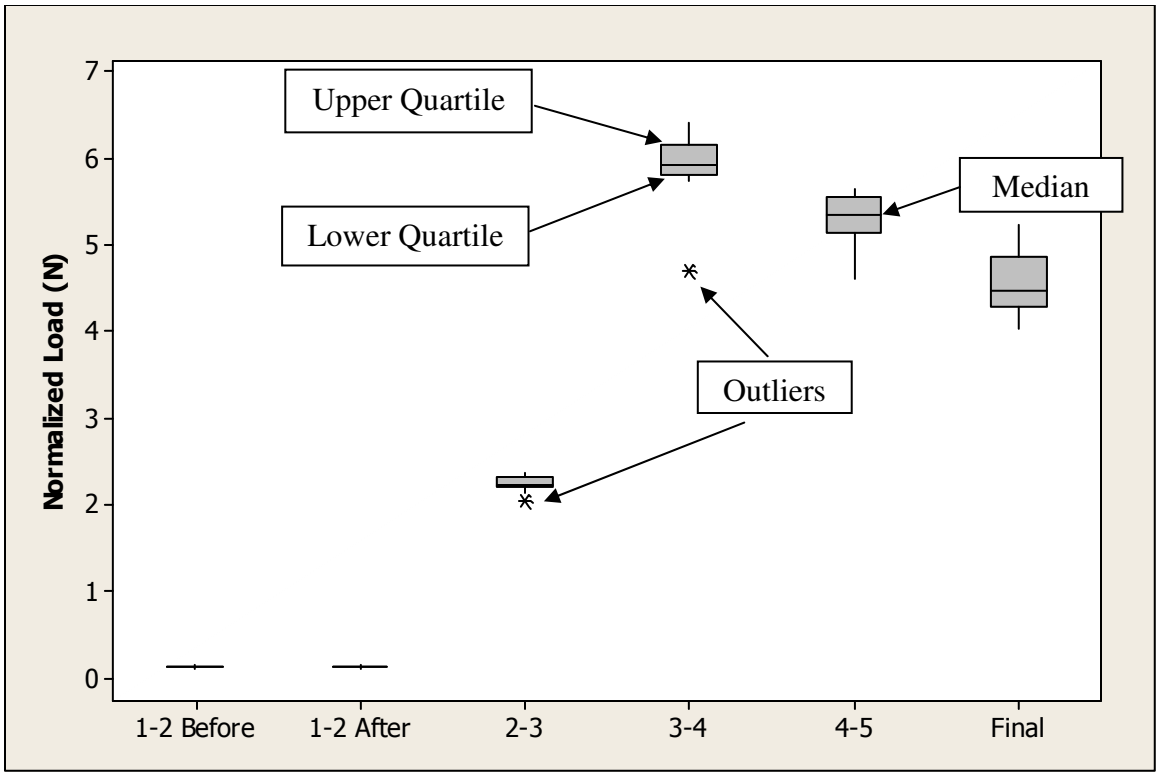


Figure **6.16**: Boxplot of loads between each stage of single steel needle penetration and the final load.

**Multiple Needle Spacing**

Six hexagonal patterns and one square needle array patterns were tested using the procedure described in Chapter 5. The hexagonal patterned arrays consist of the same steel needles used for the single needle tests and have center-to-center spacing distances of 0.75 mm, 1.00 mm, 1.25 mm, 1.50 mm, 2.00 mm, and 2.50 mm. Figure **6.17** shows a graph of average force versus displacement for each of the hexagonal patterns that was tested.

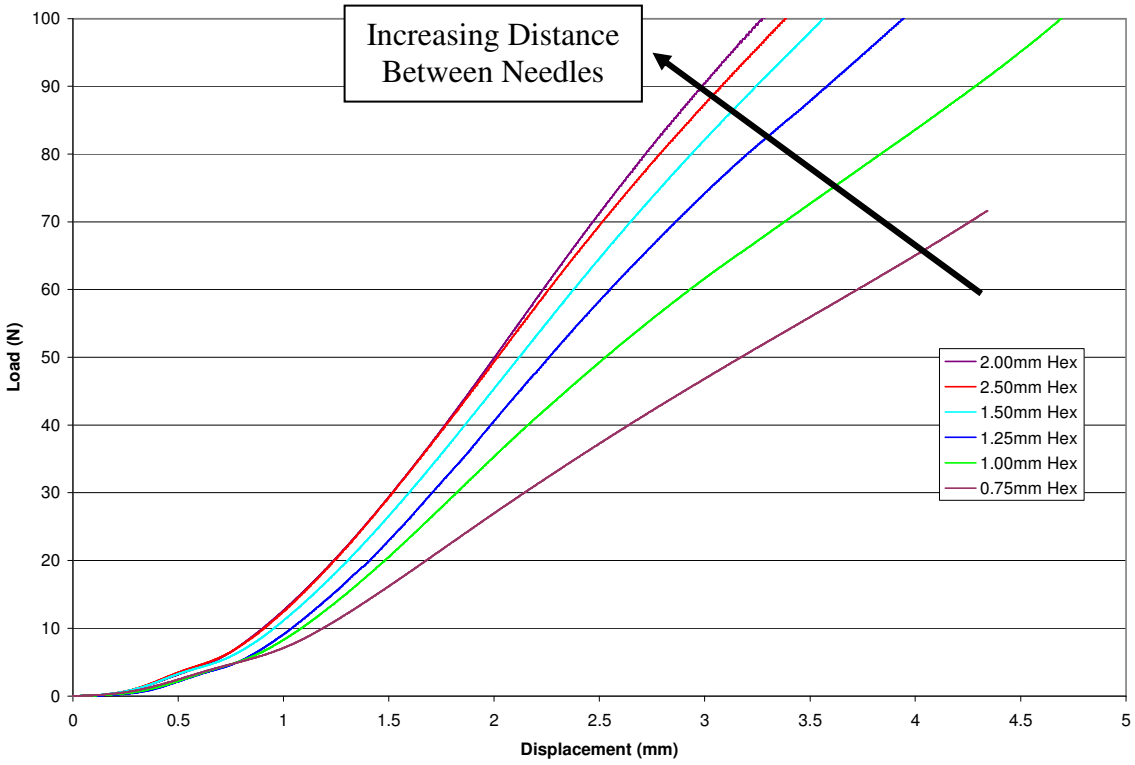


Figure **6.17**: Force versus displacement for six hexagonal steel needle patterns each with 37 needles.

Clearly there is a relationship that exists between needle spacing distance and the force required to penetrate to a certain depth. The same stages exist for multiple needle patterns as with the previously discussed single needle penetration. However, only the first three stages are present in Figure **6.17** due to the partial penetration of the rubber skin simulant.

In Figure **6.18** data for all six hex spacing patterns, the solitary square spacing pattern test data and single needle data of force-displacement is displayed. These tests are normalized by dividing the force by the number of needles present in each pattern. Again, the data show that those patterns with larger distances between needles approach

the data profile of a single needle. Note that the single needle data profile is set away from the largest needle spacing patterns at a nearly uniform distance throughout the graph. This is due to the measurement error that comes from the load cell which can only accurately measure to 0.125N. The single needle line is adjusted to better align its start of penetration with those of the multiple needle patterns.

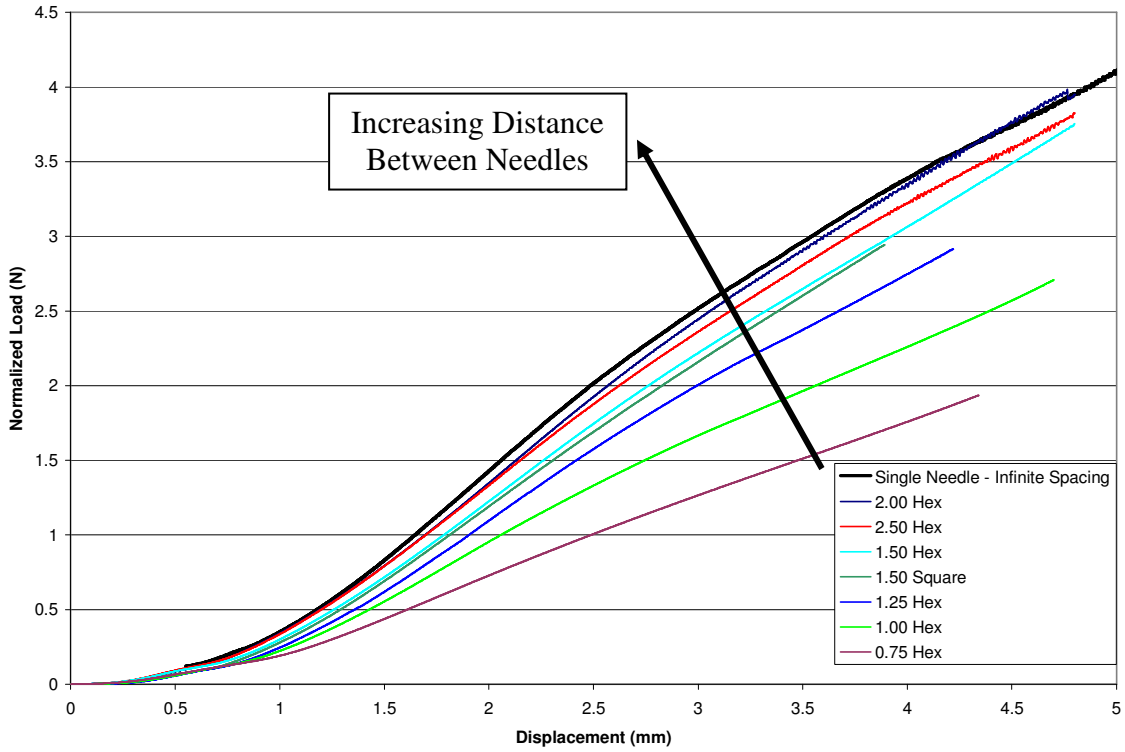


Figure **6.18**: Force versus displacement for normalized data of each pattern of steel needles.

The experimental data were analyzed to determine the points at which each stage of penetration take place. This analysis is performed for the normalized data so that hex needle pattern data, square needle pattern data, and single needle data can be compared directly. Figure **6.19** shows the region where the penetration mechanism shifts from

stage 1 to stage 2 and the needle tip(s) just begin to penetrate after overcoming the fracture toughness of the material. The transition is easy to see on a force-displacement graph as it is defined by a change in the slope of the material. Figure **6.20** shows a boxplot of the loads at which this transition occurs for each spacing regime. There is no statistical difference between any group.

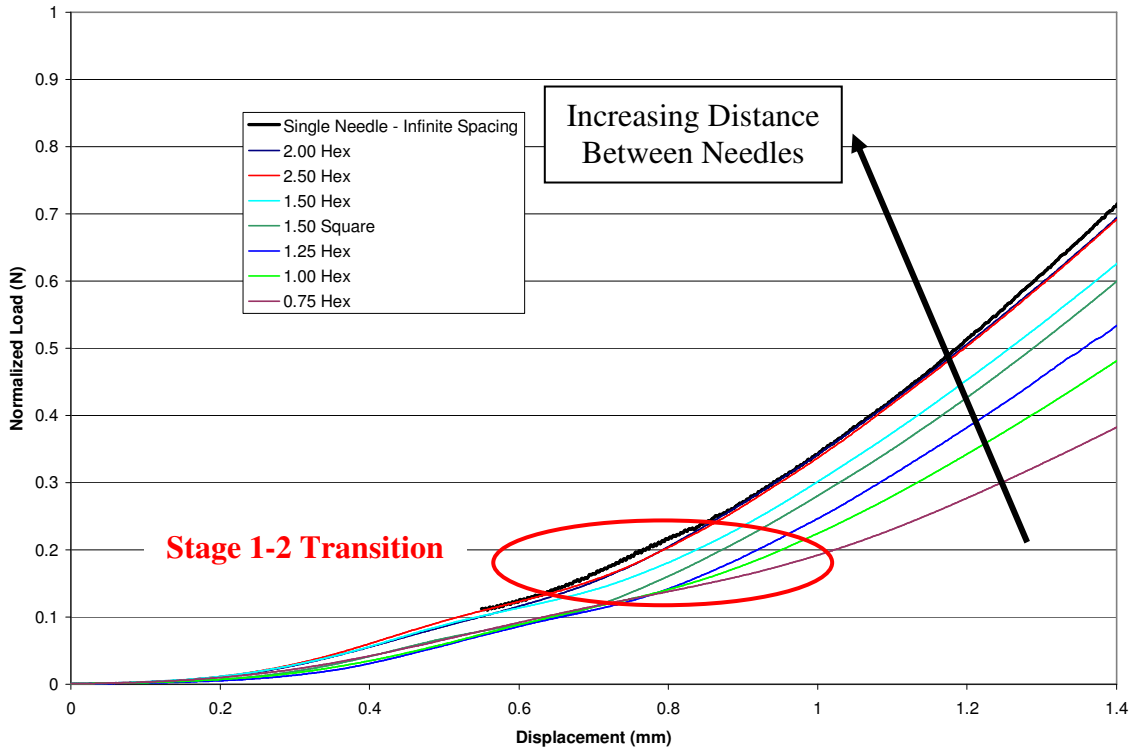


Figure **6.19**: Normalized force versus displacement for stage 1-2 transition region for steel needle spacing devices.

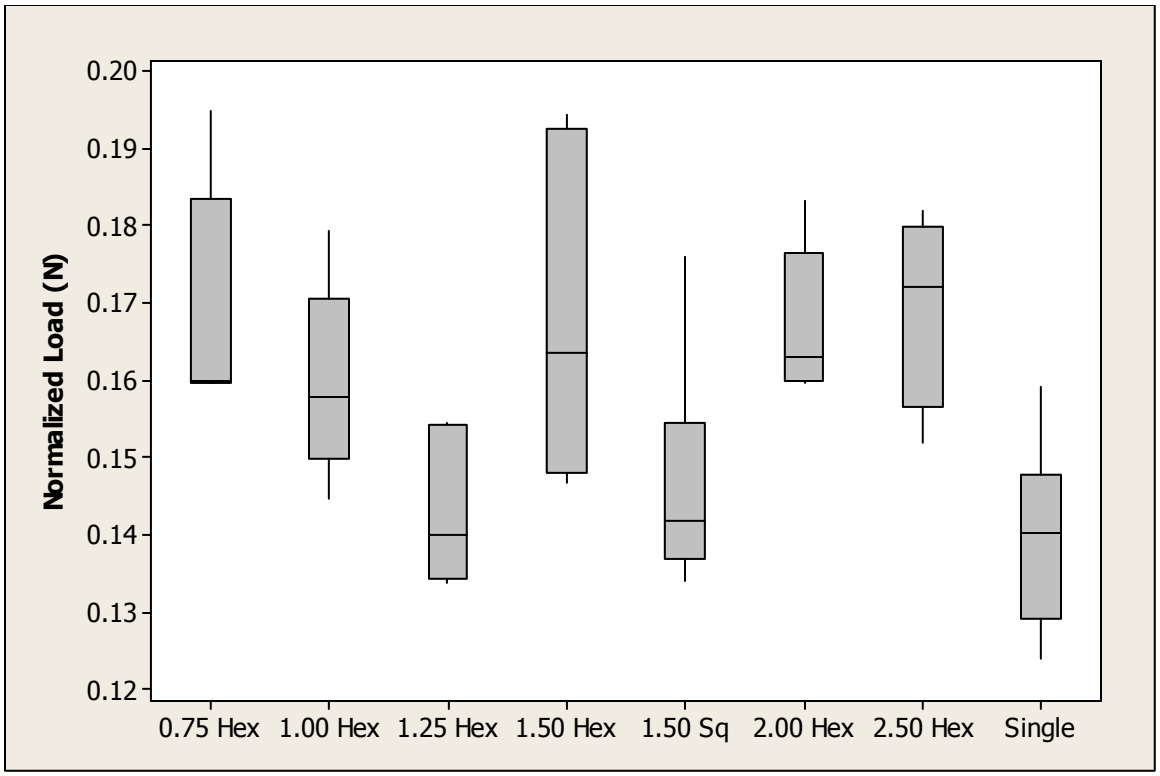


Figure **6.20**: Boxplots of normalized loads at transition from stage 1 to stage 2 for steel needle patterns.

The other transition region present for the multiple-needle patterns is the transition from the needle's angled tip to the shaft. Figure **6.21** shows the approximate region for the transition from stage 2 to stage 3. This change is defined as a leveling off of the plot into a linear region. This is due to a constant increase in force from the increasing friction of the needle shaft. Figure **6.22** shows a boxplot of loads for the transition from stage 2 to stage 3. There are small statistical differences between the single needle load, the 1.00 mm to 1.50 mm hex patterns, and the other three patterns. The 0.75 mm spacing device does not reach this stage because it no longer penetrates into the rubber and all the applied force is causing the rubber to compress.

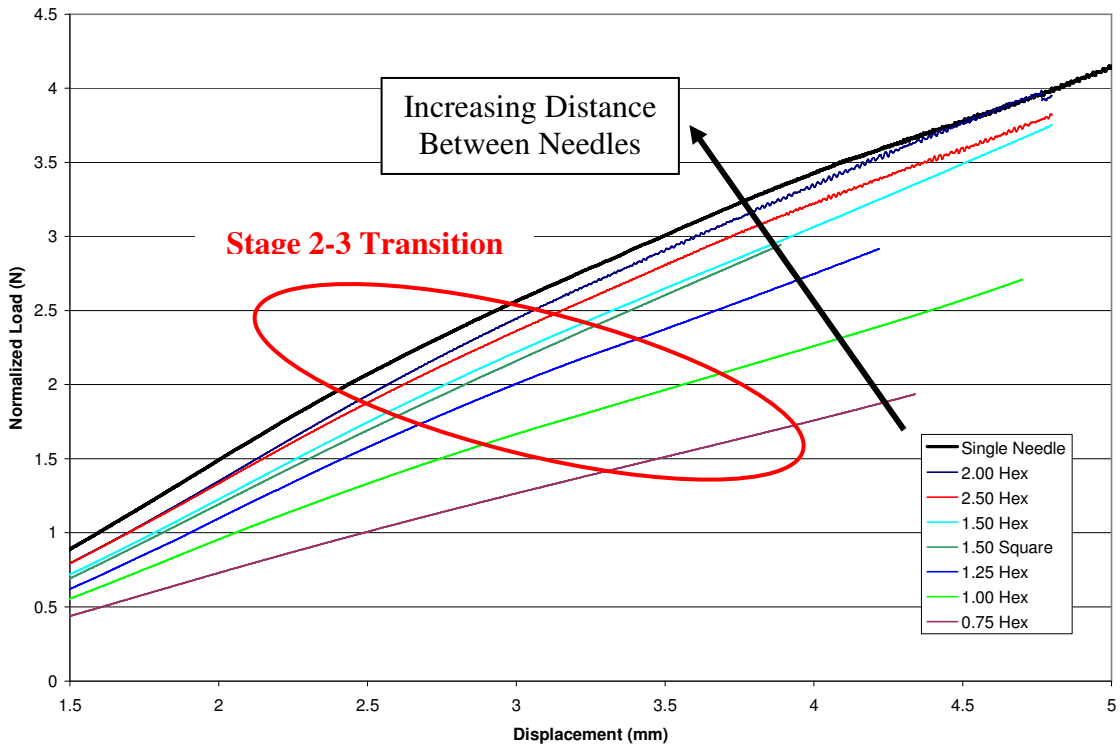


Figure **6.21**: Normalized force versus displacement for stage 2-3 transition region.

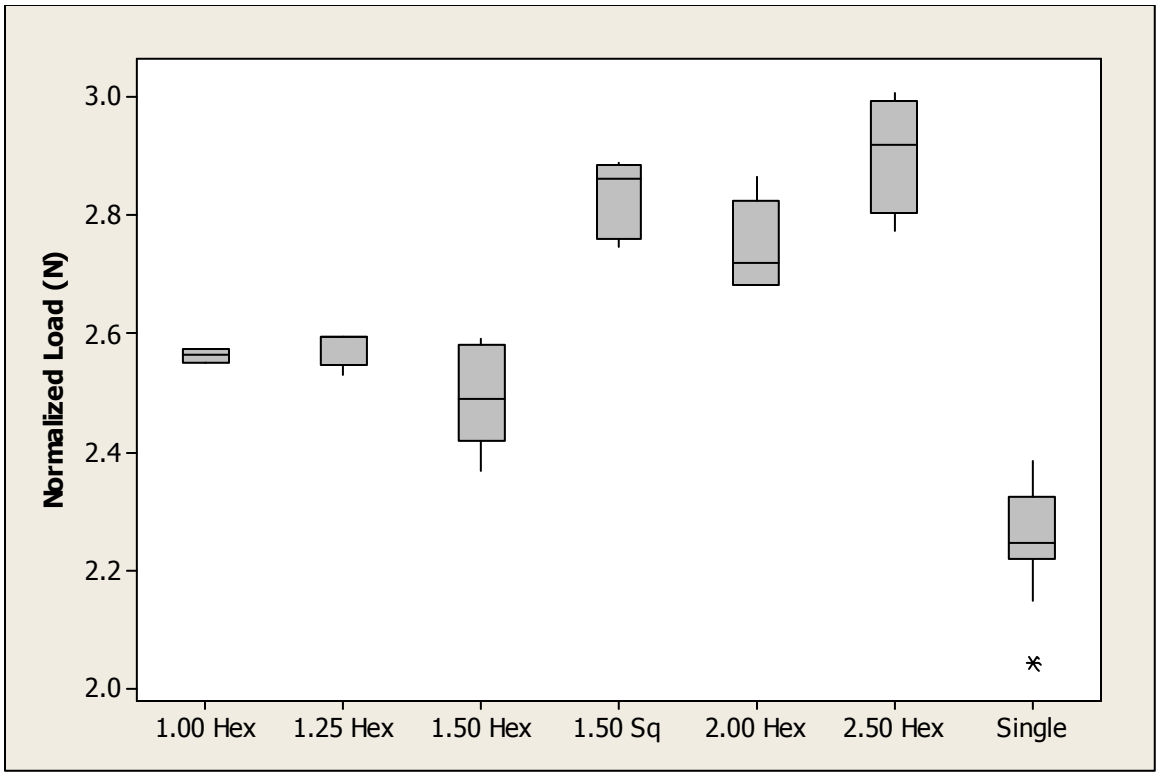


Figure **6.22**: Boxplot of loads for transition from stage 2 to stage three penetration for steel needle patterns.

The location of each region is confirmed by evaluating the actual penetration depths of each of the single and multiple-needle devices. This series of tests is performed using the method described in chapter 5 where a specific load is applied and the total displacement is recorded. The total displacement consists of both penetration and compression of the silicone. The load is then removed and the displacement is again recorded. By removing the load and measuring the penetration, the amount of compression of the silicone can be determined for each pattern. Figure **6.23** shows the normalized loads for all patterns plotted against depth of needle penetration. This shows that there is a linear correlation between penetration depth and the applied load that is constant regardless of the pattern.

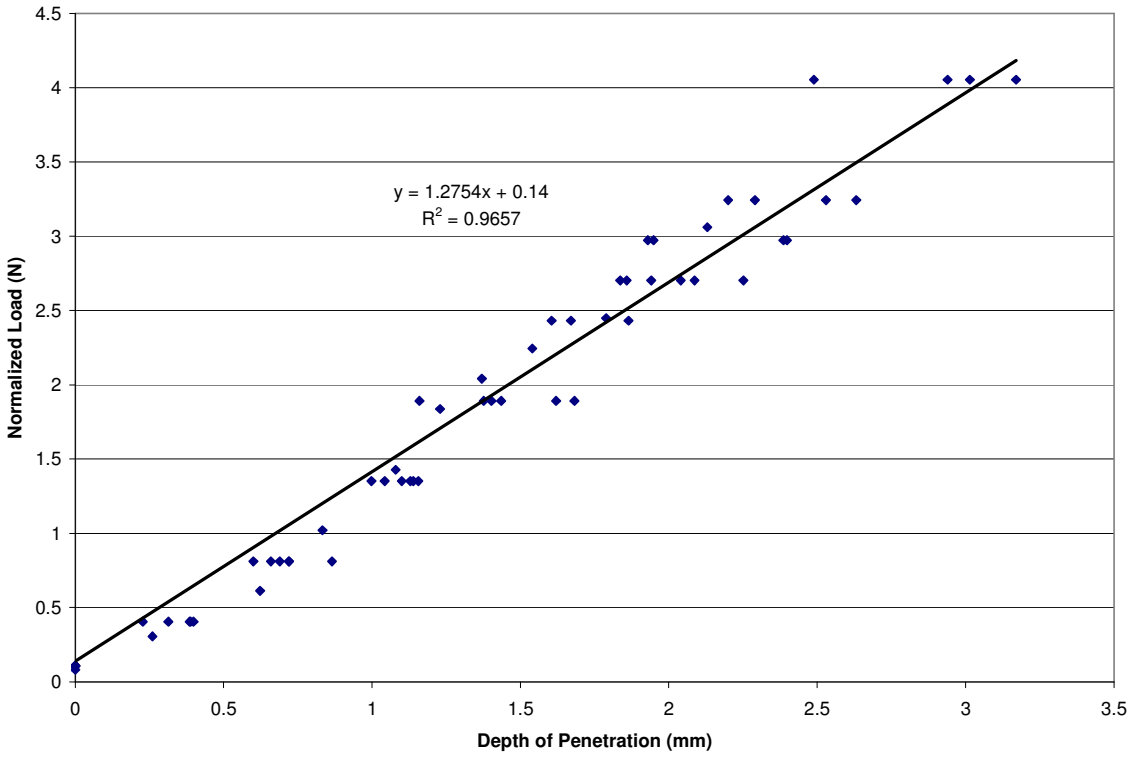


Figure **6.23**: Penetration depth versus normalized load for all steel needle pattern.

The other component of the total displacement is the compression of the silicone rubber test medium. Figure **6.24** shows the displacement plotted against load for each pattern. The figure shows that closer spacing of needles results in a far higher amount of compression of the silicone, thus resulting in less penetration. It should be noted that the closest spaced needle patterns were limited by the base of their fixtures as to how far they could penetrate. In other words, they reached a point where only material compression was taking place and no more penetration was occurring.

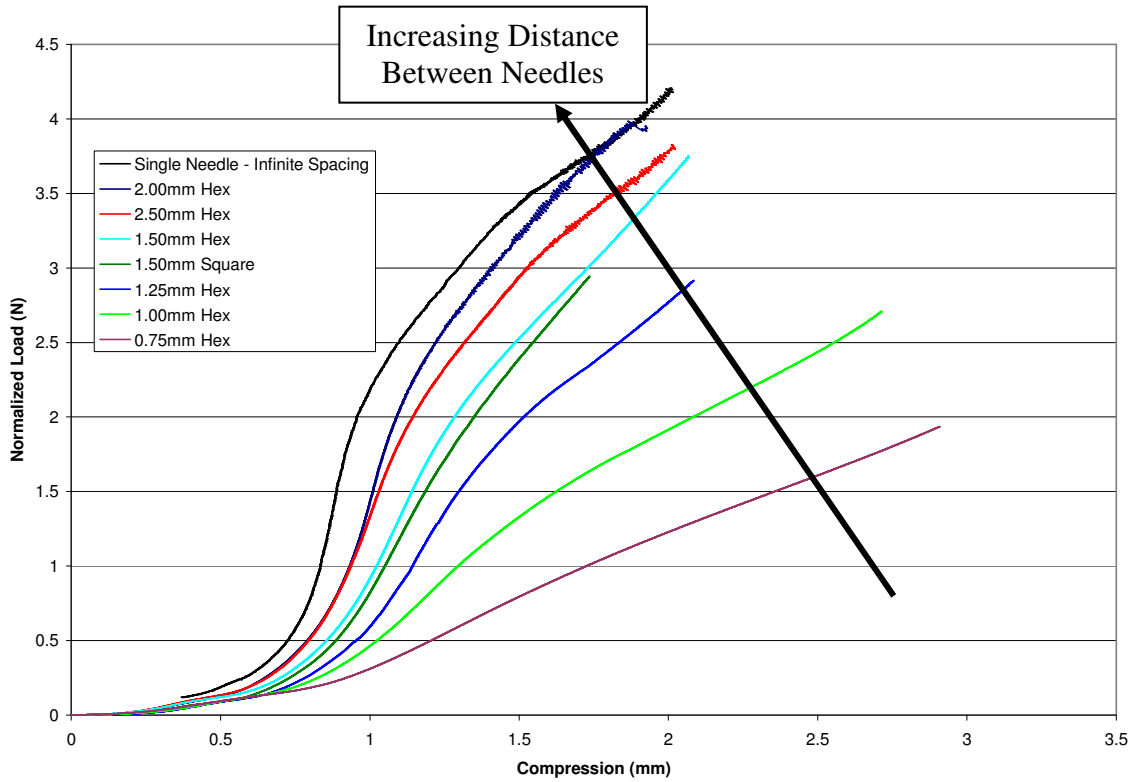


Figure **6.24**: Normalized load versus compression for each steel needle pattern.

This method is somewhat limited in its ability to describe the penetration and compression components of needle displacement. While only a small, finite number of points are recorded for these tests, the overwhelming linear nature of the data shows a clear pattern. These tests do show that there are major differences in material compression for each pattern that can explain the overall differences. This type of penetration test also reinforces the theory that each distinct stage of penetration described earlier occurs as hypothesized.

Two needle patterns can be examined to illustrate these differences. Figure **6.25** shows the total displacement along with its components of compression and penetration

for the 0.75 mm hexagonal spacing pattern. Figure **6.26** shows the total displacement along with compression and penetration components for the 2.50 mm spacing pattern.

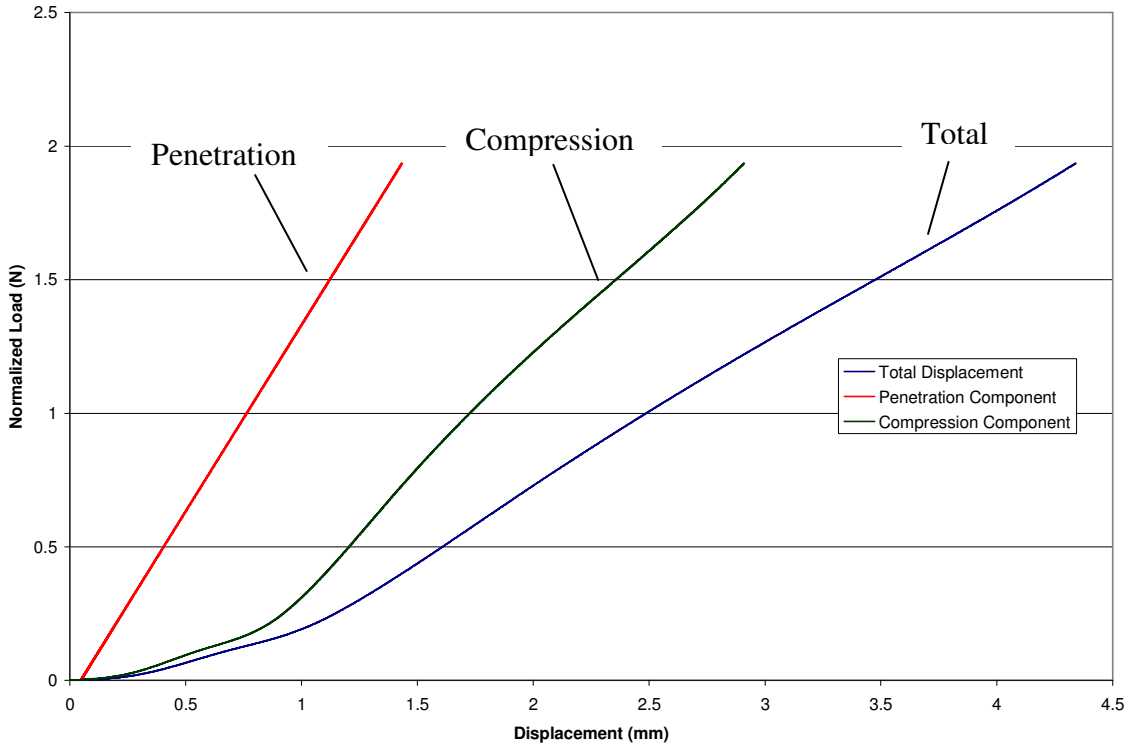


Figure **6.25**: Normalized load versus displacement for 0.75 mm hexagonal pattern showing total displacement, compression, and penetration.

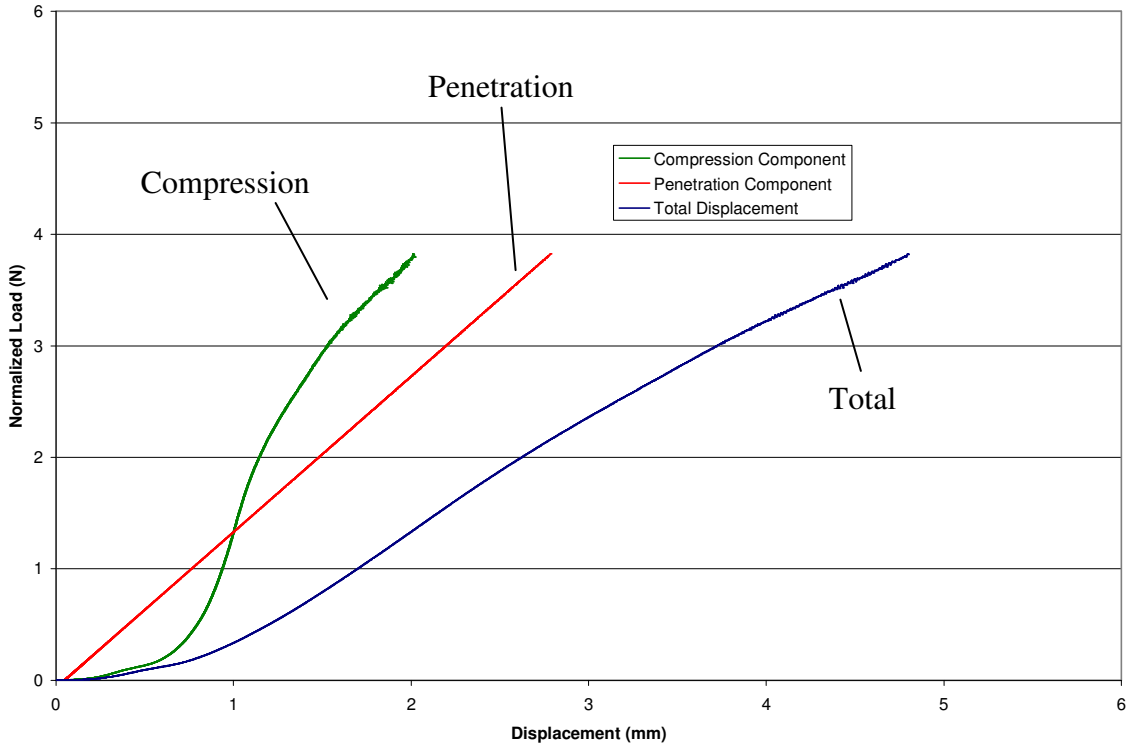


Figure **6.26**: Normalized Load versus displacement for 2.50 mm pattern showing total displacement, compression, and penetration.

The two plots show a clear difference between the most and least dense spacing patterns that were tested. The 0.75 mm pattern is dominated by compression of the silicone throughout the test, yet still shows a steady increase in needle penetration. This contrasts with the 2.50 mm pattern that shows a small, almost steady amount of compression throughout the test, and a linear increase in the amount of penetration.

**Solid Hexagonal Indenter Testing**

Six solid hexagonal shaped indenters were tested using the procedure described in Chapter 5. The bottom surfaces of the indenters have areas that are equal the steel needle

hexagonal patterns total outline. These tests represent a test case where the needle spacing is effectively zero. Figure **6.27** shows a representation of the solid indenter outline in relation to the needles that are in a 37-needle hexagonal pattern. A total of six hexagonal indenters were tested.

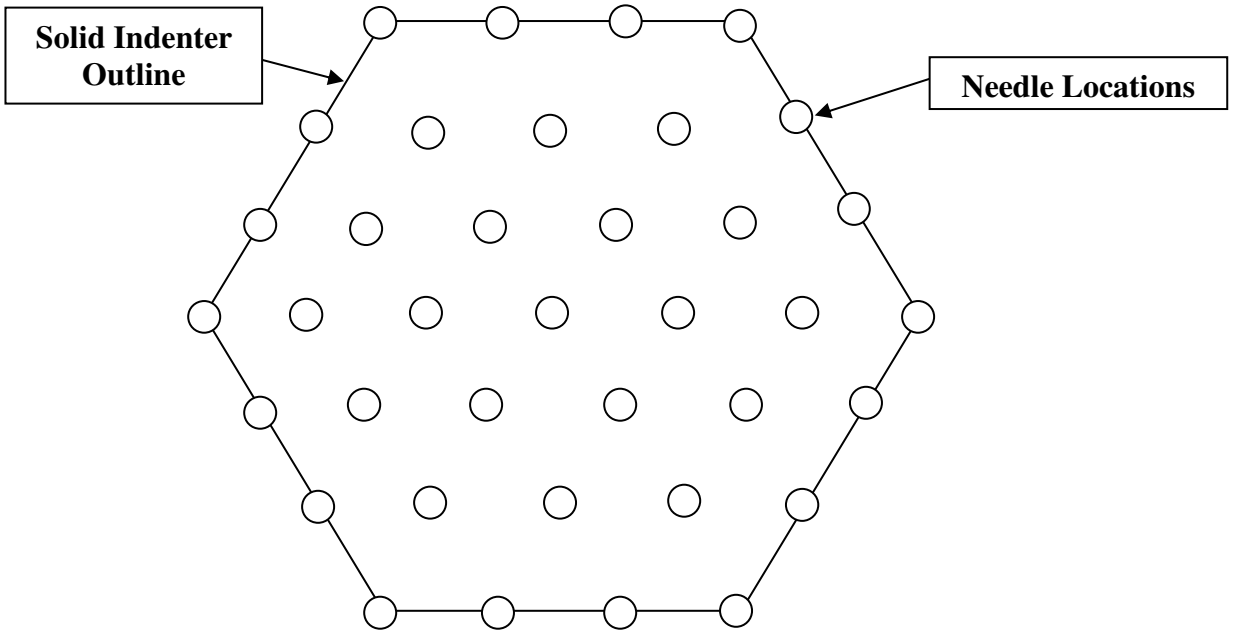


Figure **6.27**: Representation of solid indenter area compared to steel needle locations on the needle spacing device.

Figure **6.28** shows a chart for the average load versus displacement for the hexagonal shaped indenter with an area of 13.15 square mm. This is equal to the area of a needle spacing device with 0.75 mm of separation between each needle.

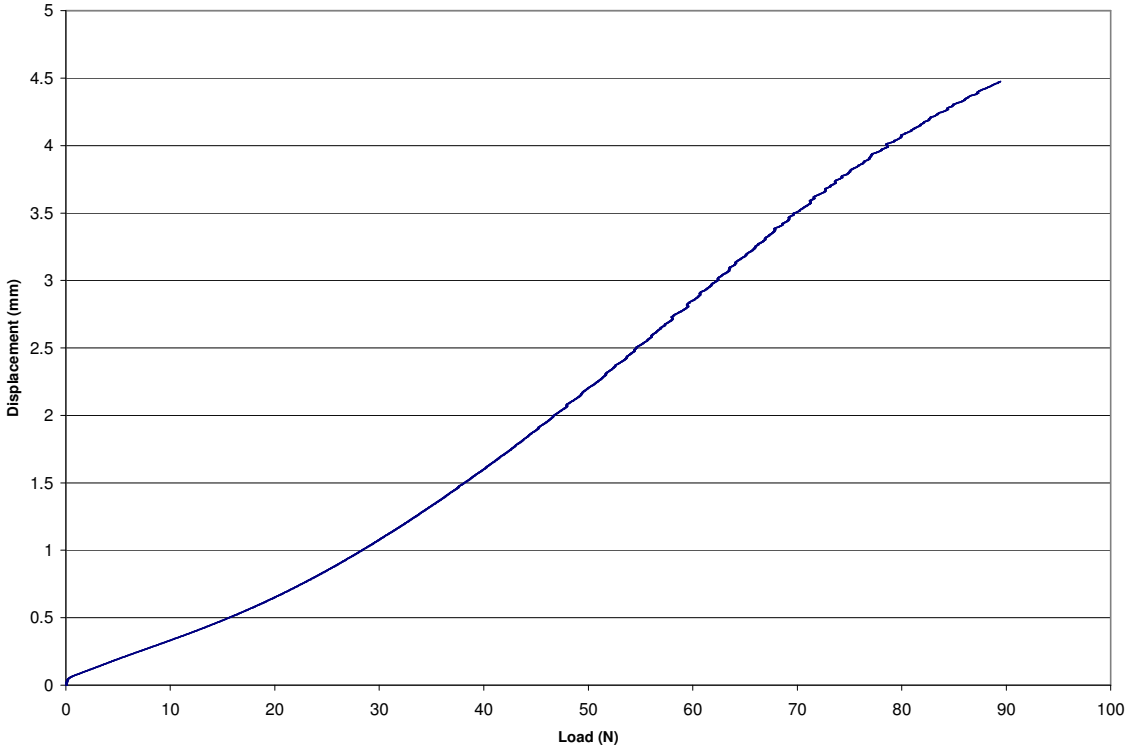


Figure **6.28**: Load versus displacement for hexagonal indenter with area equal to the needle spacing device with 0.75 mm of separation between needles.

Figure **6.29** shows the average load versus displacement for the hexagonal shaped indenter with an area of 23.38 square mm. This is equal to the area of a needle spacing device with 1.00 mm of separation between each needle.

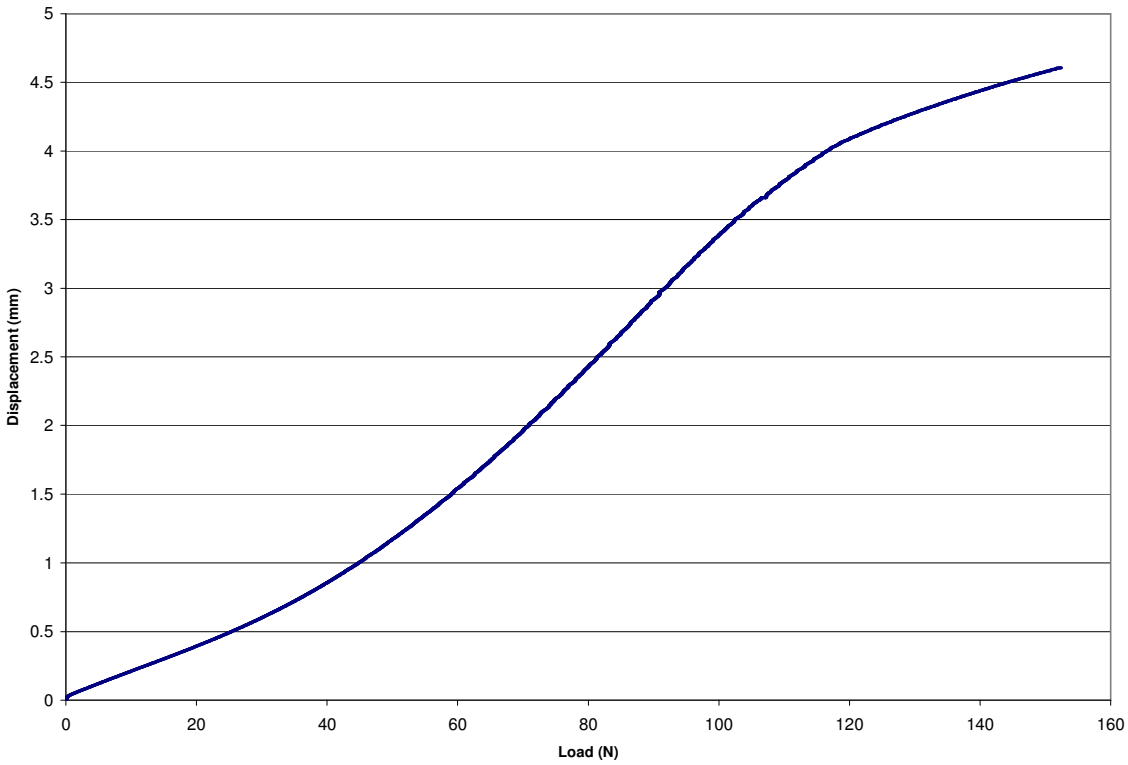


Figure **6.29**: Load versus displacement for hexagonal indenter with area equal to the needle spacing device with 1.00 mm of separation between needles.

Figure **6.30** shows the average load versus displacement for the hexagonal shaped indenter with an area of 36.54 square mm. This is equal to the area of a needle spacing device with 1.25 mm of separation between each needle.

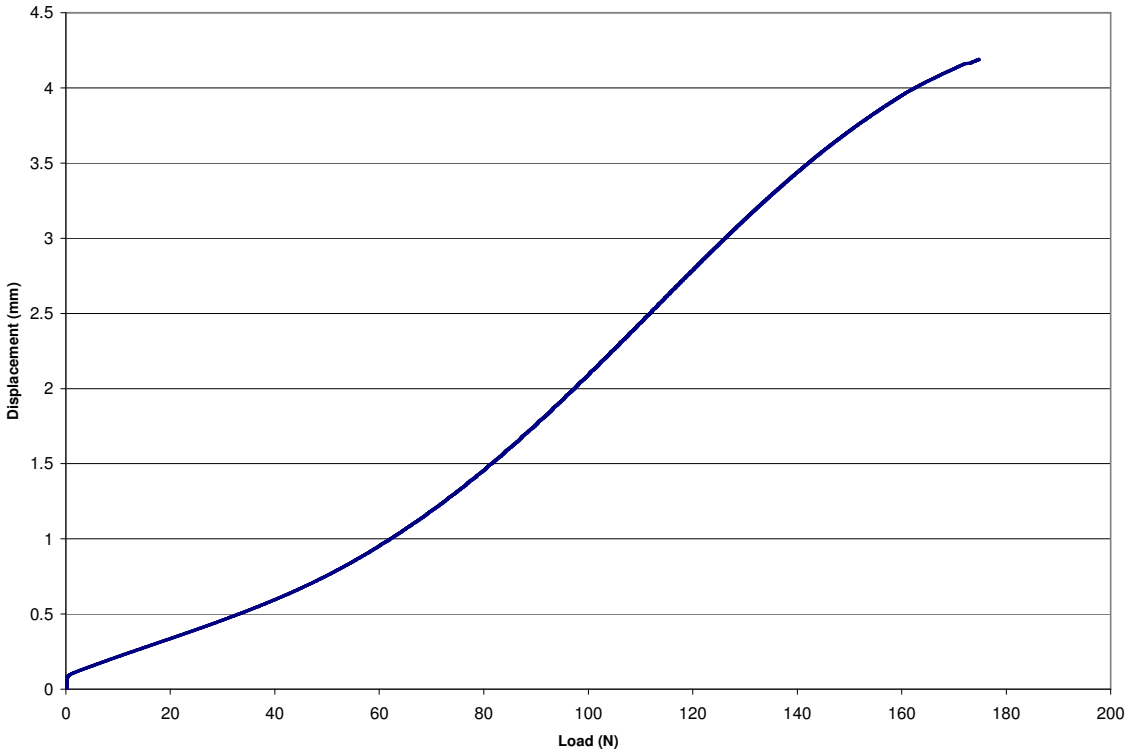


Figure **6.30**: Load versus displacement for hexagonal indenter with area equal to the needle spacing device with 1.25 mm of separation between needles.

Figure **6.31** shows the average load versus displacement for the hexagonal shaped indenter with an area of 52.61 square mm. This is equal to the area of a needle spacing device with 1.50 mm of separation between each needle.

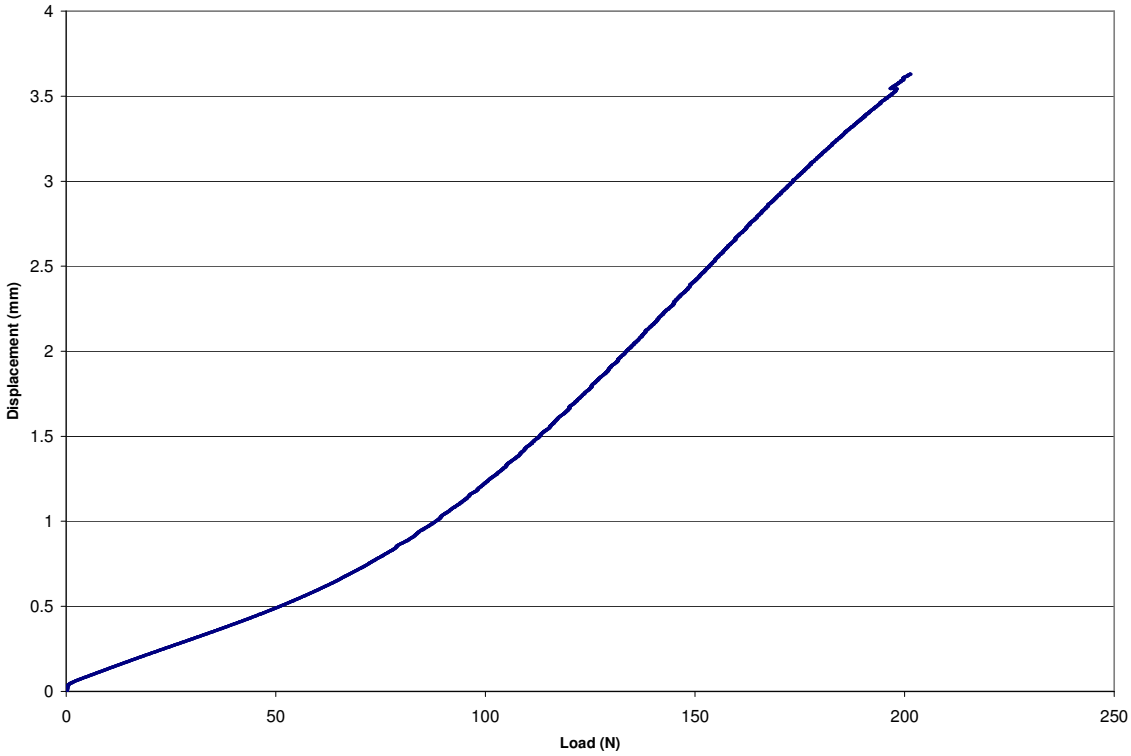


Figure **6.31**: Load versus displacement for hexagonal indenter with area equal to the needle spacing device with 1.50 mm of separation between needles.

Figure **6.32** shows the average load versus displacement for the hexagonal shaped indenter with an area of 93.53 square mm. This is equal to the area of a needle spacing device with 2.00 mm of separation between each needle.

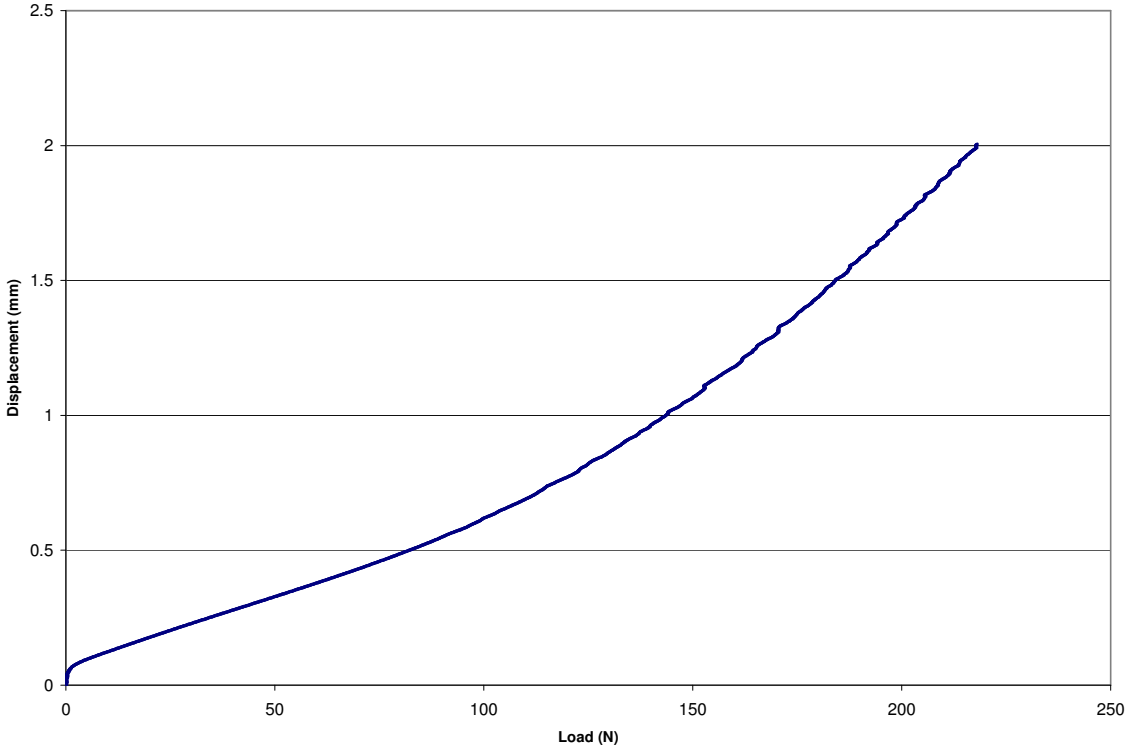


Figure **6.32**: Load versus displacement for hexagonal indenter with area equal to the needle spacing device with 2.00 mm of separation between needles.

Figure **6.33** shows the average load versus displacement for the hexagonal shaped indenter with an area of 146.14 square mm. This is equal to the area of a needle spacing device with 2.50 mm of separation between each needle.

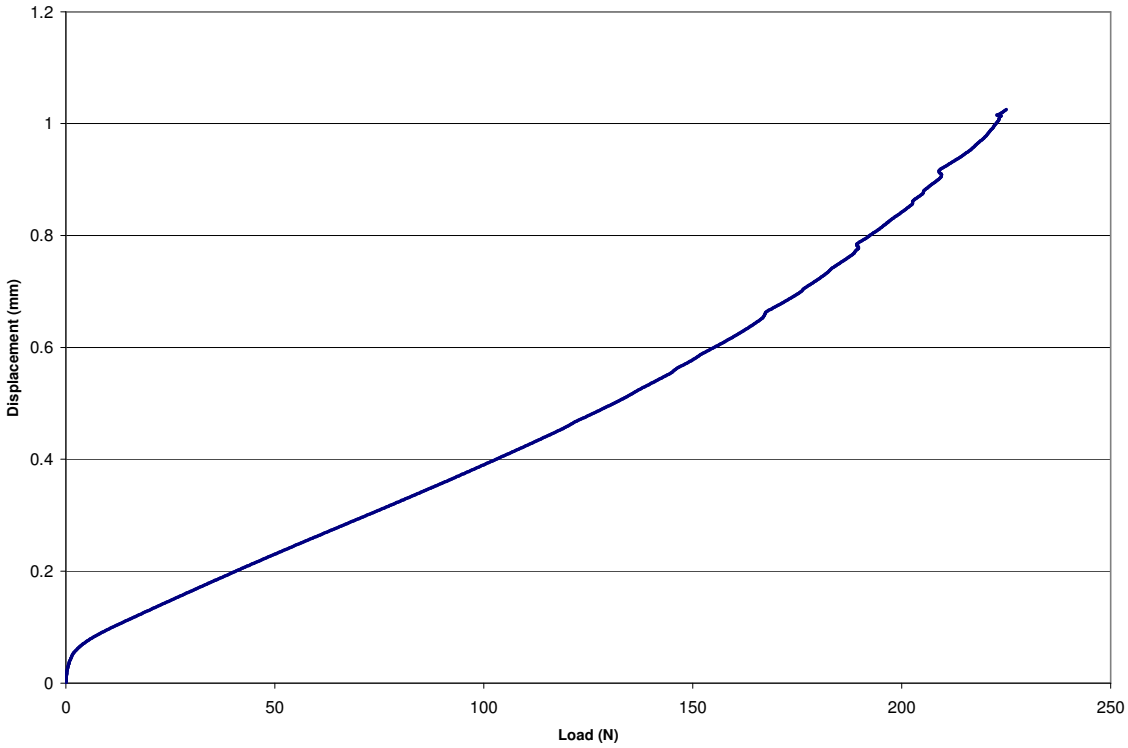


Figure **6.33**: Load versus displacement for hexagonal indenter with area equal to the needle spacing device with 2.50 mm of separation between needles.

Combining results from all indenters onto a single chart allows comparisons to be made between the various indenters. Figure **6.34** shows the results from all six hexagonal shaped indenters on a single chart. The chart shows that for larger indenter areas, a larger force is required to deflect the rubber to a given amount.

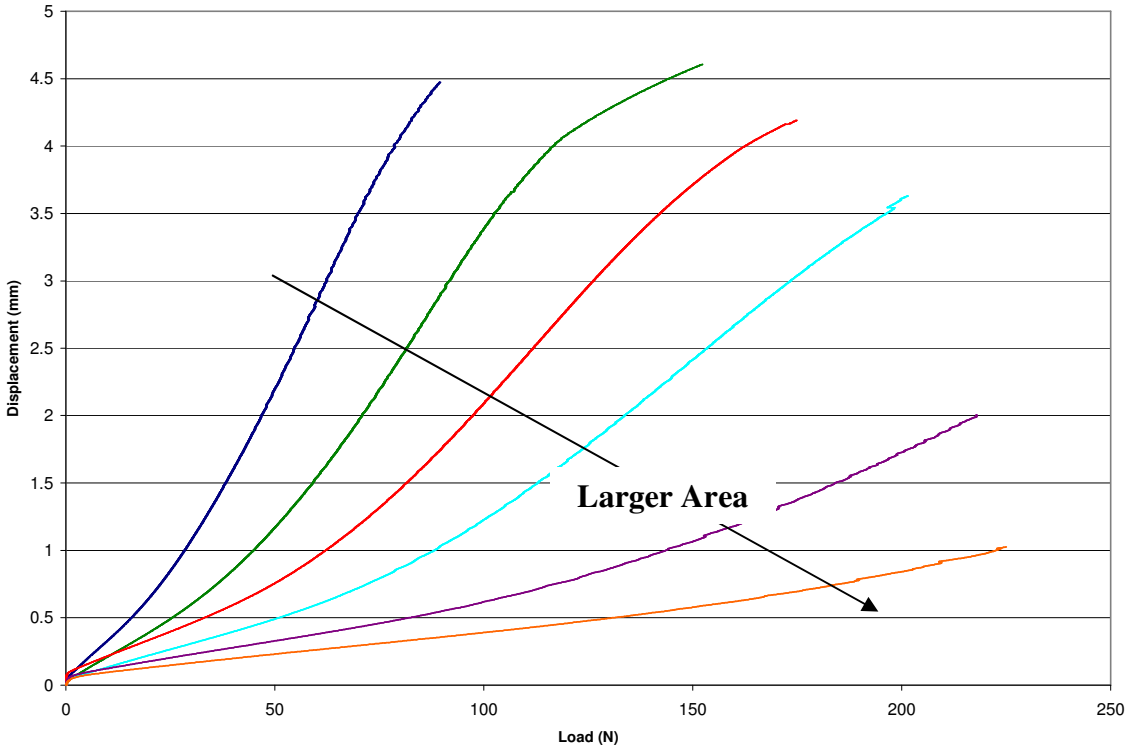


Figure **6.34**: Comparison of load versus displacement for all six hexagonal shaped indenters.

The data derived from testing these indenters will be used in Chapter 7 to describe how needle spacing affects the load required to penetrate into skin to various depths.

## Plastic Microneedle Devices

The plastic microneedle devices were tested using the procedure and testing apparatus described in chapter 5. A total of 16 groups of 20 microneedle devices in each group were tested. Figure **6.35** shows the average normalized load versus displacement for the 1.00 mm square pattern, 1.50 mm square pattern, and 1.00 mm hexagonal pattern for polystyrene microneedle devices.

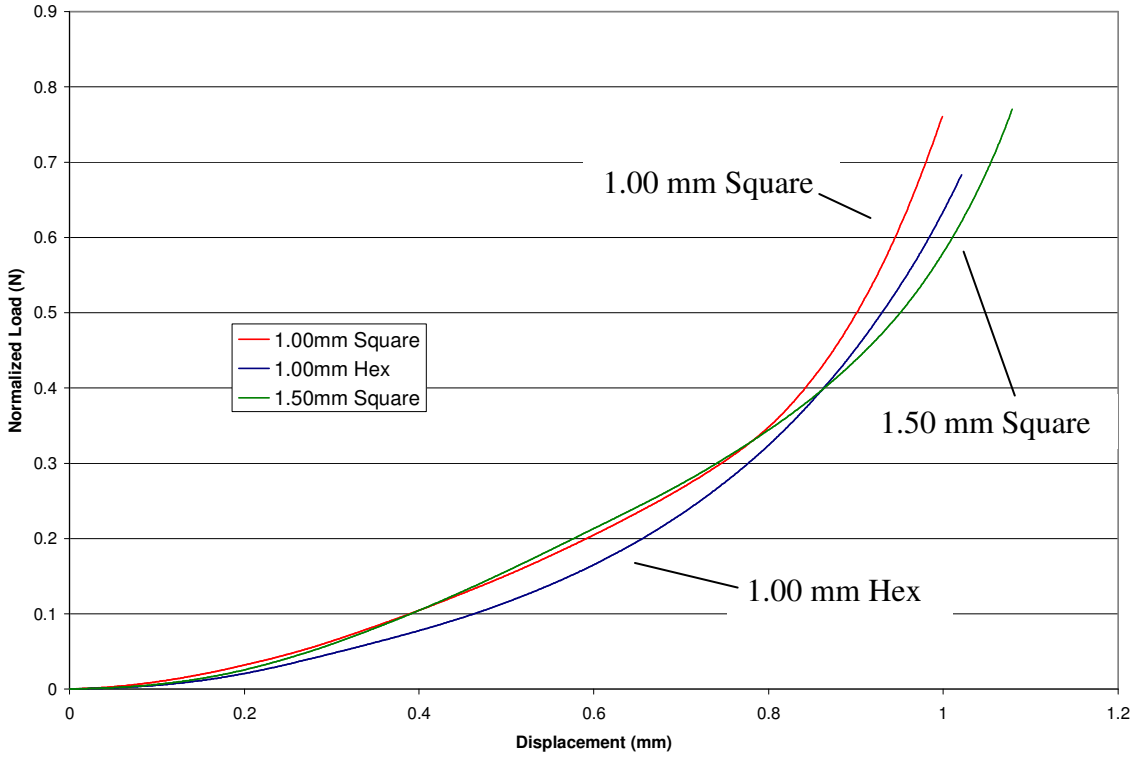


Figure **6.35**: Normalized load versus displacement plot for polystyrene microneedle devices.

Figure **6.36** shows the results of testing for the IXEF 1022 PARA microneedle devices for all four patterns.

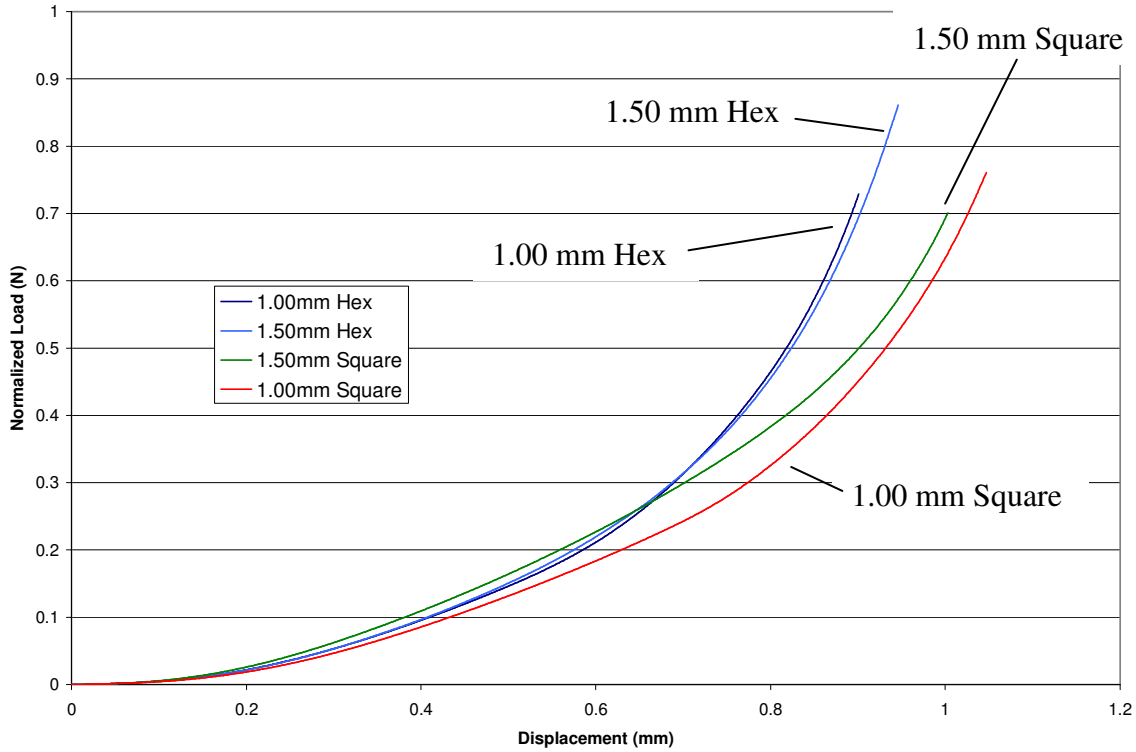


Figure **6.36**: Normalized load versus displacement for all four patterns of IXEF 1022 material.

Figure **6.37** shows the results of testing for all four patterns of Vectra A130 LCP.

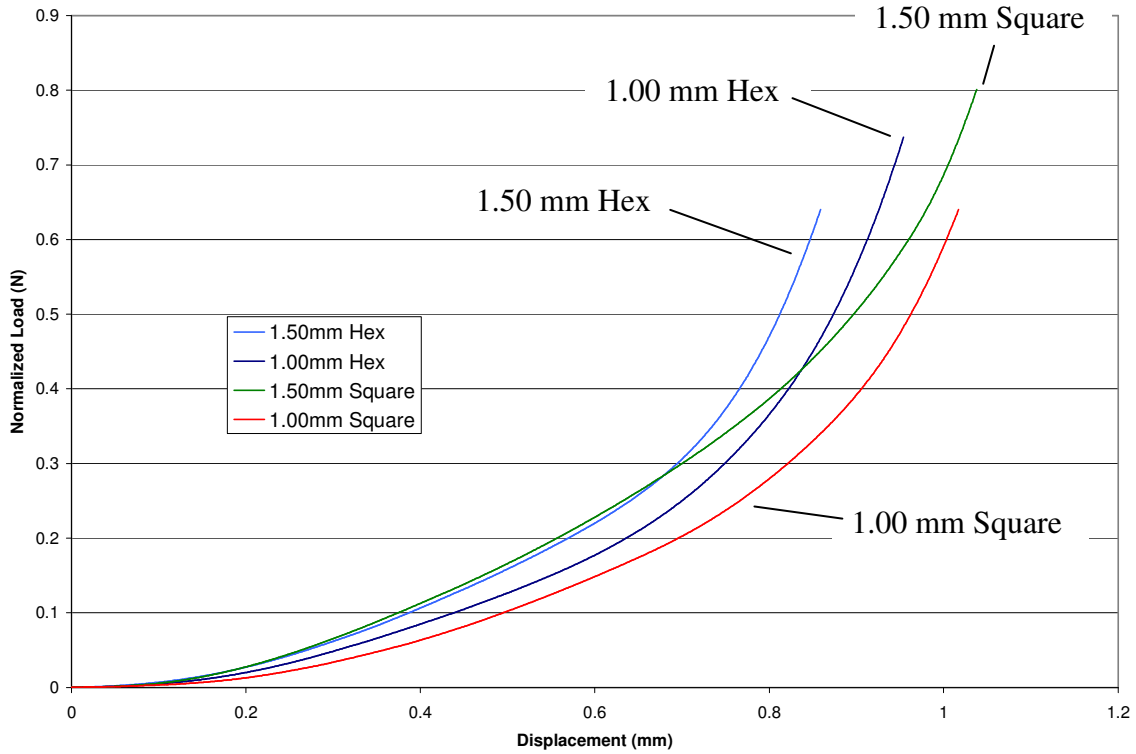


Figure **6.37**: Normalized load versus displacement for all four patterns of Vectra A130 LCP.

Figure **6.38** shows the Topas 5013-S04 COC microneedle device testing results.

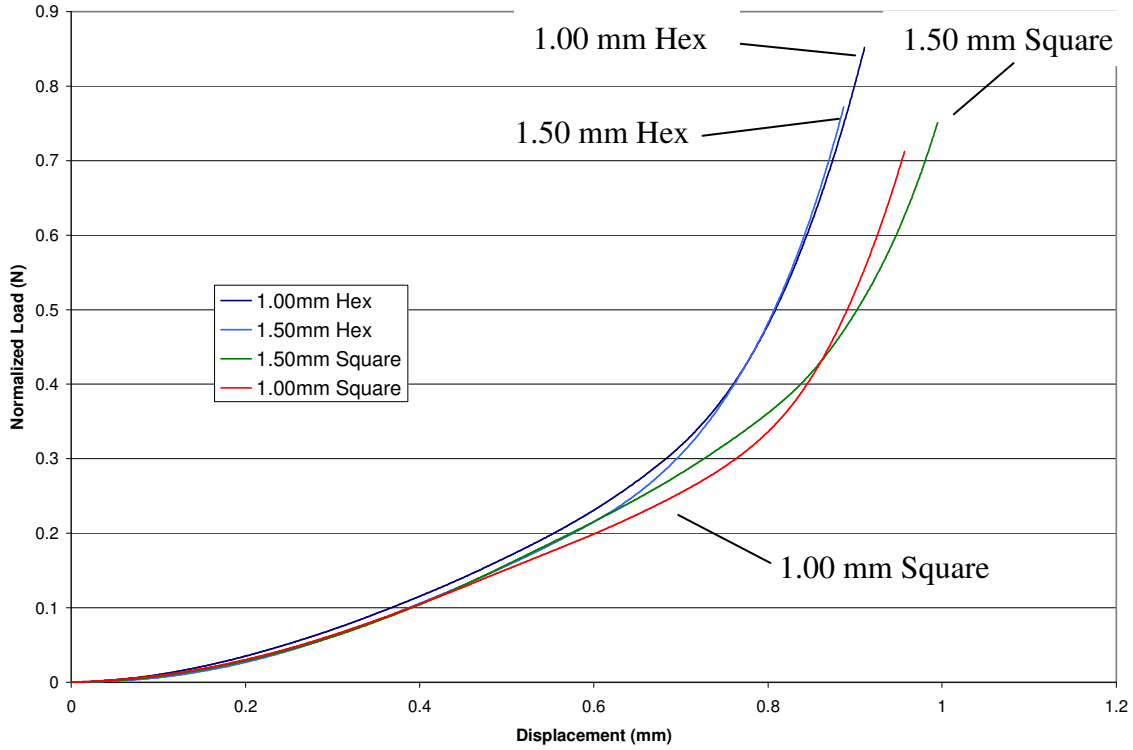


Figure **6.38**: Normalized load versus displacement for all four patterns of Topas 5013-S04 COC.

Figure **6.39** shows the testing result average from the 1.50 mm square pattern for the Makrolon 2207 polycarbonate.

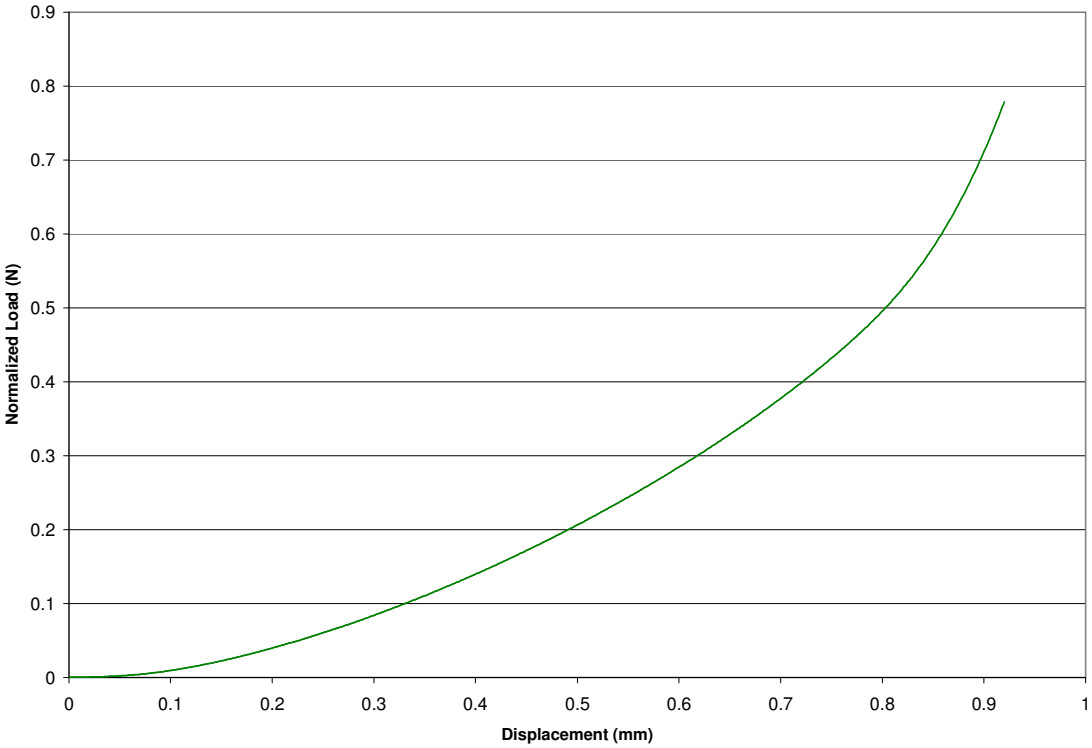


Figure **6.39**: Normalized load versus displacement for 1.50 mm square pattern made from Makrolon 2207 polycarbonate.

The shape of the plot for each injection molded plastic microneedle device shows there is little difference between various spacing patterns. The reasons for this will be explored in Chapter 7.

This chapter has presented the results of physical testing. These were the results for needle spacing apparatus tests, polymer microneedle tests, and tip radius and length measurements. Chapter 7 will discuss and analyze the results of penetration testing presented in this chapter. Those results will be used to develop an analytical model relating penetration forces, penetration depths, and material compression. Comparisons

also will be made between various attributes including the skin's mechanical properties, needle features, and friction properties.

# Chapter 7

# Discussion

This chapter will discuss the results of penetration testing presented in chapter 6. Those results will be used to develop an analytical model relating penetration forces, penetration depths, and material compression. Comparisons will be made between various attributes including mechanical skin properties, needle features, and friction properties.

## Penetration Analysis

The analysis of the penetration for microneedles requires an understanding of the mechanisms that occur during each stage of needle penetration. Figure **6.20** shows there is no statistical difference between loads at which a needle initializes penetration into the rubber skin simulant regardless of spacing pattern. Figure **6.23** shows needle penetration depth to be linear for a given load regardless of spacing pattern. The differences in the patterns, as shown in Figure **6.18**, come from additional deflection from the rubber. Each stage of penetration and the pattern differences will be explored in this section.

A discussion of microneedle array penetration analysis must begin with analysis of a single needle penetration. Several studies have examined needle penetration and the various components that contribute to forces acting on a needle. One such study by Davis *et al*. states simply, “when the energy delivered to the skin by the needle exceeds

the energy necessary to create a tear in the skin, the needle will insert into the skin" (2004, p. 1158). A study by Shergold and Fleck regarding the penetration of soft solids by a frictionless, sharp-tipped punch suggests that the work required to insert a needle consists of work required to create a crack in addition to the strain energy stored in the material (Shergold & Fleck, 2005). Several of these models will be utilized to analyze needle penetration in this thesis in order to attain an accurate description of the underlying mechanisms.

**Stage 1 - Compression and Crack Initiation**

The first stage of penetration will be discussed. During this first stage, no penetration actually occurs and the rubber experiences only compression. It is during this initial stage that enough stress must be developed under the needle tip to initiate a crack in the rubber. Analyzing this stage requires the concurrent examination of two mechanisms. These include an analysis of elastic rubber indentation and analysis of crack formation energy.

One study relates reaction force and displacement with Young's modulus for various indenter geometries (Briscoe, Sebastian & Adams, 1994). This study specifically examines indentation of rubber within their elastic region and applies well to the first stage of penetration where most of the deformation is elastic and recoverable. The general form for this relationship is shown in Eq. **7.1** where P is the applied load, g and n are functions of the indenter geometry, E* is the reduced elastic modulus, and h is the displacement.

$$P = gE^* h^n \qquad \text{Eq. } \mathbf{7.1}$$

The reduced elastic modulus is defined by the relationship shown in Eq. **7.2** where **E** is the elastic modulus and **v** is Poisson's ratio. For most rubbers, Poisson's ratio is approximately 0.5.

$$E^* = \frac{E}{(1-v^2)} \qquad \text{Eq. } \mathbf{7.2}$$

A specific relationship between load and displacement exists for a conical indenter in Eq. **7.3**. The variable $\theta$ represents the included angle of the indenter as shown in Figure **7.1**. The variable **n** shown in Eq. **7.1** has a value of 2 for a cone as shown in Eq. **7.3**. The variable g has a value of $\frac{2}{\pi}\tan(\theta)$ for a conical shaped indenter.

$$P = \frac{2}{\pi} E^* \tan(\theta) h^2 \qquad \text{Eq. } \mathbf{7.3}$$

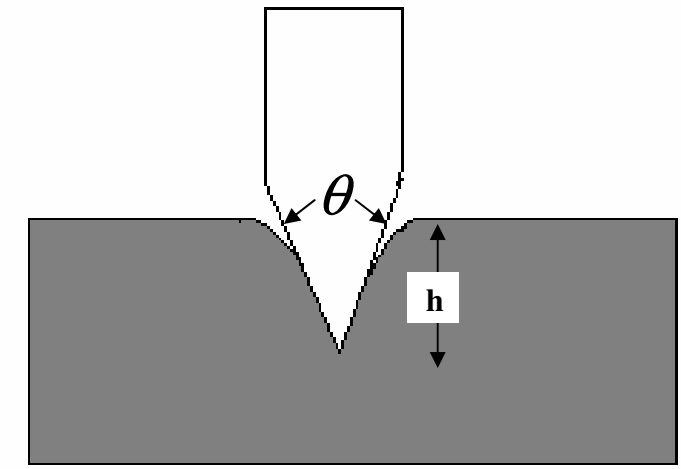


Figure **7.1**: Exaggerated schematic showing angle, $\theta$, and indentation depth, h.

Figure **7.2** shows the measured force versus displacement for a solid single steel needle from Figure **6.5** along with the curve generated by using Eq. **7.3**. The curve shows good agreement between the measured values and the theoretically derived values.

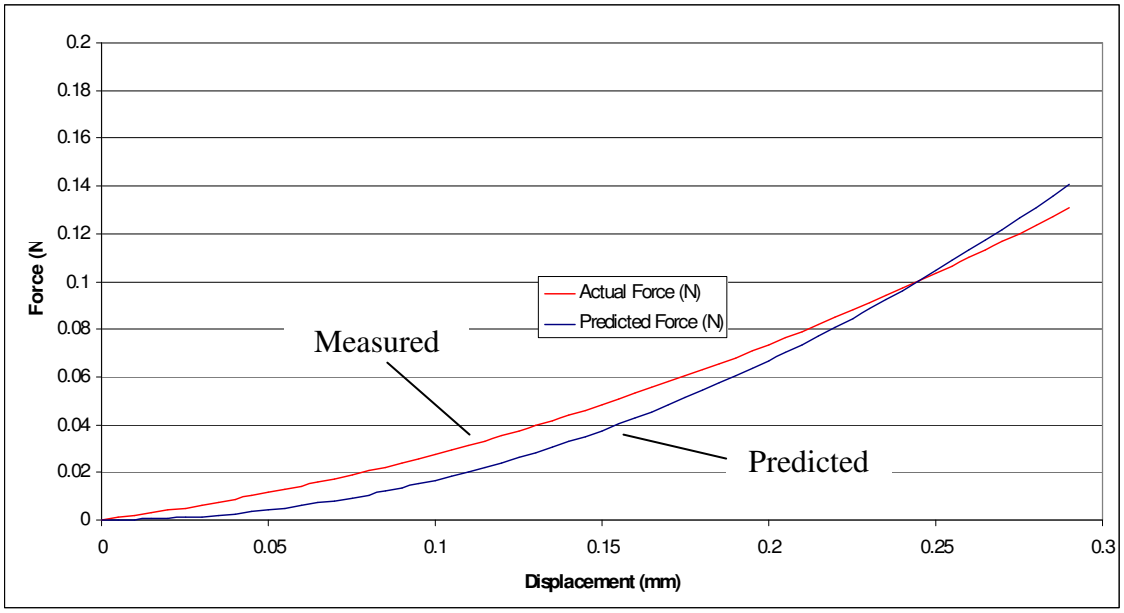


Figure **7.2**: Measured and predicted load versus displacement for a single steel needle.

A relationship now must be developed to explain the way the needle penetrates into the rubber medium. Davis *et al*. explains that the work to initiate a crack is dependent upon the puncture fracture toughness, $G_P$. The puncture fracture toughness is a property of the rubber skin simulant and is dependant upon the work input to initiate the crack and the resultant fracture area (Davis et al., 2004, p. 1158). Eq. **7.4** shows the relationship between puncture fracture toughness, work input, and surface area of the resultant fracture.

$$G_P = \left( \frac{\delta W}{\delta A} \right)_U \qquad \text{Eq. } \mathbf{7.4}$$

Davis expands on this concept and shows that the energy released during this crack initiation event can be calculated from the load versus displacement curve just before penetration occurs. Thus the energy can be calculated from Eq. **7.5** where $A_t$ is the surface area of the needle tip.

$$\int_{h=0}^{h=h_i} P \cdot dh = G_P \cdot A_t \qquad \text{Eq. } \mathbf{7.5}$$

Combining Eq. **7.3** with Eq. **7.5** and solving for $G_P$ results in Eq. **7.6**.

$$G_P = \left. \frac{\frac{2}{3\pi} E^* \tan(\theta) h^3}{A_t} \right|_{h=0}^{h=h_i} = \frac{\frac{2}{3\pi} E^* \tan(\theta) h_i^3}{A_t} \qquad \text{Eq. } \mathbf{7.6}$$

The area of the needle tip is determined by calculating the area of a sphere at the end of a conical prism. Figure **7.3** shows a representation of the needle tip contact area where $r_t$ is the tip radius and d is the perpendicular distance from the tip to the plane where the sphere and cone intersect.

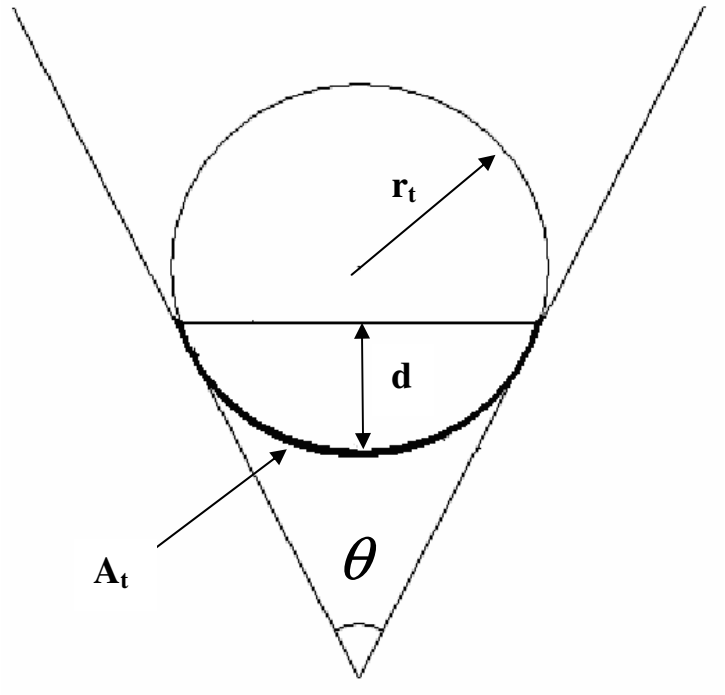


Figure **7.3**: Representation of needle tip area.

Geometric relationships can be used to determine the tip area, $A_t$, from the angle of the needle and the tip radius. This relationship is defined in Eq. **7.7**.

$$A_t = 2\pi r_t^2\left[1-\sin\left(\frac{\theta}{2}\right)\right] \qquad \text{Eq. } \mathbf{7.7}$$

Eq. **7.6** and Eq. **7.7** can be used to approximate $G_P$ for the silicone rubber being used. Using values for the actual needle geometry and the value where the penetration first occurs, the value for $G_P$ is approximately 9.3kJ/m$^2$. This is a reasonable value for the puncture fracture toughness for silicone rubber when compared to other values for various rubbers and skin samples that were found to be in the range of 7-40 kJ/m$^2$ (Burford & Potok, 1987; Davis et al., 2004; Khanna, Luongo, Strom & Bhansali, 2010; Marchal, Oldenhove, Daoust, Legras & Delannay, 1998).

The final displacement can be determined when the values for $G_P$ along with the tip radius, angle, and elastic modulus are known. Eq. **7.8** presents the equation to determine the needle displacement just before crack initiation.

$$h_i = \left( \frac{3\pi G_P A_t}{2E^* \tan(\theta)} \right)^{1/3} \qquad \text{Eq. } \mathbf{7.8}$$

Combining Eq. **7.3** and Eq. **7.8**, the final load can be calculated just prior to crack initiation as shown in Eq. **7.9**.

$$F_i = \left( \frac{2}{\pi} E^* \tan(\theta) \right)^{1/3} \left( 3G_P A_t \right)^{2/3} \qquad \text{Eq. } \mathbf{7.9}$$

**Stage 2 - Crack Propagation Force**

The model of Shergold and Fleck suggests that the energy required to advance a sharp tipped punch through a semi-infinite block of soft material can be calculated by Eq. **7.10**, where $F_S$ denotes material strain load on the punch, $F_C$ denotes the crack propagation force, $\delta\ell$ denotes a slice of material thickness, $\delta W_C$ denotes the energy required to form a crack of length 2a, and $\delta S_E$ denotes the strain energy stored in the solid.

$$\left( F_S + F_C \right) \delta\ell = \delta W_C + \delta S_E \qquad \text{Eq. } \mathbf{7.10}$$

This equation ignores frictional effects. Eq. **7.11** shows the equation to determine $\delta W_C$ where $J_{IC}$ denotes the mode I fracture toughness of the material and 2a is the crack length. Eq. **7.121** is reduced to a balance of forces by eliminating $\delta\ell$ from each side and rewriting the equation as shown in Eq. **7.12**.

$$\delta W_C = 2J_{IC} \cdot a \cdot \delta\ell \qquad \text{Eq. } \mathbf{7.11}$$

$$F_C = 2J_{IC}R_p \qquad \text{Eq. } \mathbf{7.12}$$

The value for mode I fracture toughness, $J_{IC}$, is determined first by subtracting the friction and material strain from the measured penetration force. Next, possible values for $J_{IC}$ are input into Eq. **7.11** and graphed along with the measured crack penetration plot. The value for $J_{IC}$ is determined by iteratively reducing the R-squared value to a minimum. Using this method the value for $J_{IC}$ is determined to be 2750 N-m/m$^2$. This value is reasonable compared to human skin with a value of 2500 N-m/m$^2$ and other silicone rubber with values from 3100 – 3800 N-m/m$^2$ (Shergold & Fleck, 2004). Figure **7.4** shows the plots for load versus displacement for the measured values derived from Figure **6.5** and values calculated from Eq. **7.12**. The R-squared value comparing the two plots is 0.9960 and shows a high level of correlation between the measured and calculated values.

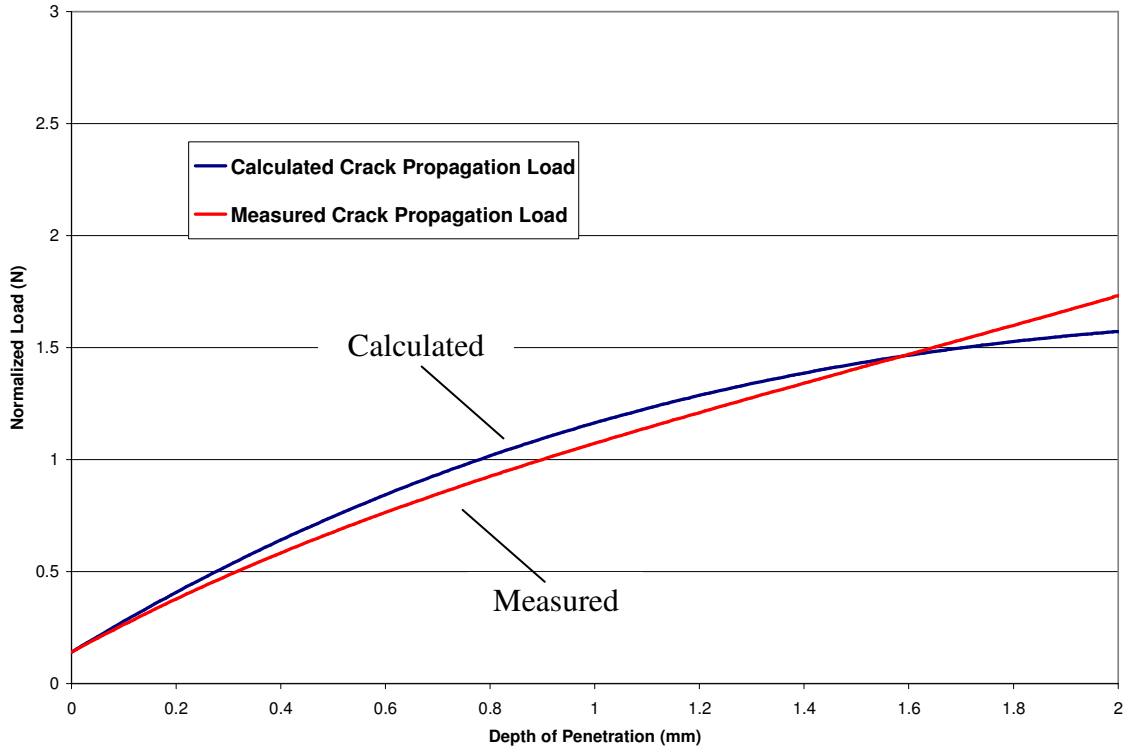


Figure **7.4**: Normalized load versus depth of penetration for calculated and measured crack propagation loads for a single steel needle.

Eq. **7.13** shows the equation for determining the value of $\delta S_E$ where $R_f$ denotes the final radius of the punch, $\mu_S$ denotes shear modulus under infinitesimal strain for the material being penetrated, and h denotes the depth of penetration.

$$\delta S_E = R_f^2 \cdot \mu_S \cdot \delta\ell \cdot h\left(\frac{a}{R_f}\right) \qquad \text{Eq. } \mathbf{7.13}$$

The equation can be reduced to signify a balance of forces by eliminating the $\delta\ell$ term from Eq. **7.13** as shown in expanded form in Eq. **7.14**.

$$F_S = R_f \mu_S D_p R_p \qquad \text{Eq. } \mathbf{7.14}$$

**Stage 2 – Friction Force**

An additional term is needed to account for the frictional effects that are not represented in the model of Shergold and Fleck that will influence needle penetration. Eq. **7.15** relates friction coefficient $\mu_f$ , elastic modulus E, depth of penetration $D_p$, and the average needle diameter $d_{avg}$ (Stellman, 2009, p. 98).

$$F_f = \mu_f E D_p d_{avg} \qquad \text{Eq. } \mathbf{7.15}$$

This equation relates the normal force to the friction force with the modulus, depth of penetration and diameter terms representing the normal force. The needle diameter refers to the average geometric diameter of the portion of the needle that has penetrated into the rubber. For example, this average diameter is calculated for a conical shaped needle by multiplying the needle diameter at the top of the rubber by 2/3. Figure **7.5** shows how the average diameter is determined for use in Eq. **7.15**. Using the average diameter is a way to simplify the calculation of the normal force acting on the needle into the normal force acting on a cylinder.

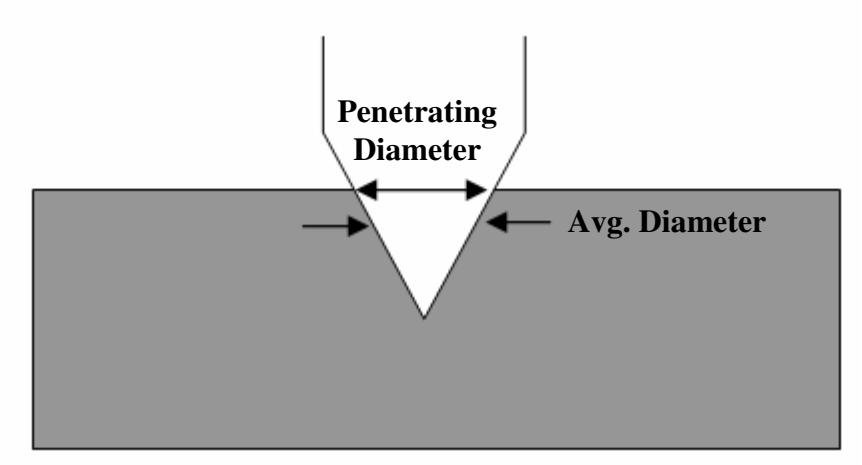


Figure **7.5**: Schematic showing how average diameter is determined.

The coefficient of friction is determined for the steel needle using data from the final stage of penetration as shown in Figure **6.14**. The data from the final stage of penetration are used to determine the coefficient of friction because friction is the only force acting on the shaft of the needle. Figure **7.6** shows a boxplot for the range of loads in the final stage of penetration.

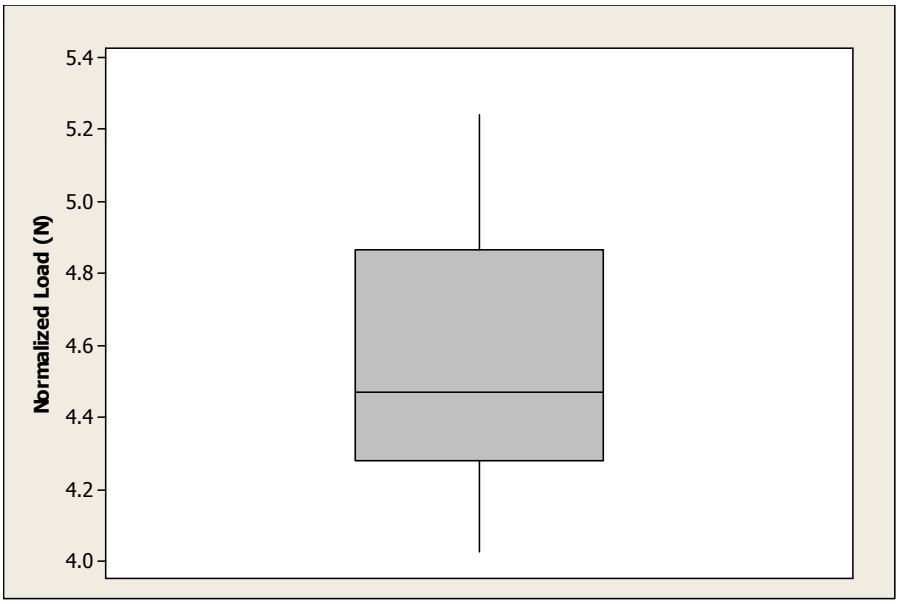


Figure **7.6**: Boxplot of normalized loads in the final stage of penetration for steel needles.

Using the data from Figure **7.6** and Eq. **7.15,** the coefficient of friction between the steel needles and the silicone rubber is calculated to be approximately 0.27 and ranges from roughly 0.24 to 0.31. Further friction testing would be needed to better confirm this calculated friction coefficient. Figure **7.7** shows a boxplot for the coefficient of friction for a steel needle penetrating silicone rubber.

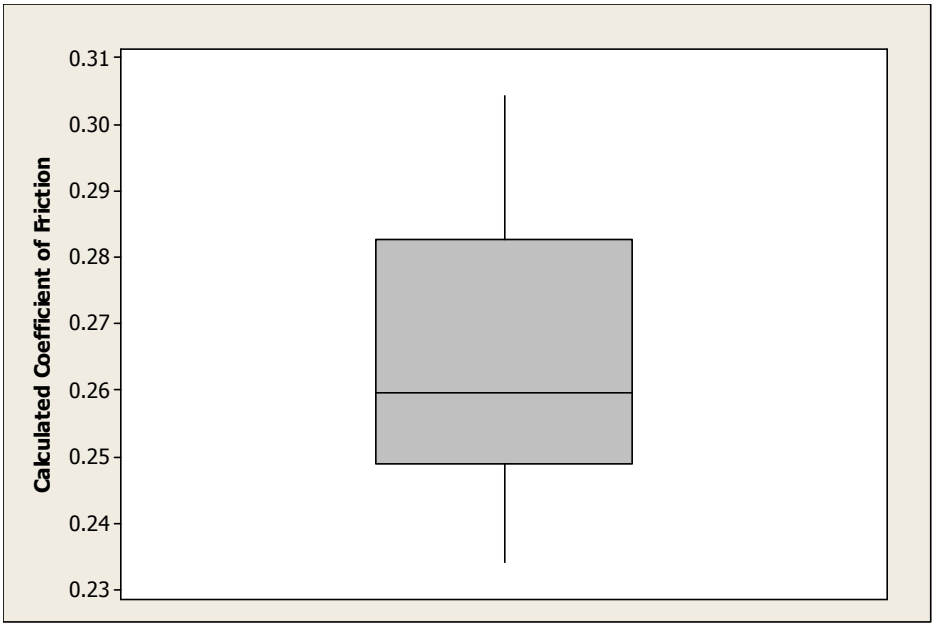


Figure **7.7**: Boxplot of calculated coefficient of friction for steel needle in silicone rubber.

Combining the crack initiation force from Eq. **7.9**, crack propagation force from Eq. **7.14**, and the friction force from Eq. **7.15** yields the total penetration force after crack initiation shown in Eq. **7.16**.

$$F_p = \left(\frac{2}{\pi} E^* \tan(\theta)\right)^{1/3} \left(3G_p A_t\right)^{2/3} + 2J_{IC} \cdot R_p + R_f \cdot \mu_S \cdot D_p \cdot R_p + \mu_f E t_f d_{avg} \qquad \text{Eq. } \mathbf{7.16}$$

The crack initiation force remains constant after initiation occurs, but crack initiation continues throughout penetration as new material is encountered continuously during penetration. The other three terms vary as the needle penetrates farther into the rubber and the crack opens and becomes larger. The crack propagation term dominates just after penetration begins and levels off and becomes constant as the angled portion of the needle transitions to the constant diameter shaft. The force generated from material

strain increases as the penetration depth increases, though it is insignificant compared to the other three terms due to the low value for material shear modulus, $\mu_S$ . The friction force will initially be small as the contact area is very small, and increase as the contact area with the needle increases. The friction force will increase linearly after the transition to the needle shaft. Figure **7.8** shows the calculated normalized loads versus depth of penetration for the steel needle force components of friction, crack propagation, and material strain.

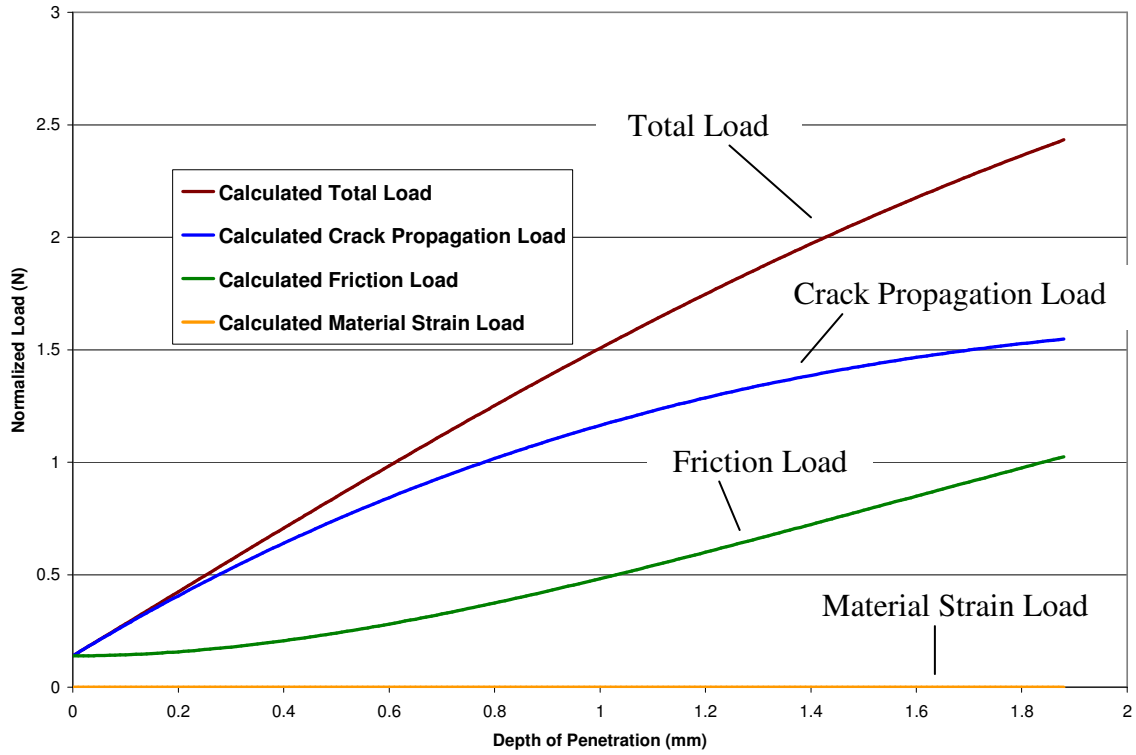


Figure **7.8**: Calculated normalized load versus depth of penetration for steel needle for material strain, crack propagation, friction components and total load.

Figure **7.9** compares the load versus depth of penetration for the calculated total load to the measured load of a single steel needle with data from Figure **6.5**. The figure

shows good agreement between the calculated and measured loads for a single steel needle. A statistical comparison shows that the R-squared value is 0.9948.

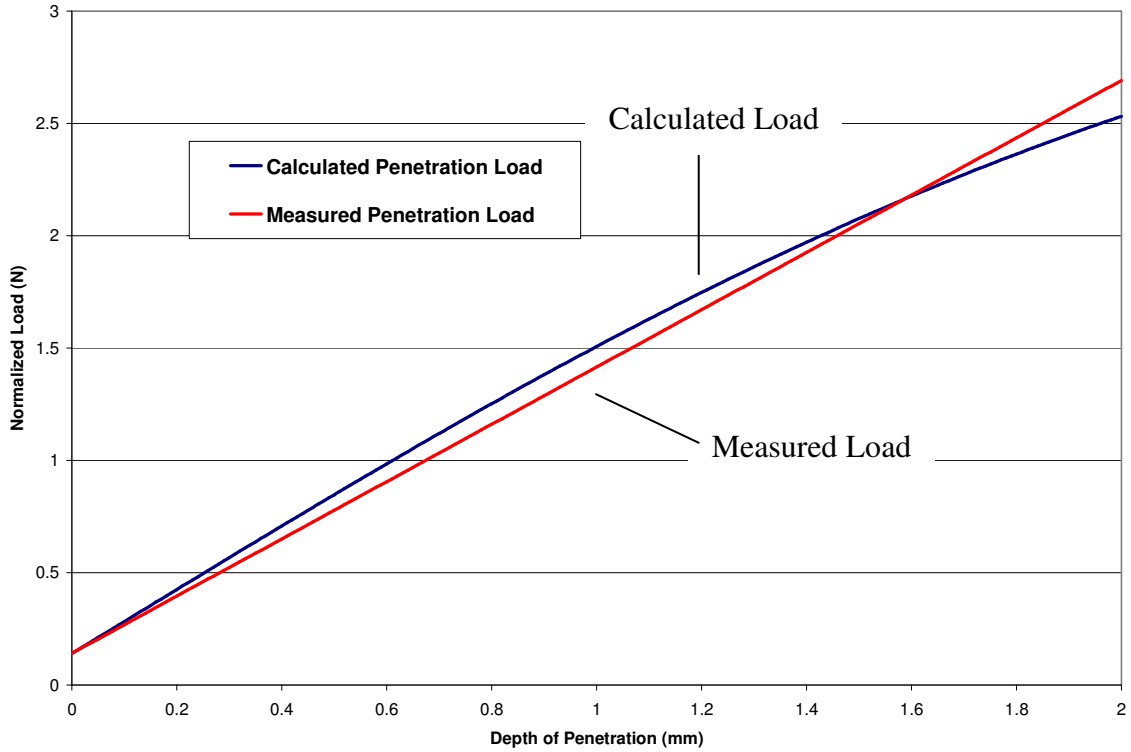


Figure **7.9**: Normalized load versus depth of penetration for single steel needle comparing the calculated and measured penetration load values.

**Stage 2 – Skin Deflection**

Many analytical models ignore or minimize the effect of skin deflection as it relates to needle penetration. While this is acceptable for the study of hypodermic and other larger scale medical needles where only peak force is important, microneedle penetration mechanics must include a material deflection component. Greater material deflection can be detrimental to skin penetration by microneedles due to their being

limited in their penetration depth by their length. This may prevent insertion of the microneedles to a depth that is sufficient for delivering drugs through the skin. Greater discomfort also may be experienced by a patient if the skin must deflect a large amount prior to penetration. Testing of several needle spacing patterns and single needles has revealed that there are two apparent components contributing to skin deflection.

One component of skin deflection comes from the skin deflecting as it does in a single needle test. This deflection occurs because of the compliance of the skin contacted by a single needle. This source of deflection is related to the material properties of the skin.

The other source of skin deflection comes from the interactions between multiple needles as they penetrate the skin. As multiple needles arranged in a pattern penetrate the skin, their spacing distance has an effect on the amount of skin deflection that is experienced. This is analogous to the classic "bed of nails" type of interaction. Needles arranged in high density patterns will interact to create in effect a solid object. This effect is also related to the skin's material properties with stiffer materials more susceptible than less stiff materials.

### *Single Needle Deflection*

The first type of post-penetration skin deflection in a microneedle array comes from the interaction of an individual needle with the skin. The deflection of the skin will increase as the penetrating diameter increases. This effect can be estimated using the equation for elastic response to indentation by a cylindrical indenter as described by

Briscoe, Sebastian, and Adams. Eq. **7.17** shows the equation for elastic response to indentation by a cylindrical indenter where $D_d$ is the amount deflection that occurs after penetration begins (Briscoe et al., 1994, p. 1157).

$$F_P = 2E^* RD_d \qquad \text{Eq. } \mathbf{7.17}$$

Eq. **7.17** relates the penetration force, $F_p$, to penetration radius, R, reduced elastic modulus, $E^*$ as computed in Eq. **7.2**, and post-penetration deflection. Rearranging Eq. **7.17** and solving for deflection yields Eq. **7.18**.

$$D_d = \frac{F_P}{2E^* R_P} \qquad \text{Eq. } \mathbf{7.18}$$

Figure **7.10** shows a representation of deflection that occurs after penetration begins. The area of skin or rubber directly under the needle will be compressed by the needle, much like a cylinder would compress the material directly beneath it when a force is applied.

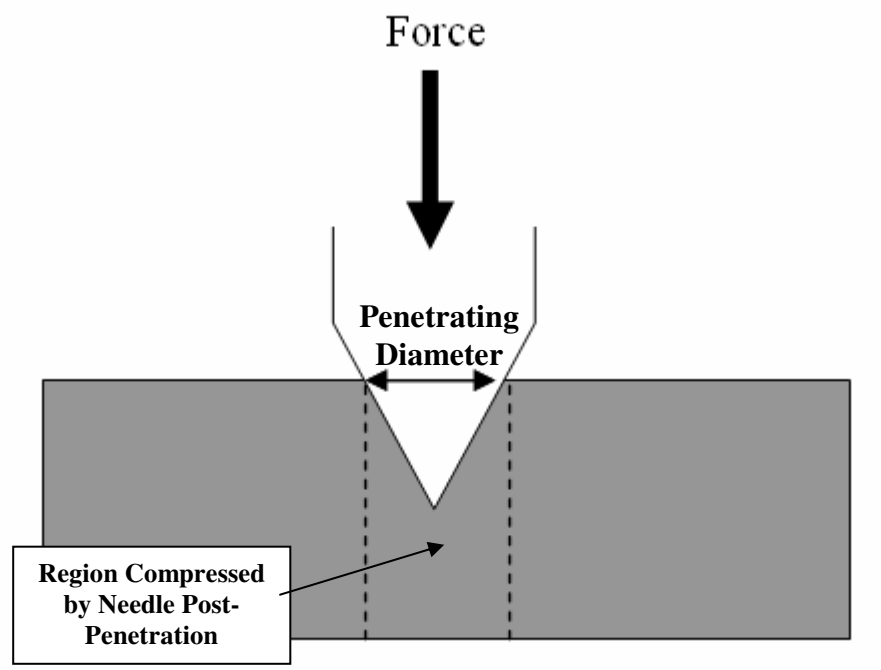


Figure **7.10**: Material under the area described by the penetrating diameter is compressed due to the force applied to the needle.

The material deflection that comes from a single needle commences after penetration begins. This type of deflection is distinct from the initial material deflection that occurs prior to the start of penetration. Both of these force-deflection curves must be plotted on the same graph. Figure **7.11** shows both the pre-penetration force deflection curve and the post-penetration single needle force-deflection curve. The vertical line describes the point where penetration begins to occur. There is a region between the start of penetration and the beginning of post-penetration deflection that is described by the crack-initiation deflection calculated from Eq. **7.3**.

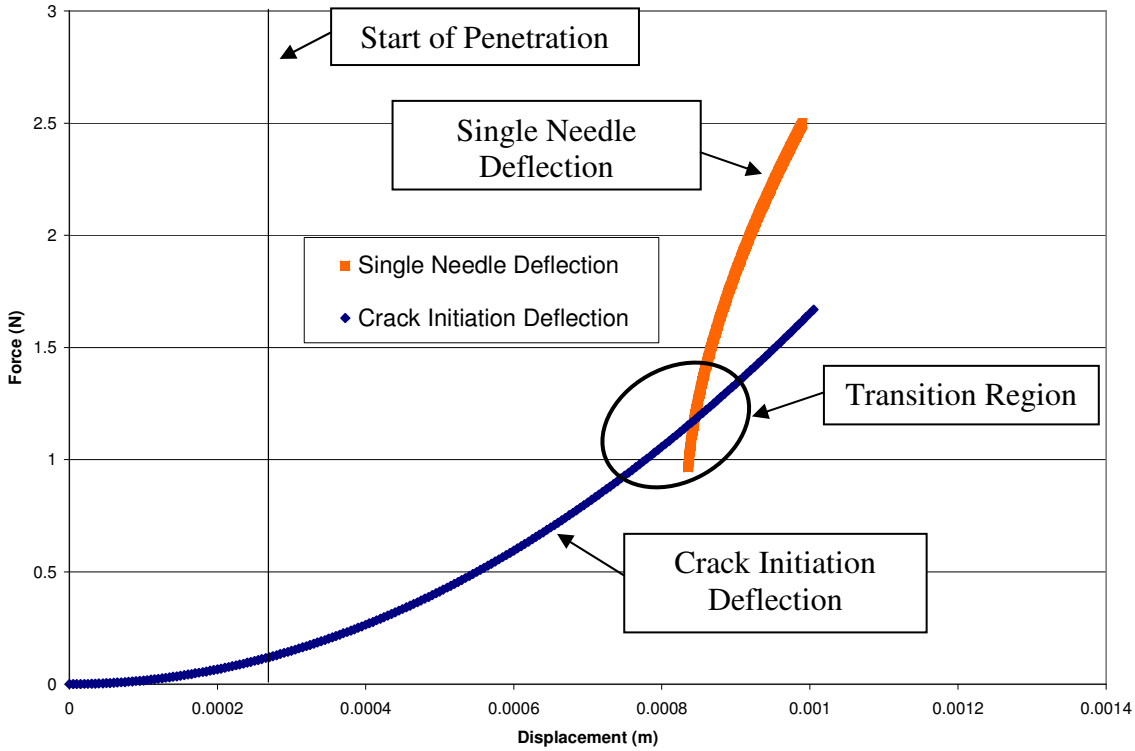


Figure **7.11**: Pre-penetration describing crack initiation force-displacement curve and post-penetration force-displacement curve.

The surface of the skin is stretching to a point of crack initiation just prior to the start of penetration. At the start of penetration, the needle will move through the skin's surface and continue to deflect the skin based on the skin's elasticity and the geometry of the needle tip. This mechanism will continue to dominate the load versus displacement curve until the penetrating radius becomes large enough to mimic a solid cylinder and the single needle deflection curve will begin to dominate. The single needle deflection curve is described by the penetrating force, the penetrating radius, and the skin's elastic modulus. Stage 1 crack initiation deflection and single needle deflection are closely related due to the elastic modulus of the skin and are differentiated by the changing

needle geometry. Transition between the two separate phases is a combination of the two types of deflection that will naturally be smoother in appearance than is shown by the figure. This will be shown to be a reasonable assumption later in the chapter.

Figure **7.12** shows results from combining the pre-penetration and post-penetration material deflection into a single plot.

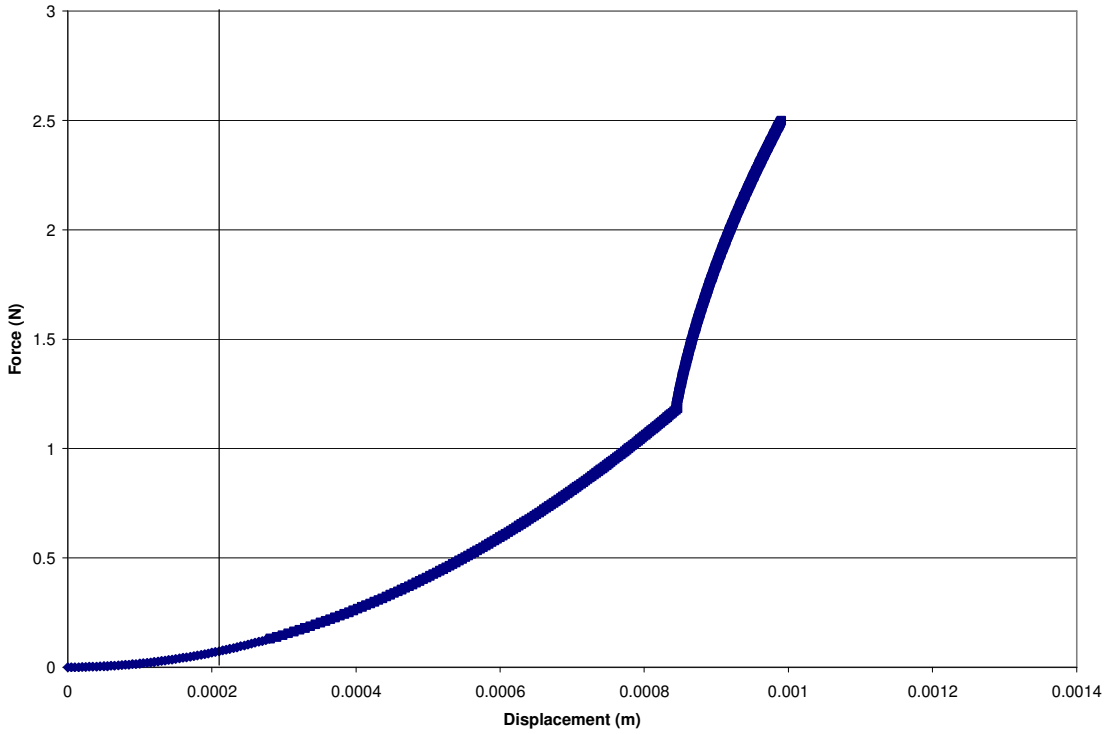


Figure **7.12**: Combined material deflection from pre-penetration and post-penetration single needle effects.

Figure **7.13** shows a comparison between the measured single needle deflection from Figure **6.24** and the calculated deflection using Eq. **7.19**. The measured value is adjusted for initial penetration force. The two plots are similar in shape, though the measured deflection is smoother than the calculated plot. A statistical comparison shows that the calculated values have an R-squared value of 0.927 compared to the measured

values. The results show that the calculations give a reasonable estimate for predicting the single needle deflection.

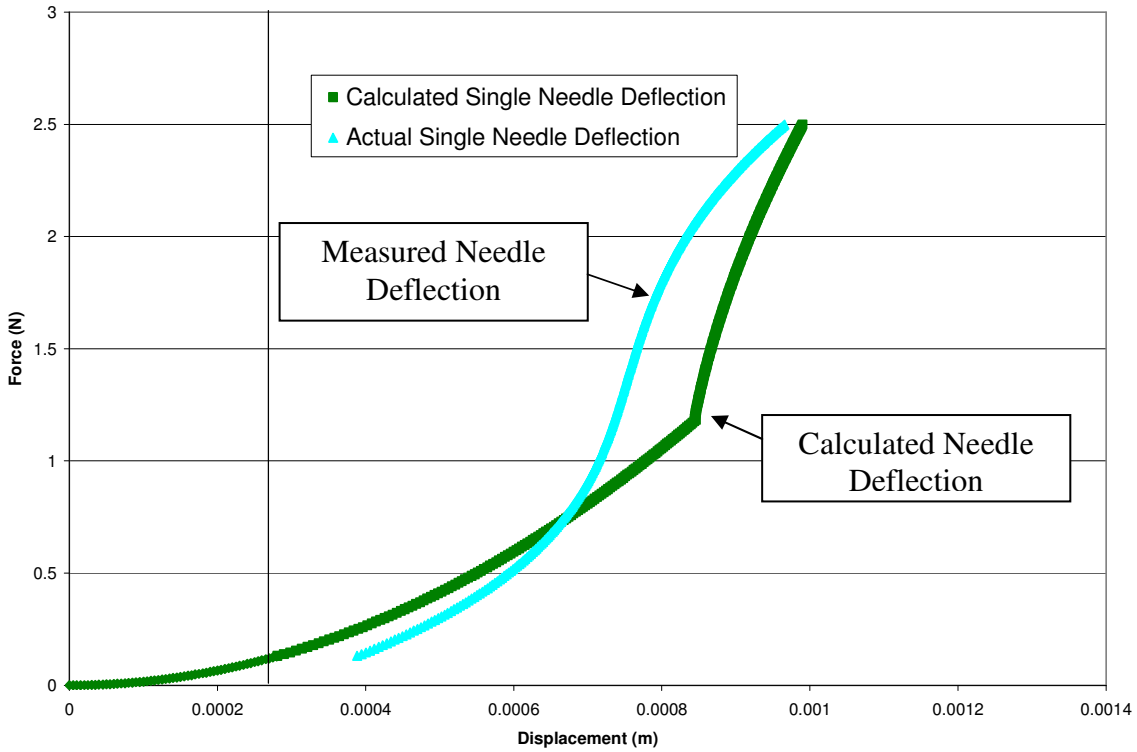


Figure **7.13**: Normalized load versus displacement of single steel needle deflection. Shown are both the calculated and measured values derived from testing a solid single steel needle.

### *Multiple Needle Deflection*

Deflection that results from the interaction of multiple needles arranged in a specific pattern is more difficult to describe using purely analytical methods. The interaction between an arrangement of needles and skin can be likened to the classic "bed of nails" experiment. In such an experiment, a participant is asked to lie on a surface

consisting of only nail points. While a single nail would penetrate the participant's skin, a closely arranged pattern does not. This is because the load on each individual nail in a "bed of nails" is not sufficient to cause penetration. This type of experiment helps explain the concepts of pressure and force to students. Various research groups have observed in their published literature the same phenomenon and have noted that high density needle patterns cause excessive skin deflection that inhibits skin penetration (Moh *et al*., 2009; Yan *et al.,* 2010). This section looks to quantify the skin deflection that occurs after penetration begins and depends on the spacing of needles in a pattern.

The method used to quantify this type of skin deflection will be largely based upon empirical data. Empirical data are used because of the difficulty that mechanical models have in properly representing the actual material behavior of a viscoelastic material such as rubber or skin. Figure **6.28** through Figure **6.34** contain charts for load versus deflection for each of the six hexagonal shaped indenters. These data are used to predict behavior for skin deflection that occurs during penetration due to the effect of multiple needles.

The data can be represented by a stress-strain curve for compression. Figure **7.14** shows the average stress-strain curve for the solid hexagonal indenters. The data shown in Figure **7.14** are normalized data from the indenter data shown in Figure **6.34**. The elastic modulus for compression can be derived from the linear regression performed on the data in Figure **7.14** . The average stress-strain curve correlates well with the regression line with an R-squared value of 0.9726. The area-normalized data appear disjointed due to the force and displacement data ending at different points for each indenter after being normalized. For example, the data for the area-normalized 2.5 mm

pitch indenter ends at 36 N, while the data for the 0.75 mm pitch indenter extends to nearly 160 N.

The empirically derived elastic modulus is shown in Eq. **7.19** and is represented by Hooke's Law where $\sigma$ represents compressive stress, E represents the elastic modulus for compression, and $\varepsilon$ represents strain. The empirically derived elastic compression modulus of 8.54MPa compares well to the elastic tensile modulus of 5.07 MPa.

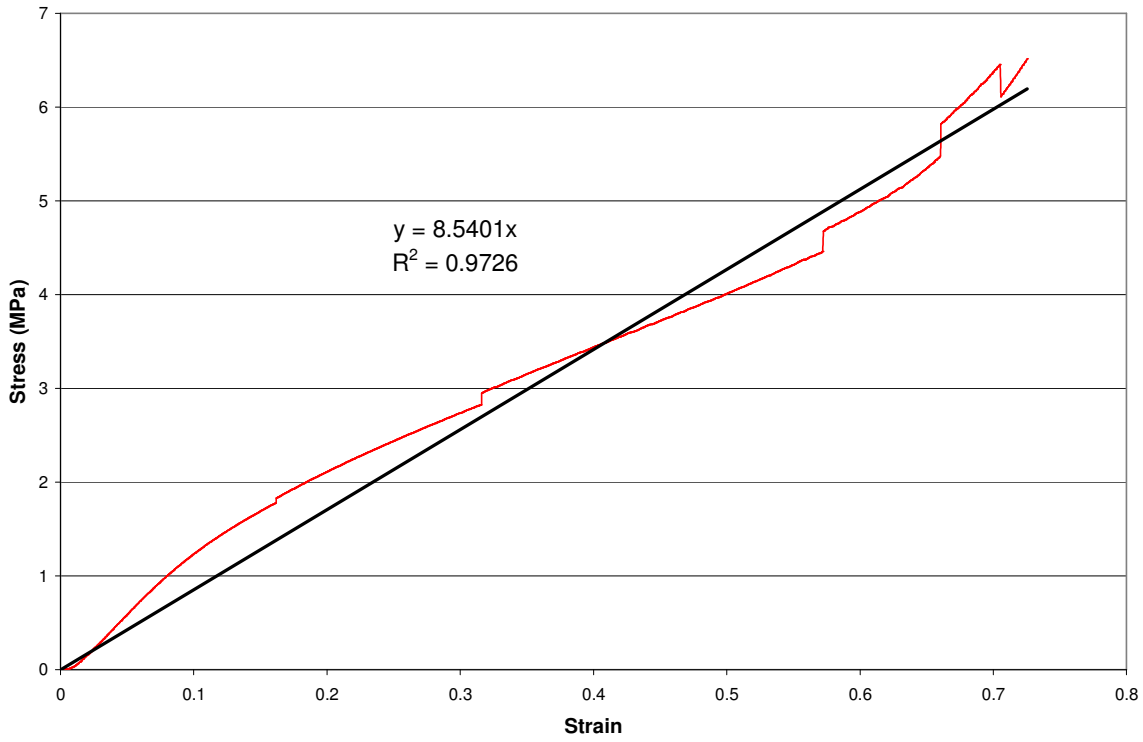


Figure **7.14**: Average stress-strain and linear regression for solid hexagonal indenters.

$$\sigma = E_C * \varepsilon$$
$$\sigma = 8.5401 MPa * \varepsilon \qquad \text{Eq. } \mathbf{7.19}$$

The compression distance can be found by expanding Hooke's Law as shown in Eq. **7.20** where F represents force, A represents indenter surface area, $E_C$ represents the elastic compression modulus, $\Delta L$ represents the change in length equivalent to material compression, and $L_0$ represents the uncompressed material thickness.

$$\frac{F}{A} = E\left(\frac{\Delta L}{L_0}\right)$$
$$\Delta L = \frac{F}{AE_C} L_0 \qquad \text{Eq. } \mathbf{7.20}$$

Eq. **7.20** is transformed in Eq. **7.21** for each needle pattern first by converting the forces from single needle values to the total number of needles in the pattern by multiplying by n. $D_I$ represents the deflection of the skin by the indenter. The force that is input into the equation is defined as the total penetration force defined in Eq. **7.16**, $F_P$, minus the effects of the crack initiation force, $F_i$. Crack initiation force must be subtracted because the effect to deflection from multiple needle patterns is not present until penetration begins.

$$D_I = \Delta L = \frac{\left(F_p - F_i\right) * n}{A_{indenter} E_C} L_0 \qquad \text{Eq. } \mathbf{7.21}$$

The concept for the deflection from multiple needles also builds on the concept of penetrating needle diameter explained in Figure **7.5**. As the needles enter the skin or rubber material being penetrated, they will cover a certain area of the surface. The ratio of the area covered by the needles to the area covered by the outline of the needle pattern will be called the Needle Area Ratio, or $N_R$. Figure **7.15** shows an example of this concept.

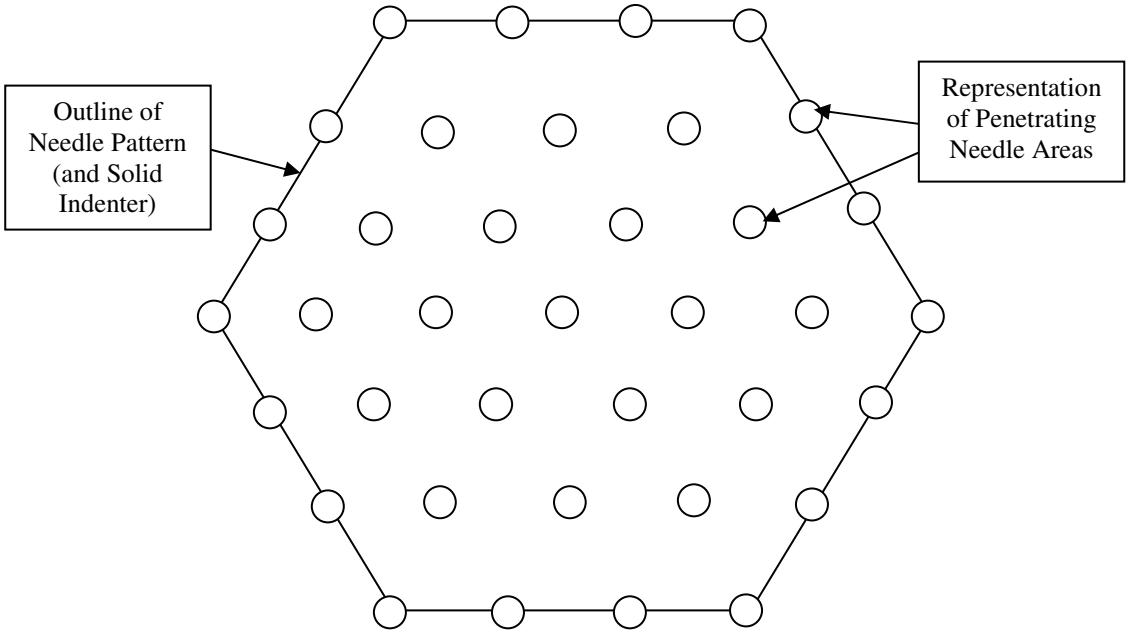


Figure **7.15**: Representation of concept of ratio penetrating needle area to the overall needle pattern outline.

Eq. **7.22** shows the equation for determining the needle area ratio, or $N_R$. The radius, $R_P$, is the radius entering the material and increases as the penetration diameter increases. $A_{total\text{-}outline}$ is the area defined by the outline of the needle pattern and also to the corresponding solid indenter; the variable n represents the number of needles represented the pattern. The ratio $N_R$ increases as $R_P$ increases and is variable throughout the penetration process. This ratio depends largely on the spacing of the needles because the ratio of area of penetrated needles to total pattern changes drastically between the various patterns.

$$N_R = \frac{n * \pi R_P^2}{A_{total-outline}} \qquad \text{Eq. } \mathbf{7.22}$$

The material deflection from the interaction of multiple needles in a pattern is estimated by multiplying the deflection of an equivalent solid indenter, $D_I$, with the needle area ratio, $N_R$. Combining Eq. **7.21** and Eq. **7.22** into Eq. **7.23** yields the deflection that comes from multiple needles arranged in an evenly spaced pattern, $D_M$ (multiple needle deflection).

$$D_M = D_I * N_R \qquad \text{Eq. } \mathbf{7.23}$$

Figure **7.16** shows a plot of force versus displacement for $D_M$ calculated using Eq. **7.23** for each of the seven needle patterns in the microneedle spacing device including six hexagonal patterns and one square pattern. The pattern with the closest spacing of 0.75 mm between each needle has much more added deflection than all others. The pattern with the largest distance between needles of 2.50 mm has almost no added deflection due to the pattern effects.

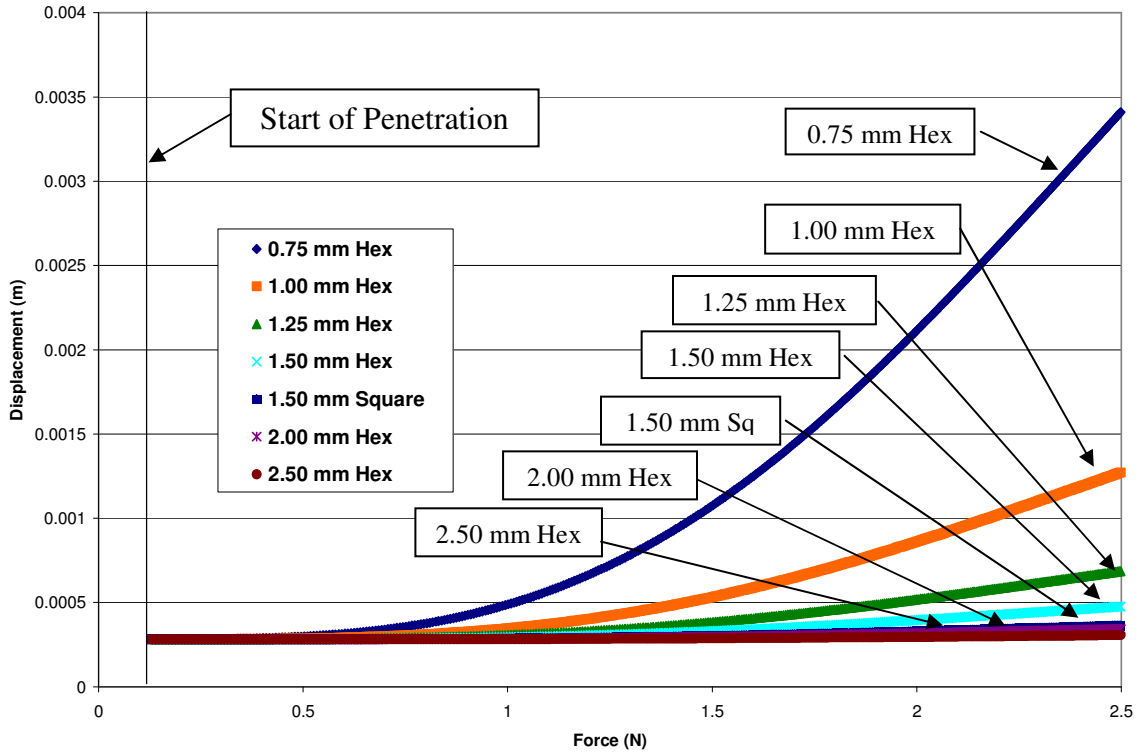


Figure **7.16**: Plot force versus displacement for $D_M$ for all six steel hexagonal microneedle spacing device patterns and one square pattern.

### *Summary of Penetration Analysis*

The preceding equations in this chapter give an analytical method for calculating each component of penetration force and displacement. Figure **7.17** gives a summary of the equation for each component of penetration force and displacement into skin.

$$\textit{Crack Initiation}: \quad P = \frac{2}{\pi} E^* \tan(\theta) h^2$$

$$\textit{Total Penetration}: \quad F_P = 2J_{IC} R_p + R_f \mu_S D_p R_p + \mu_f E D_p d_{avg}$$

$$\textit{Single Needle Deflection}: \quad D_d = \frac{F_P}{2E^* R_P}$$

$$\textit{Multiple Needle Deflection}: \quad D_M = \frac{\left(F_p - F_i\right) * n^2 \pi R_P^2}{A_{total-outline}^2 E_C} L_0$$

Figure **7.17**: Summary of equations used to create analytical model relating needle displacement and applied force.

Figure **7.18** summarizes the limits for each stage of penetration. Stage 1 begins at zero force and displacement and continues until crack initiation begins at $F_i$ and $h_i$. Stage 2 begins at crack initiation where Stage 1 leaves off at $F_i$ and $h_i$, and continues indefinitely. Stage 3 would normally begin when the angled portion of the needle tip transitions to the largest part of the needle shaft. For the study of microneedles with only a single angled section, stage 3 will never be analyzed.

Figure **7.18** also gives force as a function of the related displacement for each stage of needle penetration. During stage 2, total displacement is the sum of the penetration displacement, single needle deflection, and multiple needle deflection. Total force is the sum of penetration force and crack initiation force. Force is plotted for each value of total displacement to generate the plots shown in the chapter.

$$\underline{Stage\ 1: Crack\ Initiation}$$

$$Valid\ \ for: (0, F_i], (0, h_i]$$

$$P = f(h)$$

$$\underline{Stage\ 2: During\ Skin\ Penetration}$$

$$Valid\ \ for: [F_i, \infty), [h_i, \infty)$$

$$D_{total} = D_P + D_d + D_M + h_i$$

$$F = F_p + F_i$$

$$F = f(D_{total})$$

Figure **7.18**: Summary of limits for each stage of needle penetration.

Figure **7.19** better illustrates the interactions of each force and displacement component by separating them and also showing the resultant total displacement. The figure shows the calculated displacements for the hexagonal steel needle pattern with 0.75 mm spacing. It should be noted that the component displacements must be added for each force value across the y-axis to generate the total displacement.

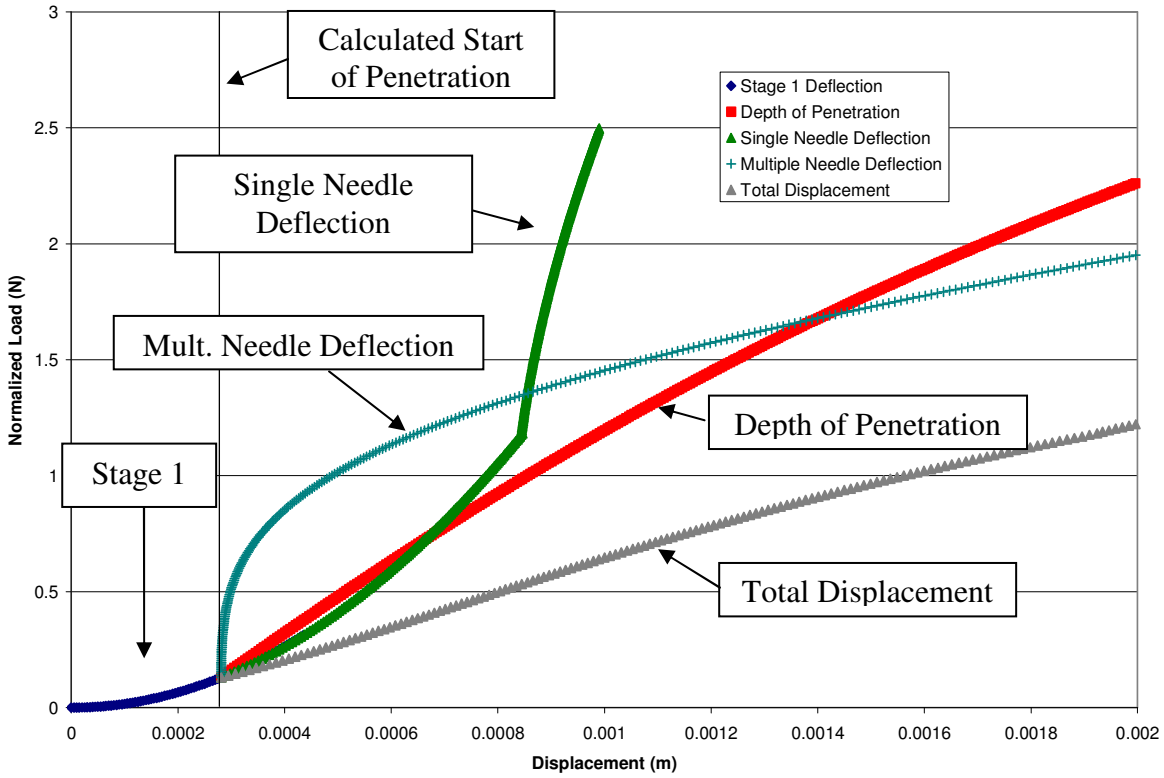


Figure **7.19** Normalized force versus displacement for each displacement component and the total displacement for the 0.75 mm hexagonal steel needle pattern.

To better explain the interactions shown in Figure **7.19**, the component displacements can be plotted as a function of the applied force as shown in Figure **7.20**. Each displacement component is added for each force value across the x-axis in this example to yield the total displacement. The figure shows that during stage 1 penetration displacement increases at a nearly constant rate, single needle deflection increases asymptotically to approximately 1 mm where the cross-section of the needle reaches a nearly constant diameter. Multiple needle displacement starts slowly as penetration is beginning and increases rapidly. The rapid rise in the multiple needle displacement is due to the close 0.75 mm spacing of the needles in the pattern arrangement. A closely

spaced pattern will cause the individual needles to act more like a single solid body as they penetrate deeper in the rubber sample.

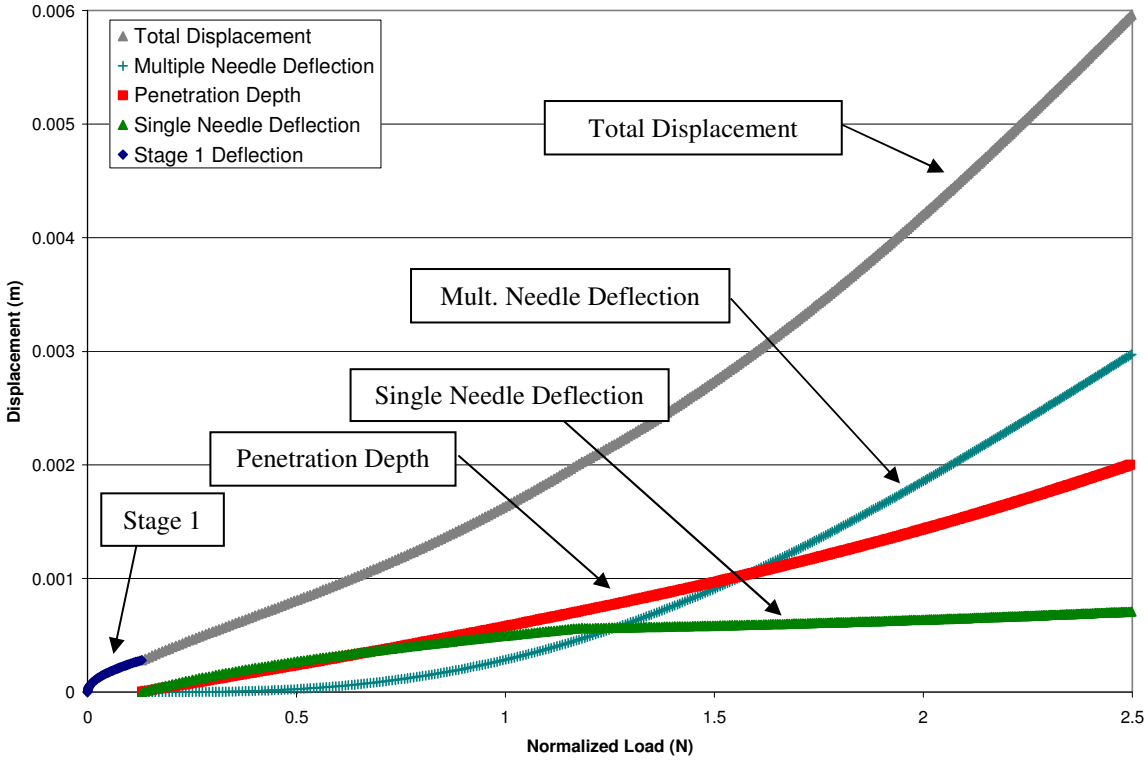


Figure **7.20**: Calculated displacement versus normalized force for each displacement component and the total displacement for the 0.75 mm hexagonal steel needle pattern.

## Comparison of Analytical Model to Measured Data for Steel Needles

This section compares the analytical model established in this chapter and the measured data presented in Chapter 6. Previous parts of this chapter have established that the constituent components of the analytical model show reasonable agreement with the comparable measured amounts.

Figure **7.21** shows the plots for load versus displacement for measured data from Figure **6.5** and data that are derived from the equations summarized in Figures **7.17** and **7.18**. The plot is for a single steel needle tested as described in Chapter 5. A statistical comparison between the measured and calculated loads shows an R-squared value of 0.8613. This shows that there is reasonable agreement between the analytical and empirical data. The additive errors from each analytical component cause a difference between the measured and calculated values. Other errors are caused by the sensitivity of the measuring devices used to generate the empirical data that are shown.

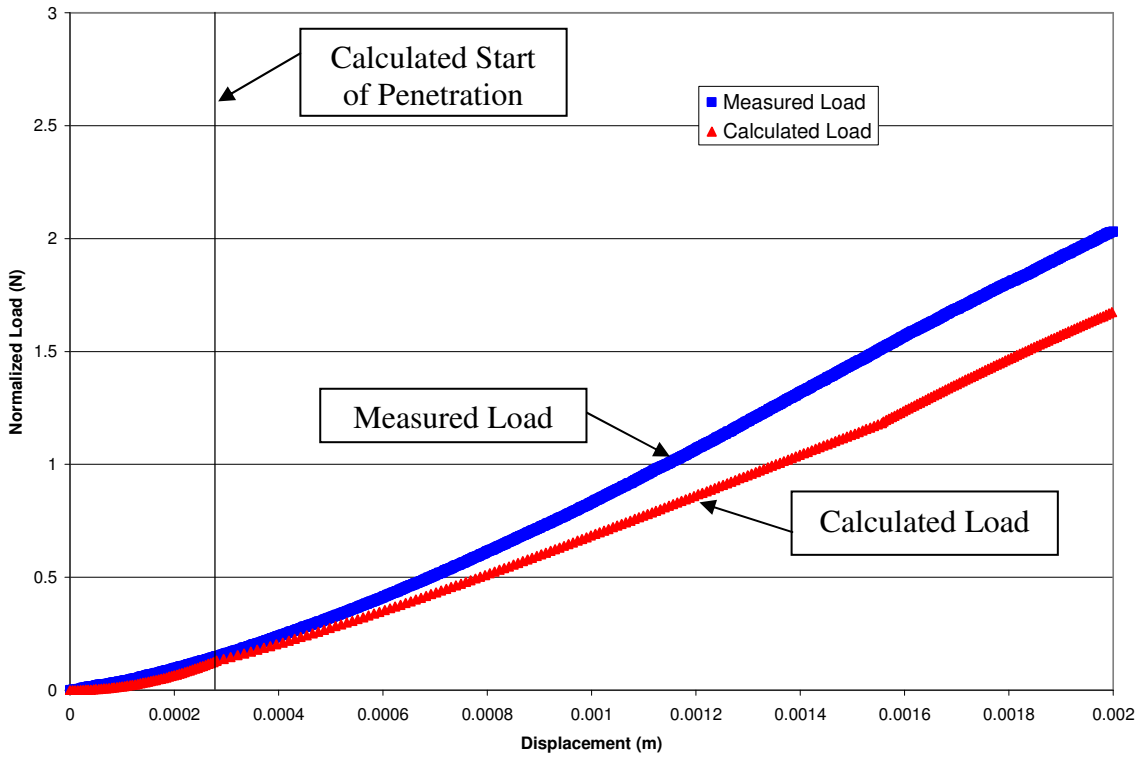


Figure **7.21**: Normalized load versus displacement showing measured and calculated loads for a single steel needle.

Figure **7.22** shows displacement versus normalized load for a single steel needle as it penetrates. The penetration depth shows the depth that needle has penetrated into the surface of the skin and increases at a nearly linear rate. The single needle deflection is the amount of skin deflection that occurs under the influence of a single needle. The single needle deflection component increases quickly until the needle reaches its full diameter and the deflection becomes constant. Multiple needle deflection does not have any influence in this case because a single needle has a theoretically infinite spacing between needles. Penetration depth is the dominant component of total displacement for the single needle case.

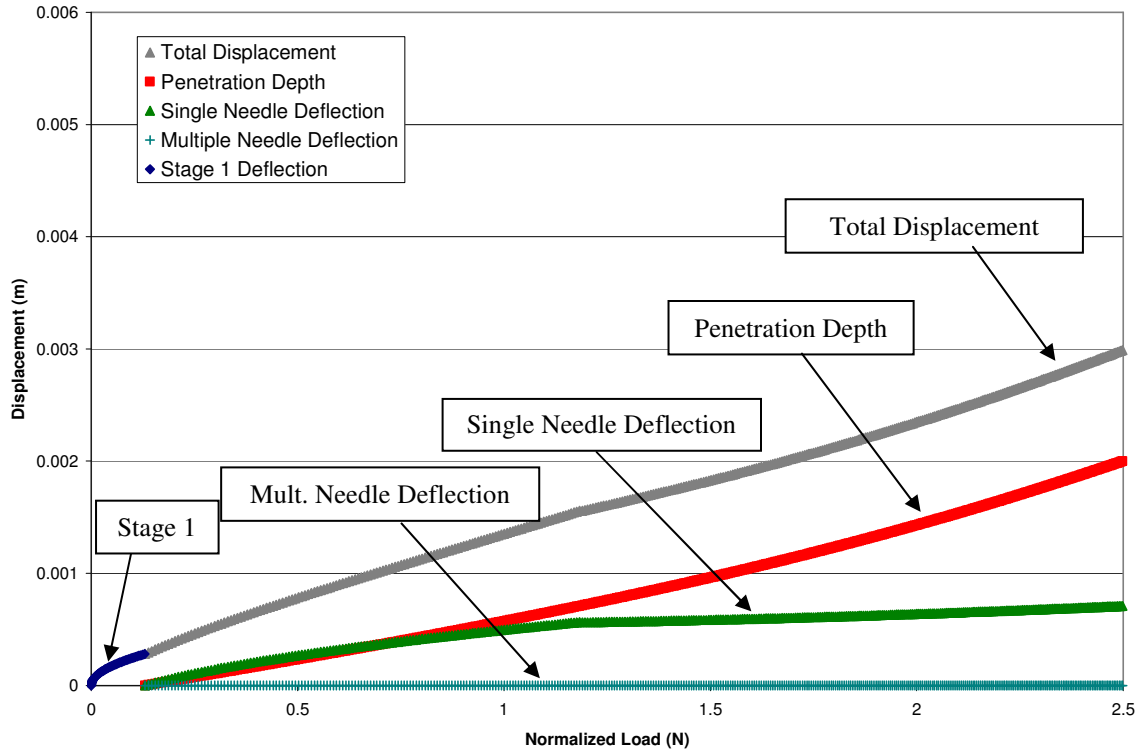


Figure **7.22**: Calculated displacement versus normalized force for each displacement component and the total displacement for a single steel needle.

Figure **7.23** shows plots for normalized load versus displacement for measured data from Figure **6.18** and analytical data for the 37-needle hexagonal spacing pattern with 2.50 mm spacing between needles. The general trend of the analytical data agrees with the measured data. A statistical comparison shows that the R-squared value of 0.9030.

The largest source of error between the calculated and actual displacements comes from the actual start of penetration being spread out over an approximate 600 micron length and forces the measured load plot to have lower load values than the calculated load. The physical source of error is caused by the effect of 37 needles each having slightly varying lengths, slightly varying tip radii, and the effect of the entire testing apparatus approaching the sample at a non-orthogonal trajectory as shown in Figure **7.24**. Due to these effects, each needle will begin penetrating the skin's surface at a different time and result in the applied force being averaged over a range of displacements as shown in each of the multiple needle figures. This is because the force is measured for all needles at once rather than measuring the force on each needle individually.

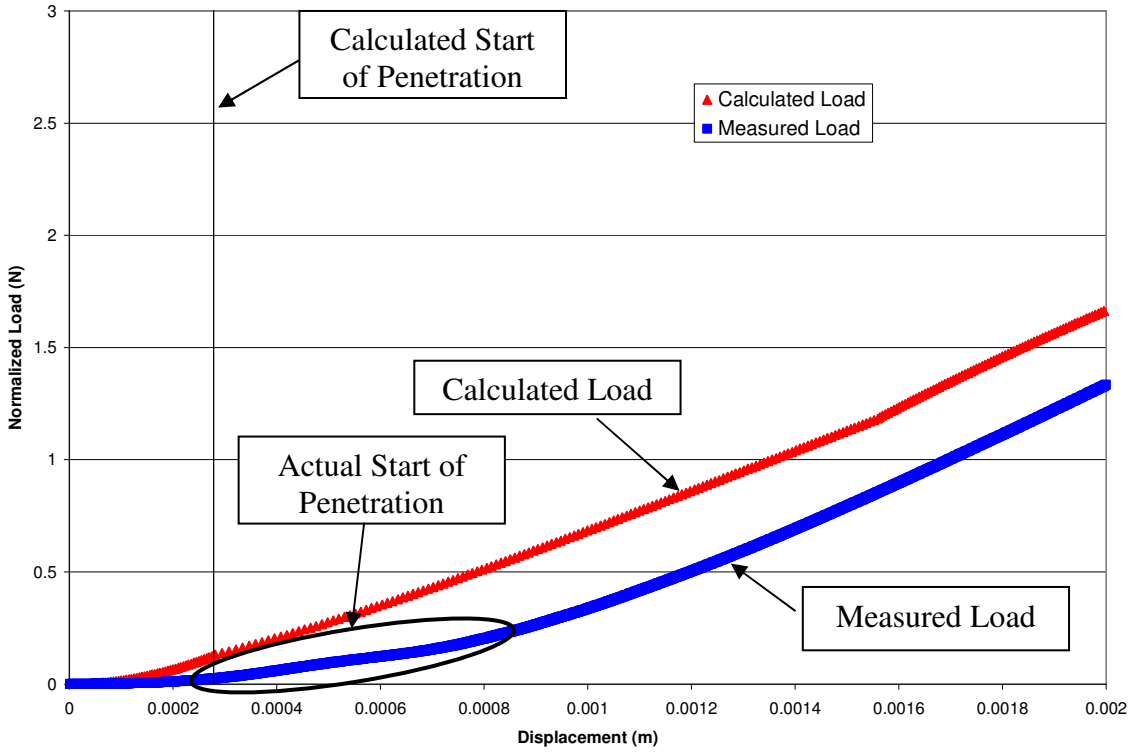


Figure **7.23**: Normalized load versus displacement showing measured and calculated loads for a multiple steel needle hexagonal pattern with 2.50 mm spacing.

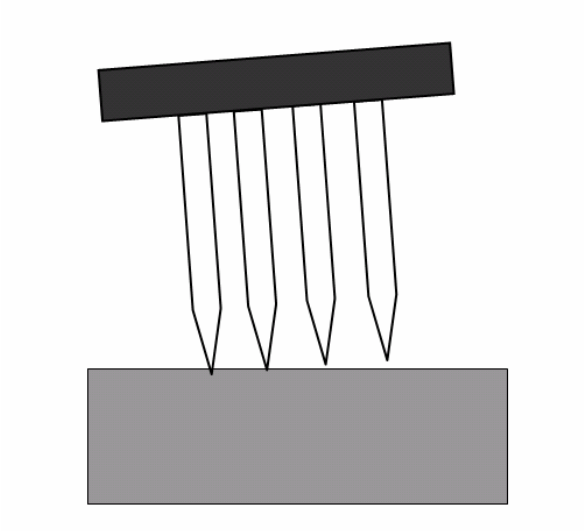

Figure **7.24**: Exaggerated example of multiple needle pattern entering rubber sample at an angle and causing the actual start of penetration to differ for each needle

Error that is displayed in Figure **7.23** and is most evident in the area labeled "Actual Start of Penetration" can be replicated using a method to statistically average the force versus displacement data for individual needles within a patterned array. This is accomplished by creating statistically normal data with various standard deviations that represent the variation in needle lengths or angle of approach to the rubber sample. Each random data point generated represents the staggered start of total displacement of a needle within the pattern. The random normal data are created using Minitab® statistical software. Figure **7.25** shows the random normal data created for 37 data points with a standard deviation of 100 microns. Each data point represents the staggered start of needle displacement for each needle in the pattern.

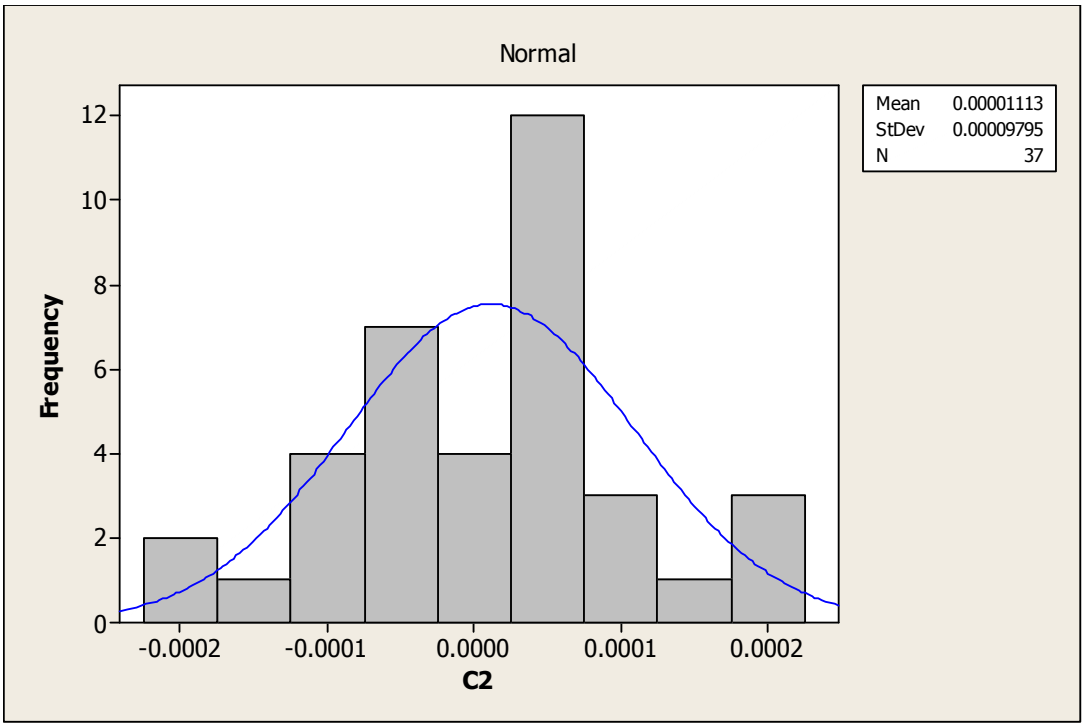


Figure **7.25**: Random normal data representing start of needle displacement for 37 needles in an array with standard deviation of 100 microns.

The calculated load curve, such as the one shown in Figure **7.23**, is determined for each needle at the staggered start of displacement values as determined by the random data points. This provides a load versus displacement curve that accounts for error in the length of the needles within a pattern. Table **7.1** shows an example of data for seven needles in a pattern that represent a staggered start of needle contact with a rubber or skin section. The final two columns contain the displacement and force that represents the output used to plot the adjusted calculated load curve. The force column is the average force across each row that represents displacement. The displacement column is constant. This represents each needle contacting the rubber surface at different displacement values, but measured with a single load that records loads from each needle

simultaneously. The validity of this concept will be further explored in the Error Analysis section of this chapter.

Table **7.1**: Example showing load for seven needles contacting the rubber surface at varying displacement values and the resulting average force and displacement.

| | Force (N) | | | | | | | | |
|---|---|---|---|---|---|---|---|---|---|
| Offset Start Distance (m) | 0 | 0.000008 | 0.000027 | 0.00005 | 0.000058 | 0.000065 | 0.000104 | | |
| | | | | | | | | Displacement (m) | Force (N) |
| | 0 | | | | | | | 0 | 0 |
| 4.13E-05 | 0 | | | | | | | 0.000005 | 2.06497E-05 |
| 0.000165 | 4.13E-05 | | | | | | | 0.00001 | 0.000103249 |
| 0.000372 | 0.000165 | | | | | | | 0.000015 | 0.000268446 |
| 0.000661 | 0.000372 | | | | | | | 0.00002 | 0.000516243 |
| 0.001032 | 0.000661 | 0 | | | | | | 0.000025 | 0.000564426 |
| 0.001487 | 0.001032 | 4.13E-05 | | | | | | 0.00003 | 0.000853522 |
| 0.002024 | 0.001487 | 0.000165 | | | | | | 0.000035 | 0.001225217 |
| 0.002643 | 0.002024 | 0.000372 | | | | | | 0.00004 | 0.001679511 |
| 0.003345 | 0.002643 | 0.000661 | | | | | | 0.000045 | 0.002216404 |
| 0.00413 | 0.003345 | 0.001032 | 0 | | | | | 0.00005 | 0.002126922 |
| 0.004997 | 0.00413 | 0.001487 | 4.13E-05 | | | | | 0.000055 | 0.002663814 |
| 0.005947 | 0.004997 | 0.002024 | 0.000165 | 0 | | | | 0.00006 | 0.002626645 |
| 0.00698 | 0.005947 | 0.002643 | 0.000372 | 4.13E-05 | 0 | | | 0.000065 | 0.002663814 |
| 0.008095 | 0.00698 | 0.003345 | 0.000661 | 0.000165 | 4.13E-05 | | | 0.00007 | 0.003214474 |
| 0.009292 | 0.008095 | 0.00413 | 0.001032 | 0.000372 | 0.000165 | | | 0.000075 | 0.003847732 |
| 0.010573 | 0.009292 | 0.004997 | 0.001487 | 0.000661 | 0.000372 | | | 0.00008 | 0.004563589 |
| 0.011936 | 0.010573 | 0.005947 | 0.002024 | 0.001032 | 0.000661 | | | 0.000085 | 0.005362045 |
| 0.013381 | 0.011936 | 0.00698 | 0.002643 | 0.001487 | 0.001032 | | | 0.00009 | 0.0062431 |
| 0.014909 | 0.013381 | 0.008095 | 0.003345 | 0.002024 | 0.001487 | | | 0.000095 | 0.007206754 |
| 0.01652 | 0.014909 | 0.009292 | 0.00413 | 0.002643 | 0.002024 | | | 0.0001 | 0.008253006 |
| 0.018213 | 0.01652 | 0.010573 | 0.004997 | 0.003345 | 0.002643 | 0 | | 0.000105 | 0.008041593 |
| 0.019989 | 0.018213 | 0.011936 | 0.005947 | 0.00413 | 0.003345 | 4.13E-05 | | 0.00011 | 0.009085879 |
| 0.021847 | 0.019989 | 0.013381 | 0.00698 | 0.004997 | 0.00413 | 0.000165 | | 0.000115 | 0.010212764 |
| 0.023788 | 0.021847 | 0.014909 | 0.008095 | 0.005947 | 0.004997 | 0.000372 | | 0.00012 | 0.011422247 |
| 0.025812 | 0.023788 | 0.01652 | 0.009292 | 0.00698 | 0.005947 | 0.000661 | | 0.000125 | 0.011125039 |
| 0.027918 | 0.025812 | 0.018213 | 0.010573 | 0.008095 | 0.00698 | 0.001032 | | 0.00013 | 0.010962709 |
| 0.030107 | 0.027918 | 0.019989 | 0.011936 | 0.009292 | 0.008095 | 0.001487 | | 0.000135 | 0.012114505 |
| 0.032379 | 0.030107 | 0.021847 | 0.013381 | 0.010573 | 0.009292 | 0.002024 | | 0.00014 | 0.0133489 |

Figure **7.26** shows data for each of 37 individual steel needles in a 2.50 mm hexagonal pattern plotted according to staggered start of displacement as shown in Table **7.1**. The standard deviation of needle length for the figure is 175 microns. The average of the individual needle forces results in the plot that is compared to the measured data. Such a comparison is valid because of how the needle force is measured.

During testing, the load cell measures the load on the entire pattern of needles simultaneously. However, variations in needle length will cause individual needles to

exert force on the load cell at varying displacements. The individual needle plots shown in Figure **7.26** are analogous to having a force gauge on each individual needle and plotting the force as a function of displacement. The average force of all of the individual needle forces is equal to the output of the entire needle pattern.

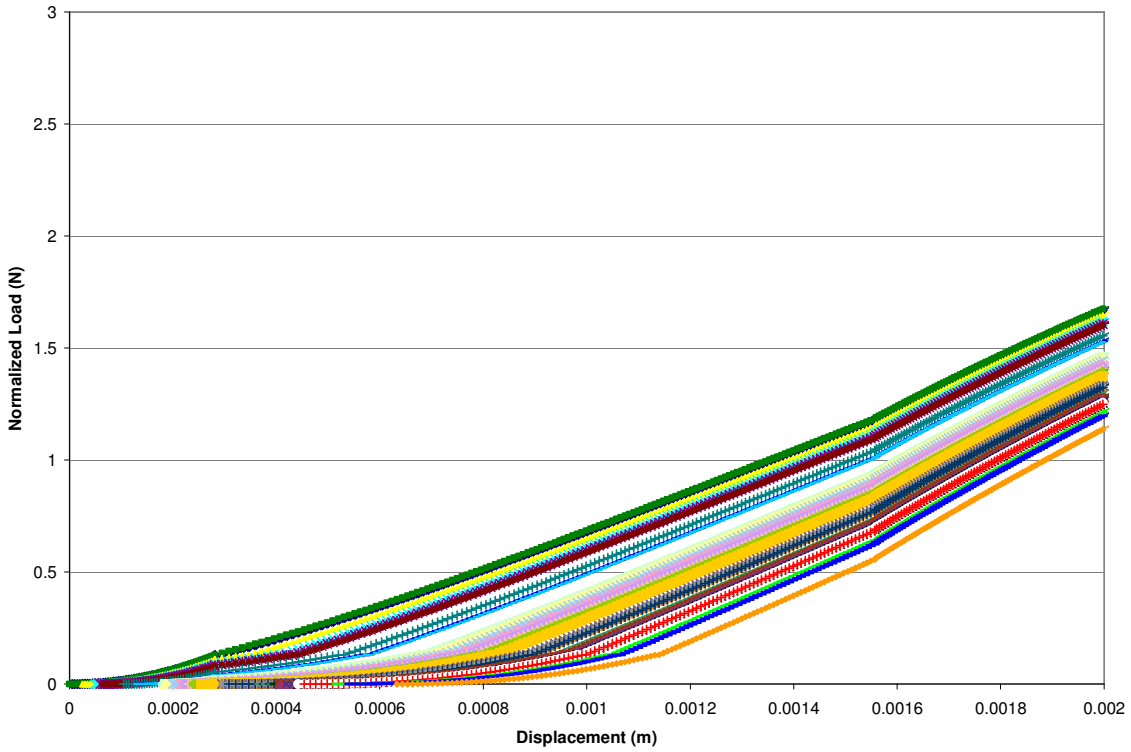


Figure **7.26**: Normalized load versus displacement for individual needles for varying needle lengths.

The concept of random needle variation can be applied to each patterned array of needles. Figure **7.27** shows plots for normalized load versus displacement for measured data and uncorrected calculated data from Figure **7.23** for the 37-needle hexagonal spacing pattern with 2.50 mm spacing between needles. Figure **7.27** also shows a series of plots of normalized load versus displacement using varying needle lengths to account

for the difference between the calculated and measured data. The random length variation plots show that progressively larger standard deviations in needle length tends to shift the calculated load plot to display lower average loads for given displacement values. The calculated load plot is a normalized load versus displacement plot with zero needle length deviation. Figure **7.27** shows that a needle length standard deviation of 100 to 200 microns closely matches the measured load plot shown.

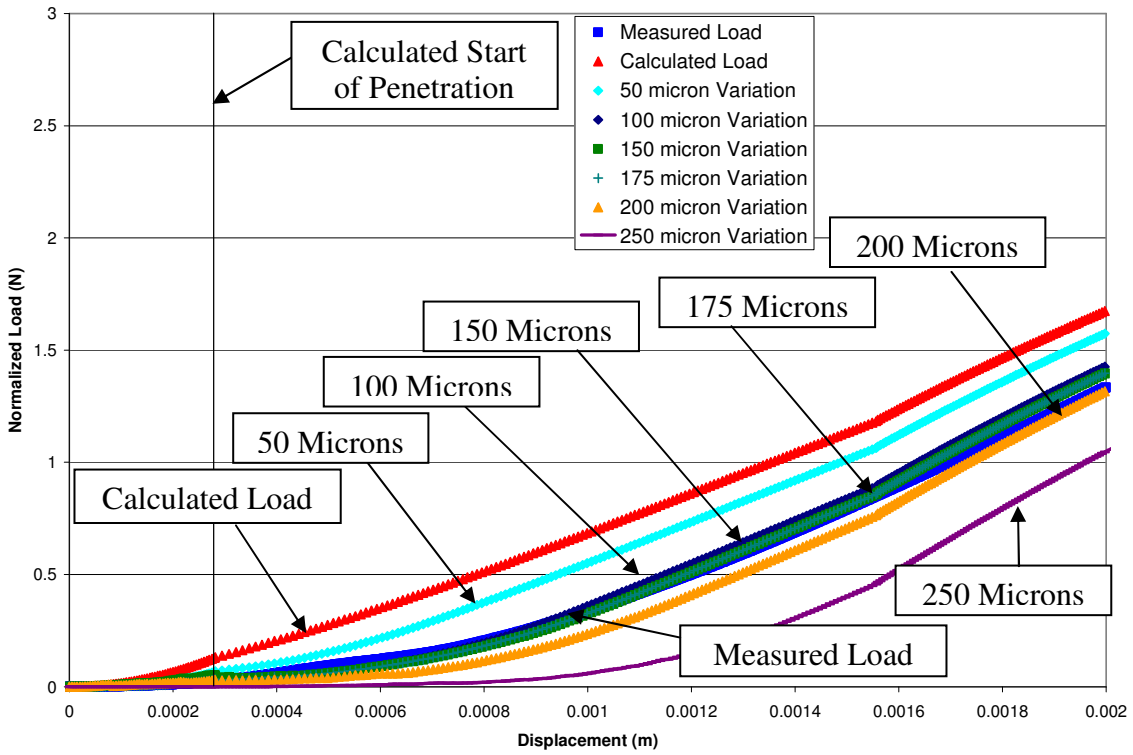


Figure **7.27**: Normalized load versus displacement showing measured loads, unadjusted calculated loads, and calculated loads adjusted for length variation for a multiple steel needle hexagonal pattern with 2.50 mm spacing.

Figure **7.28** contains the data from Figure **7.27** showing only the measured data, unadjusted calculated data, and the closest matching length adjusted calculated load data. In the case of the 2.50 mm steel hexagonal needle pattern, the 175 micron standard

deviation for length most closely matches the measured data. A statistical comparison between the calculated 175 micron length standard deviation data and the measured data shows an R-squared value of 0.9931. This high level of correlation indicates a good fit between the measured and length-adjusted calculated data and an improvement from the previous non-length adjusted calculated data.

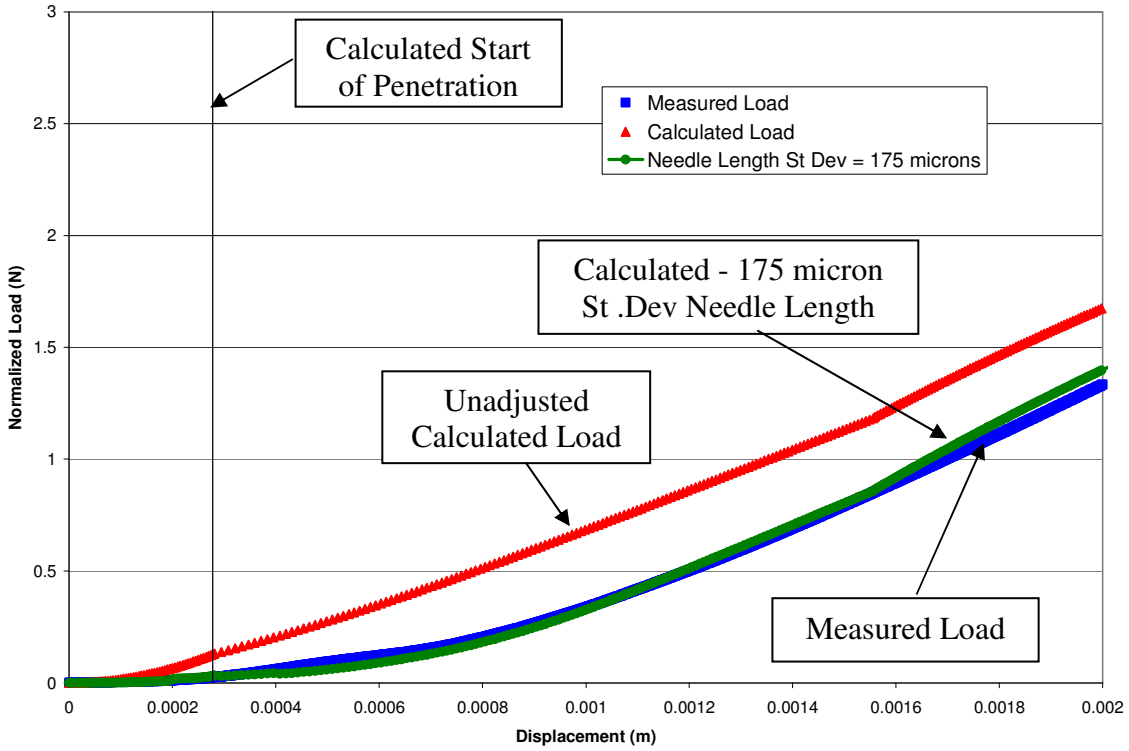


Figure **7.28**: Normalized load versus displacement showing measured, unadjusted calculated, and length-adjusted calculated loads for a multiple steel needle hexagonal pattern with 2.50 mm spacing.

Figure **7.29** shows calculated displacement versus normalized load for a 2.50 mm hexagonal steel needle pattern as it penetrates. Multiple needle deflection has only a small influence in this case due to the large 2.50 mm distance between needles.

Penetration depth is the dominant component of total displacement for the case of the 2.50 mm pattern.

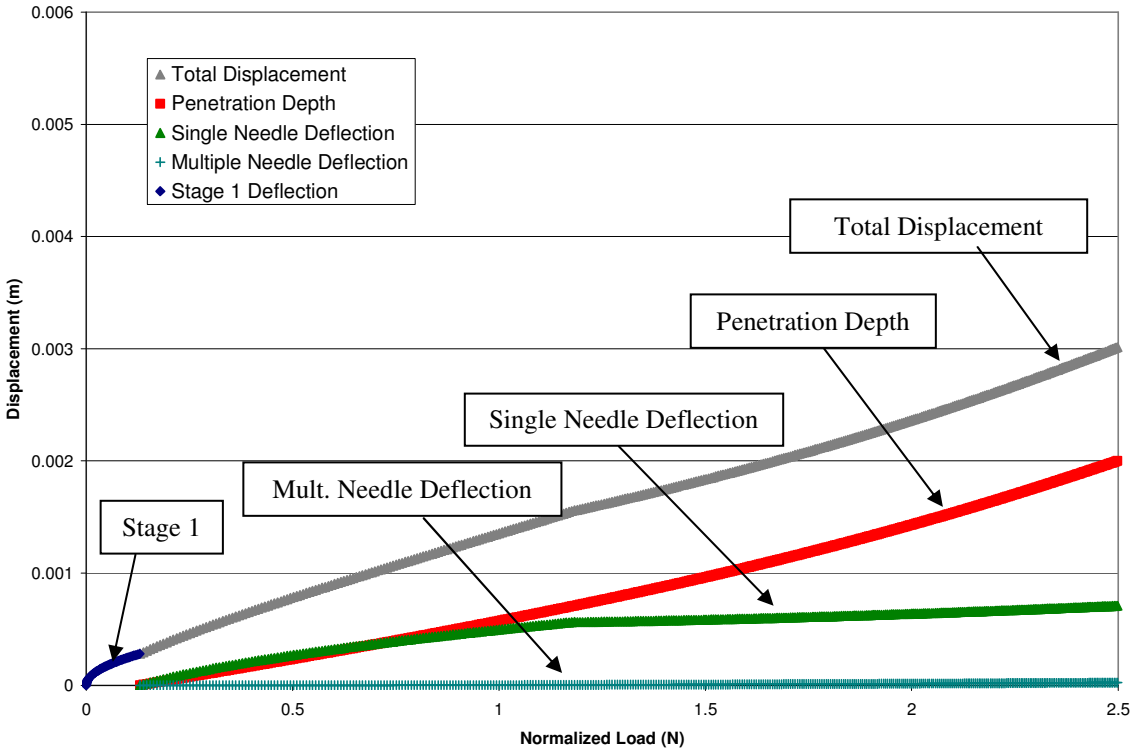


Figure **7.29**: Calculated displacement versus normalized force for each displacement component and the total displacement for the multiple steel hexagonal pattern with 2.50 mm spacing.

Figure **7.30** shows plots for normalized load versus displacement for the 37-needle hexagonal spacing pattern with 2.00 mm spacing between needles. The figure shows plots for measured data from Figure **6.18**, non-length adjusted calculated data, and calculated data with needle length variation with a standard deviation of 175 microns. A statistical comparison between the calculated random-length variation data and the measured data shows an R-squared value of 0.9971. This indicates a high level of correlation between the two data sets.

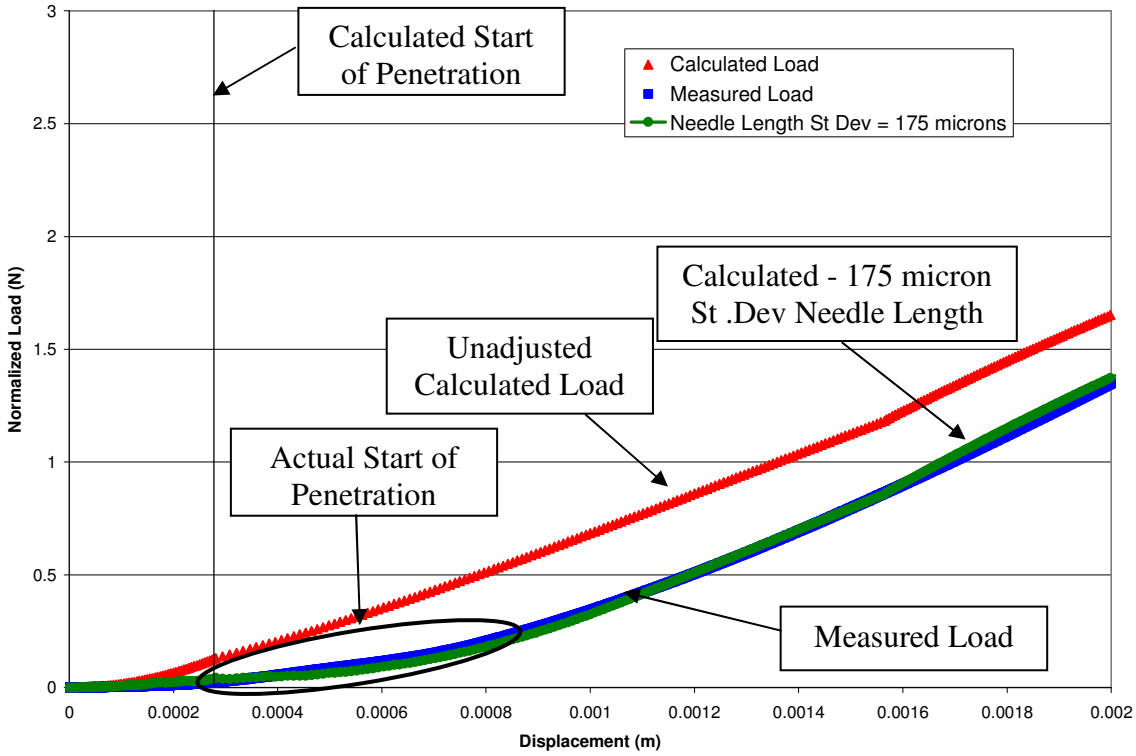


Figure **7.30**: Normalized load versus displacement showing measured and calculated loads for a multiple steel needle hexagonal pattern with 2.00 mm spacing.

Figure **7.31** shows calculated displacement versus normalized load for a 2.00 mm hexagonal steel needle pattern as it penetrates. Multiple needle deflection has only a small influence in this case due to the large 2.00 mm distance between needles. Penetration depth is the dominant component of total displacement for the case of the 2.00 mm pattern.

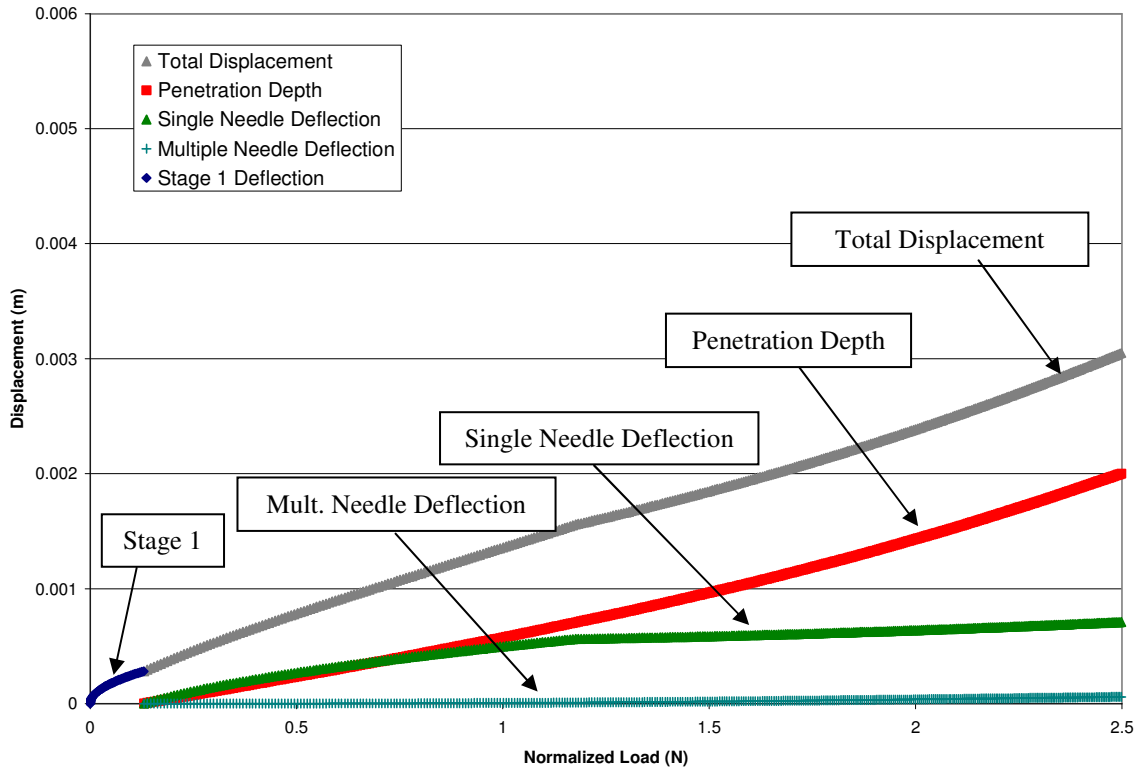


Figure **7.31**: Calculated displacement versus normalized force for each displacement component and the total displacement for the multiple steel hexagonal pattern with 2.00 mm spacing.

Figure **7.32** shows plots for normalized load versus displacement for the 37-needle hexagonal spacing pattern with 1.50 mm spacing between needles. The figure shows plots for measured data from Figure **6.18**, non-length adjusted calculated data, and calculated data with needle length variation with a standard deviation of 175 microns. A statistical comparison between the calculated random-length variation data and the measured data shows an R-squared value of 0.9963.

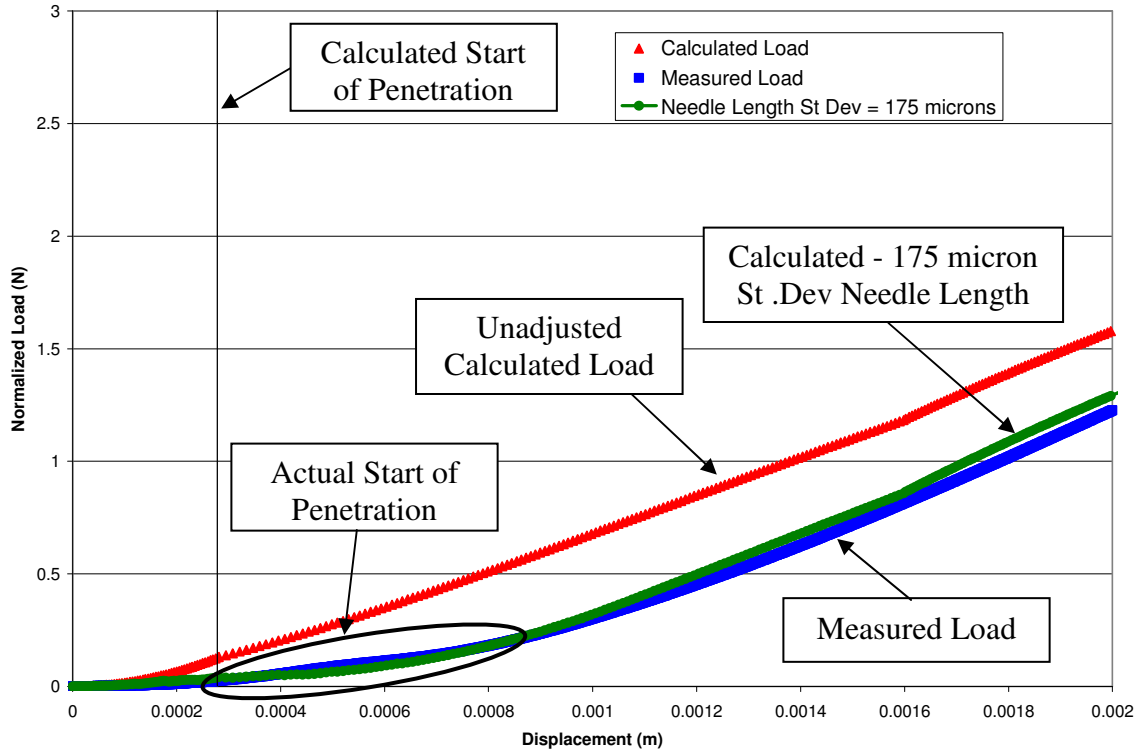


Figure **7.32**: Normalized load versus displacement showing measured and calculated loads for a multiple steel needle hexagonal pattern with 1.50 mm spacing.

Figure **7.33** shows calculated displacement versus normalized load for a 1.50 mm hexagonal steel needle pattern as it penetrates. Multiple needle deflection begins to have a small influence in this case around 1.75 N due to the 1.50 mm distance between needles becoming closer compared to the 2.00 mm and 2.50 mm patterns. Penetration depth is still the dominant component of total displacement for the case of the 1.50 mm hexagonal pattern.

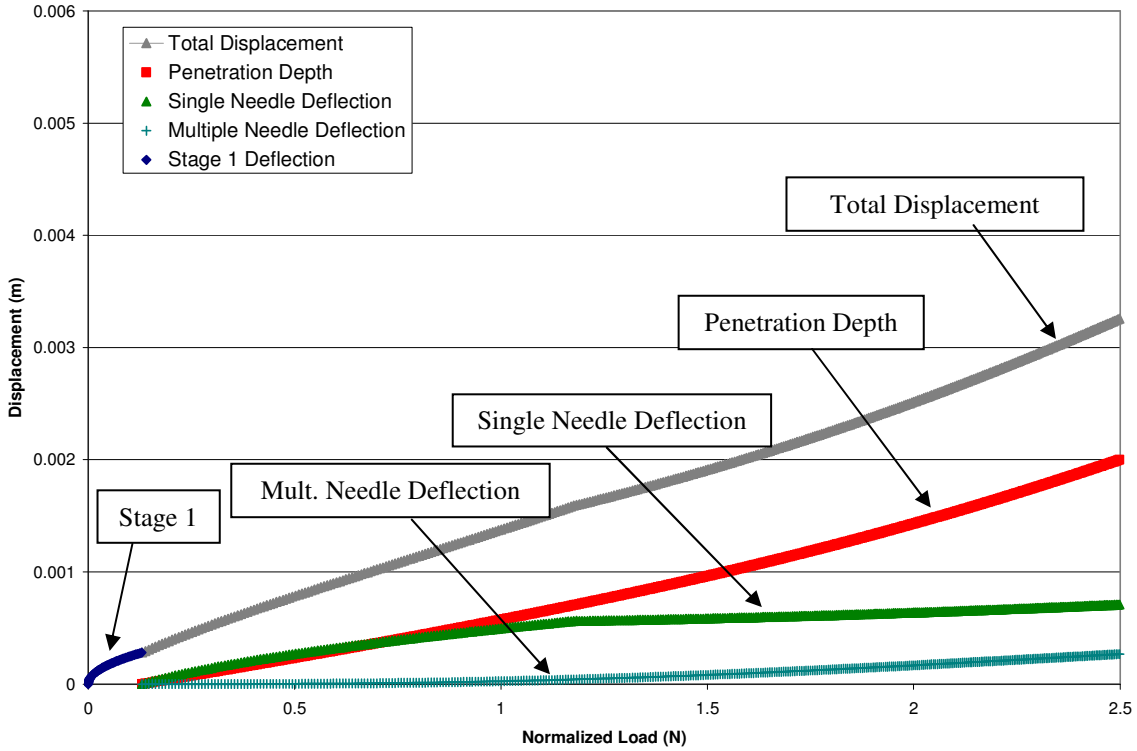


Figure **7.33**: Calculated displacement versus normalized force for each displacement component and the total displacement for the multiple steel hexagonal pattern with 1.50 mm spacing.

Figure **7.34** shows plots for normalized load versus displacement for the 37-needle square spacing pattern with 1.50 mm spacing between needles. The figure shows plots for measured data from Figure **6.18**, calculated non-length adjusted data, and calculated data with needle length variation with a standard deviation of 175 microns. A statistical comparison between the calculated random-length variation data and the measured data shows an R-squared value of 0.9738.

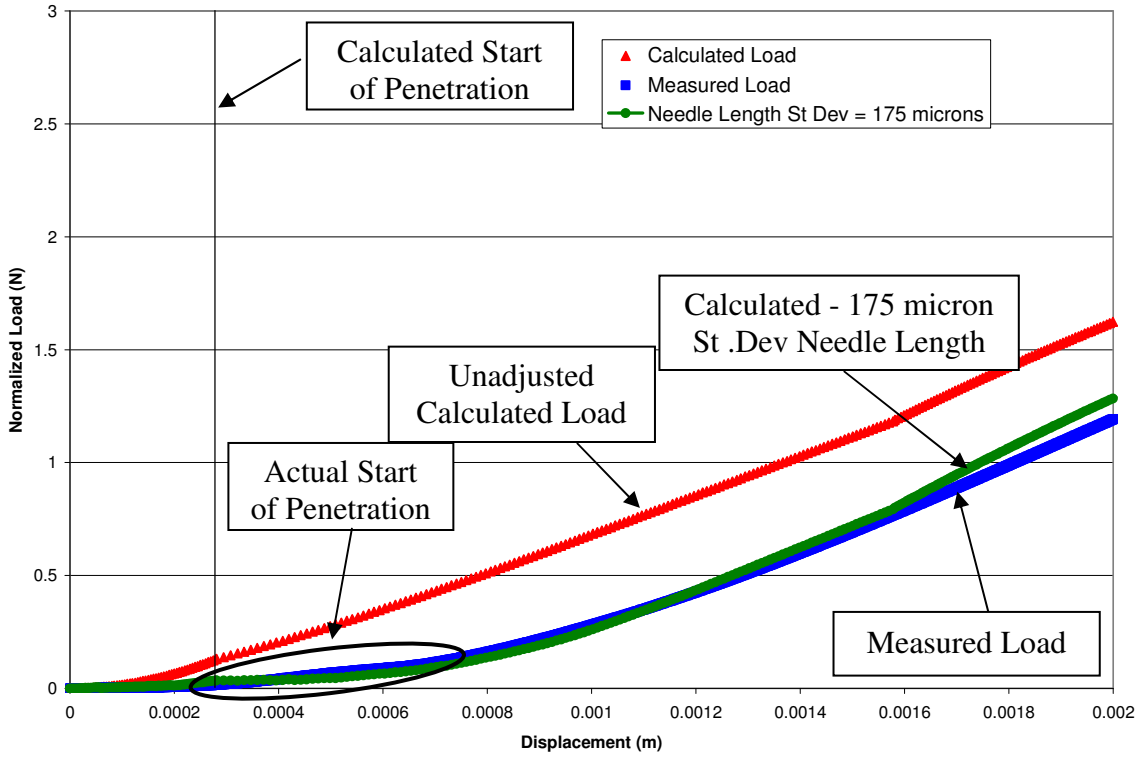


Figure **7.34**: Normalized load versus displacement showing measured and calculated loads for a multiple steel needle square pattern with 1.50 mm spacing.

Figure **7.35** shows displacement versus normalized load for a 1.50 mm square steel needle pattern as it penetrates. Multiple needle deflection has only a small influence in this case similar to the 2.00 mm and 2.50 mm hexagonal patterns. Penetration depth is still the dominant component of total displacement for the case of the 1.50 mm square pattern.

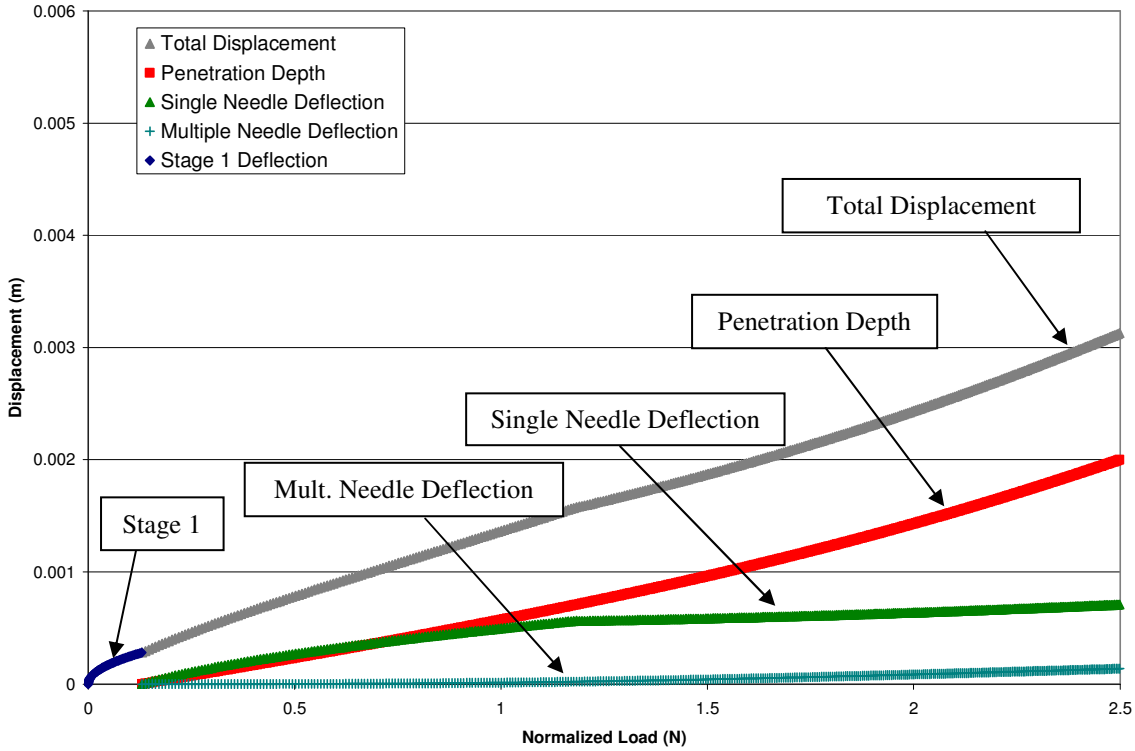


Figure **7.35**: Calculated displacement versus normalized force for each displacement component and the total displacement for the multiple steel square pattern with 1.50 mm spacing.

Figures **7.33** and **7.35** show that a square pattern will experience a smaller influence from the multiple needle deflection component compared to the hexagonal pattern of similar spacing between needles. This is due to the difference in the distance between needles in different directions for square patterns. This difference will cause the square pattern of the same apparent spacing as a hexagonal pattern to act like a pattern with a larger distance between needles. The distances between all adjacent needles in a hexagonal pattern are equal. Figure **7.36** shows the distances between adjacent needles for a square pattern and a hexagonal pattern.

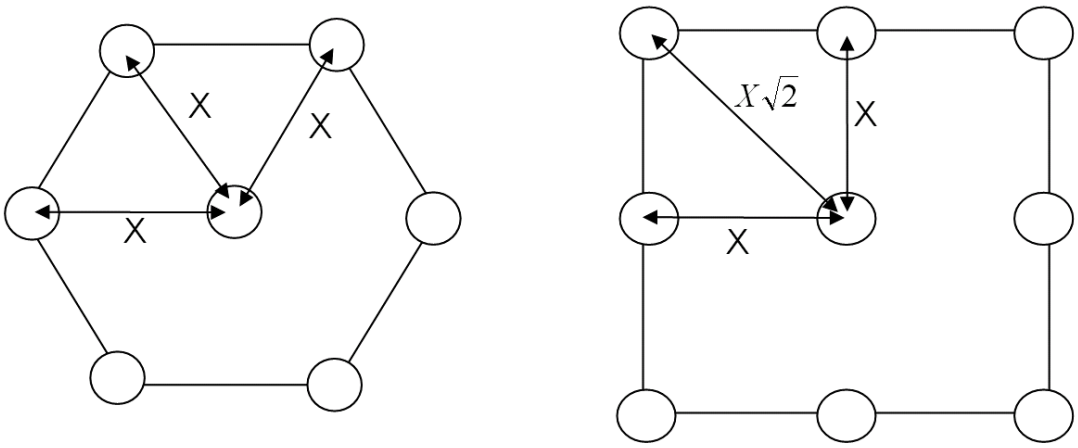


Figure **7.36**: Distance between adjacent needles for square patterns versus hexagonal patterns.

The distances between adjacent needles in a square pattern are different for diagonal needles and orthogonal needles, while a hexagonal pattern has equal distances between all adjacent needles. The difference can be expressed by Eq. **7.24** which shows that the average distance between needles for square patterns is approximately 21% larger than an equally spaced hexagonal pattern. This means that for a 1.50 mm square pattern, the average distance between adjacent needles is approximately equivalent to a hexagonal pattern with 1.81 mm between adjacent needles.

$$\begin{aligned}
&\text{Square Pattern}: 8 \text{ adjacent needles} \rightarrow \\
&4 \text{ needles at distance} = X \ \& \ 4 \text{ needles at distance} = X\sqrt{2} \\
&\therefore \text{Avg. Distance} = \left(4X + 4X\sqrt{2}\right)\Big/_{8} = 1.21X \\
&\text{Hex Pattern}: 6 \text{ adjacent needles} \rightarrow \\
&6 \text{ needles at distance} = \text{X} \\
&\therefore \text{Avg. Distance} = 6X\Big/_{6} = X
\end{aligned}$$

Eq. **7.24**

Figure **7.37** shows plots for normalized load versus displacement for analytical data that compare a 1.50 mm square pattern to a 1.81 mm hexagonal pattern using the adjustment for average spacing shown in Eq. **7.24**. The figure shows that normalizing the needle spacing of a square pattern will cause the square pattern to mimic a hexagonal pattern of a larger spacing due to the lower density of needles.

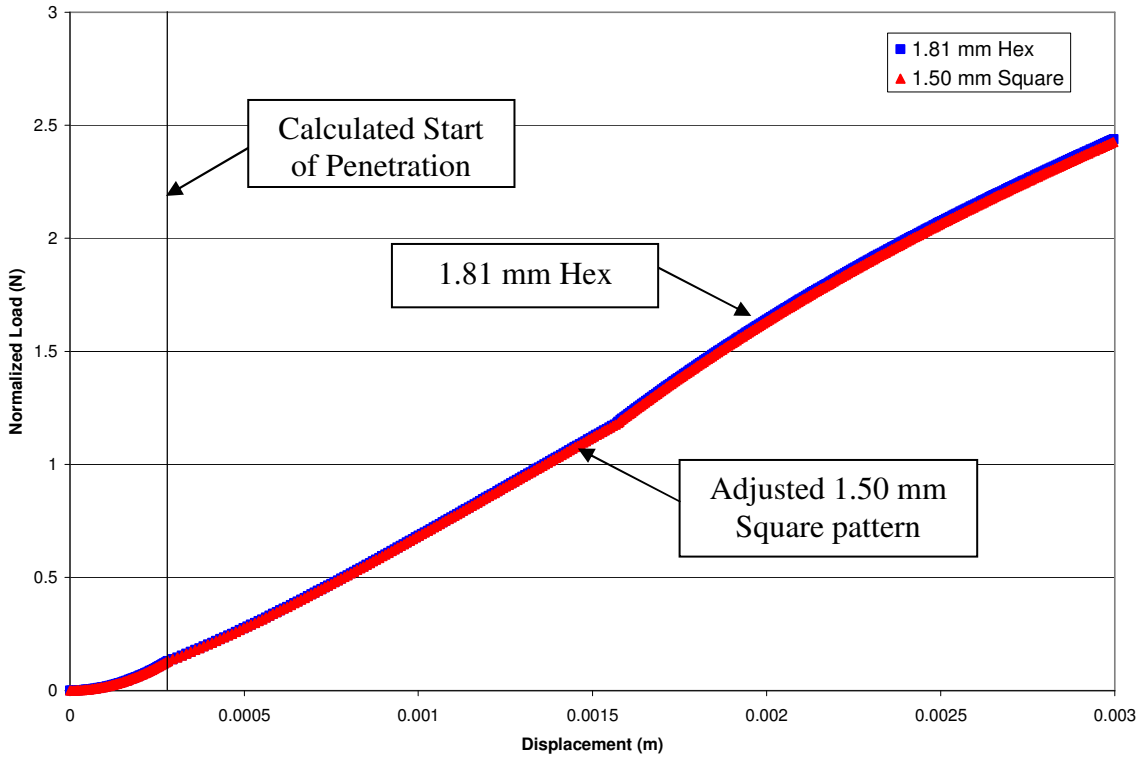


Figure **7.37**: Normalized calculated load versus displacement showing multiple steel needle pattern with 1.50 mm normalized square spacing and 1.81 mm hexagonal spacing.

Figure **7.38** shows plots for normalized load versus displacement for the 37-needle hexagonal spacing pattern with 1.25 mm spacing between needles. The figure shows plots for measured data from Figure **6.18**, non-length adjusted calculated data, and calculated data with needle length variation with a standard deviation of 175 microns. A

statistical comparison between the calculated random-length variation data and the measured data shows an R-squared value of 0.9355.

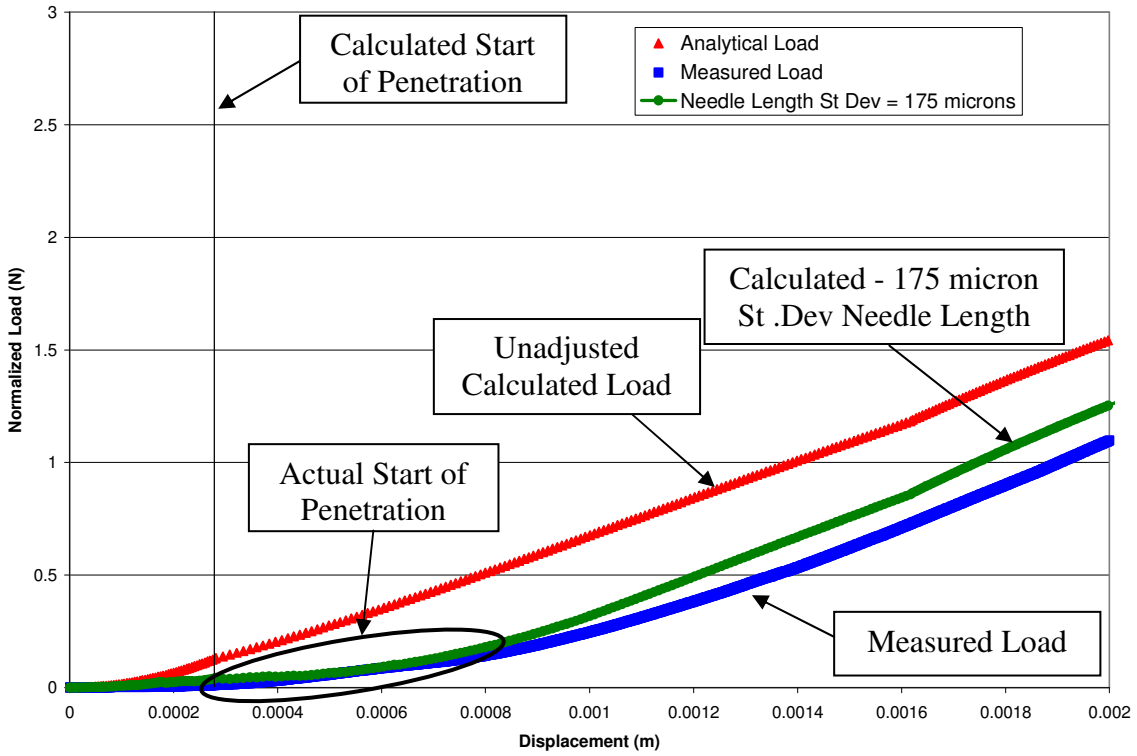


Figure **7.38**: Normalized load versus displacement showing measured and calculated loads for a multiple steel needle hexagonal pattern with 1.25 mm spacing.

Figure **7.39** shows displacement versus normalized load for a 1.25 mm hexagonal steel needle pattern as it penetrates. Multiple needle deflection begins to have a small influence in this case around 1.5 N due to the 1.25 mm distance between needles becoming closer compared to the 1.50 mm pattern. Penetration depth is still the dominant component of total displacement for the case of the 1.25 mm hexagonal pattern.

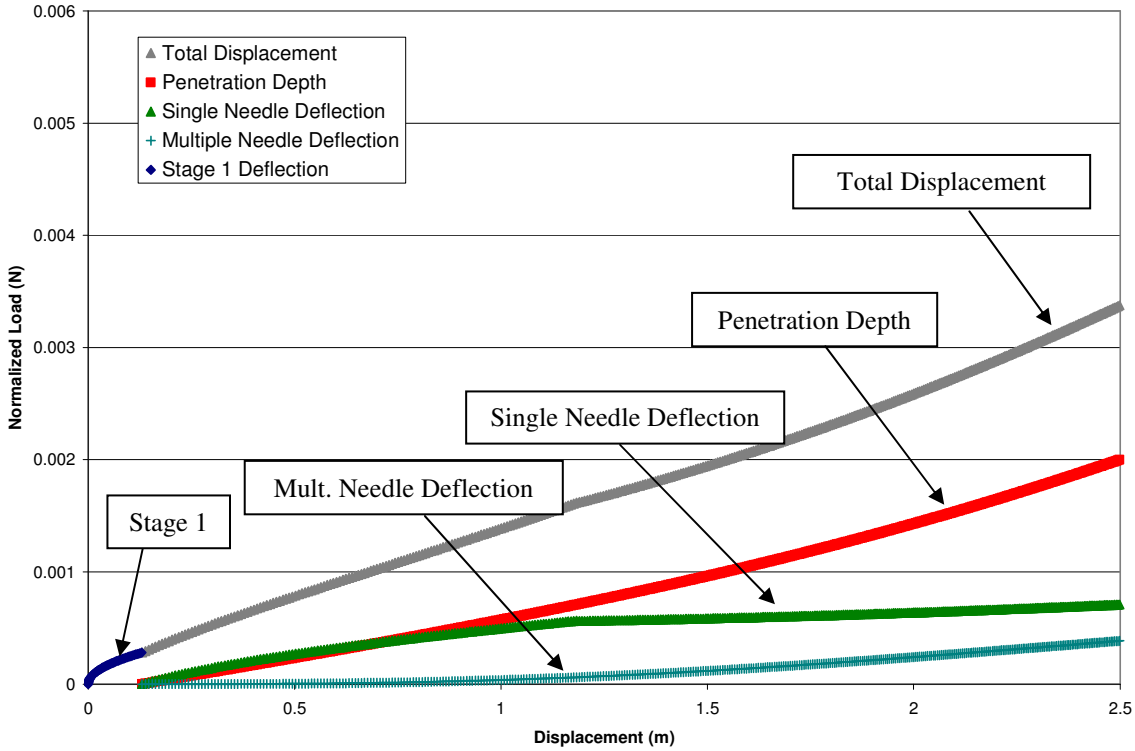


Figure **7.39**: Calculated displacement versus normalized force for each displacement component and the total displacement for the multiple steel hexagonal pattern with 1.25 mm spacing.

Figure **7.40** shows plots for normalized load versus displacement for the 37-needle hexagonal spacing pattern with 1.00 mm spacing between needles. The figure shows plots for measured data from Figure **6.18**, non-length adjusted calculated data, and calculated data with needle length variation with a standard deviation of 200 microns. A statistical comparison between the calculated random-length variation data and the measured data shows an R-squared value of 0.9519.

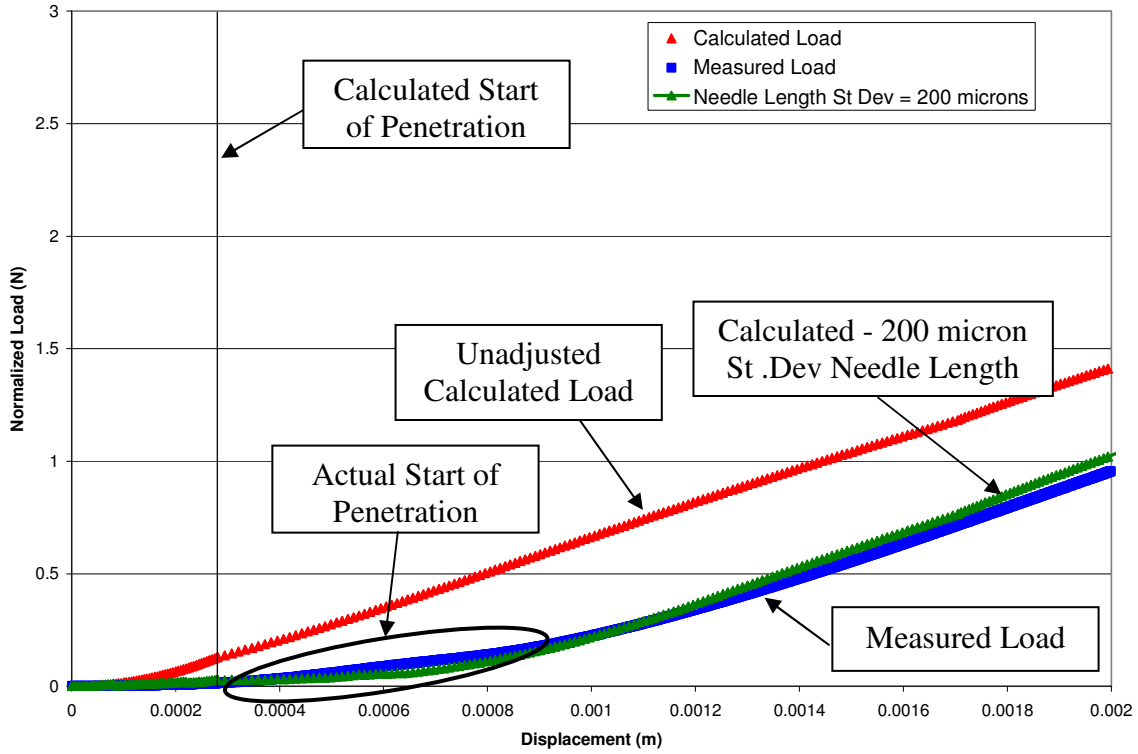


Figure **7.40**: Normalized load versus displacement showing measured and calculated loads for a multiple steel needle hexagonal pattern with 1.00 mm spacing.

Figure **7.41** shows displacement versus normalized load for a 1.00 mm hexagonal steel needle pattern as it penetrates. The effect of multiple needles in a close pattern causes the multiple needle deflection to have a larger influence on total displacement than single needle deflection around 2 N. Penetration depth is still the dominant component of total displacement for the case of the 1.00 mm hexagonal pattern through 2.5 N of applied force.

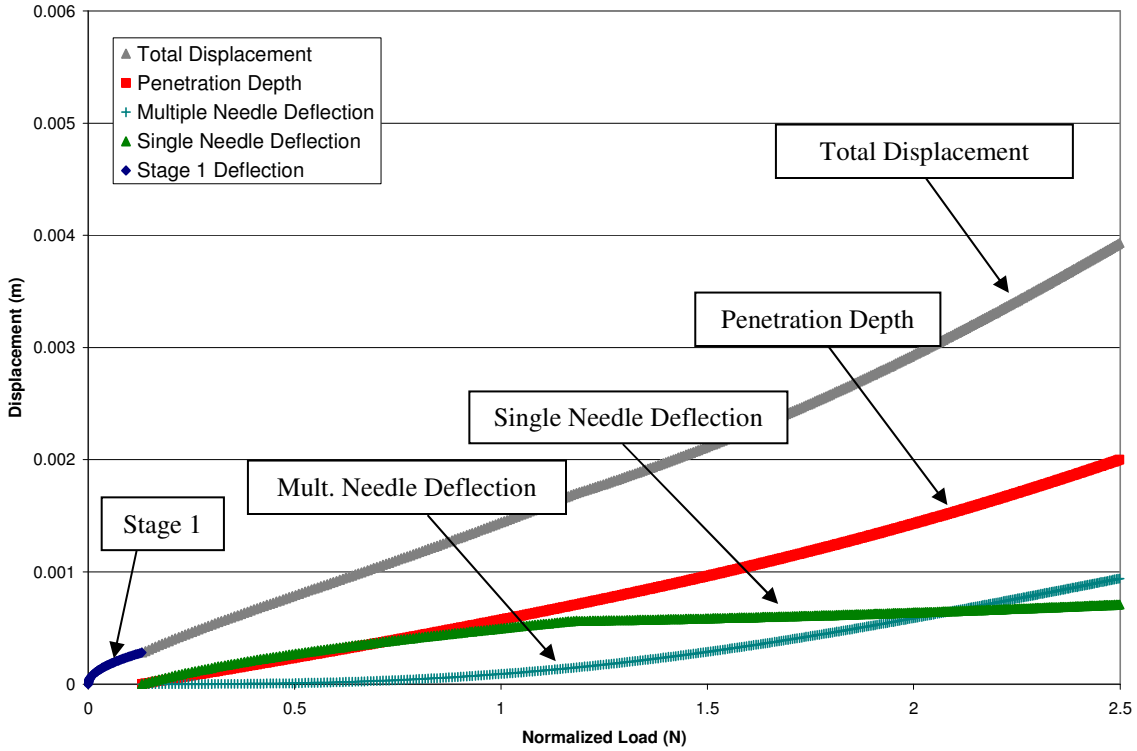


Figure **7.41**: Calculated displacement versus normalized force for each displacement component and the total displacement for the multiple steel hexagonal pattern with 1.00 mm spacing.

Figure **7.42** shows plots for normalized load versus displacement for the 37-needle hexagonal spacing pattern with 0.75 mm spacing between needles. The figure shows plots for measured data from Figure **6.18**, non-length adjusted calculated data, and calculated data with needle length variation with a standard deviation of 200 microns. A statistical comparison between the calculated random-length variation data and the measured data shows an R-squared value of 0.9669.

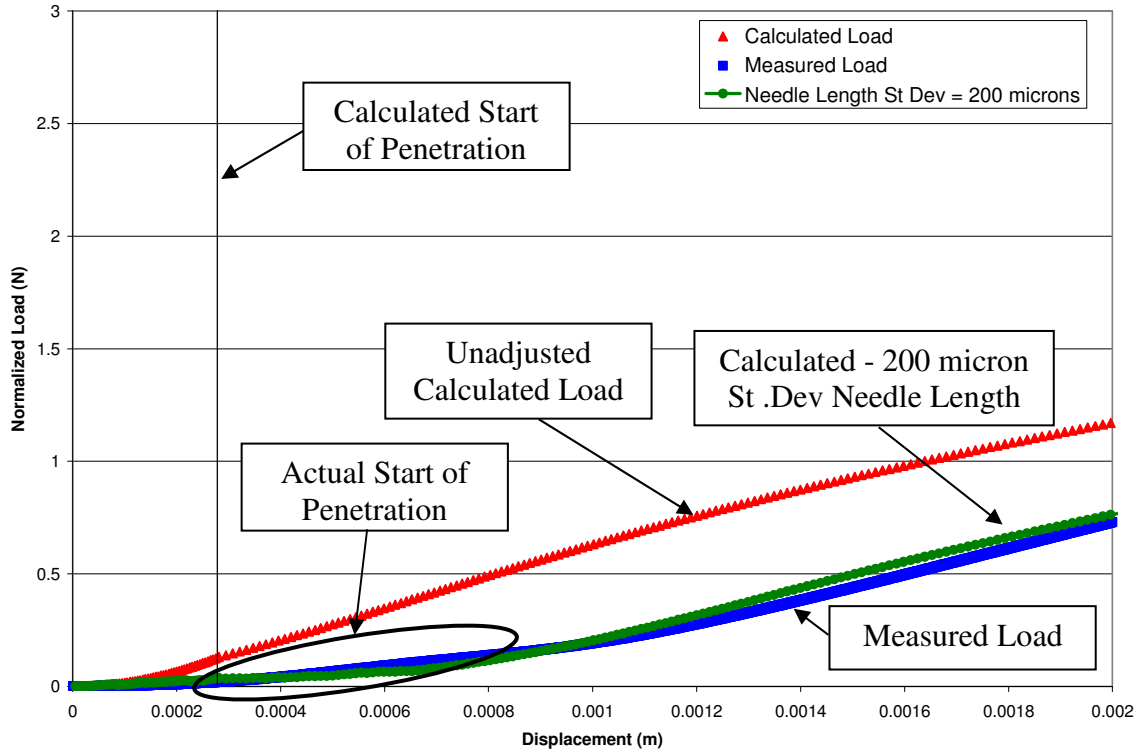


Figure **7.42**: Normalized load versus displacement showing measured and calculated loads for a multiple steel needle hexagonal pattern with 0.75 mm spacing.

Figure **7.43** shows displacement versus normalized load for a 0.75 mm hexagonal steel needle pattern as it penetrates. The effect of multiple needles in a close pattern causes the multiple needle deflection to have a larger influence on total displacement than both single needle deflection and penetration depth at approximately 1.5 N. Multiple needle deflection is the dominant component of total displacement for the case of the 0.75 mm hexagonal pattern.

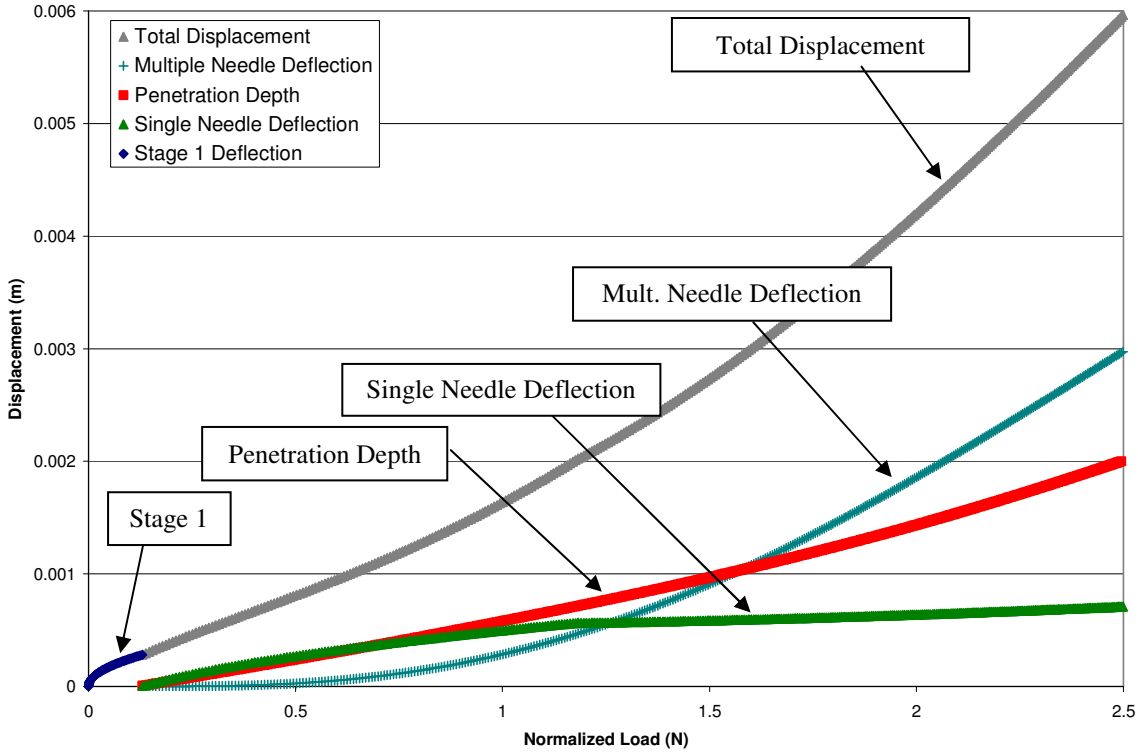


Figure **7.43**: Calculated displacement versus normalized force for each displacement component and the total displacement for the multiple steel hexagonal pattern with 0.75 mm spacing.

This section has compared the calculated and measured values for each steel needle pattern in Figures **7.21** through **7.42**. Table **7.2** shows the R-squared values for comparisons for each needle pattern of measured data to length-adjusted calculated data. The table shows the calculated data that have been unadjusted for needle length and adjusted for length at the standard deviations shown. The best fit between the length-adjusted calculated data and measured data are highlighted in orange. There is a wide range of agreement between the calculated data unadjusted for length and measured data; the R-squared values range from 0.6252 to 0.9237. Data that have been adjusted for length shows a high level of correlation between calculated and measured data with R-

squared values ranging from 0.9355 to 0.9971. This suggests that there must be some level of variation in needle length that is influencing the measured data.

Table **7.2**: R-squared values for each multiple steel needle pattern at varying levels of adjustment for needle length standard deviation.

| | Needle Pattern | | | | | | |
|---|---|---|---|---|---|---|---|
| Needle Length St Dev | 0.75 mm Hex | 1.00 mm Hex | 1.25 mm Hex | 1.50 mm Hex | 1.50 mm Sq | 2.00 mm Hex | 2.5 mm Hex |
| Unadjusted | 0.6886 | 0.6252 | 0.7497 | 0.9144 | 0.7378 | 0.9237 | 0.9030 |
| 150 microns | 0.8561 | | | | | | 0.9922 |
| 175 microns | 0.8362 | 0.8715 | 0.9355 | 0.9963 | 0.9738 | 0.9971 | 0.9931 |
| 200 microns | 0.9669 | 0.9519 | | | | | 0.9352 |

Comparing each steel needle pattern gives a good basis for evaluating the concept of multiple needle deflection. The needle patterns range from a 0.75 mm hexagonal pattern to a single needle with a theoretically infinite needle spacing between needles. Figures **7.22, 7.29, 7.31, 7.33, 7.35, 7.39**, **7.41**, and **7.43** give a breakdown of each calculated deflection component for each needle pattern. The only deviation between any of the figures comes as a result of the multiple needle deflection. This is because the needle geometries are all assumed to be the same in the model with the only differences coming from the pattern spacing. These figures clearly show that patterns with closely spaced needles like the 0.75 mm pattern experience a large influence from multiple needle deflection while a pattern with 2.50 mm needle spacing experiences only a very minor influence. This indicates that penetration depth is the same for all patterns for a given force and the only difference comes from the multiple needle deflection component. This was verified by the steel needle tests summarized in Figure **6.23** that show that penetration depth is related only to applied force and is not sensitive to distance

between needles. Single needle deflection is also the same for all patterns because the geometries of individual needles are the same for all patterns.

Only multiple needle deflections differentiate between each pattern as shown in Figure **7.44** showing the difference between the total length-adjusted calculated displacements for each pattern. Comparing this to Figure **6.19** showing measured test data shows that the needle spacing patterns follow the same trend for both calculated and measured data. This helps to confirm that larger needle spacing patterns will have less of the multiple needle deflection effects that come from the pattern acting like a solid indenter.

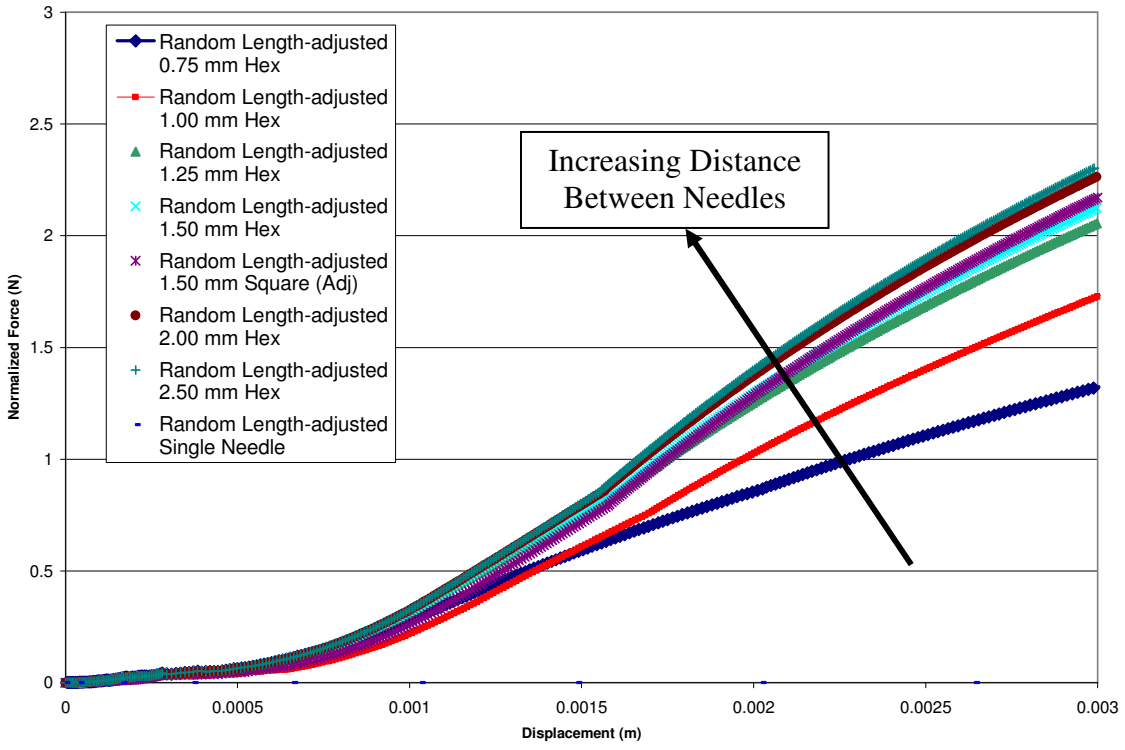


Figure **7.44**: Calculated random length-adjusted normalized load versus total displacement for all seven multiple steel needle patterns and single steel needle.

This section also explored the difference between square and hexagonal needle patterns. As shown in Figure **7.36** and Eq. **7.24**, a square pattern has a lower average density of needles compared to a similar hexagonal pattern. The equation for the adjusting the 1.50 mm square spacing shown in Eq. **7.24** is plotted in Figure **7.54** to normalize its spacing to simulate a hexagonal spacing pattern. This results in less influence from the multiple needle deflection component on total displacement.

Finally, the effect of small variations between needles in the tested patterns was discussed. Figures **7.23, 7.30, 7.32, 7.34, 7.38, 7.40,** and **7.42** show that for measured data there is a range of values for the start of penetration that exist for each multiple needle pattern. These variations exist as small differences in needle lengths, the angle of approach for the needle pattern as shown in Figure **7.24**, and differences in needle tip radii for individual needles in a pattern. These small variations between needles cause the measured data to deviate from the unadjusted calculated data. Adjustments for needle length variation are small, on the order of standard deviation of 175-200 microns for a needle that penetrates at least 2 mm. Adjusting the calculated by applying statistically normal random variation will result in a much higher level of correlation between with the measured data. This concept will be discussed further in the Error Analysis section of this chapter.

The preceding section discussed the results of steel needle testing and made comparisons to calculated results that come from the equations summarized in Figure **7.17** and Figure **7.18**. Steel needle testing has been used to form the basis for those equations because of the ability to isolate the constituent components of penetration, single needle deflection, and multiple needle deflection. Inducing random

length variation into the calculated data shows a high level of correlation between the calculated and measured data. This analysis will be applied to plastic microneedle devices in the next section.

## Plastic Microneedle Device Comparison to Analytical Model

This section details comparisons between the previously established analytical relationships and measured data from injection molded plastic microneedles. There are differences between the plastic microneedle devices and the assembled steel needle devices including material, number of needle tips, and length of needles. Each of these attributes plays some role in the shape of the force versus displacement plots and will be discussed throughout this section. Parameters such as the friction coefficient between the needle and silicone rubber are unknown and are therefore kept the same as the values measured from the steel needles. Friction is known to have an influence on the calculated curves and its effects are discussed more fully in a later section.

### *Polystyrene Microneedle Analysis*

Figure **7.45** shows plots for normalized load versus displacement for measured data from Figure **6.35** and analytical data for the 100-needle square spacing pattern with 1.00 mm spacing between needles. Unadjusted calculated and random needle length-adjusted calculated data sets are plotted for comparison to the measured data. The length-adjusted calculated data are generated using the method described in the steel

needle analysis section. In the case of all plastic microneedle analyses, data points are randomly generated using Minitab® that represent varying needle lengths within a pattern. Each data point represents the start of needle tip contact with the rubber surface and, thus, the starting displacement value when force is applied for each needle. This concept is shown in Table **7.1** where each column with offset starting displacements represents one needle. The highest correlation needle length standard deviation value is chosen and plotted for each plastic microneedle pattern.

The needles on this device are 735 microns in length. The needle length is indicated by a line on the figure. The length of the needles indicated in the figure is the average measured length from Table **6.2**. The length of the needles as measured from the base will limit the depth that they can penetrate as shown by the increase in the slope of the measured data after the measured needle length. A statistical comparison between the calculated random-length variation data with a standard deviation for needle length of 100 microns and the measured data shows an R-squared value of 0.9416.

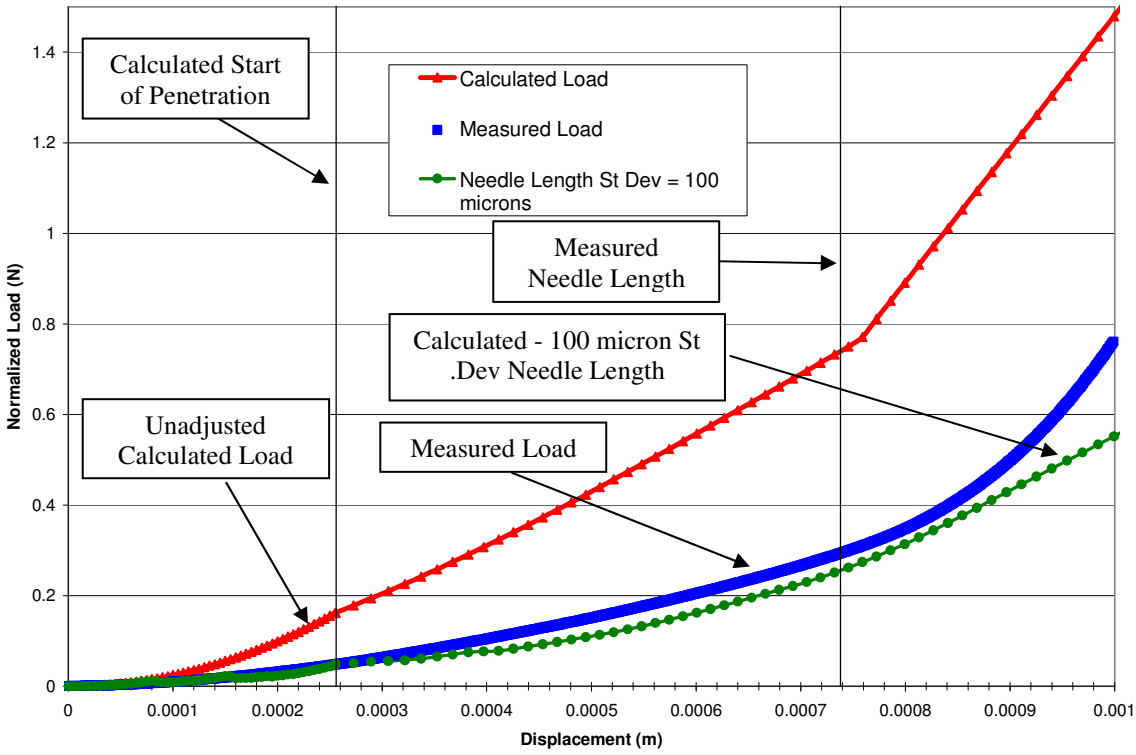


Figure **7.45**: Normalized load versus displacement for polystyrene microneedle device with 1.00 mm spacing arranged in a square pattern.

Figure **7.46** shows the measured data shown in Figure **7.45** broken down into their component parts and displacement plotted versus normalized load. Within the region of interest, located below the measured needle length to the left of the vertical line, the penetration depth continues to increase at a nearly constant rate after the start of penetration. The effect of multiple needle deflection is small compared to the depth of penetration and single needle deflection. This indicates that the effect of the close 1.00 mm distance between needle tips in the pattern has little effect on the total displacement of the needle. The depth of penetration for this pattern is calculated to be only about 170 microns.

The figure shows that total needle displacement is dominated by single needle deflection until the measured needle length of 735 microns. This is largely due to the conical shape of the needle tips with a large 30 degree angle. A smaller angle would create less projected area for a given needle depth and allow more needle penetration as dictated by the single needle deflection equation shown in Figure **7.17**. The equation shows that a smaller penetrating radius will produce less single needle deflection. A smaller penetrating radius comes from a smaller tip angle.

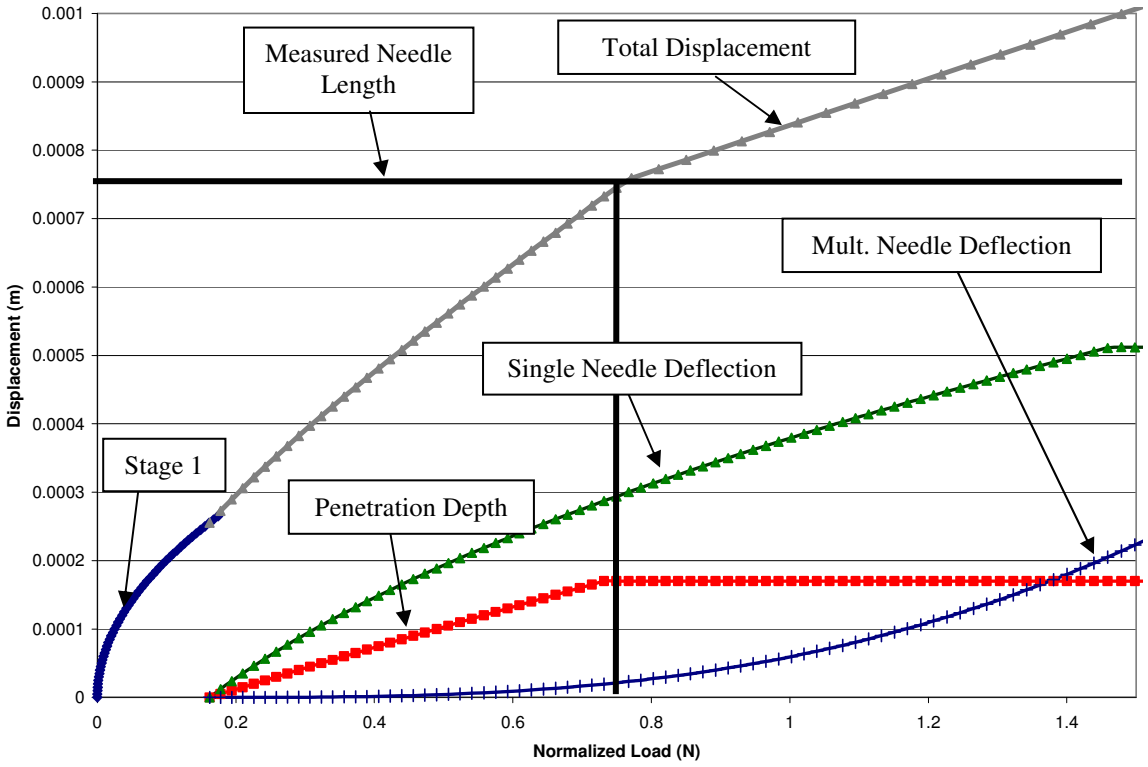


Figure **7.46**: Calculated displacement versus normalized force for each displacement component and the total displacement for a square polystyrene pattern with 1.00 mm spacing.

The increase in slope for the measured data in Figure **7.45** shows that the slope increases after penetrating to their full length and the entire base of the device begins compressing the rubber. Figure **7.47** shows an example of the base of a microneedle device beginning to compress the surface of the rubber. The figure shows that at the needle length, the base of the microneedle device begins compressing the rubber sample without further penetration. The start of penetration and the length of the needle tips will determine the limit of penetration depth for the microneedle device.

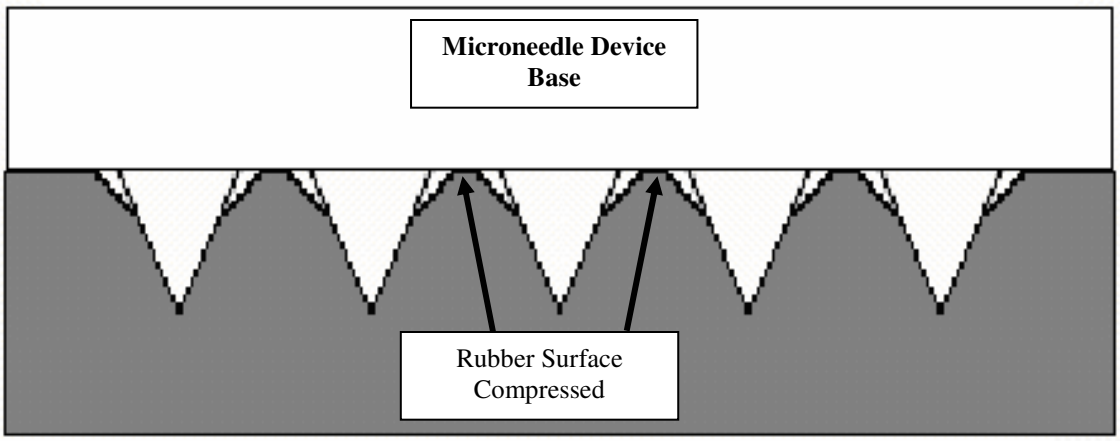


Figure **7.47**: Cross-section of microneedle device at the limit of its penetration depth by the base of the device.

The start of penetration is indicated by a line on Figure **7.45**. The distance between the start of penetration and the needle length is the amount of actual penetration estimated to occur. The distance from zero to the start of penetration represents only compression where the rubber is pushing back on the needle tip until reaching the fracture point of the rubber. Therefore the estimated penetration distance occurs between two lines shown on the plot. Figure **7.48** shows an exaggerated example of this concept. The open area below the needle tip represents material that has not yet been penetrated.

The area near the surface of the skin that has been pushed down by the needle represents the compression of the skin by the needle. The distance between these two regions represents the depth of penetration.

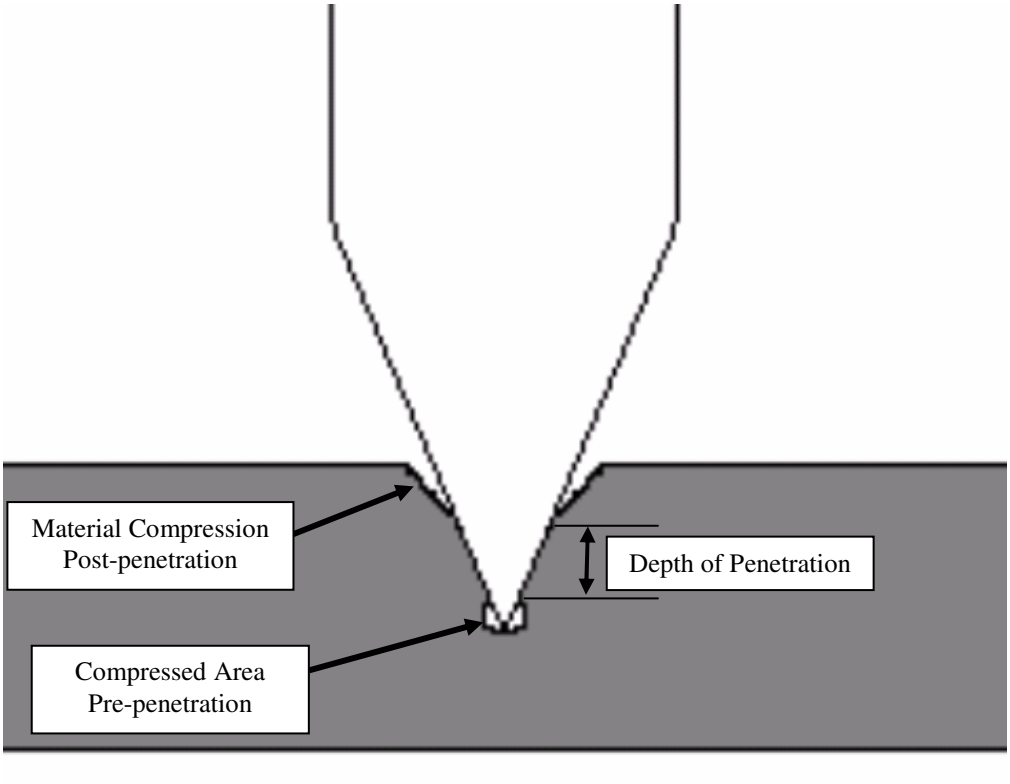


Figure **7.48**: Example showing the three basic components of total needle displacement and their relationships to each other.

The penetration distance into the skin may have an effect on drug delivery. A penetration that is too shallow may be detrimental to drug delivery and penetration that is too deep may stimulate nerves thereby causing pain.

The measured data show that there is error between the calculated and measured data. This error comes from several possible sources. One source of error comes from the variation in geometry for the injection molded needles. Each individual needle tip

cavity has a slightly different geometry that comes from the process of manufacturing the molds. The injection molding process itself may not entirely fill the mold cavity, causing a needle tip with a larger or smaller radius than the measured average. The length of the needle tips is also affected by the mold-making and injection molding process and could cause variation in the needle length.

Another source of error is the effect shown in Figure **7.24** where the microneedle device does not take an orthogonal approach to the surface of the rubber sample due to variations in the test fixture. This will cause multiple penetration events to occur simultaneously and spread the measured load along the axis indicating needle displacement. For example, this effect will mean that some needle tips will begin rubber penetration at the indicated start of penetration, while other needle tips will not start penetrating the rubber surface until the Instron cross-head has advanced another 200-300 microns.

A similar error is recorded near at the measured needle length of 735 microns. At that point, the figure should show a quick increase in slope. However the increase is delayed because of the simultaneous penetration and material deflection events that tend to spread the slope increase across the displacement axis. These errors are the result of measuring 100 needle tips with a single load cell and trying to isolate specific events for all needle tips. This discrepancy between the unadjusted calculated data and measured data are resolved by adjusting the calculated data using the previously described method using random normal variation in needle length.

Figure **7.49** shows plots for normalized load versus displacement for measured data from Figure **6.35** and analytical data for the 100-needle square spacing pattern with

1.50 mm spacing between needles. Unadjusted calculated and random needle length-adjusted calculated data sets are plotted for comparison to the measured data. The average needle length on this device is 737 microns. The increase in slope at the measured needle length comes from the compression of the rubber section by the base of the microneedle device. The difference between the measured and calculated plots comes from measurement error as shown in Figure **7.24** and small variations in needle lengths. A statistical comparison between the calculated random-length variation data with a standard deviation for needle length of 75 microns and the measured data shows an R-squared value of 0.9059.

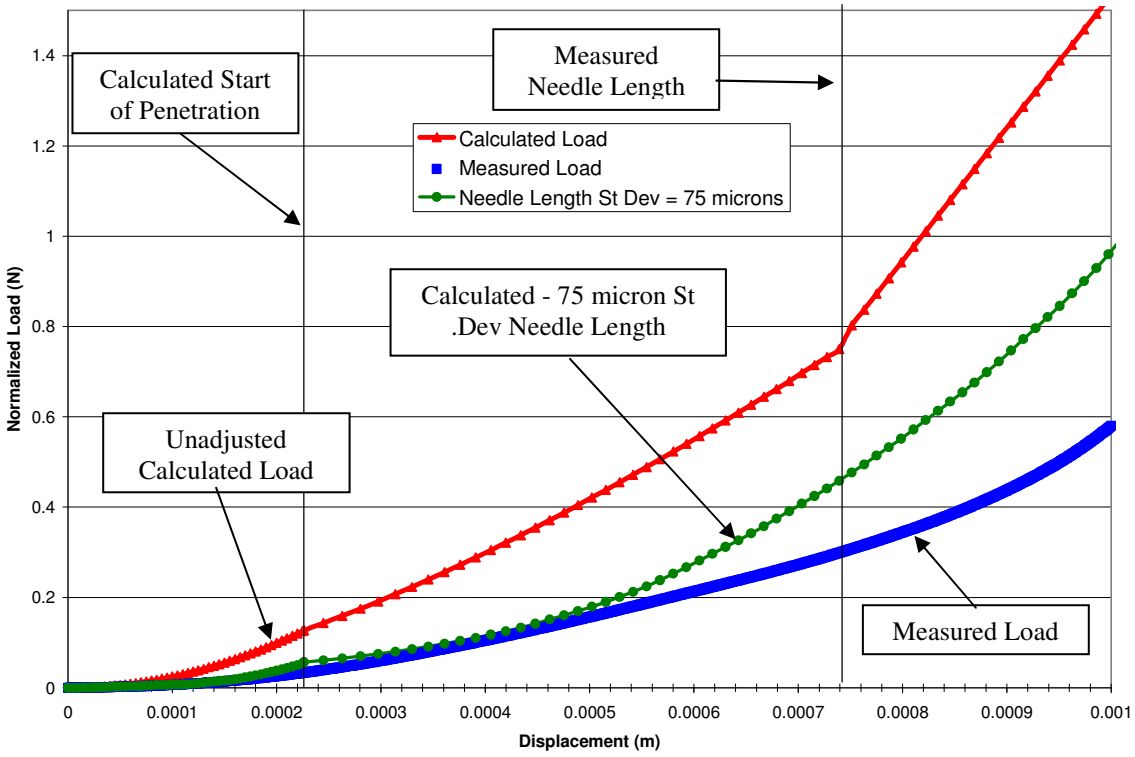


Figure **7.49**: Normalized load versus displacement for polystyrene microneedle device with 1.50 mm spacing arranged in a square pattern.

Figure **7.50** shows the measured data shown in Figure **7.49** broken down into their component parts and displacement plotted versus normalized load. The figure shows that at the measured needle length, the base of the microneedle device begins compressing the rubber sample without further penetration. Within the region of interest, located below the measured needle length to the left of the vertical line, the penetration depth continues to increase at a nearly constant rate after the start of penetration. The effect of multiple needle deflection is negligible compared to the depth of penetration and single needle deflection. The effect of the 1.50 mm distance between needle tips in the square pattern has a smaller effect on total displacement compared to the 1.00 mm square pattern. The depth of penetration for this pattern is calculated to be about 190 microns. Single needle deflection dominates the total displacement due to the large tip angle of 30 degrees that causes more material deflection than penetration.

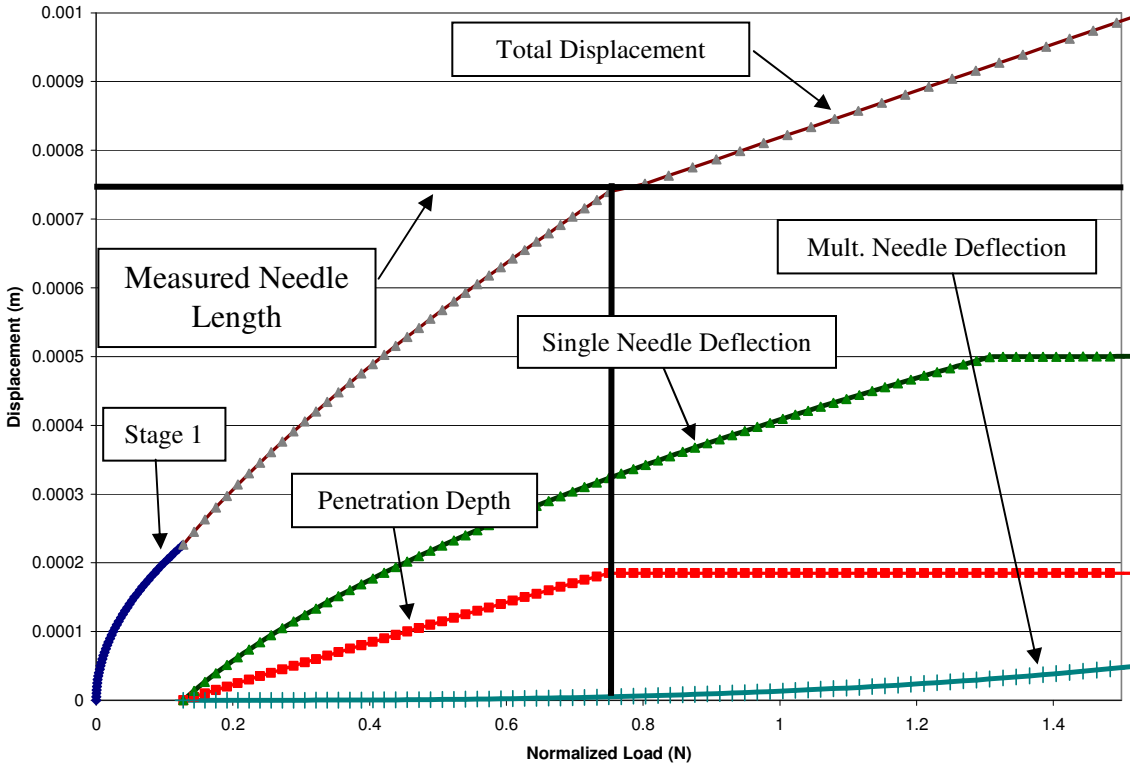


Figure **7.50**: Calculated displacement versus normalized force for each displacement component and the total displacement for a square polystyrene pattern with 1.50 mm spacing.

Figure **7.51** shows plots for normalized load versus displacement for measured data from Figure **6.35** and analytical data for the 91-needle square spacing pattern with 1.00 mm spacing between needles. Unadjusted calculated and random needle length-adjusted calculated data sets are plotted for comparison to the measured data. The average needle length on this device is 656 microns. The increase in slope at the measured needle length comes from the compression of the rubber section by the base of the microneedle device. The difference between the measured and calculated plots comes from measurement error as shown in Figure **7.24** and small variations in needle lengths. A statistical comparison between the calculated random-length variation data

with a standard deviation for needle length of 100 microns and the measured data shows an R-squared value of 0.9420.

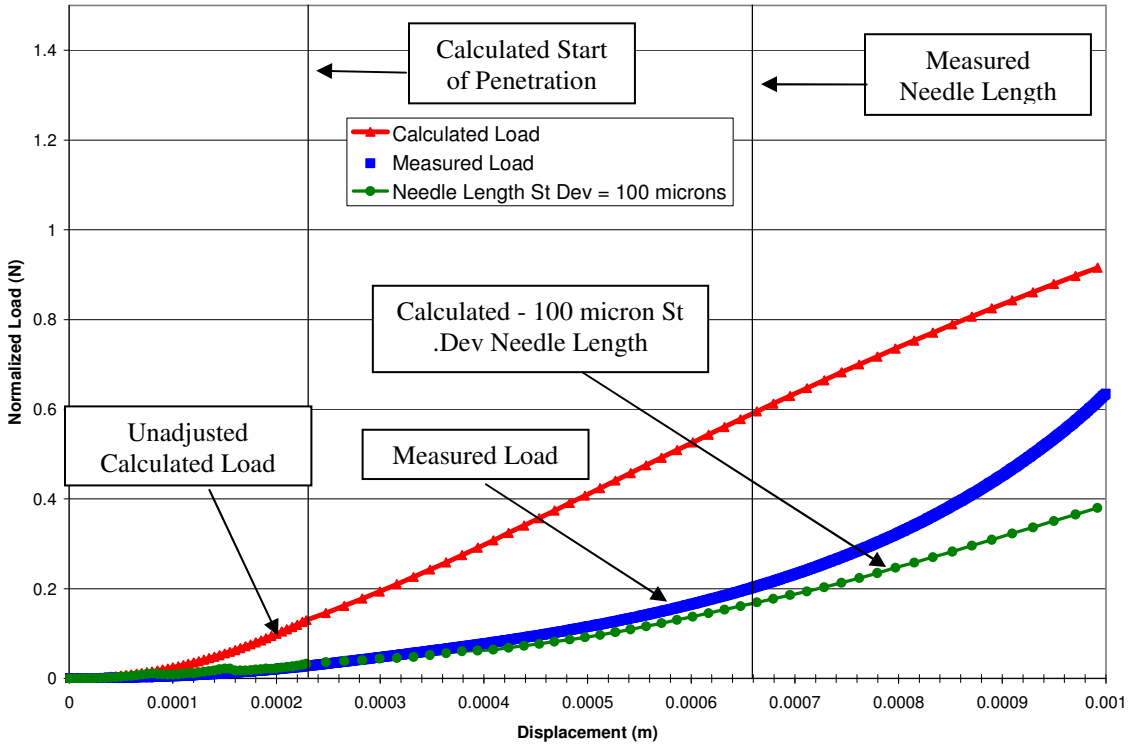


Figure **7.51**: Normalized load versus displacement for polystyrene microneedle device with 1.00 mm spacing arranged in a hexagonal pattern.

Figure **7.52** shows the displacement components plotted versus normalized load of the measured data shown in Figure **7.51**. The figure shows that at the measured needle length, the base of the microneedle device begins compressing the rubber sample without further penetration as indicated by a change of slope. Within the region of interest, located below the measured needle length to the left of the vertical line, the penetration depth continues to increase at a nearly constant rate after the start of penetration. The effect of multiple needle deflection is negligible compared to the depth of penetration and

single needle deflection. The effect of the 1.00 mm distance between needle tips in a hexagonal pattern has a larger effect on total displacement compared to the square patterns. The depth of penetration for this pattern is calculated to be about 140 microns. Single needle deflection dominates the total displacement due to the large tip angle of 30 degrees that causes more material deflection than penetration.

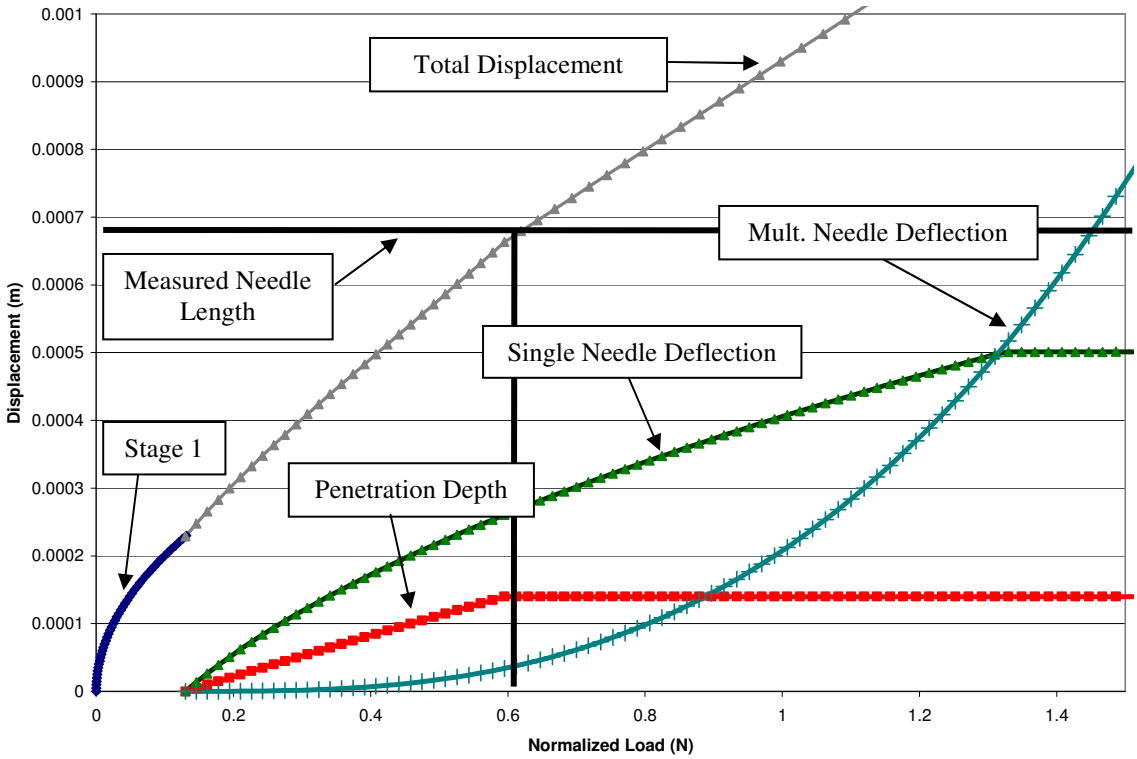


Figure **7.52**: Calculated displacement versus normalized force for each displacement component and the total displacement for a hexagonal polystyrene pattern with 1.00 mm spacing.

Figure **7.53** shows a comparison of the unadjusted analytical model plots for each of the tested polystyrene microneedle patterns. The plots show that there is little distinguishable difference between each of the three patterns until total displacement exceeds 700 microns where the patterns begin to diverge due to multiple needle

deflection that comes from pattern spacing differences. Varying needle lengths also differentiate the three patterns as shown in the sharp change in slope that occurs in the figure between 650 and 750 microns. The similarity of the three plots is due to the needle tips in all patterns having similar geometries. The biggest difference between the patterns comes from the deflection of the rubber from the effect of multiple needle deflection described earlier in the section of the chapter entitled *Multiple Needle Deflection*. The 1.00 mm patterns experience less total displacement than the 1.50 mm pattern but also have less calculated needle penetration.

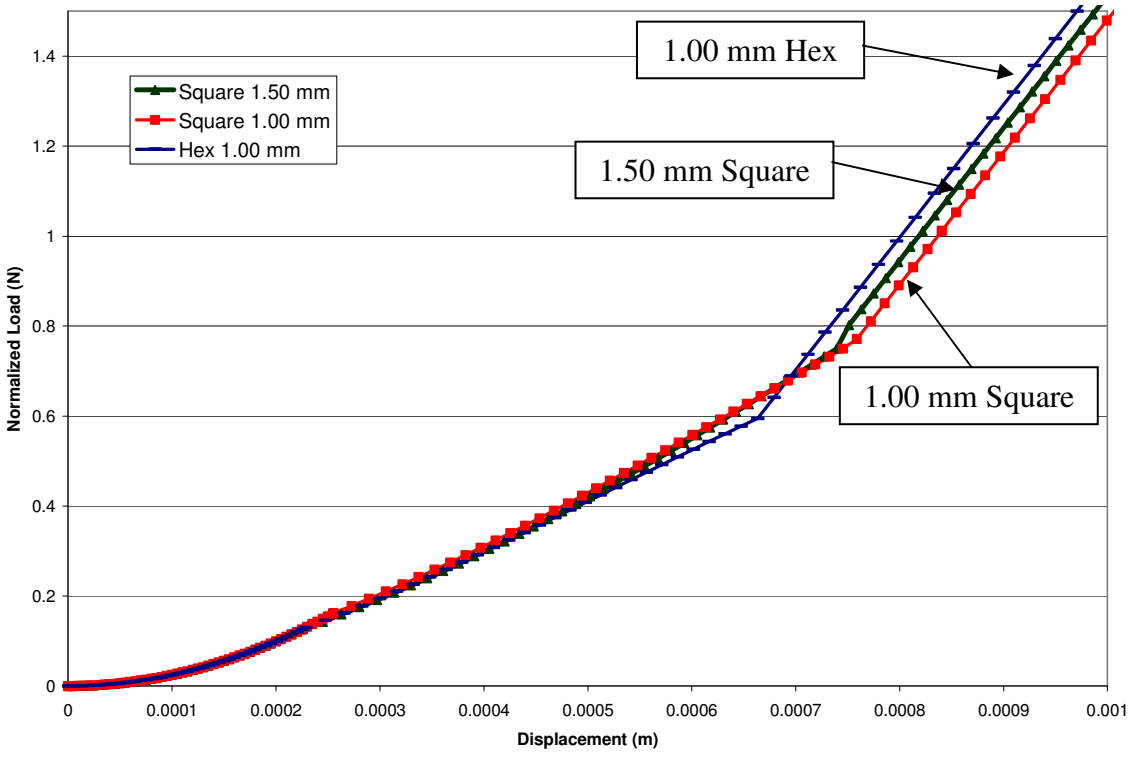


Figure **7.53**: Normalized load versus displacement plot for the analytical model of each tested polystyrene microneedle device.

Figure **7.54** shows the length adjusted plot for each polystyrene microneedle device. This figure shows how each calculated data set is adjusted with the addition of random normal length variation compared to the unadjusted data in Figure **7.53**. The adjusted data intensify the differences between each pattern. The data show that for displacements less than 400 microns, there is little difference between the patterns. The largest differentiator between each pattern is the effect of multiple needle displacement.

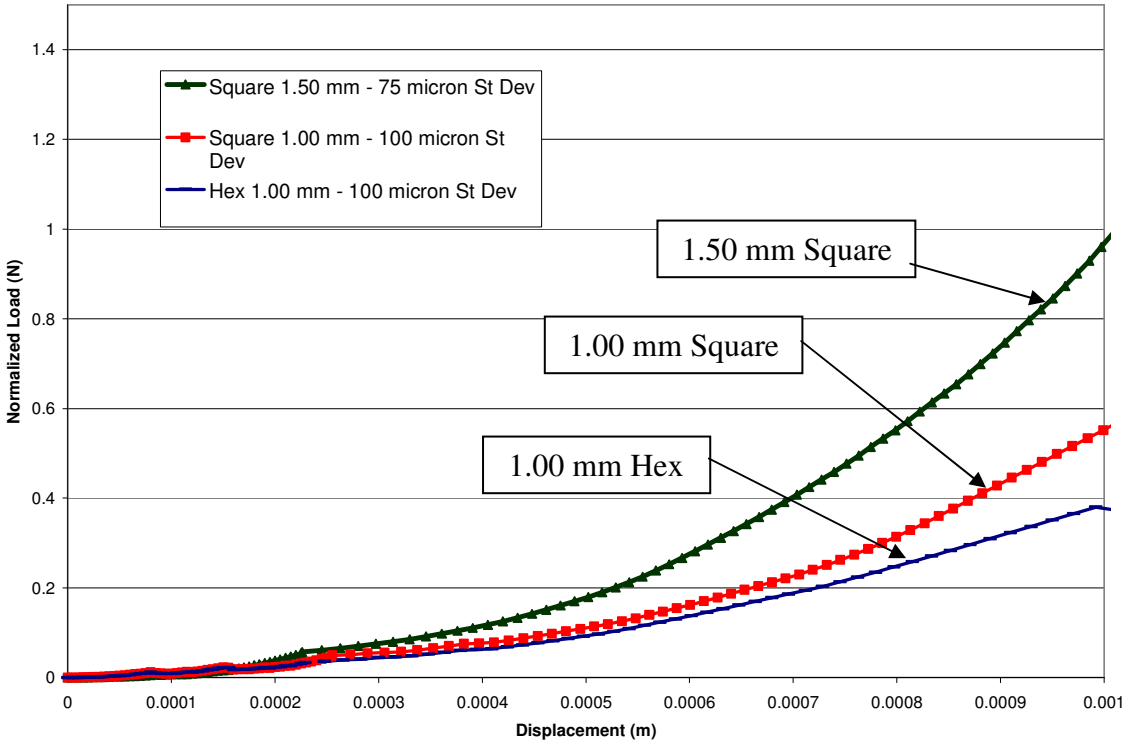


Figure **7.54**: Normalized load versus displacement plot for the length-adjusted calculated model of each tested polystyrene microneedle device.

Analysis of the polystyrene microneedle device data shows that the needle length-adjusted analytical data compare well with the measured data. The figures in this section show that the measured and length-adjusted calculated data correlate with R-squared

values greater than 90% in all cases. The errors in the measured data likely come from the skew of the test fixture during testing and variations in needle length and tip radii. These errors can show up as an averaging of multiple penetration events and act to flatten the shape of the measured data. Both length deviation and test fixture skew will have the same effect that is accounted for in the calculated length-adjusted data.

Figure **7.53** shows that the calculated model reflects that longer needles allow for deeper needle penetration as shown by the change in slope that comes from the microneedle device's base compressing the rubber sample. The change in slope that comes from compression of the rubber sample by the microneedle base is reflected in both the calculated and measured plots at similar displacements.

The effect of multiple needle deflection is small compared to the penetration and single needle deflection components of total displacement. The effect of multiple needle displacement comes from the closely spaced needles acting as a solid indenter. However, the needles are still far enough apart at lengths ranging from about 600 to 740 microns that each individual needle has a force versus displacement response similar to a single needle and the added multiple needle displacement has little effect. The fast rise in the slope of multiple needle deflection after the measured needle lengths in Figures **7.46**, **7.50**, and **7.52** indicates that multiple needle deflection would be more significant for longer needle lengths of the same geometry. Figure **7.53** compares the unadjusted calculated data for the three polystyrene patterns and shows a small difference in the 1.00 mm hexagonal pattern versus the two 1.50 mm patterns. This is reflective of the small difference in the multiple needle deflections. The length-adjusted calculated data provide

good capacity to predict average load versus displacement for polystyrene microneedle devices.

### *Vectra A130 Liquid Crystal Polymer Microneedle Analysis*

Figure **7.55** shows plots for normalized load versus displacement for measured data from Figure **6.37** and analytical data for the 100-needle square spacing pattern with 1.00 mm spacing between needles. Unadjusted calculated and random needle length-adjusted calculated data sets are plotted for comparison to the measured data. The needles on this device are 738 microns in length. The increase in slope at the measured needle length comes from the compression of the rubber section by the base of the microneedle device. The difference between the measured and calculated plots comes from measurement error as shown in Figure **7.24** and small variations in needle lengths. A statistical comparison between the calculated random-length variation data with a standard deviation for needle length of 100 microns and the measured data shows an R-squared value of 0.9237.

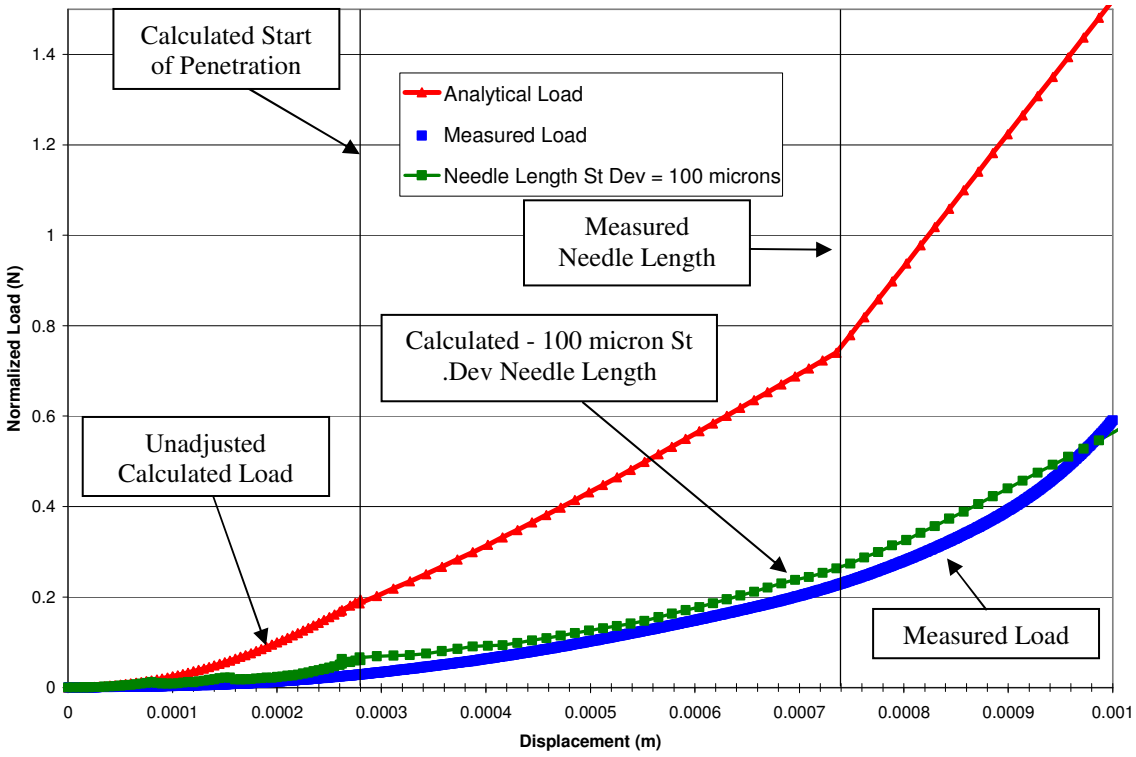


Figure **7.55**: Normalized load versus displacement for Vectra A130 LCP microneedle device with 1.00 mm spacing arranged in a square pattern.

Figure **7.56** shows the displacement components plotted versus normalized load of the measured data shown in Figure **7.55**. The figure shows that at the measured needle length, the base of the microneedle device begins compressing the rubber sample without further penetration as indicated by a change of slope. Within the region of interest, located below the measured needle length to the left of the vertical line, the penetration depth continues to increase at a nearly constant rate after the start of penetration. The effect of multiple needle deflection is negligible compared to the depth of penetration and single needle deflection. The effect of the 1.00 mm distance between needle tips in the square pattern has a nearly negligible impact on total displacement. The depth of

penetration for this pattern is shown to be about 180 microns. Single needle deflection dominates the total displacement due to the large tip angle of 30 degrees that causes more material deflection than penetration. Smaller tip radii and smaller tip angles would decrease single needle deflection and increase penetration depth as ratios of total displacement.

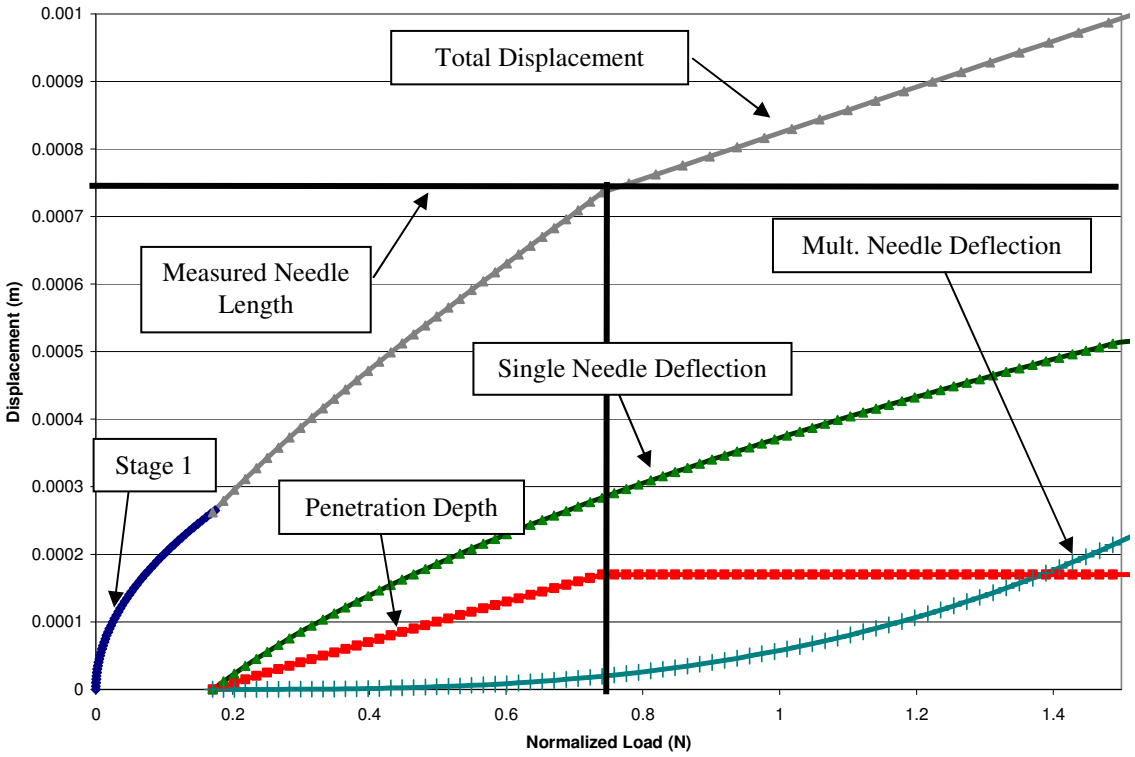


Figure **7.56**: Calculated displacement versus normalized force for each displacement component and the total displacement for a square Vectra A130 LCP pattern with 1.00 mm spacing.

Figure **7.57** shows plots for normalized load versus displacement for measured data from Figure **6.37** and analytical data for the 100-needle square spacing pattern with 1.00 mm spacing between needles. Unadjusted calculated and random needle length-adjusted calculated data sets are plotted for comparison to the measured data. The

average needle length on this device is 732 microns. The increase in slope at the measured needle length comes from the compression of the rubber section by the base of the microneedle device. The difference between the measured and calculated plots comes from measurement error as shown in Figure **7.24** and small variations in needle lengths. A statistical comparison between the calculated random-length variation data with a standard deviation for needle length of 100 microns and the measured data shows an R-squared value of 0.9667.

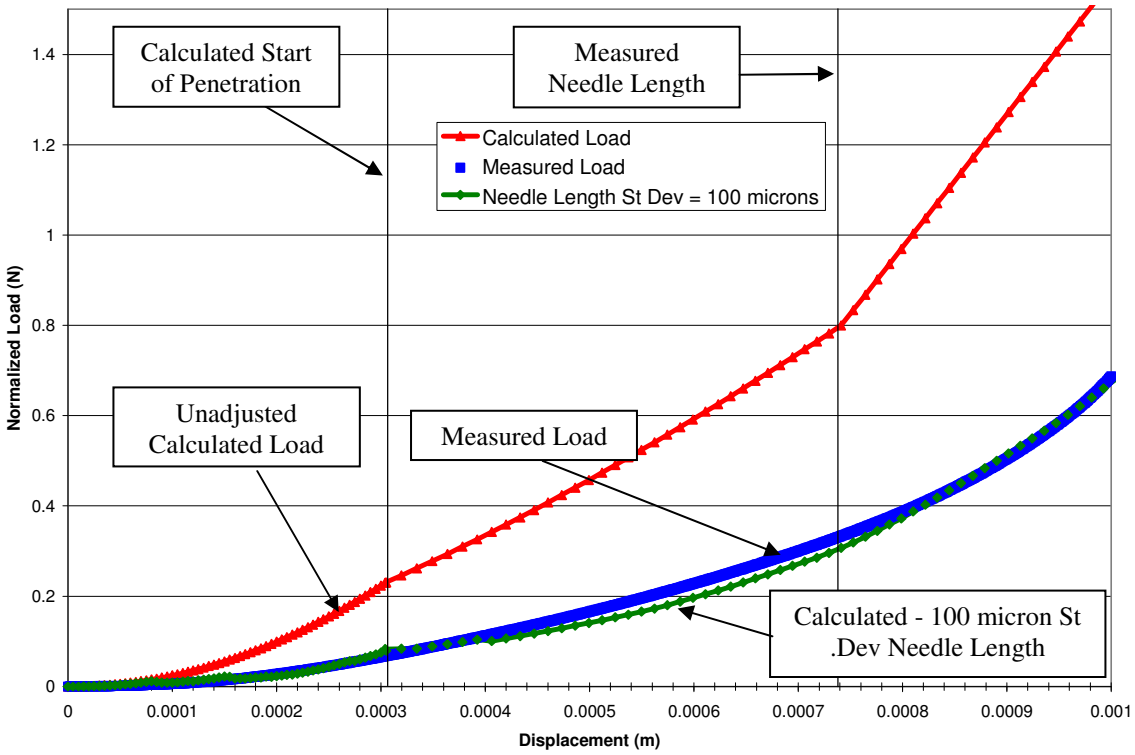


Figure **7.57**: Normalized load versus displacement for Vectra A130 LCP microneedle device with 1.50 mm spacing arranged in a square pattern.

Figure **7.58** shows the displacement components plotted versus normalized load of the measured data shown in Figure **7.57**. The figure shows that at the measured needle

length, the base of the microneedle device begins compressing the rubber sample without further penetration as indicated by a change of slope. Within the region of interest, located below the measured needle length to the left of the vertical line, the penetration depth continues to increase at a nearly constant rate after the start of penetration. The effect of multiple needle deflection is negligible compared to the depth of penetration and single needle deflection. The effect of the 1.50 mm distance between needle tips in the square pattern has a smaller impact on total displacement compared to the 1.00 mm square pattern. The depth of penetration for this pattern is shown to be about 170 microns. Single needle deflection dominates the total displacement due to the large tip angle of 30 degrees that causes more material deflection than penetration. Smaller tip radii and smaller tip angles would decrease single needle deflection and increase penetration depth as ratios of total displacement.

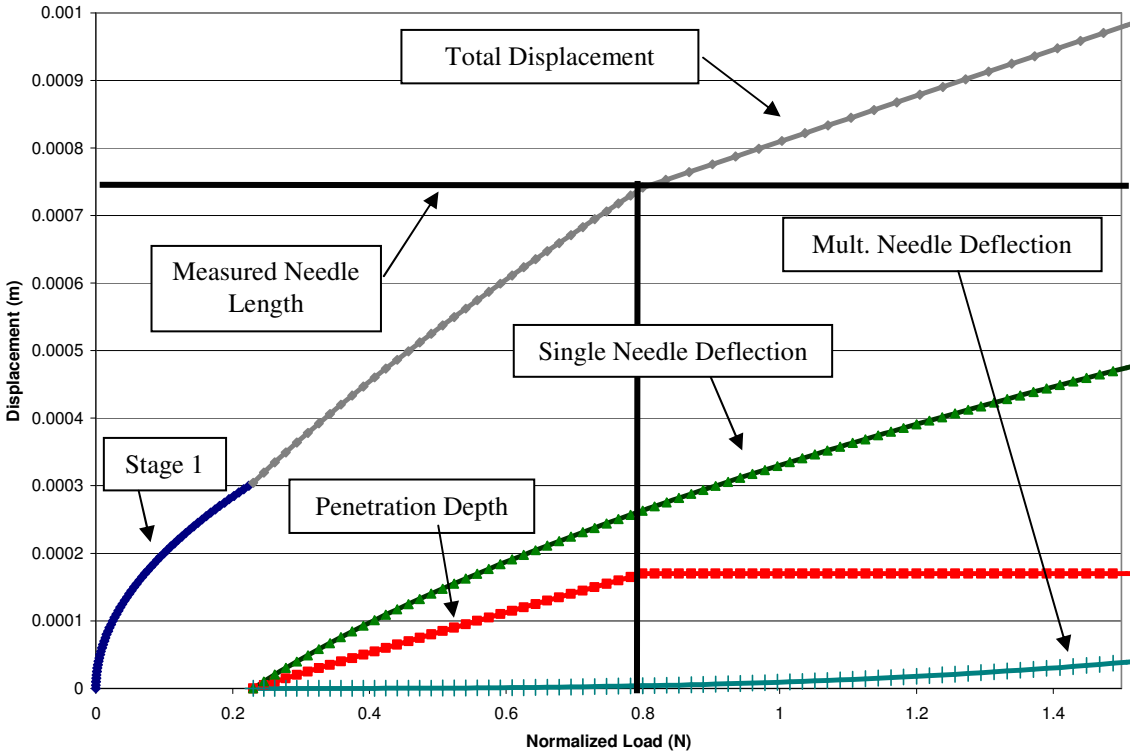


Figure **7.58**: Calculated displacement versus normalized force for each displacement component and the total displacement for a square Vectra A130 LCP pattern with 1.50 mm spacing.

Figure **7.59** shows plots for normalized load versus displacement for measured data from Figure **6.37** and analytical data for the 91-needle hexagonal spacing pattern with 1.00 mm spacing between needles. Unadjusted calculated and random needle length-adjusted calculated data sets are plotted for comparison to the measured data. The average needle length on this device is 656 microns. The increase in slope at the measured needle length comes from the compression of the rubber section by the base of the microneedle device. The difference between the measured and calculated plots comes from measurement error as shown in Figure **7.24** and small variations in needle lengths. A statistical comparison between the calculated random-length variation data

with a standard deviation for needle length of 75 microns and the measured data shows an R-squared value of 0.9896.

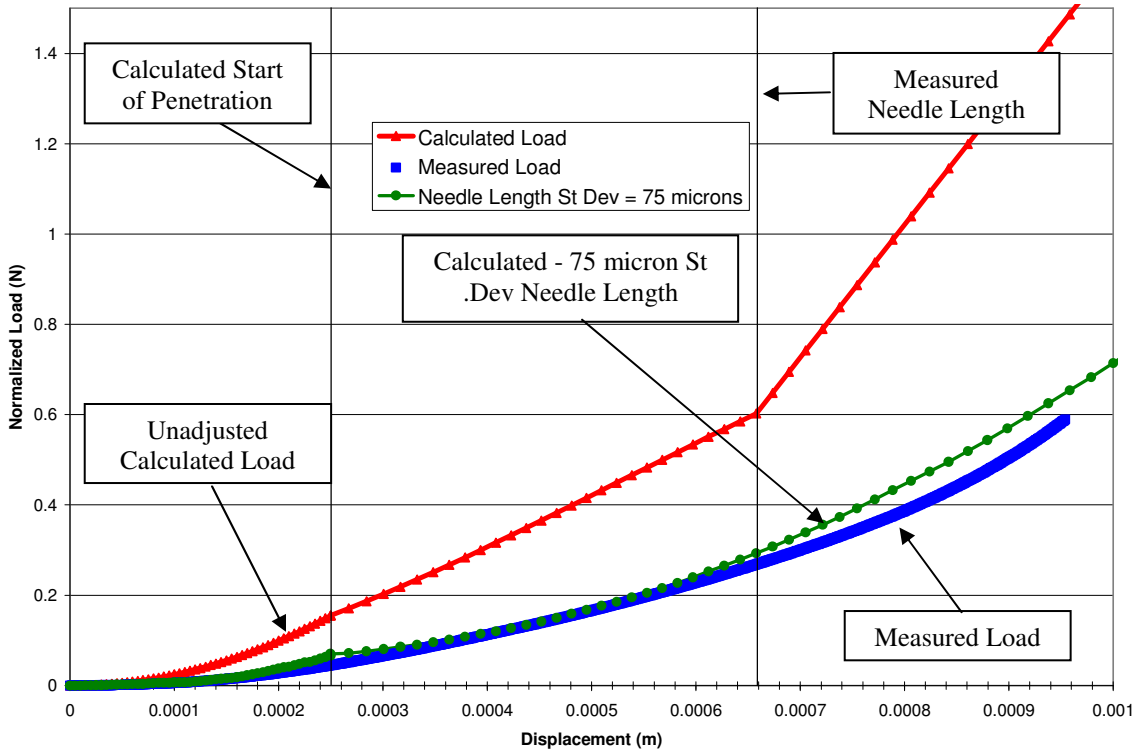


Figure **7.59**: Normalized load versus displacement for Vectra A130 LCP microneedle device with 1.00 mm spacing arranged in a hexagonal pattern.

Figure **7.60** shows the displacement components plotted versus normalized load of the measured data shown in Figure **7.59**. The figure shows that at the measured needle length, the base of the microneedle device begins compressing the rubber sample without further penetration as indicated by a change of slope. Within the region of interest, located below the measured needle length to the left of the vertical line, the penetration depth continues to increase at a nearly constant rate after the start of penetration. The effect of multiple needle deflection is negligible compared to the depth of penetration and

single needle deflection. The effect of the 1.00 mm distance between needle tips in the hexagonal pattern has a larger impact on total displacement compared to the square patterns. The depth of penetration for this pattern is shown to be about 135 microns. Single needle deflection dominates the total displacement due to the large tip angle of 30 degrees that causes more deflection than penetration. Smaller tip radii and smaller tip angles would decrease single needle deflection and increase penetration depth as ratios of total displacement.

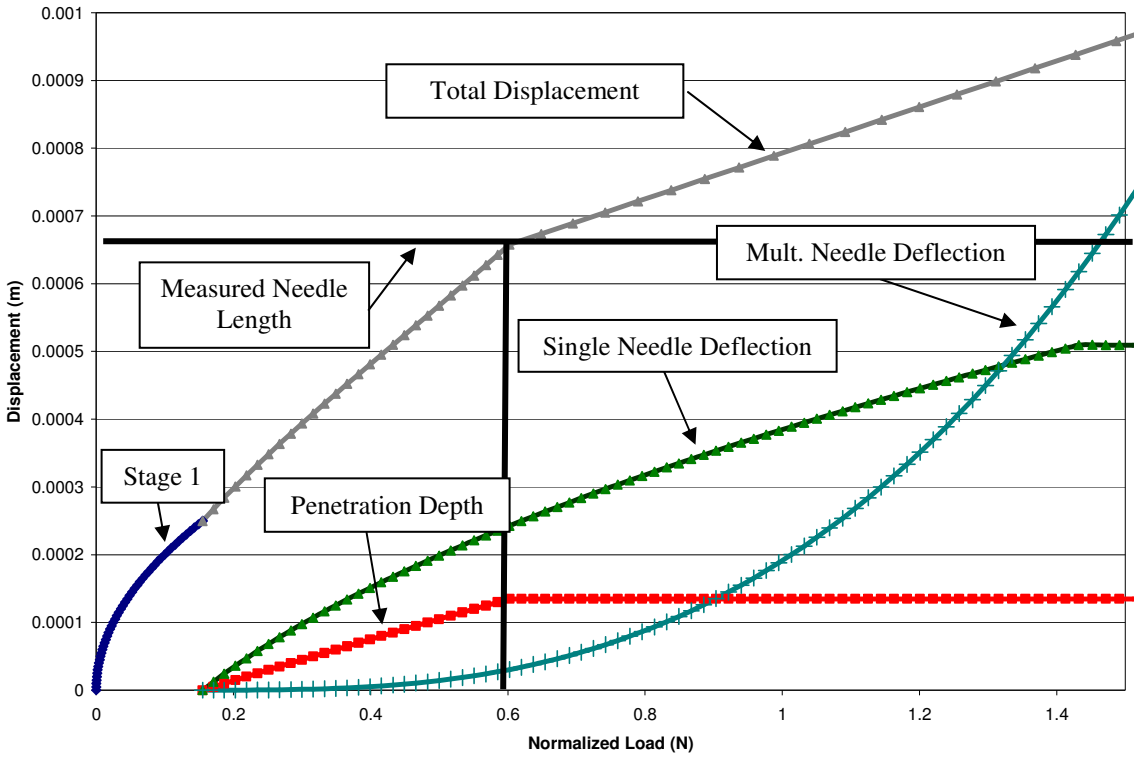


Figure **7.60**: Calculated displacement versus normalized force for each displacement component and the total displacement for a hexagonal Vectra A130 LCP pattern with 1.00 mm spacing.

Figure **7.61** shows plots for normalized load versus displacement for measured data from Figure **6.37** and analytical data for the 91-needle hexagonal spacing pattern with 1.50 mm spacing between needles. Unadjusted calculated and random needle length-adjusted calculated data sets are plotted for comparison to the measured data. The average needle length on this device is 594 microns. The increase in slope at the measured needle length comes from the compression of the rubber section by the base of the microneedle device. The difference between the measured and calculated plots comes from measurement error as shown in Figure **7.24** and small variations in needle lengths. A statistical comparison between the calculated random-length variation data with a standard deviation for needle length of 75 microns and the measured data shows an R-squared value of 0.9786.

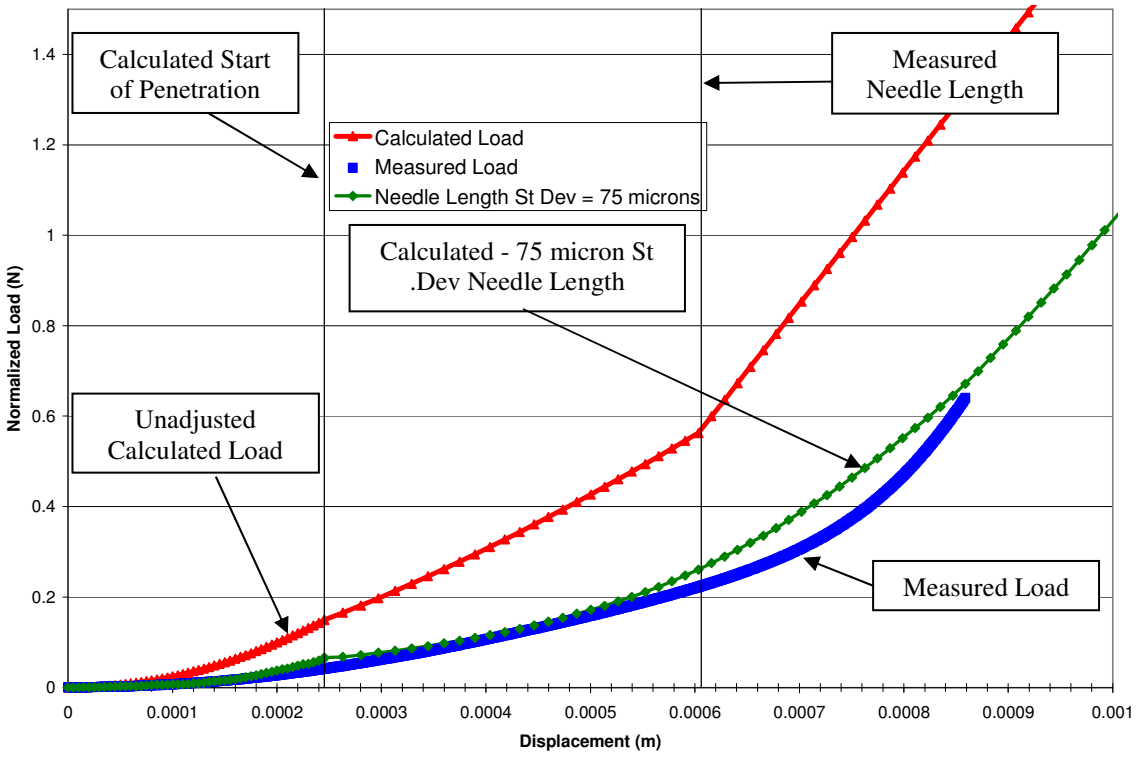


Figure **7.61**: Normalized load versus displacement for Vectra A130 LCP microneedle device with 1.50 mm spacing arranged in a hexagonal pattern.

Figure **7.62** shows the displacement components plotted versus normalized load of the measured data shown in Figure **7.61**. The figure shows that at the measured needle length, the base of the microneedle device begins compressing the rubber sample without further penetration as indicated by a change of slope. Within the region of interest, located below the measured needle length to the left of the vertical line, the penetration depth continues to increase at a nearly constant rate after the start of penetration. The effect of multiple needle deflection is negligible compared to the depth of penetration and single needle deflection. The effect of the 1.50 mm distance between needle tips in the hexagonal pattern has a negligible impact on total displacement. The depth of

penetration for this pattern is shown to be about 120 microns. Single needle deflection dominates the total displacement due to the large tip angle of 30 degrees that causes more deflection than penetration. Smaller tip radii and smaller tip angles would decrease single needle deflection and increase penetration depth as ratios of total displacement.

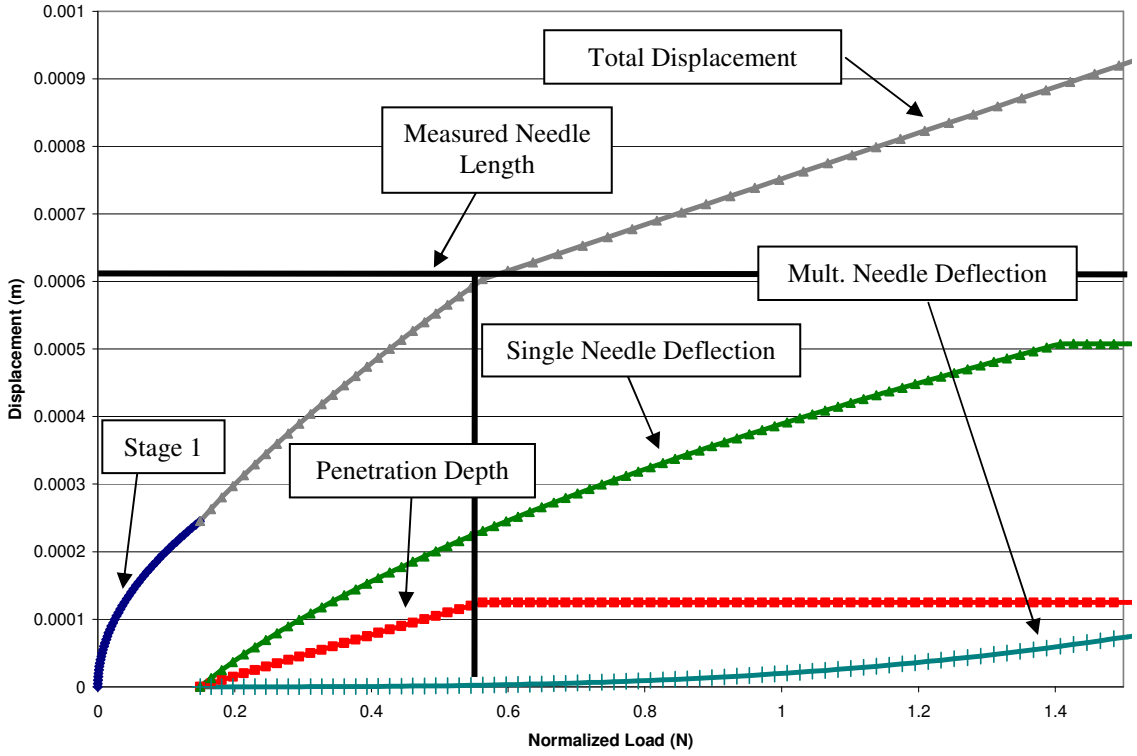


Figure **7.62**: Calculated displacement versus normalized force for each displacement component and the total displacement for a hexagonal Vectra A130 LCP pattern with 1.50 mm spacing.

Figure **7.63** shows a comparison of the analytical model plots for each of the tested Vectra A130 LCP microneedle patterns. The plots show that there is little distinguishable difference between each of the three patterns until total displacement exceeds 700 microns. This similarity is due to the needle tips in all patterns having similar geometries. The largest difference between the patterns comes from the

deflection of the rubber from the effect of multiple needle deflection described earlier in the chapter.

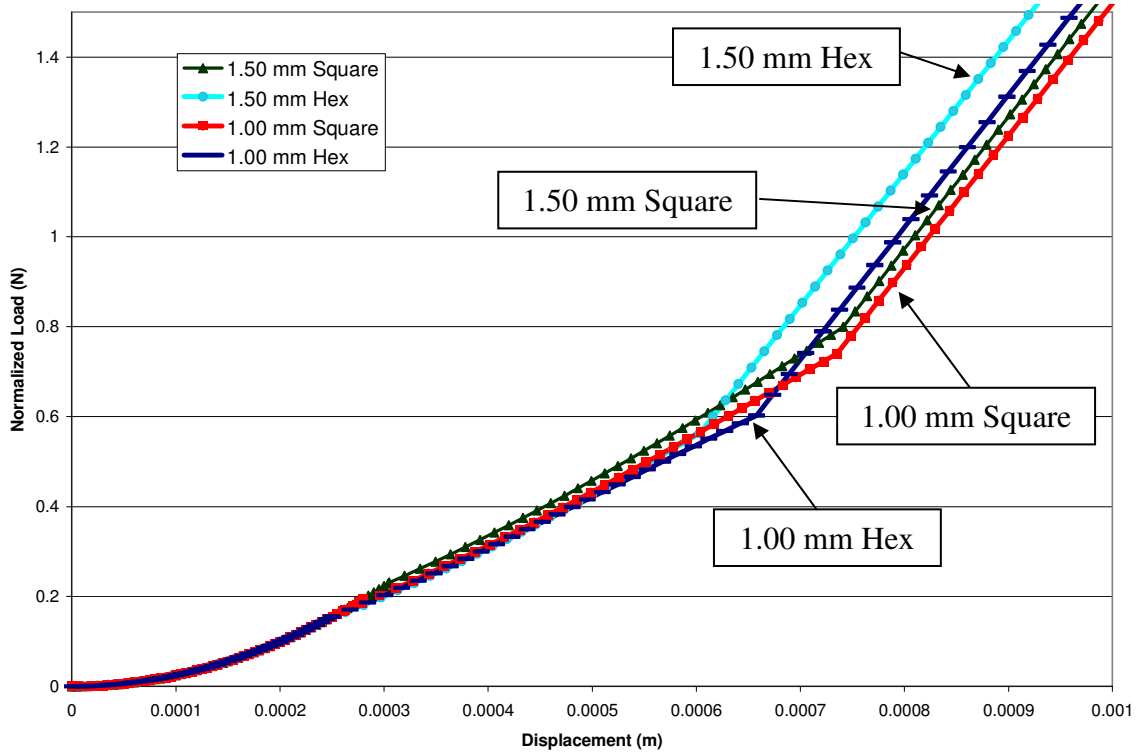


Figure **7.63**: Normalized load versus displacement plots for the analytical model of each tested Vectra A130 LCP microneedle device.

Figure **7.64** shows the length-adjusted plot for each LCP microneedle device. This figure shows how each calculated data set is adjusted with the addition of random normal length variation compared to the unadjusted data in Figure **7.53**. The adjusted data intensify the differences between each pattern. The data show that for displacements less than 400 microns, there is little difference between the patterns.

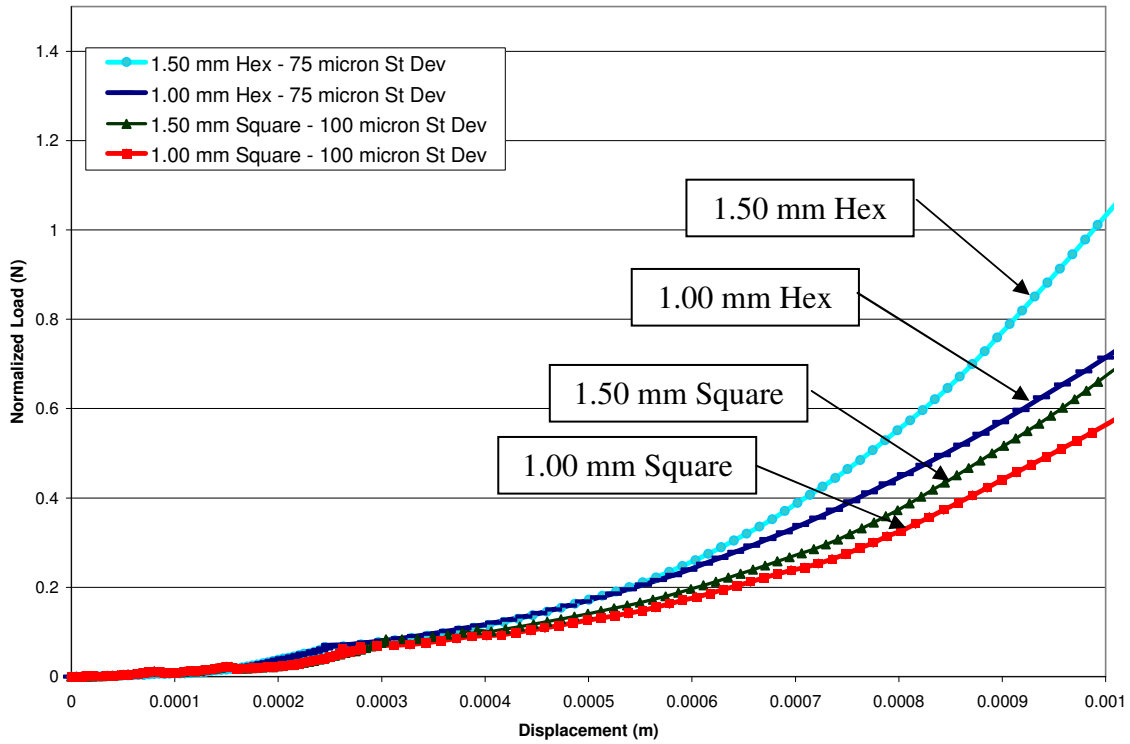


Figure **7.64**: Normalized load versus displacement plot for the length-adjusted calculated model of each tested LCP microneedle device.

Analysis of the LCP microneedle device data show that the analytical model compares well with the measured data. The figures in this section show that the measured and length-adjusted calculated data have correlations with R-squared values greater than 90% in all cases. The errors in the measured data likely come from the skew of the test fixture during testing and variations in needle length and tip radii. These errors can show up as an averaging of multiple penetration events and act to flatten the shape of the measured data. Both length deviation and test fixture skew will have the same effect that is accounted for in the calculated needle length-adjustment data.

Figure **7.63** shows that the calculated model reflects that longer needles allow for deeper needle penetration as shown by the change in slope that comes from the microneedle device's base compressing the rubber sample. The change in slope that comes from compression of the rubber sample by the microneedle base is reflected in both the calculated and measured plots at similar displacements.

The effect of multiple needle deflection is small compared to the penetration depth and single needle deflection components of total displacement. The effect of multiple needle displacement comes from the closely spaced needles acting as a solid indenter. However, the needles are still far enough apart at lengths ranging from about 600 to 740 microns that each individual needle has a force versus displacement response similar to a single needle and the added multiple needle displacement has little effect. The fast rise in the slope of multiple needle deflection after the measured needle lengths in figures **7.56**, **7.58**, **7.60**, and **7.62** indicates that multiple needle deflection would be more significant for longer needle lengths of the same geometry. Figure **7.63** compares the calculated data for the four LCP patterns and shows a small difference between the 1.00 mm patterns and the 1.50 patterns. This is reflective of the small difference in the multiple needle deflections. The calculated data provide reasonably good capacity to predict load versus displacement for LCP microneedle devices.

### *IXEF Microneedle Analysis*

Figure **7.65** shows plots for normalized load versus displacement for measured data from Figure **6.36** and analytical data for the 100-needle square spacing pattern with

1.00 mm spacing between needles. Unadjusted calculated and random needle length-adjusted calculated data sets are plotted for comparison to the measured data. The average needle length on this device is 738 microns. The increase in slope at the measured needle length comes from the compression of the rubber section by the base of the microneedle device. Much of the difference between the measured and calculated plots comes from measurement error as shown in Figure **7.24** and small variations in needle lengths. A statistical comparison between the calculated random-length variation data with a standard deviation for needle length of 100 microns and the measured data shows an R-squared value of 0.9494.

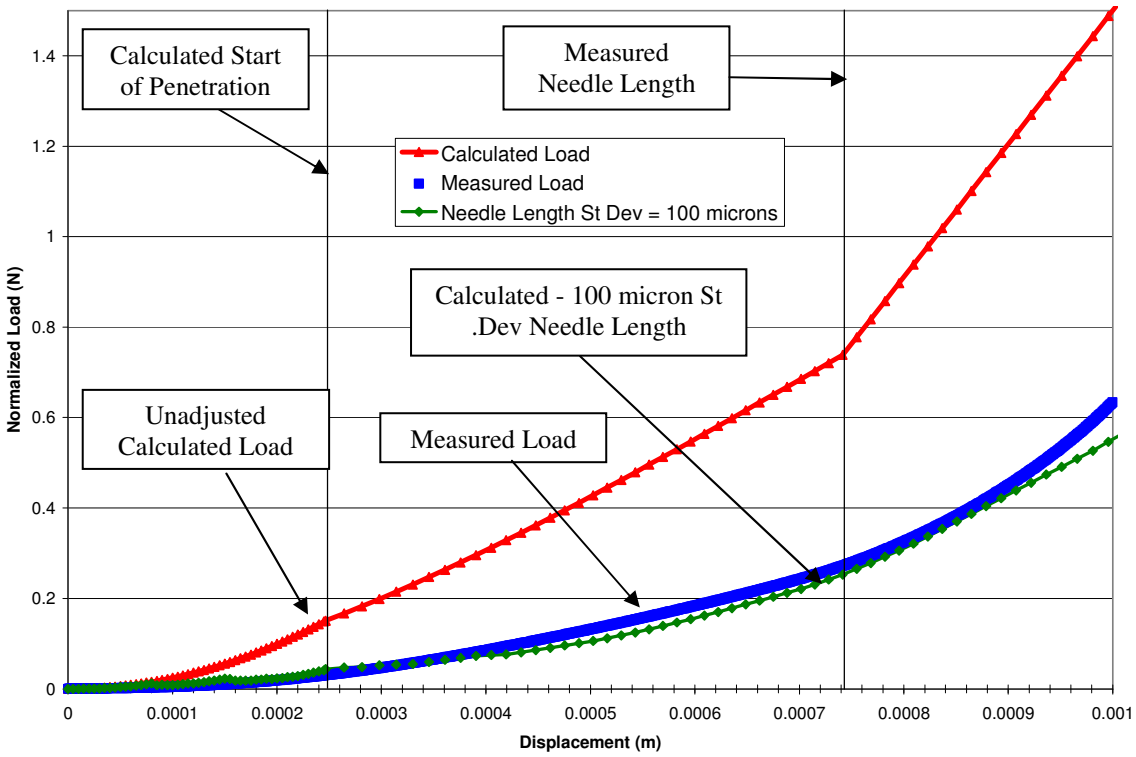


Figure **7.65**: Normalized load versus displacement for IXEF 1022 microneedle device with 1.00 mm spacing arranged in a square pattern.

Figure **7.66** shows the displacement components plotted versus normalized load of the measured data shown in Figure **7.65**. The figure shows that at the measured needle length, the base of the microneedle device begins compressing the rubber sample without further penetration as indicated by a change of slope. Within the region of interest, located below the measured needle length and to the left of the vertical line, the penetration depth continues to increase at a nearly constant rate after the start of penetration. The effect of multiple needle deflection is negligible compared to the depth of penetration and single needle deflection. The effect of the 1.00 mm distance between needle tips in the square pattern has only a small impact on total displacement. The depth of penetration for this pattern is shown to be about 180 microns. Single needle deflection dominates the total displacement due to the large tip angle of 30 degrees that causes more deflection than penetration. Smaller tip radii and smaller tip angles would decrease single needle deflection and increase penetration depth as ratios of total displacement.

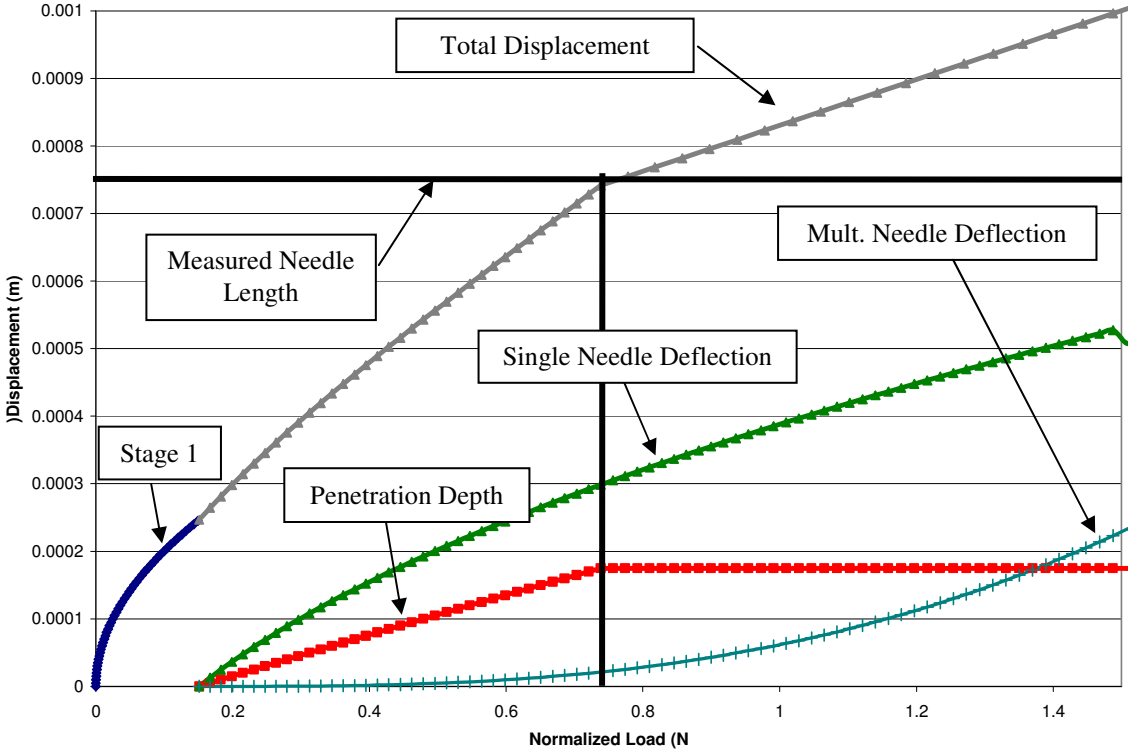


Figure **7.66**: Calculated displacement versus normalized force for each displacement component and the total displacement for a square IXEF 1022 pattern with 1.00 mm spacing.

Figure **7.67** shows plots for normalized load versus displacement for measured data from Figure **6.36** and analytical data for the 100-needle square spacing pattern with 1.50 mm spacing between needles. Unadjusted calculated and random needle length-adjusted calculated data sets are plotted for comparison to the measured data. The average needle length on this device is 728 microns. The increase in slope at the measured needle length comes from the compression of the rubber section by the base of the microneedle device. The difference between the measured and calculated plots comes from measurement error as shown in Figure **7.24** and small variations in needle lengths. A statistical comparison between the calculated random-length variation data

with a standard deviation for needle length of 100 microns and the measured data shows an R-squared value of 0.9312.

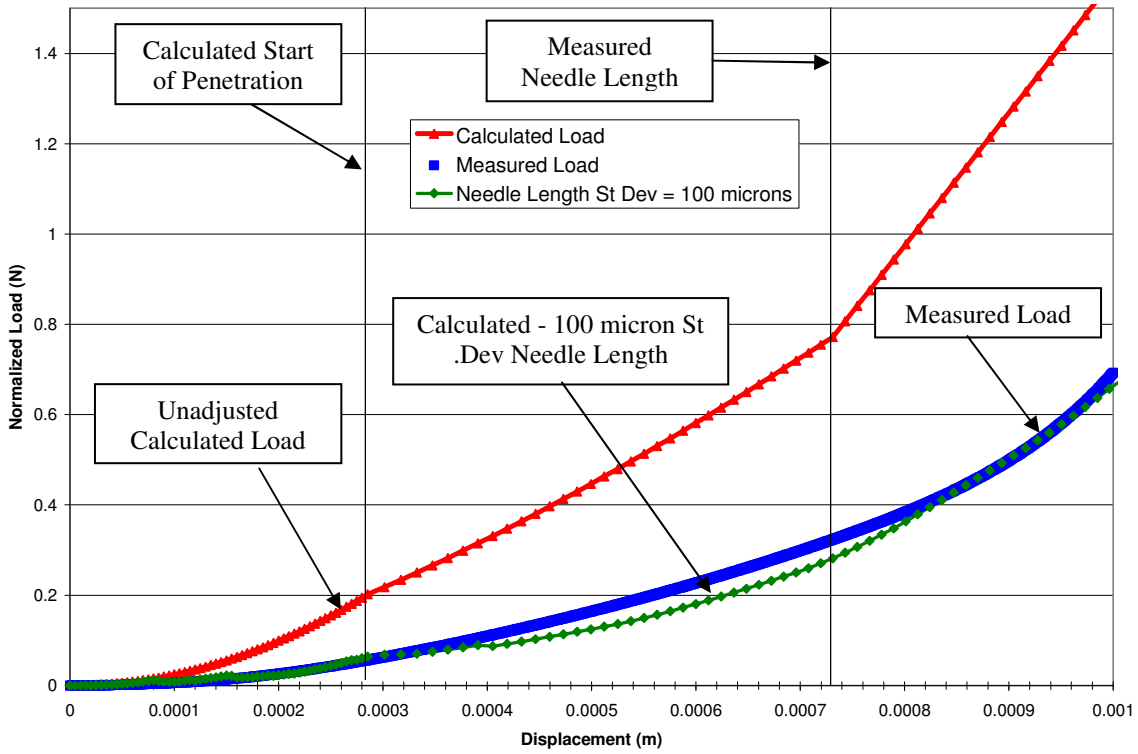


Figure **7.67**: Normalized load versus displacement for IXEF 1022 microneedle device with 1.50 mm spacing arranged in a square pattern.

Figure **7.68** shows the displacement components plotted versus normalized load of the measured data shown in Figure **7.67**. The figure shows that at the measured needle length, the base of the microneedle device begins compressing the rubber sample without further penetration as indicated by a change of slope. Within the region of interest, located below the measured needle length and to the left of the vertical line, the penetration depth continues to increase at a nearly constant rate after the start of penetration. The effect of multiple needle deflection is negligible compared to the depth

of penetration and single needle deflection. The effect of the 1.50 mm distance between needle tips in the square pattern has a negligible impact on total displacement. The depth of penetration for this pattern is shown to be about 170 microns. Single needle deflection dominates the total displacement due to the large tip angle of 30 degrees that causes more deflection than penetration. Smaller tip radii and smaller tip angles would decrease single needle deflection and increase penetration depth as ratios of total displacement.

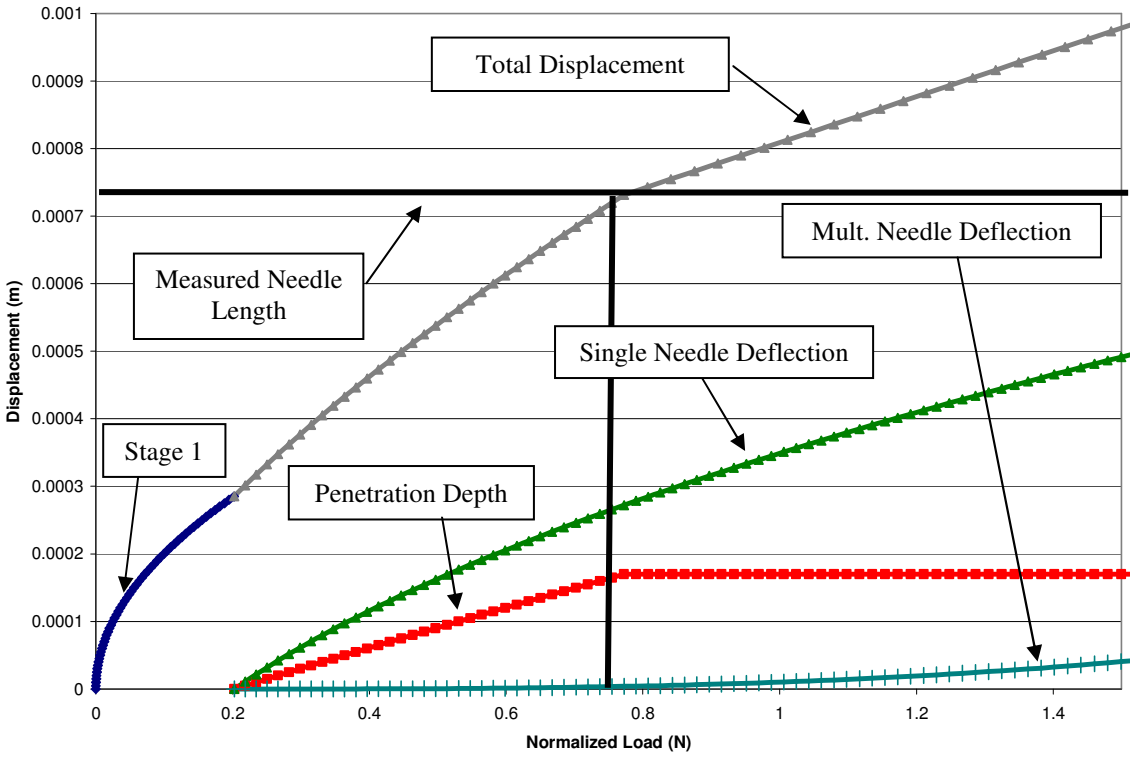


Figure **7.68**: Calculated displacement versus normalized force for each displacement component and the total displacement for a square IXEF 1022 pattern with 1.50 mm spacing.

Figure **7.69** shows plots for normalized load versus displacement for measured data from Figure **6.36** and analytical data for the 91-needle hexagonal spacing pattern with 1.00 mm spacing between needles. Unadjusted calculated and random needle

length-adjusted calculated data sets are plotted for comparison to the measured data. The average needle length on this device is 647 microns. The increase in slope at the measured needle length comes from the compression of the rubber section by the base of the microneedle device. The difference between the measured and calculated plots comes from measurement error as shown in Figure **7.24** and small variations in needle lengths. A statistical comparison between the calculated random-length variation data with a standard deviation for needle length of 75 microns and the measured data shows an R-squared value of 0.9470.

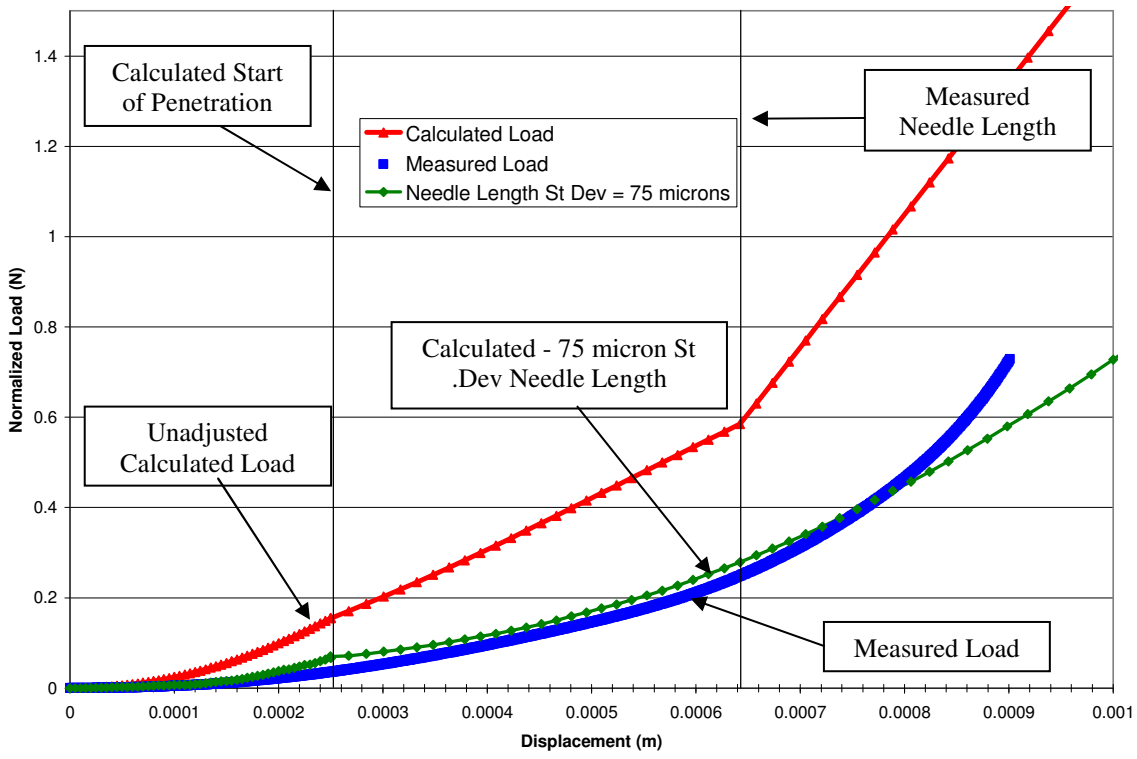


Figure **7.69**: Normalized load versus displacement for IXEF 1022 microneedle device with 1.00 mm spacing arranged in a hexagonal pattern.

Figure **7.70** shows the displacement components plotted versus normalized load of the measured data shown in Figure **7.69**. The figure shows that at the measured needle length, the base of the microneedle device begins compressing the rubber sample without further penetration as indicated by a change of slope. Within the region of interest, located below the measured needle length and to the left of the vertical line, the penetration depth continues to increase at a nearly constant rate after the start of penetration. The effect of multiple needle deflection is small compared to the depth of penetration and single needle deflection. The effect of the 1.00 mm distance between needle tips in the hexagonal pattern has a large impact on total displacement compared to the square pattern. The depth of penetration for this pattern is shown to be about 130 microns. Single needle deflection dominates the total displacement due to the large tip angle of 30 degrees that causes more deflection than penetration. Smaller tip radii and smaller tip angles would decrease single needle deflection and increase penetration depth as ratios of total displacement.

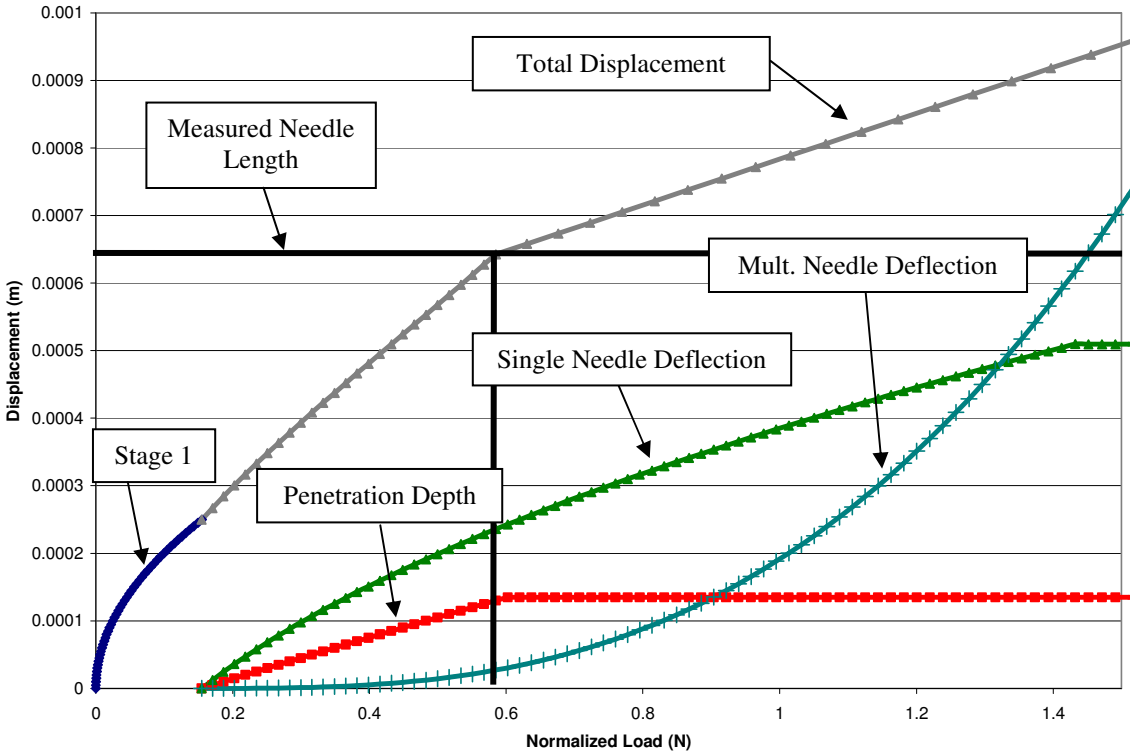


Figure **7.70**: Calculated displacement versus normalized force for each displacement component and the total displacement for a hexagonal IXEF 1022 pattern with 1.00 mm spacing.

Figure **7.71** shows plots for normalized load versus displacement for measured data from Figure **6.36** and analytical data for the 91-needle hexagonal spacing pattern with 1.50 mm spacing between needles. Unadjusted calculated and random needle length-adjusted calculated data sets are plotted for comparison to the measured data. The average needle length on this device is 595 microns. The increase in slope at the measured needle length comes from the compression of the rubber section by the base of the microneedle device. Much of the difference between the measured and calculated plots comes from measurement error as shown in Figure **7.24** and small variations in needle lengths. A statistical comparison between the calculated random-length variation

data with a standard deviation for needle length of 100 microns and the measured data shows an R-squared value of 0.9229.

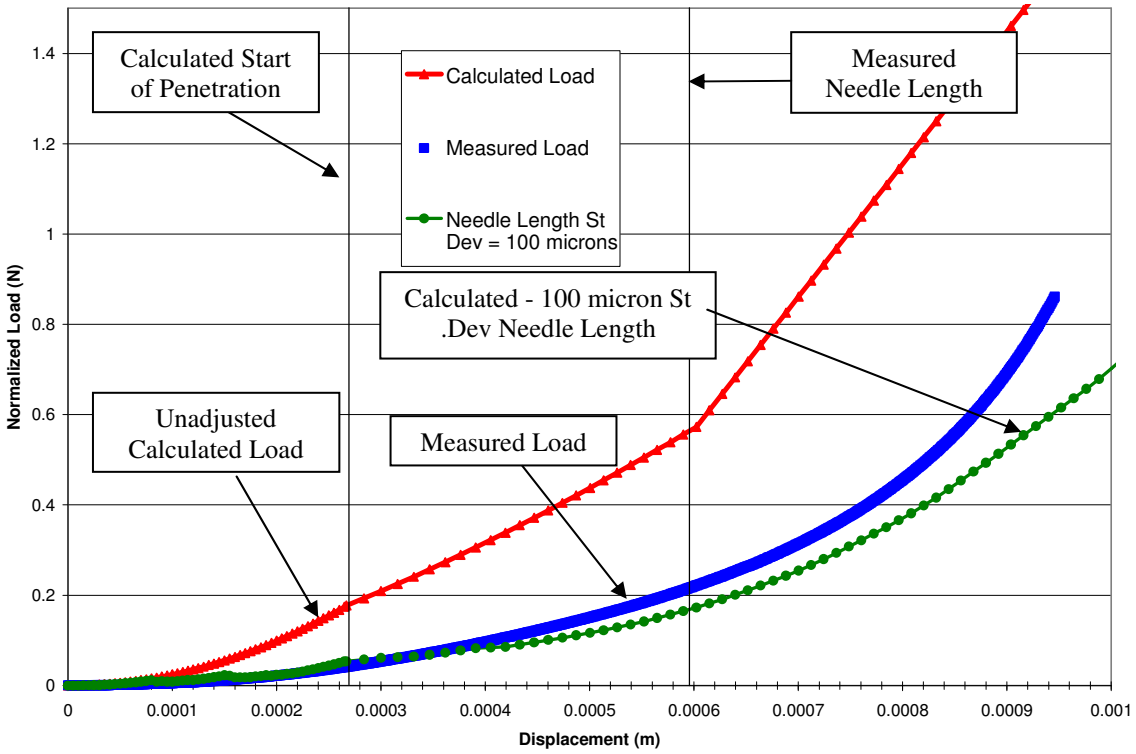


Figure **7.71**: Normalized load versus displacement for IXEF 1022 microneedle device with 1.50 mm spacing arranged in a hexagonal pattern.

Figure **7.72** shows the displacement components plotted versus normalized load of the measured data shown in Figure **7.71**. The figure shows that at the measured needle length, the base of the microneedle device begins compressing the rubber sample without further penetration as indicated by a change of slope. Within the region of interest, located below the measured needle length and to the left of the vertical line, the penetration depth continues to increase at a nearly constant rate after the start of penetration. The effect of multiple needle deflection is small compared to the depth of

penetration and single needle deflection. The effect of the 1.50 mm distance between needle tips in the hexagonal pattern only has a small impact on total displacement. The depth of penetration for this pattern is shown to be about 120 microns. Single needle deflection dominates the total displacement due to the large tip angle of 30 degrees that causes more deflection than penetration. Smaller tip radii and smaller tip angles would decrease single needle deflection and increase penetration depth as ratios of total displacement.

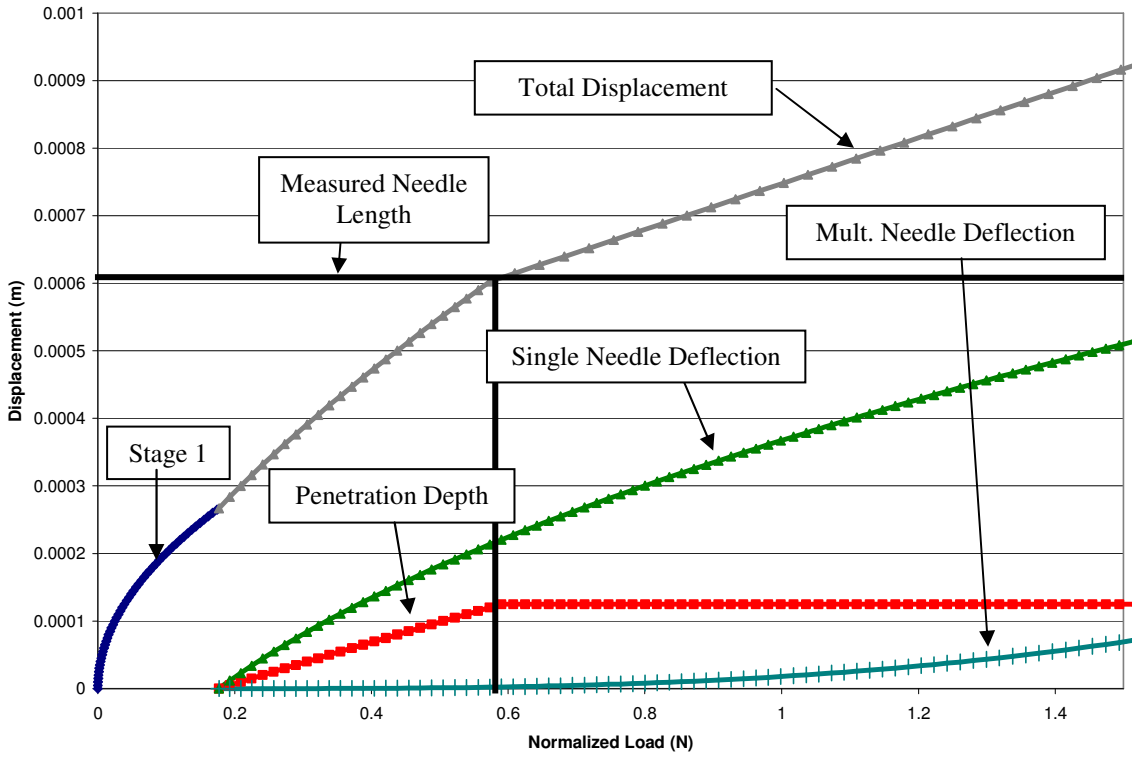


Figure **7.72**: Calculated displacement versus normalized force for each displacement component and the total displacement for a hexagonal IXEF 1022 pattern with 1.50 mm spacing.

Figure **7.73** shows a comparison of the analytical model plots for each of the tested IXEF 1022 microneedle patterns. The plots show that there is little distinguishable difference between each of the three patterns until total displacement exceeds 700 microns. This similarity is due to the needle tips in all patterns having similar geometries. The biggest difference between the patterns comes from the deflection of the rubber from the effect of multiple needle deflection described earlier in the chapter. The 1.00 mm patterns experience less total displacement than the 1.50 mm patterns but they also have less needle penetration at a given load.

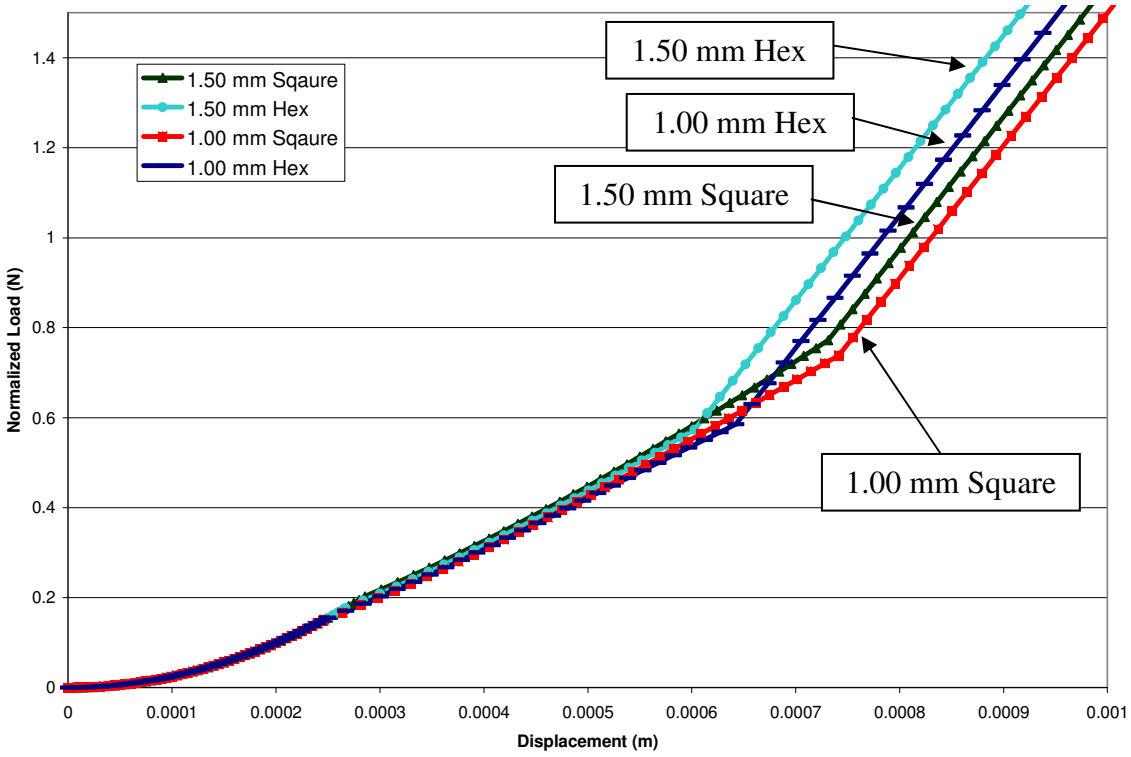


Figure **7.73**: Normalized load versus displacement plot for the analytical model of each tested IXEF 1022 microneedle device.

Figure **7.74** shows the length adjusted plot for each IXEF 1022 microneedle device. This figure shows how each calculated data set is adjusted with the addition of random normal length variation compared to the unadjusted data in Figure **7.53**. The adjusted data intensify the differences between each pattern. The data show that for displacements less than 400 microns, there is little difference between the patterns. The largest differentiator between each pattern is the effect of multiple needle displacement.

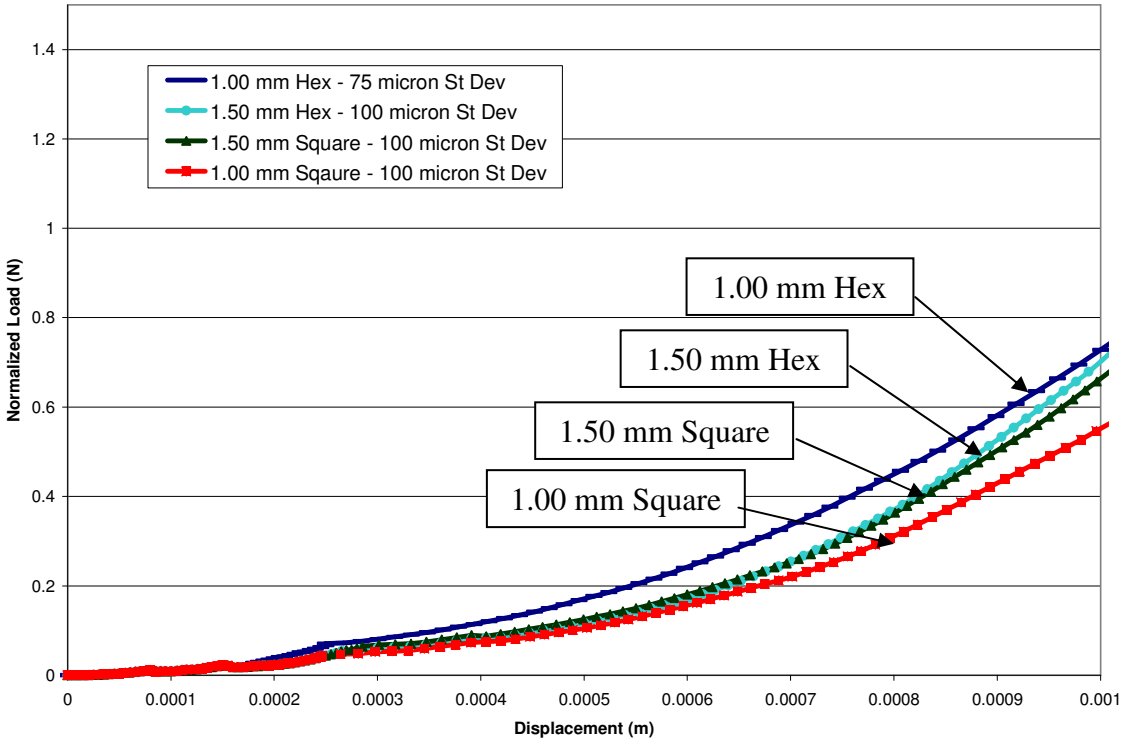


Figure **7.74**: Normalized load versus displacement plot for the length-adjusted calculated model of each tested IXEF microneedle device.

Analysis of the IXEF 1022 microneedle device data shows that the analytical model compares well with the measured data. The figures in this section show that the measured and length-adjusted calculated data have correlations with R-squared values

greater than 90% in all cases. The errors in the measured data likely come from the skew of the test fixture during testing and variations in needle length and tip radii. These errors can show up as an averaging of multiple penetration events and act to flatten the shape of the measured data. Both length deviation and test fixture skew will have the same effect that is accounted for in the calculated length-adjustment data.

Figure **7.73** shows that the calculated model reflects that longer needles allow for deeper needle penetration as shown by the change in slope that comes from the microneedle device's base compressing the rubber sample. The change in slope that comes from compression of the rubber sample by the microneedle base is reflected in both the calculated and measured plots at similar displacements.

The effect of multiple needle deflection is small compared to the penetration depth and single needle deflection components of total displacement. The effect of multiple needle displacement comes from the closely spaced needles acting as a solid indenter. However, the needles are still far enough apart at lengths ranging from about 600 to 740 microns that each individual needle has a force versus displacement response similar to a single needle and the added multiple needle displacement has little effect. The fast rise in the slope of multiple needle deflection after the measured needle lengths in figures **7.66**, **7.68**, **7.70**, and **7.72** indicates that multiple needle deflection would be more significant for longer needle lengths of the same geometry. Figure **7.73** compares the calculated data for the four IXEF 1022 patterns and shows a small difference between the 1.00 mm patterns and the 1.50 patterns. This is reflective of the small difference in the multiple needle deflections. The calculated data provide reasonably good capacity to predict load versus displacement for IXEF 1022 microneedle devices.

### *COC 5013 Microneedle Analysis*

Figure **7.75** shows plots for normalized load versus displacement for measured data from Figure **6.38** and analytical data for the 100-needle square spacing pattern with 1.00 mm spacing between needles. Unadjusted calculated and random needle length-adjusted calculated data sets are plotted for comparison to the measured data. The average needle length on this device is 744 microns. The increase in slope at the measured needle length comes from the compression of the rubber section by the base of the microneedle device. The difference between the measured and calculated plots comes from measurement error as shown in Figure **7.24** and small variations in needle lengths. A statistical comparison between the calculated random-length variation data with a standard deviation for needle length of 75 microns and the measured data shows an R-squared value of 0.9731.

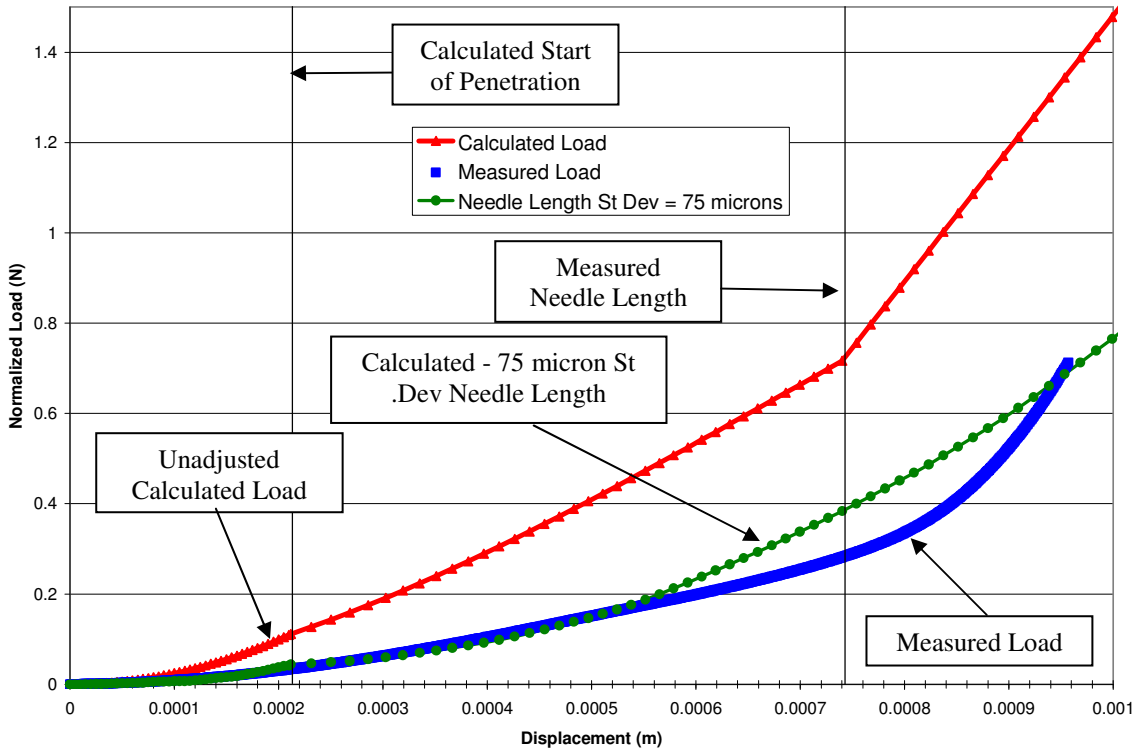


Figure **7.75**: Normalized load versus displacement for COC 5013 microneedle device with 1.00 mm spacing arranged in a square pattern.

Figure **7.76** shows the displacement components plotted versus normalized load of the measured data shown in Figure **7.75**. The figure shows that at the measured needle length, the base of the microneedle device begins compressing the rubber sample without further penetration as indicated by a change of slope. Within the region of interest, located below the measured needle length and to the left of the vertical line, the penetration depth continues to increase at a nearly constant rate after the start of penetration. The effect of multiple needle deflection is small compared to the depth of penetration and single needle deflection. The effect of the 1.00 mm distance between needle tips in the square pattern has a small impact on total displacement. The depth of

penetration for this pattern is shown to be about 200 microns. Single needle deflection dominates the total displacement due to the large tip angle of 30 degrees that causes more deflection than penetration. Smaller tip radii and smaller tip angles would decrease single needle deflection and increase penetration depth as ratios of total displacement.

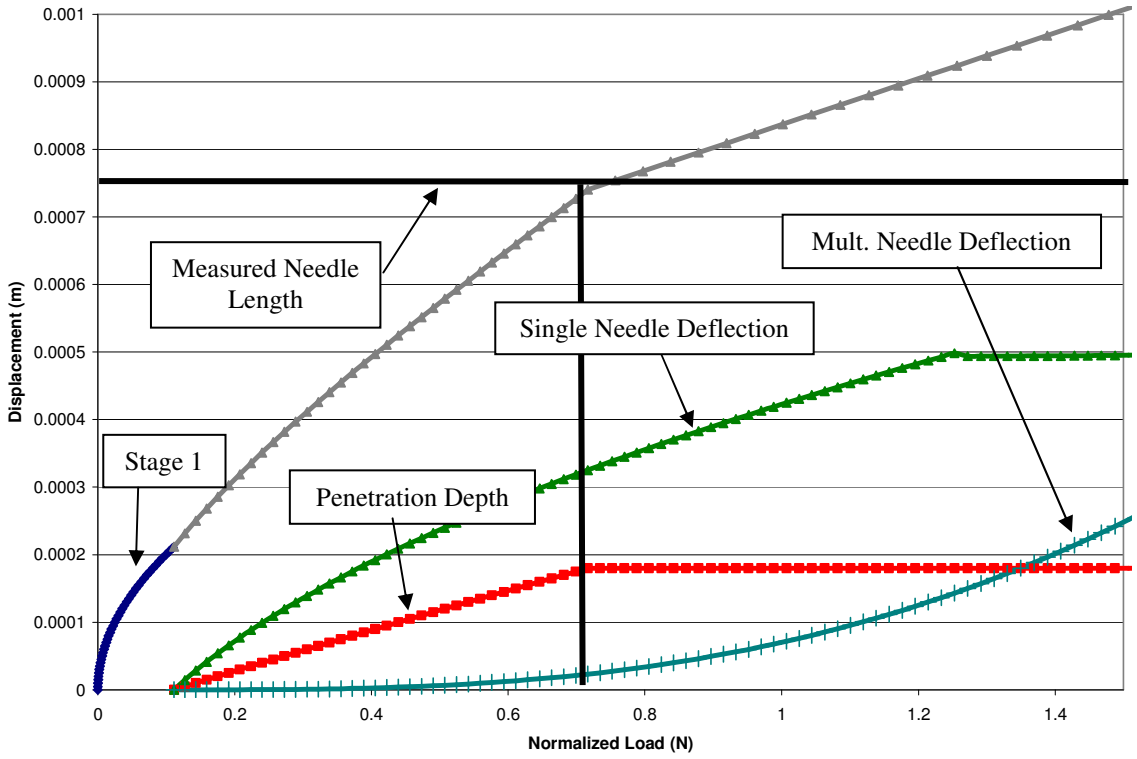


Figure **7.76**: Calculated displacement versus normalized force for each displacement component and the total displacement for a square COC 5013 pattern with 1.00 mm spacing.

Figure **7.77** shows plots for normalized load versus displacement for measured data from Figure **6.38** and analytical data for the 100-needle square spacing pattern with 1.50 mm spacing between needles. Unadjusted calculated and random needle length-adjusted calculated data sets are plotted for comparison to the measured data. The average needle length on this device is 732 microns. The increase in slope at the

measured needle length comes from the compression of the rubber section by the base of the microneedle device. The difference between the measured and calculated plots comes from measurement error as shown in Figure **7.24** and small variations in needle lengths. A statistical comparison between the calculated random-length variation data with a standard deviation for needle length of 75 microns and the measured data shows an R-squared value of 0.9890.

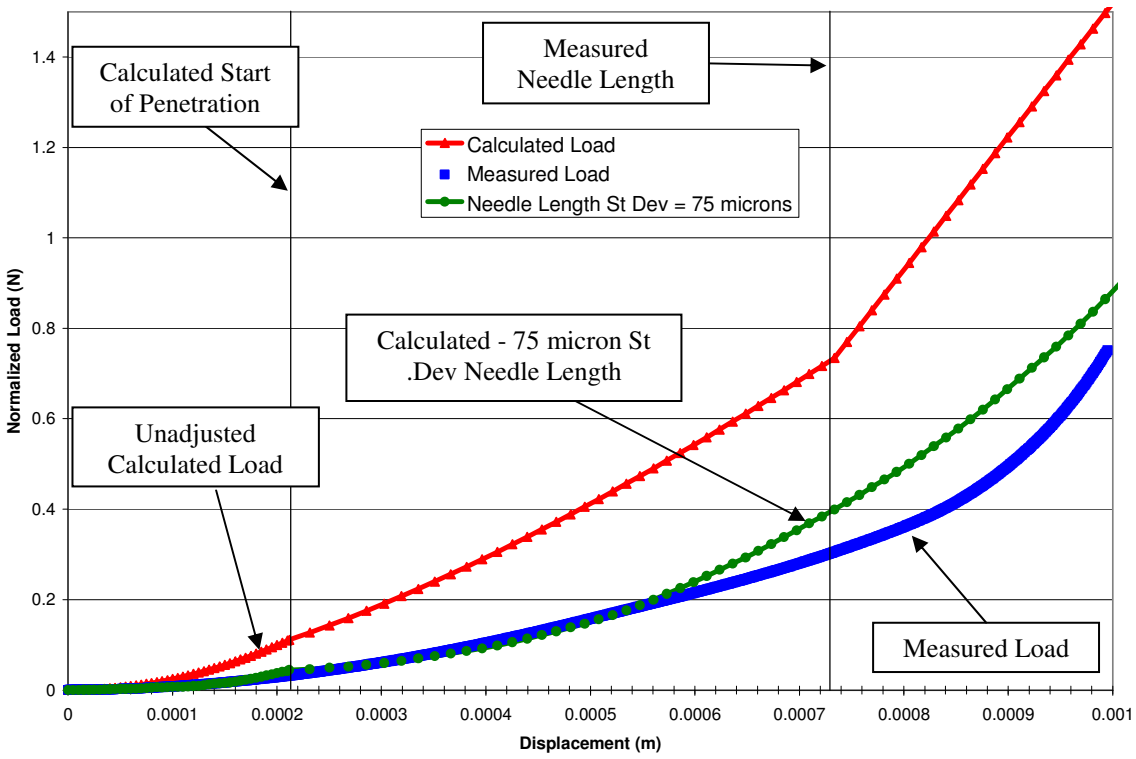


Figure **7.77**: Normalized load versus displacement for COC 5013 microneedle device with 1.50 mm spacing arranged in a square pattern.

Figure **7.78** shows the displacement components plotted versus normalized load of the measured data shown in Figure **7.77**. The figure shows that at the measured needle length, the base of the microneedle device begins compressing the rubber sample without

further penetration as indicated by a change of slope. Within the region of interest, located below the measured needle length and to the left of the vertical line, the penetration depth continues to increase at a nearly constant rate after the start of penetration. The effect of multiple needle deflection is small compared to the depth of penetration and single needle deflection. The effect of the 1.50 mm distance between needle tips in the square pattern only has a small impact on total displacement. The depth of penetration for this pattern is shown to be about 200 microns. Single needle deflection dominates the total displacement due to the large tip angle of 30 degrees that causes more deflection than penetration. Smaller tip radii and smaller tip angles would decrease single needle deflection and increase penetration depth as ratios of total displacement.

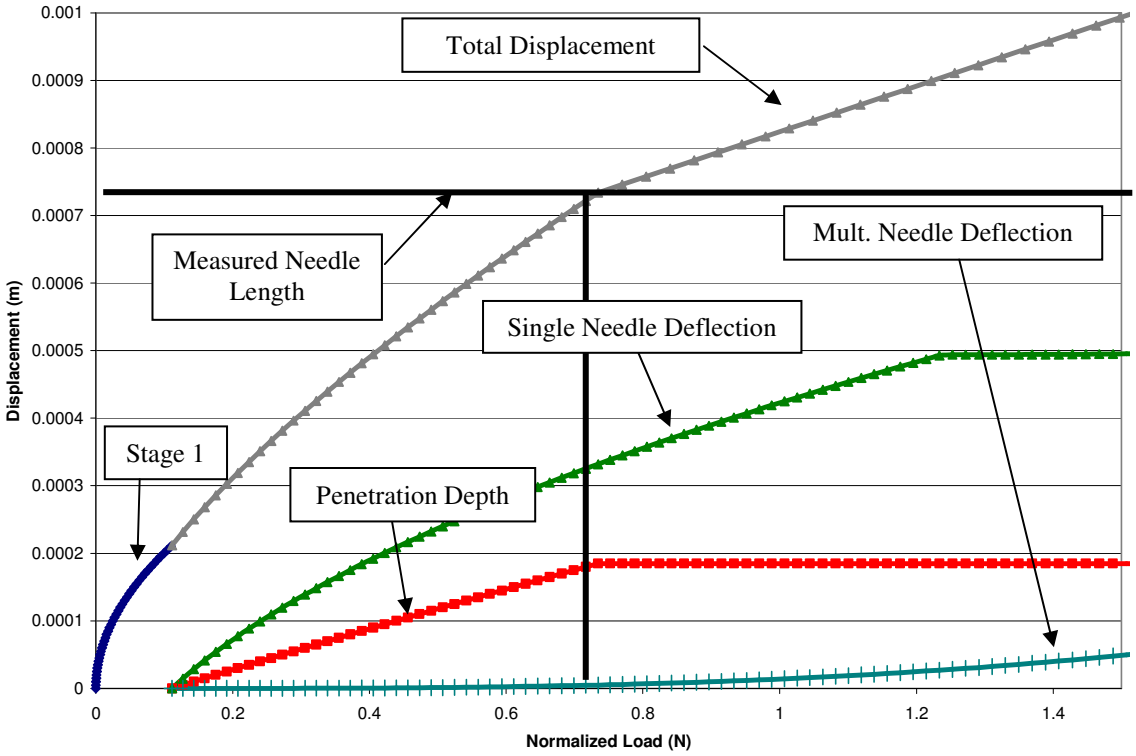


Figure **7.78**: Calculated displacement versus normalized force for each displacement component and the total displacement for a square COC 5013 pattern with 1.50 mm spacing.

Figure **7.79** shows plots for normalized load versus displacement for measured data from Figure **6.38** and analytical data for the 91-needle hexagonal spacing pattern with 1.00 mm spacing between needles. Unadjusted calculated and random needle length-adjusted calculated data sets are plotted for comparison to the measured data. The average needle length on this device is 656 microns. The increase in slope at the measured needle length comes from the compression of the rubber section by the base of the microneedle device. The difference between the measured and calculated plots comes from measurement error as shown in Figure **7.24** and small variations in needle lengths. A statistical comparison between the calculated random-length variation data

with a standard deviation for needle length of 75 microns and the measured data shows an R-squared value of 0.9485.

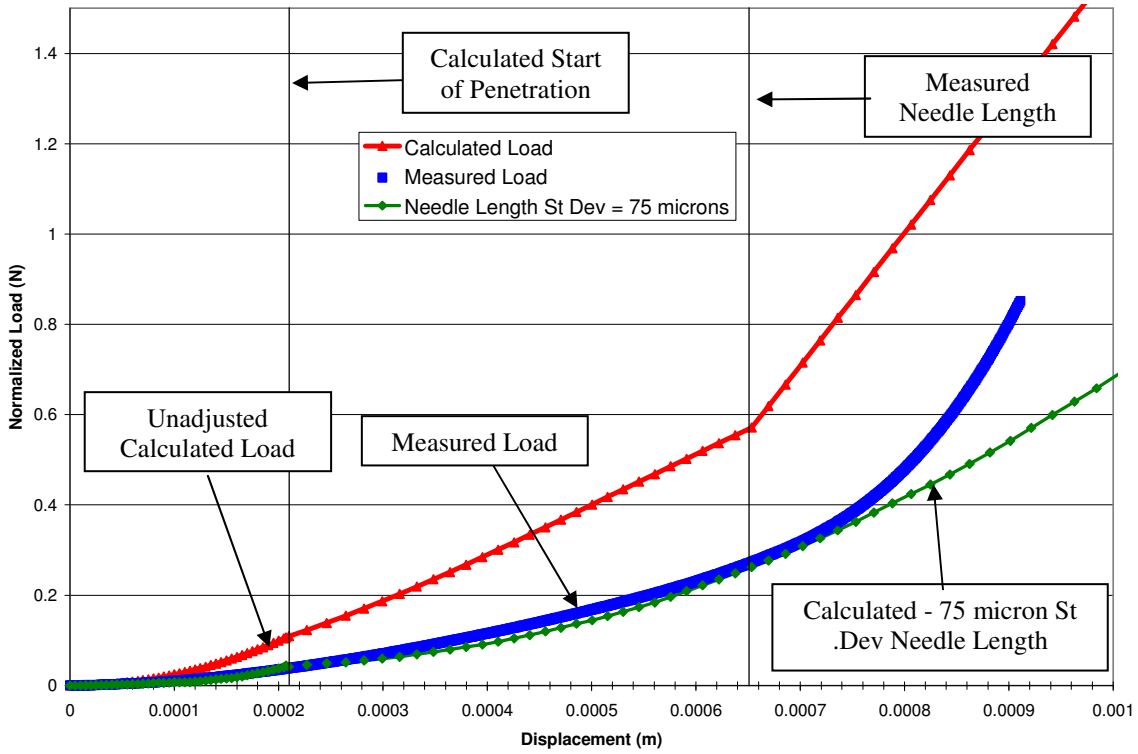


Figure **7.79**: Normalized load versus displacement for COC 5013 microneedle device with 1.00 mm spacing arranged in a hexagonal pattern.

Figure **7.80** shows the displacement components plotted versus normalized load of the measured data shown in Figure **7.79**. The figure shows that at the measured needle length, the base of the microneedle device begins compressing the rubber sample without further penetration as indicated by a change of slope. Within the region of interest, located below the measured needle length and to the left of the vertical line, the penetration depth continues to increase at a nearly constant rate after the start of penetration. The effect of multiple needle deflection is small compared to the depth of

penetration and single needle deflection. The effect of the 1.00 mm distance between needle tips in the hexagonal pattern has a large impact on total displacement compared to the square pattern. The depth of penetration for this pattern is shown to be about 140 microns. Single needle deflection dominates the total displacement due to the large tip angle of 30 degrees that causes more deflection than penetration. Smaller tip radii and smaller tip angles would decrease single needle deflection and increase penetration depth as ratios of total displacement.

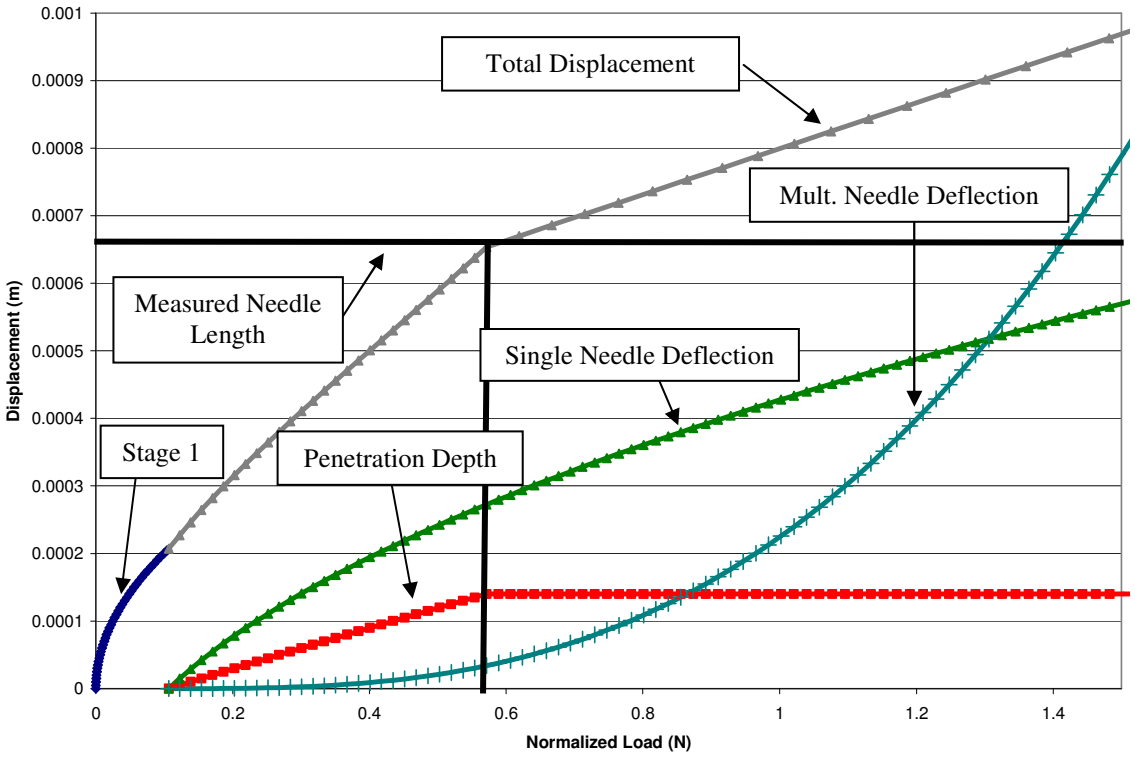


Figure **7.80**: Calculated displacement versus normalized force for each displacement component and the total displacement for a hexagonal COC 5013 pattern with 1.00 mm spacing.

Figure **7.81** shows plots for normalized load versus displacement for measured data from Figure **6.38** and analytical data for the 91-needle hexagonal spacing pattern with 1.50 mm spacing between needles. Unadjusted calculated and random needle length-adjusted calculated data sets are plotted for comparison to the measured data. The average needle length on this device is 595 microns. The increase in slope at the measured needle length comes from the compression of the rubber section by the base of the microneedle device. The difference between the measured and calculated plots comes from measurement error as shown in Figure **7.24** and small variations in needle lengths. A statistical comparison between the calculated random-length variation data with a standard deviation for needle length of 75 microns and the measured data shows an R-squared value of 0.9356.

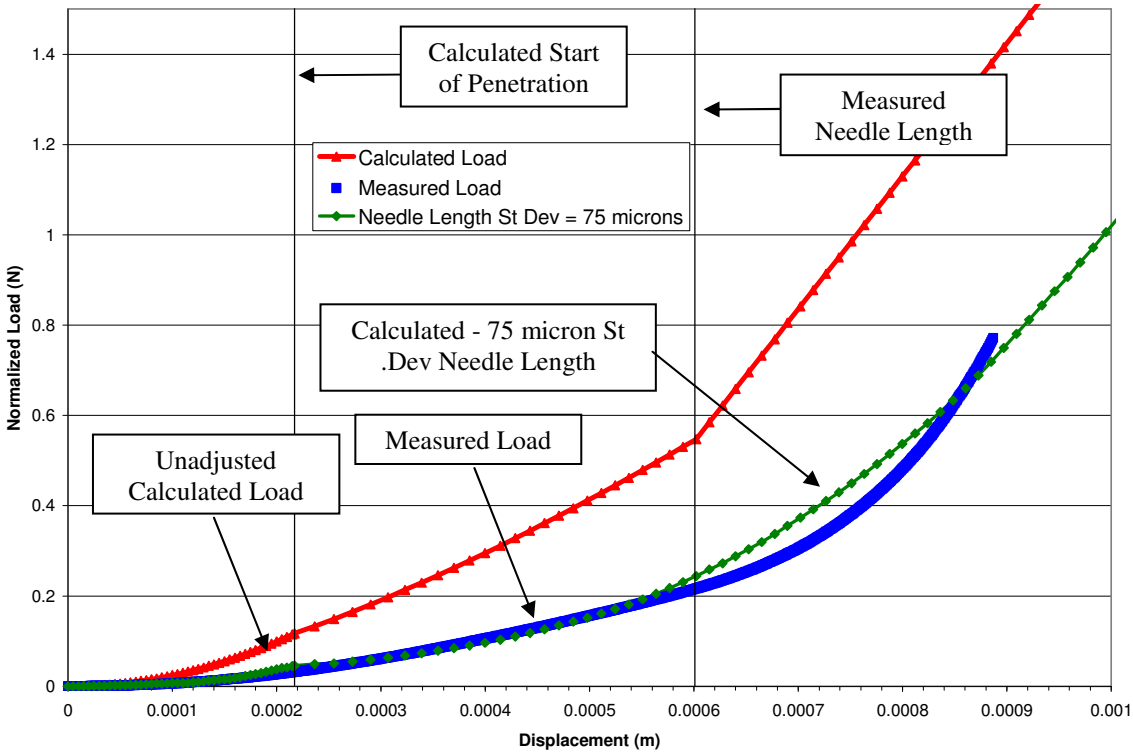


Figure **7.81**: Normalized load versus displacement for COC 5013 microneedle device with 1.50 mm spacing arranged in a hexagonal pattern.

Figure **7.82** shows the displacement components plotted versus normalized load of the measured data shown in Figure **7.81**. The figure shows that at the measured needle length, the base of the microneedle device begins compressing the rubber sample without further penetration as indicated by a change of slope. Within the region of interest, located below the measured needle length and to the left of the vertical line, the penetration depth continues to increase at a nearly constant rate after the start of penetration. The effect of multiple needle deflection is small compared to the depth of penetration and single needle deflection. The effect of the 1.50 mm distance between needle tips in the hexagonal pattern has a small impact on total displacement. The depth

of penetration for this pattern is shown to be about 130 microns. Single needle deflection dominates the total displacement due to the large tip angle of 30 degrees that causes more deflection than penetration. Smaller tip radii and smaller tip angles would decrease single needle deflection and increase penetration depth as ratios of total displacement.

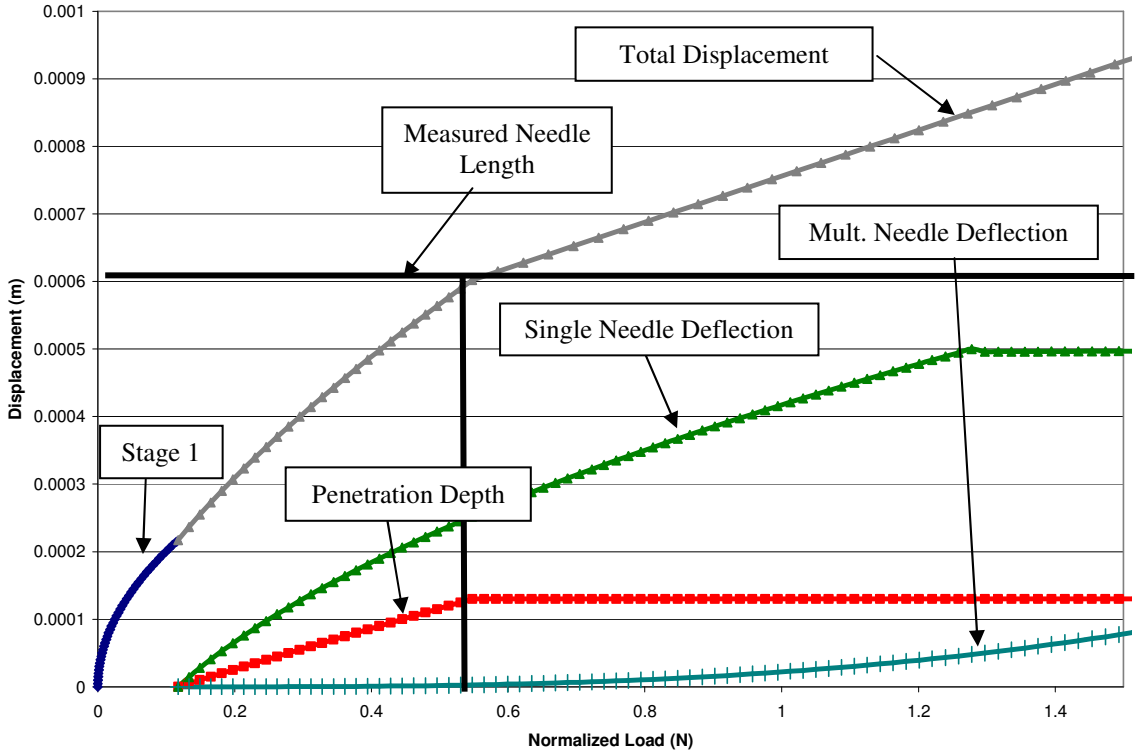


Figure **7.82**: Calculated displacement versus normalized force for each displacement component and the total displacement for a hexgaonal COC 5013 pattern with 1.50 mm spacing.

Figure **7.83** shows a comparison of the analytical model plots for each of the tested COC 5013 microneedle patterns. The plots show that there is little distinguishable difference between each of the three patterns until total displacement exceeds 700 microns. This similarity is due to the needle tips in all patterns having similar geometries. The biggest difference between the patterns comes from the deflection of the

rubber from the effect of multiple needle deflection described earlier in the chapter. The 1.00 mm patterns experience less total displacement than the 1.50 mm patterns but they also have less needle penetration at a given load.

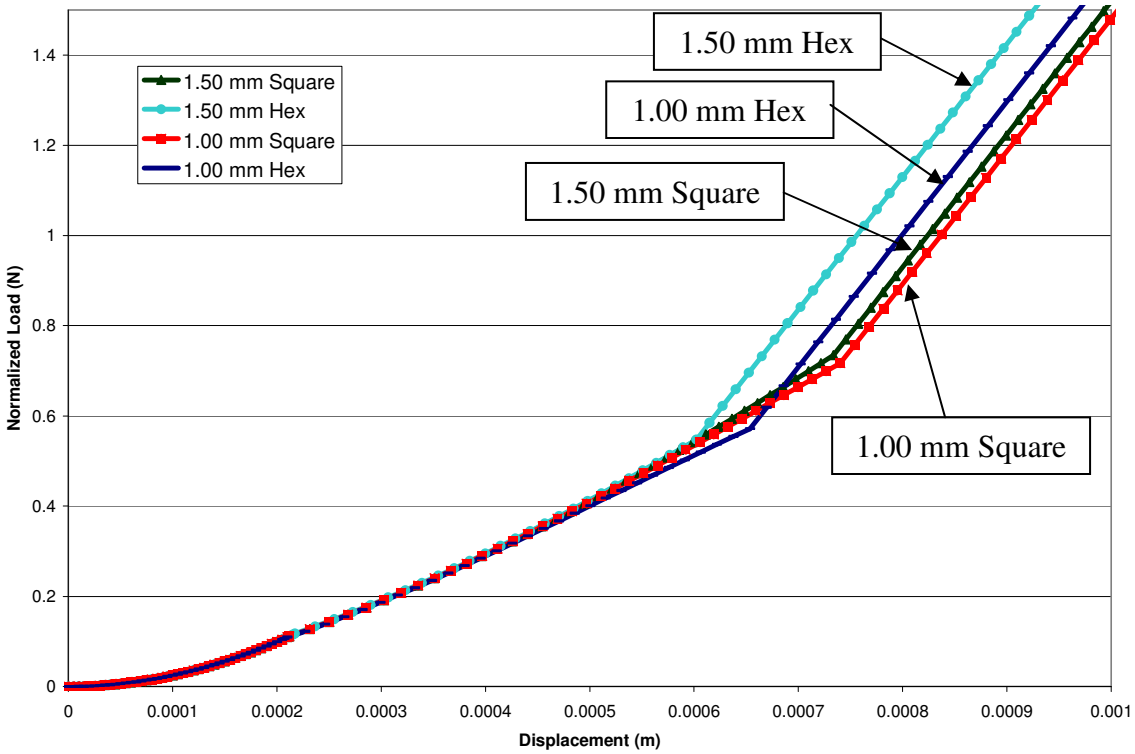


Figure **7.83**: Normalized load versus displacement plot for the analytical model of each tested COC 5013 microneedle device.

Figure **7.84** shows the length adjusted plot for each COC microneedle device. This figure shows how each calculated data set is adjusted with the addition of random normal length variation compared to the unadjusted data in Figure **7.53**. The adjusted data intensify the differences between each pattern. The data show that for displacements less than 600 microns, there is little difference between the patterns. The largest

differentiator between each pattern is the effect of multiple needle displacement, although this effect is not a major contributor prior to the base of the microneedle device contacting the rubber surface.

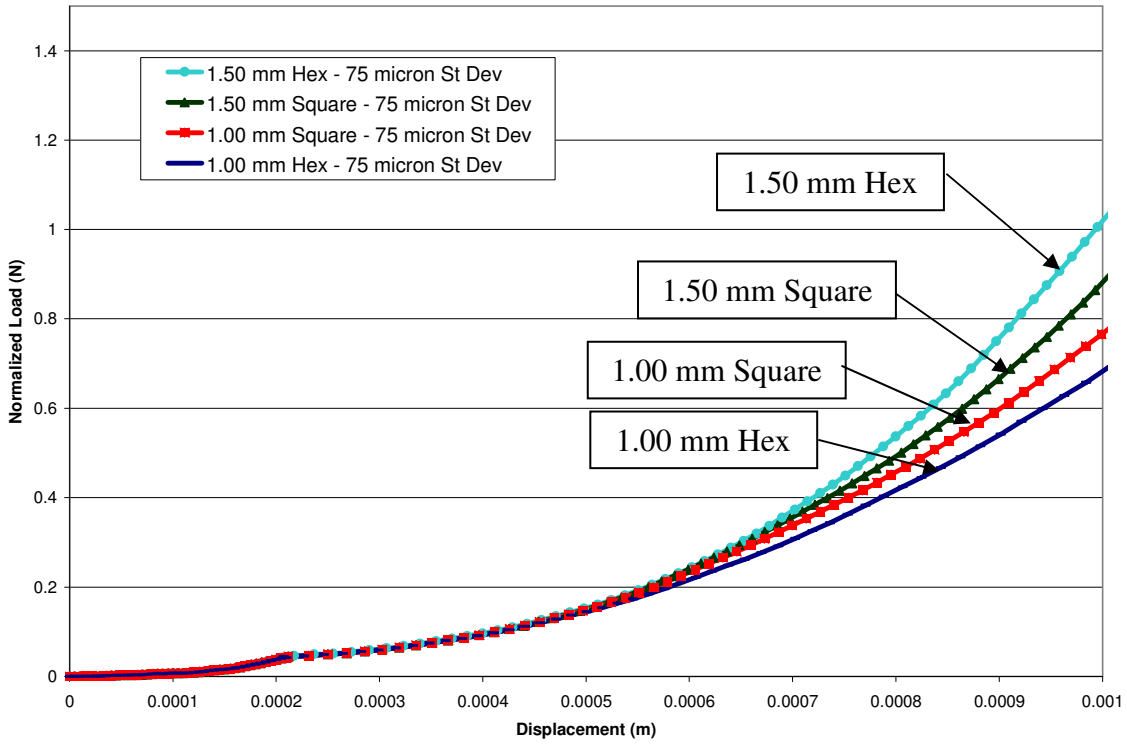


Figure **7.84**: Normalized load versus displacement plot for the length-adjusted calculated model of each tested COC microneedle device.

Analysis of the COC 5013 microneedle device data shows that the analytical model compares well with the measured data. The figures in this section show that the measured and length-adjusted calculated data have correlations with R-squared values greater than 90% in all cases. The errors in the measured data likely come from the skew of the test fixture during testing and variations in needle length and tip radii. These errors can show up as an averaging of multiple penetration events and act to flatten the shape of

the measured data. Both length deviation and test fixture skew will have the same effect that is accounted for in the calculated length-adjustment data.

Figure **7.83** shows that the calculated model reflects that longer needles allow for deeper needle penetration as shown by the change in slope that comes from the microneedle device's base compressing the rubber sample. The change in slope that comes from compression of the rubber sample by the microneedle base is reflected in both the calculated and measured plots at similar displacements.

The effect of multiple needle deflection is small compared to the penetration depth and single needle deflection components of total displacement. The effect of multiple needle displacement comes from the closely spaced needles acting as a solid indenter. However, the needles are still far enough apart at lengths ranging from about 600 to 740 microns that each individual needle has a force versus displacement response similar to a single needle and the added multiple needle displacement has little effect. The fast rise in the slope of multiple needle deflection after the measured needle lengths in figures **7.76**, **7.78**, **7.80**, and **7.82** indicates that multiple needle deflection would be more significant for longer needle lengths of the same geometry. Figure **7.83** compares the calculated data for the four COC 5013 patterns and shows a small difference between the 1.00 mm patterns and the 1.50 patterns. This is reflective of the small difference in the multiple needle deflections. The calculated data provide reasonably good capacity to predict load versus displacement for COC 5013 microneedle devices.

### *Makrolon Microneedle Analysis*

Figure **7.85** shows plots for normalized load versus displacement for measured data from Figure **6.39** and analytical data for the 100-needle square spacing pattern with 1.50 mm spacing between needles. Unadjusted calculated and random needle length-adjusted calculated data sets are plotted for comparison to the measured data. The average needle length on this device is 679 microns. The increase in slope at the measured needle length comes from the compression of the rubber section by the base of the microneedle device. The difference between the measured and calculated plots comes from measurement error as shown in Figure **7.24** and small variations in needle lengths. A statistical comparison between the calculated random-length variation data with a standard deviation for needle length of 100 microns and the measured data shows an R-squared value of 0.9867.

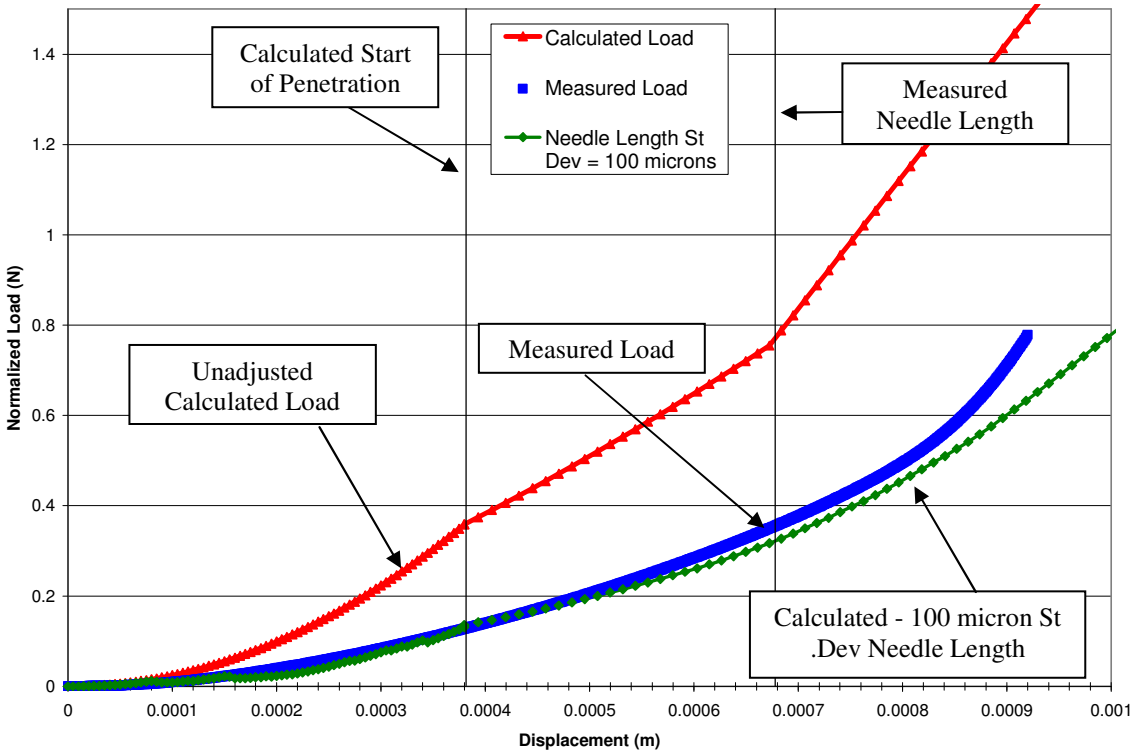


Figure **7.85**: Normalized load versus displacement for Makrolon 2207 microneedle device with 1.50 mm spacing arranged in a square pattern.

Figure **7.86** shows the displacement components plotted versus normalized load of the measured data shown in Figure **7.85**. The figure shows that at the measured needle length, the base of the microneedle device begins compressing the rubber sample without further penetration as indicated by a change of slope. Within the region of interest, located below the measured needle length and to the left of the vertical line, the penetration depth continues to increase at a nearly constant rate after the start of penetration. The effect of multiple needle deflection is small compared to the depth of penetration and single needle deflection. The effect of the 1.50 mm distance between needle tips in the square pattern has a small impact on total displacement. The depth of

penetration for this pattern is shown to be about 120 microns. Single needle deflection dominates the total displacement due to the large tip angle of 30 degrees that causes more deflection than penetration. Smaller tip radii and smaller tip angles would decrease single needle deflection and increase penetration depth as ratios of total displacement.

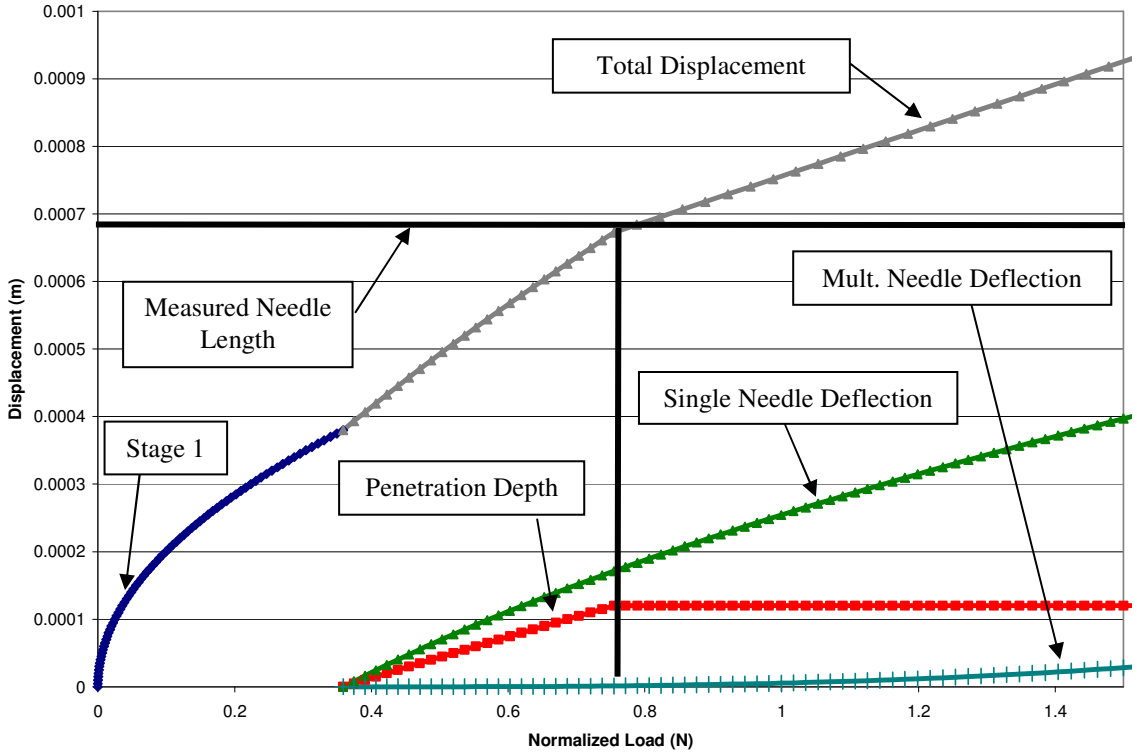


Figure **7.86**: Calculated displacement versus normalized force for each displacement component and the total displacement for a square Makrolon 2207 pattern with 1.50 mm spacing.

Figure **7.87** shows a comparison of measured force versus displacement for all five of the 1.50 mm square pattern microneedle devices made from the tested polymers, each with varying average tip radii. The figure shows a clear difference between the Makrolon 2207 and the other four polymers. This difference results from larger tip radii for the Makrolon 2207 averaging 32 microns compared to the other polymers with tip

radii averaging 15 to 23 microns. The larger measured tip radii of the Makrolon 2207 devices results from the material not filling the mold as well as the other polymers during injection molding. The larger needle tip radii will require larger forces and larger displacement to initiate penetration into the rubber. The relationship between larger tip radius and larger force requirement follows the relationship suggested by Eq. **7.7** and Eq. **7.9**.

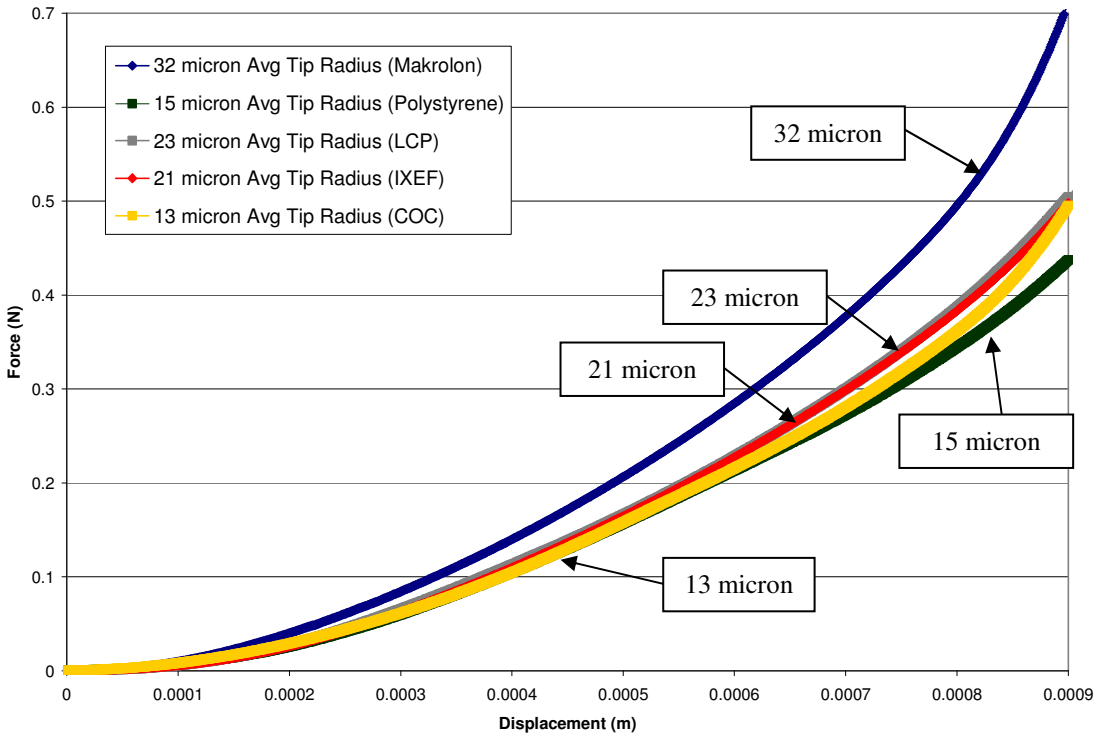


Figure **7.87**: Measured force versus displacement for 1.50 mm square microneedle devices plotted by tip radii.

The penetration depth for the Makrolon 2207 microneedle devices will be smaller than the other materials for the same pattern arrangement due to the larger required initial deflection before start of penetration. This will prevent deeper skin penetration into skin for a given total displacement.

### *Plastic Microneedle Analysis Summary*

Table **7.3** compares the average tip radii, average measured needle length, calculated initiation deflection, and estimated penetration depth for each material and pattern. Appendix 2 contains the measured needle lengths and tip radii. Penetration depth is calculated to be equal to total displacement minus all material deflection and is gathered directly from the analytical data. The chart shows that as tip radius decreases, the amount of deflection at which penetration starts decreases, therefore total penetration depth decreases. Needles shorter in length will penetrate skin to shallower depths.

The 1.50 mm square Makrolon 2207 devices, with an average measured tip radius of 32 microns and needle length of 679 microns, is estimated to penetrate to a depth of 120 microns. This is the lowest estimated penetration depth of all polymer microneedle devices. The 1.50 mm square COC 5013 devices have an average measured tip radius of 13 microns and average needle length of 745 microns and are estimated to penetrate to a depth of 185 microns. This is the deepest of all the tested polymer microneedle devices. The difference between the microneedle devices with the highest and lowest penetration depths comes mainly from the difference in tip radii. The Makrolon 2207 devices require an additional 168 microns to start penetration compared to the COC 5013 devices. Smaller tip radii are critical to increasing penetration depth.

Table **7.3**: Average tip radii, calculated initiation deflection, and calculated penetration depth for each pattern and material. All values listed are in microns.

| Square Patterns | | | | |
|---|---|---|---|---|
| Material | Square - 1.00 mm | | | |
| | Tip Radius | Initial Deflection | Measured Length | Est Penetration Depth |
| Vectra A130 | 19 | 262 | 738 | 170 |
| IXEF 1022 | 17 | 247 | 738 | 175 |
| COC 5013 | 13 | 212 | 745 | 180 |
| PS | 18 | 256 | 735 | 170 |
| Makrolon 2207 | | | | |
| Material | Square - 1.50 mm | | | |
| | Tip Radius | Initial Deflection | Measured Length | Est Penetration Depth |
| Vectra A130 | 23 | 304 | 732 | 167 |
| IXEF 1022 | 21 | 286 | 728 | 168 |
| COC 5013 | 13 | 212 | 732 | 185 |
| PS | 15 | 226 | 737 | 185 |
| Makrolon 2207 | 32 | 380 | 679 | 120 |

| Hexagonal Patterns | | | | |
|---|---|---|---|---|
| Material | Hex - 1.00 mm | | | |
| | Tip Radius | Initial Deflection | Measured Length | Est Penetration Depth |
| Vectra A130 | 17 | 250 | 656 | 135 |
| IXEF 1022 | 17 | 250 | 647 | 132 |
| COC 5013 | 13 | 207 | 656 | 140 |
| PS | 15 | 229 | 646 | 137 |
| Material | Hex - 1.50 mm | | | |
| | Tip Radius | Initial Deflection | Measured Length | Est Penetration Depth |
| Vectra A130 | 17 | 245 | 595 | 125 |
| IXEF 1022 | 19 | 267 | 595 | 125 |
| COC 5013 | 14 | 217 | 595 | 127 |
| PS | | | | |

This section compared data generated from equations shown in figures **7.17** and **7.18** to measured data derived from testing described in Chapter 6. The comparisons show that the equations have a good ability to predict load versus displacement for plastic microneedle devices when a certain amount of error is induced to simulate the errors that are inherent to the measurement of multiple needles. Table **7.4** shows the R-squared values for comparisons for each plastic microneedle pattern of measured data to length-adjusted calculated data. The level of needle length variation was selected based on the

highest R-squared value. The highest R-squared value for each pattern is highlighted in the table.

Table **7.4**: R-squared values for each plastic microneedle pattern at varying levels of adjustment for standard deviation of needle length.

| | St Dev (microns) | 1.00 mm Sq | 1.50 mm Sq | 1.00 mm Hex | 1.50 mm Hex |
|---|---|---|---|---|---|
| PS | 75 | 0.8938 | N/A | 0.9016 | 0.9059 |
| | 100 | 0.9420 | | 0.9416 | 0.8479 |
| LCP | 75 | 0.9896 | 0.9786 | 0.7487 | |
| | 100 | 0.7913 | | 0.9237 | 0.9667 |
| IXEF | 75 | 0.9470 | 0.9130 | | |
| | 100 | | 0.9229 | 0.9494 | 0.9312 |
| COC | 75 | 0.9731 | 0.9890 | 0.9485 | 0.9356 |
| | 100 | | | 0.8142 | 0.8412 |
| MAK | 75 | N/A | | N/A | N/A |
| | 100 | | 0.9867 | | |

Table **7.4** shows the R-squared values for each device pattern using either 75 or 100 microns of standard deviation to adjust the calculated data to match the measured data. One question that may arise from examination of this data is whether the selection of 75 or 100 microns is due only to random variation, such as sloppiness of the fixture during testing, or if there is an explicit cause for these variations. There is likely elements of both common and special cause variation present in this situation. Figure **7.88** compares the length adjusted calculated data for each plastic microneedle device with the measured standard deviation of length.

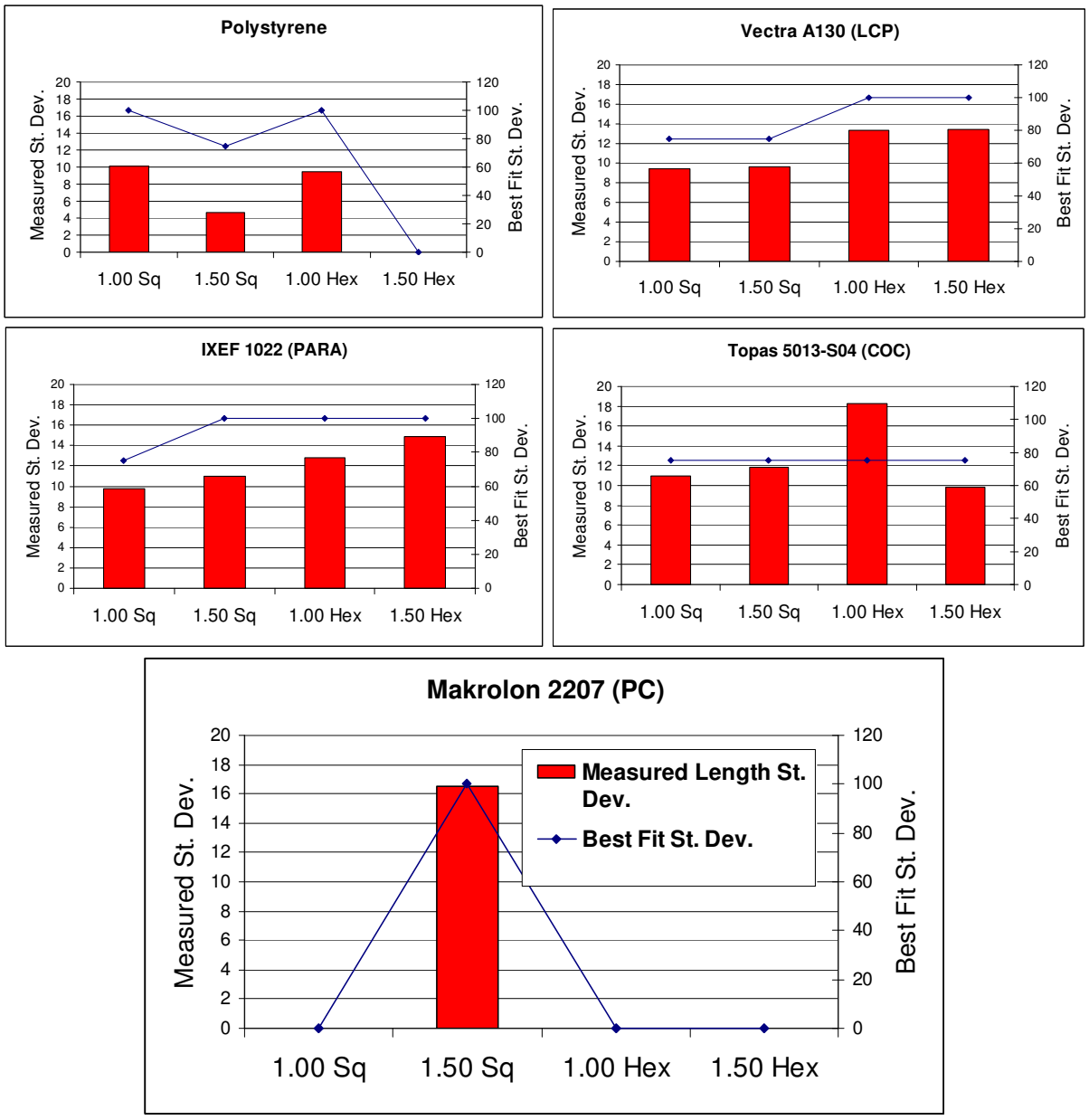


Figure **7.88**: Comparison of length adjusted standard deviation and the measured standard deviation of length, all in microns.

Comparing the measured standard deviation with the best fit standard deviation shows a trend. As the measured standard deviation increases the length adjusted model's standard deviation also increases. This is true in all cases except for the COC 1.00 mm

Hexagonal pattern. Although the magnitudes are different, there does seem to be a correlation between the measured and estimated differences. Also, it should be noted that the length-adjusted models are meant to catch all errors including angle variations of the fixtures during testing, tip radius variations, and other common cause variation that is not easily identified.

Finally, by examining the R-squared values in Table **7.4**, it is apparent that in cases when the correlation coefficient was calculated for both 75 and 100 microns, there is not a large difference between the two values. The biggest difference is seen for the 1.00 mm hexagonal LCP device that shows an R-squared value of 75% for the 75 micron version and a 92% correlation for the 100 micron version. While this is significant and the 100 micron version is more accurate, the 75 micron model can still predict 75% of the data. The best-fit length variation for each pattern was selected between either 75 or 100 micron standard deviations and was not further refined due to the large overlap between the two data sets and the inability to resolve finer gradations.

Another issue that becomes apparent after examination of Table **7.3** and Table **7.4** is the magnitude of the predicted errors due to the penetration distance. Table **7.3** shows that the estimated penetration depth for the plastic microneedle devices ranges from 120 to 180 microns. This is compared to a standard deviation in needle length of 75 to 100 microns. At first sight, this seems to mean that many of the needles may not penetrate the skin to the predicted depth, while other needles may penetrate much farther. However, this standard deviation is presented as the aggregate error that is part of the uncertainty in attempting to measure such small penetration forces and distances. On a flat surface in a laboratory environment with ideal fixtures, this would likely be reduced.

Further studies of uncertainty in needle penetration depth for commercial products would benefit for the purposes of delivering the proper dosage of a drug therapy. The estimated penetration depth is intended to predict the average distance that any one needle will penetrate the rubber sample, while the standard deviation of needle length is meant to encompass the errors believed to be present in the system.

Errors that differentiate measured and calculated data were discussed and come mainly from inaccuracies in measurement data. These errors are a result of the microneedle device penetrating the rubber sample at a non-perpendicular angle, variations in needle lengths, and variations in tip radii. Calculated data show that multiple needle deflection has little effect on the polymer microneedle devices that were tested. This indicates that microneedle patterns with similar needle geometries to those tested will experience little effect by spacing the needles as close as 1.00 mm.

**Error Analysis**

Several sources of error can help explain many of the inaccuracies in both the experimental and calculated values presented in this project. Some sources of error are explicit and explainable, such as known equipment measurement errors and variations in the lengths of needles in an array. Other error that is present in the calculated penetration results comes from obscure sources like the non-linear response of rubber and skin to load that cannot be easily documented. Such error will be compounded when examining in vivo and in vitro skin samples than can have varying properties based on hydration, genetics, and other factors.

Explicit error sources include error from equipment and known variations in needle heights and friction properties. First, there is a known magnitude of error in the load cell that was used. The Instron 2525-816 load cell has a 500N capacity with an error of plus or minus 0.25% (Instron, 2009). Though the rated error is small, it could present an effect on the overall analysis.

Another source of equipment error comes from imperfections in keeping the needles orthogonal to the plane of the rubber during testing as shown in Figure **7.24**. This can cause one side of a needle array to contact the surface of the rubber before the rest of the array. This tilt can skew the tested results by measuring the various stages of needle penetration simultaneously. Such skew will essentially provide the measured load of an average of various needles at one time. A related source of known error comes from the variation of needle lengths present in any array. The needle lengths as measured from the base of the needle devices are suspected to have some amount of variation. These length variations come from the injection molding and mold manufacturing process for plastic needles and come from imperfections in needle length and fixture fabrication for the steel needles. The needle length differential can manifest, along with the tilt of the needle testing fixture, to become quite significant and affect measured results.

The method used for the plastic and steel needle analysis sections is similar to a Monte Carlo distribution because randomly generated numeric inputs help to explain the variance better than the analytical model alone. Adjustments were made in the calculated needle data by utilizing random needle lengths generated using Minitab® for various standard deviations. The calculated data were then adjusted using these randomly

generated needle lengths to simulate each needle applying force at varying displacement values. The magnitude of induced random variation, as revealed by the standard deviation in needle lengths, was selected for each needle pattern based on the best fit with the measured data.

The plots in Figure **7.23** through Figure **7.85** show that the random needle length data are much more accurate at describing the measured data than the unadjusted data. This is because things like needle length, angle of the needles to the rubber sample, and needle tip radii can not be easily classified for each needle within every pattern. The adjustments made using this technique allow generalizations to be made about the imperfections in the needle patterns and testing methods, and use that uncertainty to provide a better fitting model. The needle length adjustments for each needle pattern vary from 75 microns for the plastic needles to 200 microns for the steel needles. The needle lengths are assumed to have a normal distribution as shown in Figure **7.89** for the needle length standard deviations ranging from 50 microns to 200 microns. For example, for a random normally distributed set of needle lengths with a standard deviation of 50 microns, 67% of all needle lengths will be within 50 microns of the nominal assumed length.

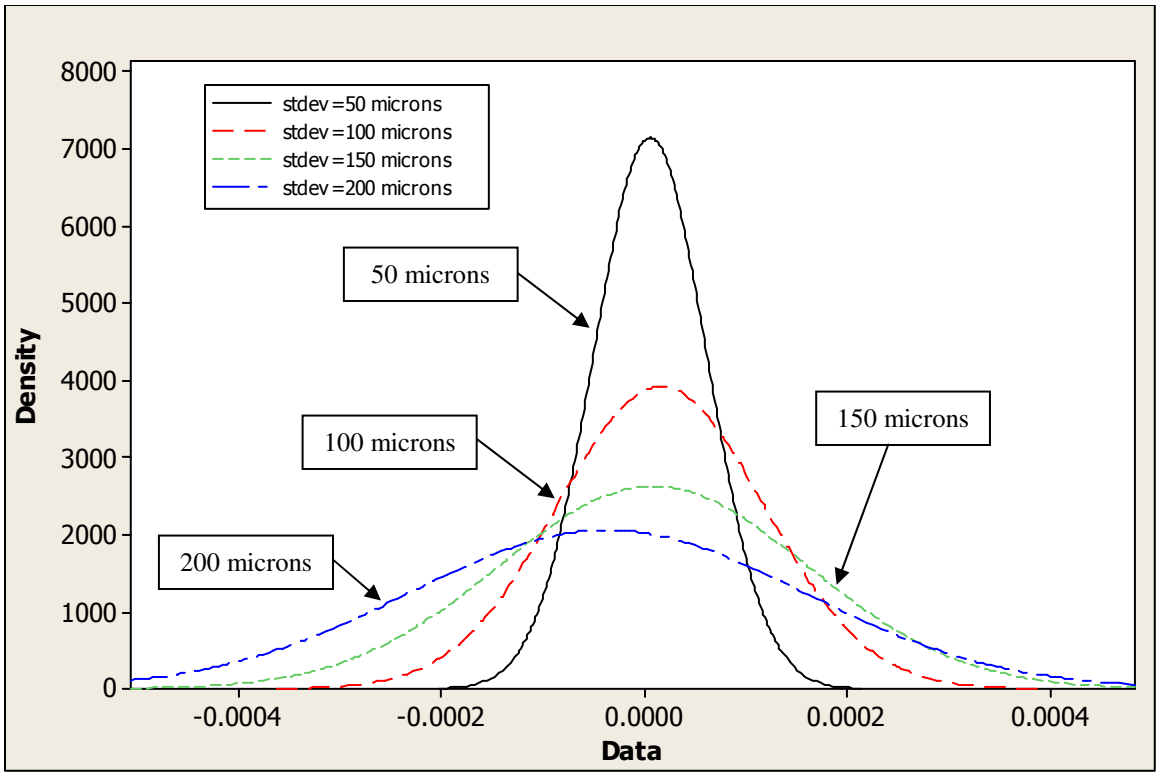


Figure **7.89**: Random normally distributed deviation in needle lengths for standard deviations of 50 to 200 microns.

Table **7.5** shows the standard deviations for measured needle lengths for each set of plastic needles. The table shows that the standard deviations range from under 5 microns to more than 18 microns. This compares to the needle length standard deviation of 75 to 100 microns to obtain a close correlation between the measured and calculated data. This suggests that the angle of approach for the needles to the rubber skin simulant's surface must not be orthogonal and this has a significant role in the error.

Table **7.5**: Standard deviation for needle length for each plastic needle pattern and material in microns.

| | Vectra A130 (LCP) | IXEF 1022 (PARA) | Topas 5013-S04 (COC) | Polystyrene | Makrolon 2207 (PC) |
|---|---|---|---|---|---|
| **1.00 Sq** | 9.4 | 9.8 | 11 | 10.1 | N/A |
| **1.50 Sq** | 9.6 | 11 | 11.8 | 4.7 | 16.5 |
| **1.00 Hex** | 13.3 | 12.8 | 18.3 | 9.5 | N/A |
| **1.50 Hex** | 13.4 | 14.9 | 9.8 | N/A | N/A |

The angled approach of the needle devices during testing as shown in Figure **7.24** is a large source of error. This error source is simulated by the induced random variation as shown in the steel and plastic needle analysis sections. This can be shown by Figure **7.90** that shows the calculated plot for a multiple needle 0.75 mm steel needle device adjusted using both the random length variation technique and a similar technique that adjusts the data for three angles. This plot shows that both random needle length variation and angled testing will yield results of the same shape and magnitude. Only the random needle length adjustments are performed for the analyses shown in the previous sections comparing the calculated and measured data due to the similarity in results of this technique to angled adjustment. Both methods will effectively quantify the error between the calculated and measured data.

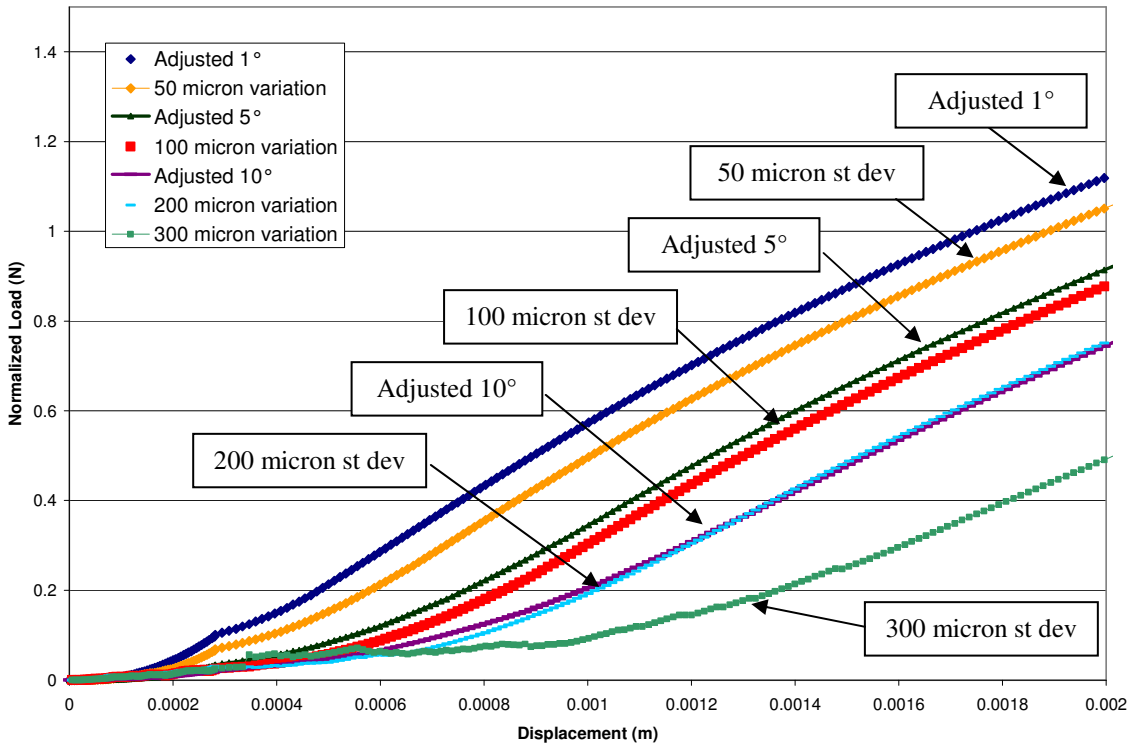


Figure **7.90**: Comparison of calculated results for angled needle device plots to needle length variation results.

For the 0.75 mm steel needle device, a 200 micron standard deviation of needle length yielded the best correlation with the measured test results. From the plot this would correlate well with an angled approach of 10° from perpendicular. A small deviation from perpendicular as small as 10° to adjust for nearly all error between the calculated and measured data suggests that such data adjustment is valid and reasonable.

Figure **7.91** shows a 1.5 mm square microneedle device at angles of 5 and 10 degrees as it approaches the surface of the sample. The representations show that for small angles of approach toward the sample's surface, such small angles are reasonable and are likely imperceptible during testing. The representations shown in the figure

embody the microneedle device as tilted in a single reference plane which is unlikely to occur. More likely, the actual angle to the sample's surface will be a more complex dihedral angle between the two planes. The confounding of needle length variation and angle explains most of the error between the measured and predicted results.

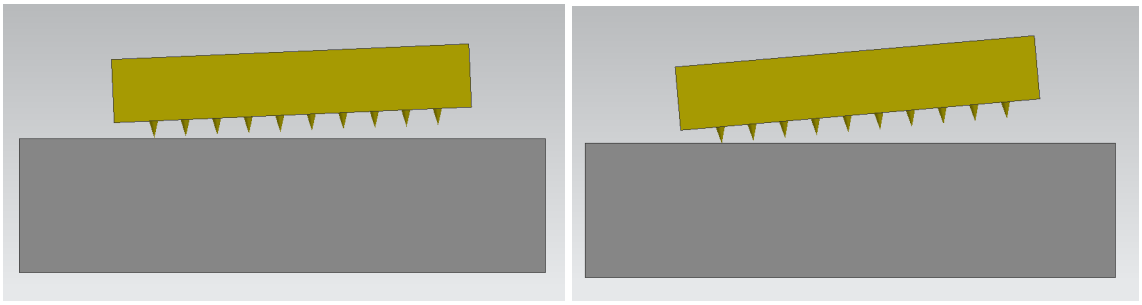

Figure **7.91**: Representations of a microneedle device approaching a sample at a 5 degree angle (left) and 10 degree angle (right).

Other error comes from variations in surface finishes and lubrication. More testing is likely needed to quantify the friction coefficient between each type of polymer and the penetrated testing media. The average friction coefficient that was calculated for single steel needle data was reused as the friction coefficient between each plastic microneedle material and the rubber skin simulant. Testing would likely reveal that the friction coefficient is different from that of the steel needles and differs amongst different plastic needle materials.

It should also be noted that the non-linear response to force of rubber and skin testing media is difficult to quantify in a model. Although work is ongoing in non-linear mechanics to develop rubber constitutive models, these are specific to each material. A linear response to force is assumed in the analytical model due to the small deflections.

For a viscoelastic material like rubber or skin an assumption of a linear response carries some amount of error.

Other factors not included in the analytical model will contribute to the force versus deflection response of the needles during penetration. One source of such error will be the added contribution of normal force from needles in a patterned array. As the needles penetrate the rubber skin simulant, the rubber between the needles deflects as the needle passes through it. Although frictional effects are currently accounted for a single needle as shown in Eq. **7.15**, multiple needles in a closely spaced pattern will change the amount of normal force acting on each needle. Figure **7.92** shows a diagram of the deflection that occurs between needles in close patterns.

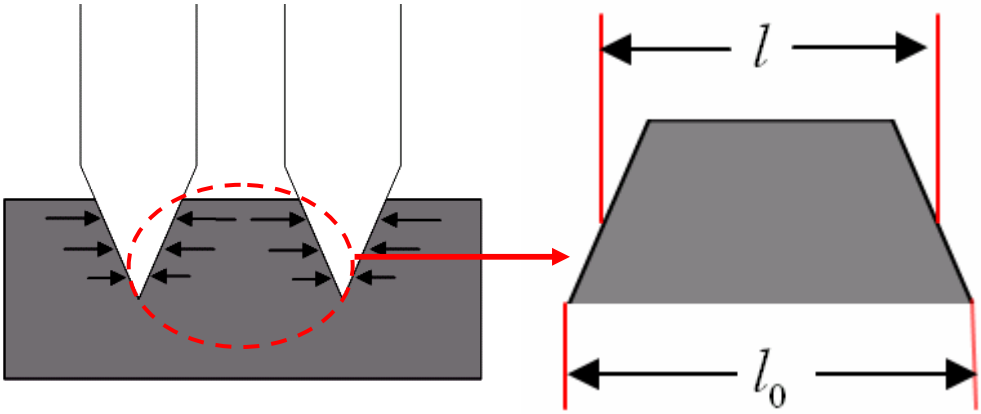


Figure **7.92**: Deflection that occurs between needles will differ from a single needle due to a higher material stretch ratio causing higher normal force on the needles.

Eq. **7.25** shows the equation for normal force on each needle based on the diagram in Figure **7.92**. This will act to modify the equation for friction force as shown in Eq. **7.15**. The rubber or skin between adjacent needles will be strained more than a single needle penetrating the same material. This is due to the increased stretch ratio.

Closer needle spacing will act to increase the normal force, and thus, the friction force on multiple needle patterns. Single needles will have a smaller stretch ratio due to the larger undeformed length, $l_0$. This multiple needle effect on normal force is not accounted for in the analytical model and will result in increased error between the measured and calculated plots.

$$F_{N\_mult} = E_C A_0 \left( \frac{l_0 - l}{l_0} \right) \qquad \text{Eq. } \mathbf{7.25}$$

A final source of error comes from the compression of the needles themselves. Both the steel needles and plastic needles are made from materials with much higher stiffness than the rubber skin simulant. The steel needles have a Young's modulus of approximately 200 GPa and the plastic needles have Young's modulii ranging from 2.4 to 20 GPa. This compares to the modulus of elasticity of 5.07 MPa for the rubber skin simulant. This means that even polystyrene, with the lowest needle stiffness, is three orders of magnitude stiffer than the rubber skin simulant. The stiffest human skin, as described in the section "Effect of Material Properties in Analysis" of this chapter, has a stiffness of 200 MPa which is still an order of magnitude less stiff than polystyrene. Although the assumption is made that the needles are infinitely stiffer than the rubber and the deflections are negligible, this is another source of error that is unaccounted in the analysis.

The cumulative effect of the sources of error will be revealed by the difference seen between the predicted and measured plots for force versus displacement. The effect

of needle length variation, testing the needles at an angle, and tip radii variations seem to be the largest source of error. Such effects are indistinguishable in the data and the Monte Carlo method described is be used to classify these types of error. Errors resulting from the load cell and from the deflection of the needles as they penetrate the skin simulant are small but likely have some effect on the results.

**Effect of Tip Radii & Tip Angle on Initial Penetration Force**

The radius and angle of a needle tip can have a substantial impact on the force required to initiate penetration into skin or rubber media. Eq. **7.9** is used to determine the force required to initiate penetration and involves the material property values of puncture fracture toughness and elastic modulus and the needle geometry values of tip radius and tip angle. Figure **7.93** is generated by plotting the initiation force with respect to tip radius and angle. The elastic modulus and puncture fracture toughness values are kept constant at the values defined for the silicone rubber used for testing throughout testing.

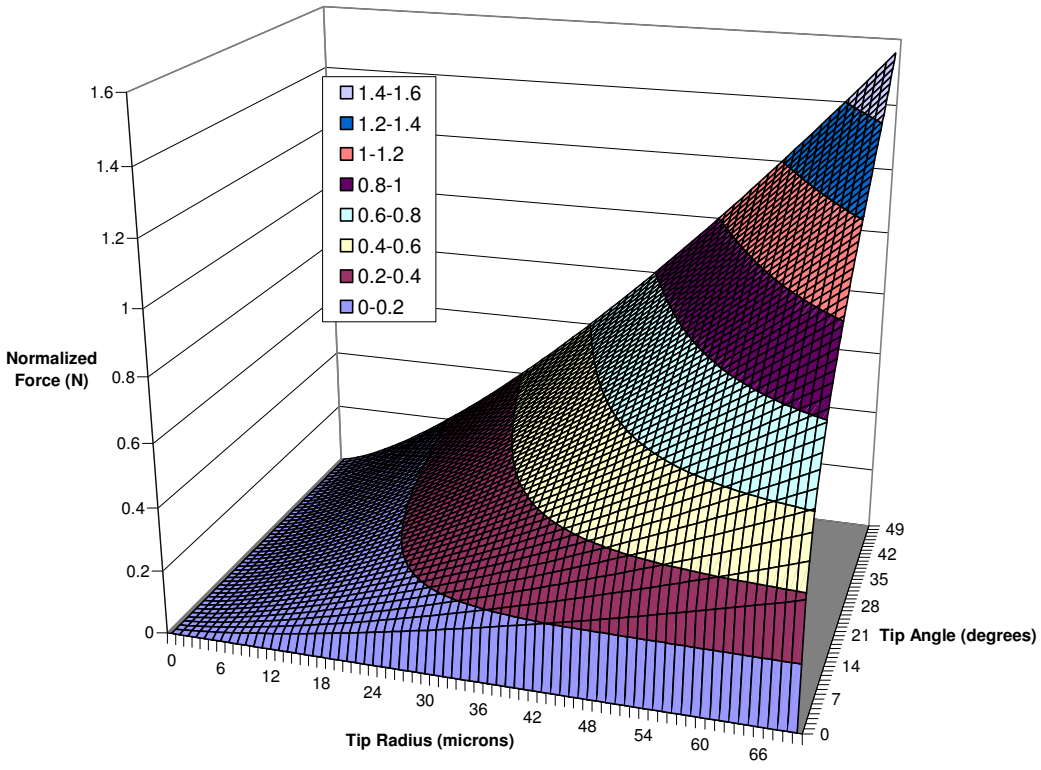


Figure **7.93**: Normalized penetration initiation force versus tip radius and tip angle.

The figure clearly shows that needles with a larger tip radii and larger included tip angles will require more force to initiate penetration. Larger tip radii are less desirable than those with smaller tip radii due to the higher required penetration force just to begin penetration. Larger included tip angles also are less desirable than smaller included angles due to the higher required penetration force. This follows a similar pattern observed by Khanna that shows that smaller projected areas will result in less required insertion force (Khanna *et al.*, 2010, p. 1).

Reduced tip angles and radii are a large concern in manufacturing microneedles in order to reduce the required force to start penetration. This becomes more important in injection molding where the shape of the mold determines the shape of the part. Sharp

tipped-mold cavities are critical to manufacturing out-of-plane microneedles with small tip radii. The design of the microneedles will determine the tip angle, which can be minimized for decreased penetration force. However, the tip angle also will have an effect on the strength of the microneedles. Microneedle strength is not taken into account here, but may be a factor when examining robust designs that will not buckle or break under the applied load.

**Effect of Material Properties in Analysis**

Only a single material was used during testing to simulate skin. The silicone rubber used for testing has mechanical properties that are within the range of mechanical properties of human skin. However, other materials including human skin may have properties that are different than those of the silicone rubber. Such mechanical property differences will have an effect on the analysis. Young's modulus, Poisson's ratio, puncture fracture toughness, and mode I fracture toughness are all material properties that will affect needle penetration. This section will show the effect of the range of possible values for Young's Modulus, puncture fracture toughness, and mode I fracture toughness that affects needle penetration. Table **7.6** shows the range and average values for human skin for three mechanical properties used in the analysis of penetration forces (Busillo, 2008; Davis et al., 2004; Roxhed, Gasser, Griss, Holzapfel & Stemme, 2007; Shergold & Fleck, 2004). Only one value was found for the mode I fracture toughness and is listed as the average.

Table **7.6**: Range of values for puncture fracture toughness, mode I fracture toughness, and Young's Modulus in human skin.

| | $G_P$ (KJ $m^{-2}$) | $J_{IC}$ (KJ $m^{-2}$) | E (MPa) |
|---|---|---|---|
| **Max** | 7.0 | --- | 200.00 |
| **Avg** | 23.5 | 2.5 | 16.00 |
| **Min** | 40.0 | --- | 6.00 |
| **Tested** | 9.3 | 2.75 | 5.07 |

The ranges for the properties for human skin shown in Table **7.6** can be plotted to display the variation that may be present in expanded testing. Figure **7.94** shows the effect of varying puncture fracture toughness, $G_p$, and keeping Young's modulus, E, constant in the model. The largest difference between the three plots is the difference in force and displacement at the initial puncture of skin. Higher values of puncture fracture toughness will require higher loads and more skin displacement to initiate penetration. Eq. **7.8** and **7.9** show just this effect. This is sensible from a physics standpoint because the puncture fracture toughness is equivalent to the energy required to initiate a crack in the surface. This equates to higher loads and displacements to produce a more energy to initiate a surface crack.

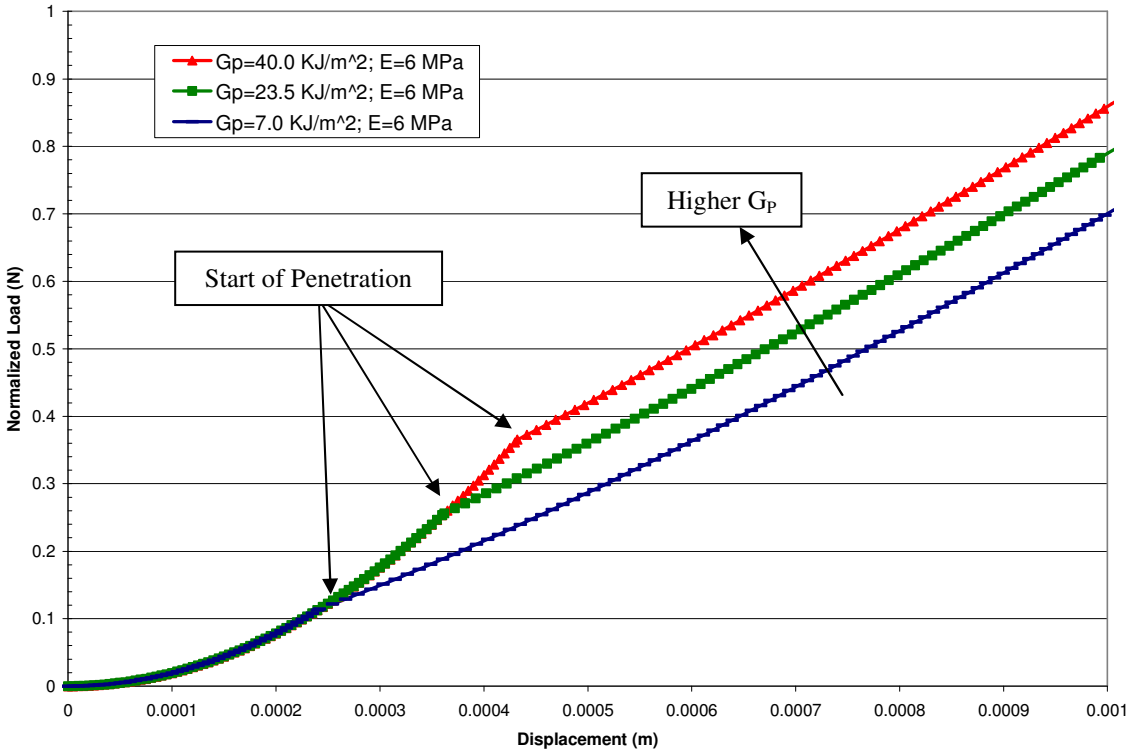


Figure **7.94**: Normalized load versus displacement for a constant Young's modulus, E, of 6.0 MPa and three values of puncture fracture toughness, $G_p$, within the range of values for human skin.

Figure **7.95** shows the effect of varying puncture fracture toughness, $G_p$, and keeping Young's modulus, E, constant in the model. The largest difference between the three plots is the difference in force and displacement at the initial puncture of skin. Like figure **7.94**, higher puncture fracture toughness will require higher loads and more skin displacement to initiate penetration. Also, compared to figure **7.94**, the overall load and displacement required to initiate penetration is increased due to the higher elastic modulus. Eq. **7.8** and **7.9** show just this effect. This is sensible from a physics standpoint because the puncture fracture toughness is equivalent to the energy required to initiate a crack in the surface.

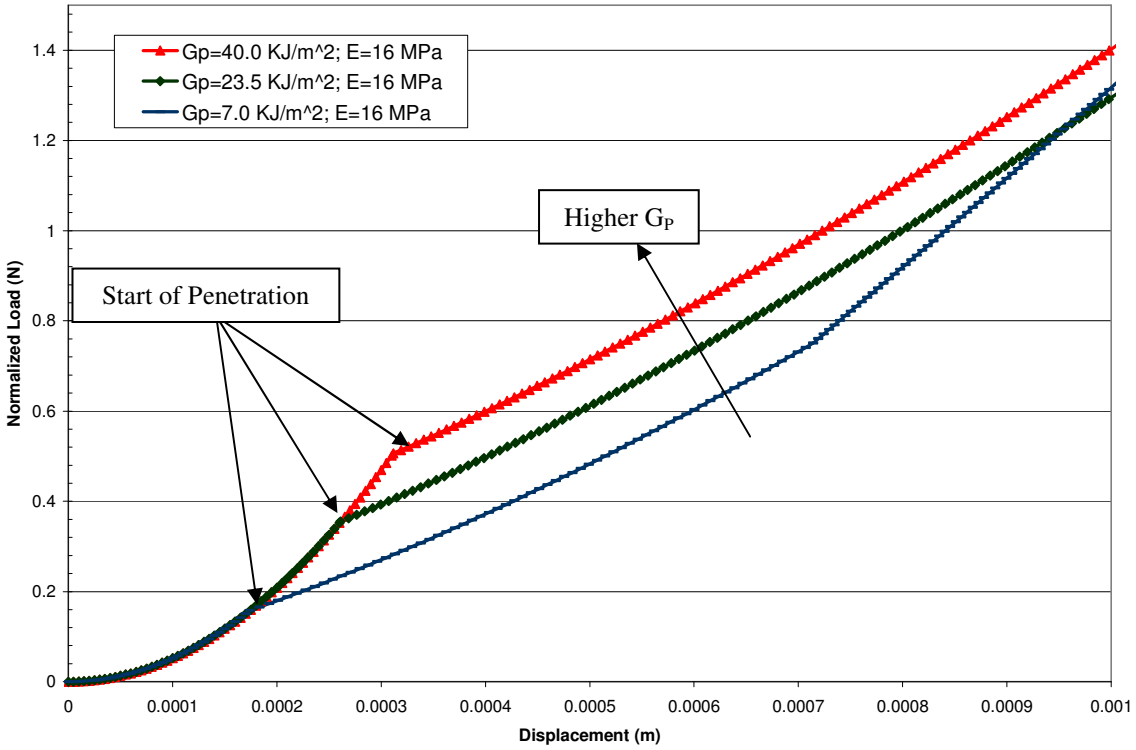


Figure **7.95**: Normalized load versus displacement for a constant Young's modulus, E, of 16.0 MPa and three values of puncture fracture toughness, $G_p$, within the range of values for human skin.

Figure **7.96** shows the effect of varying puncture fracture toughness, $G_p$, and keeping Young's modulus, E, constant in the model. The largest difference between the three plots is the difference in force and displacement at the initial puncture of skin. This effect dissipates at approximately 0.5 mm as the plots converge. It is worth noting that the load scale in this figure is an order of magnitude larger than the scales in Figure **7.94** and Figure **7.95**. This is due to the elastic modulii being between one and two orders of magnitude larger than in the other figures. This reflects on the large role that elastic modulus plays in the calculated friction force and single needle deflection. Higher elastic

modulii will require more energy to deflect the skin and result in higher penetration forces.

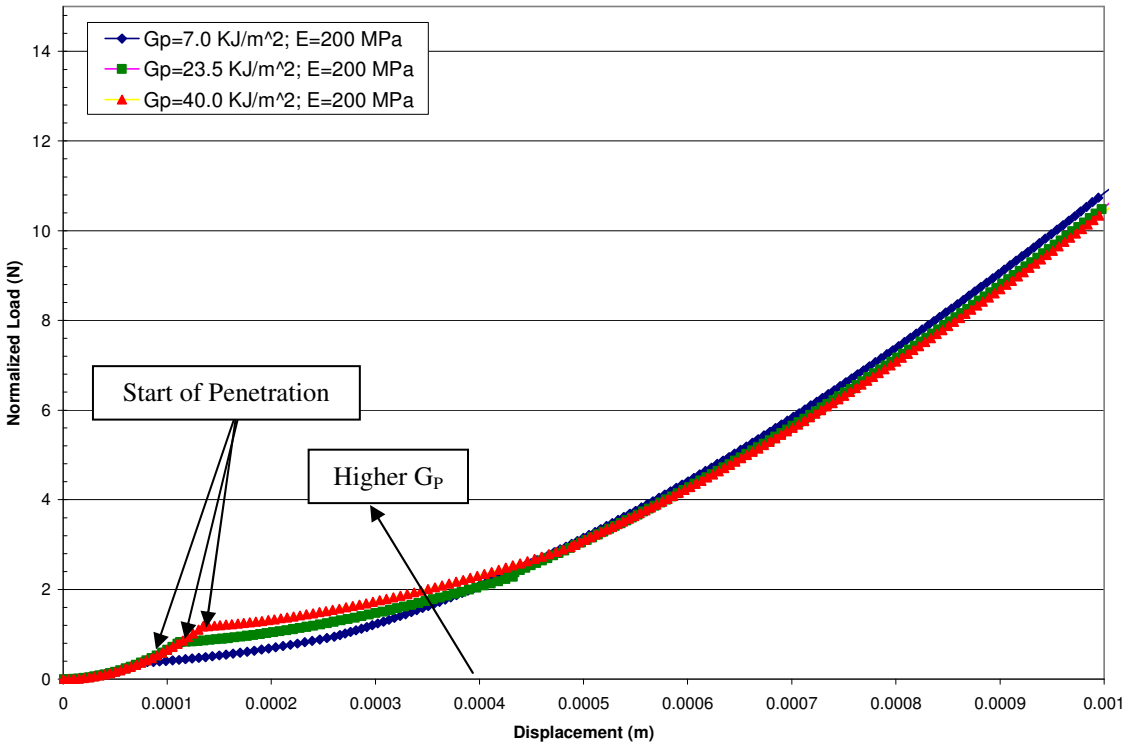


Figure **7.96**: Normalized load versus displacement for a constant Young's modulus, E, of 200.0 MPa and three values of puncture fracture toughness, $G_p$, within the range of values for human skin.

Figure **7.97** shows the effect of varying Young's modulus for skin, while keeping the puncture fracture toughness at a constant value of 7.0 KJ-$m^{-2}$. The plots show a large sensitivity to elastic modulus. While there is not a large difference in initial force and deflection, the plots quickly diverge due to the large of influence of modulus on friction forces and single needle deflections. This suggests that the force required to initiate penetration are more sensitive to changes in puncture fracture toughness than elastic

modulus. Eq. **7.9** shows that penetration initiation force, $F_i$, is related to puncture fracture toughness by $G_P^{2/3}$, while it is related to elastic modulus by $E^{1/3}$.

Elastic modulus has the largest impact on single needle deflection. Larger elastic modulii values for skin necessitate higher loads for the same amount of deflection. This is shown by Eq. **7.17,** which shows that single needle deflection is directly proportional to elastic modulus. Higher elastic modulii will also create higher friction forces that resist penetration.

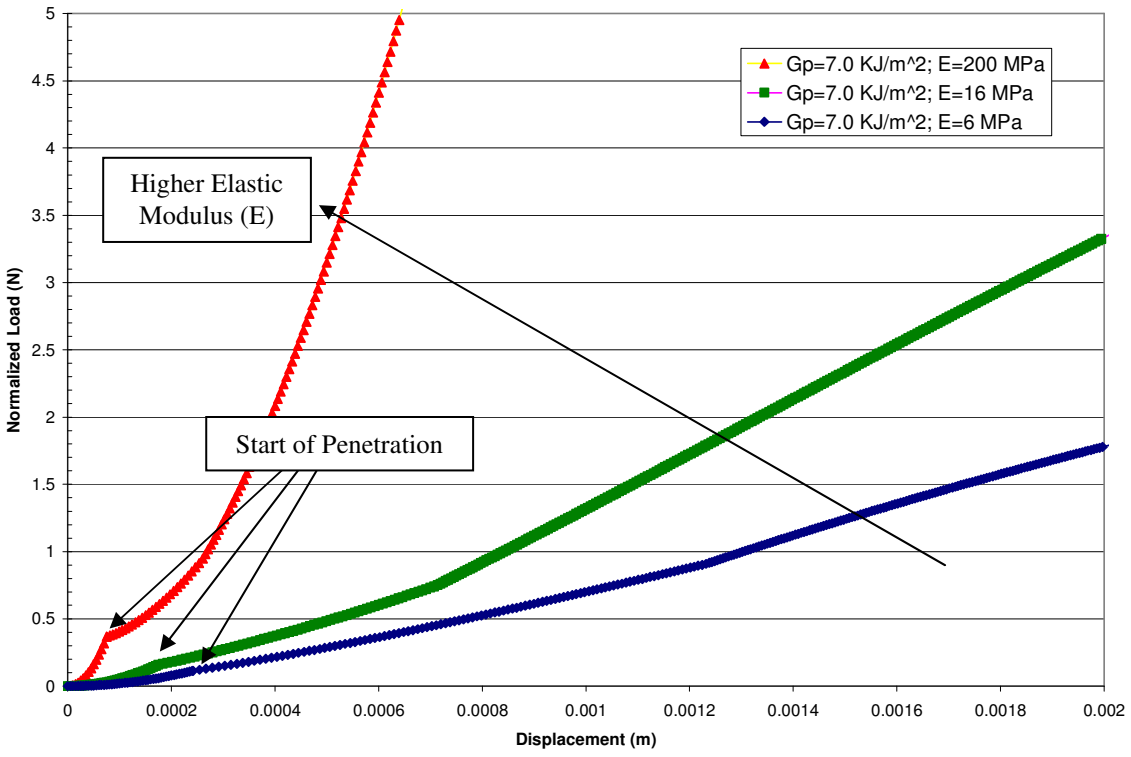


Figure **7.97**: Normalized load versus displacement for a constant puncture fracture toughness, $G_p$, of 7.0 KJ/m^2 and three values of Young's modulus, E, within the range of values for human skin.

Another consideration worth noting is that human skin is multi-layered with fat and muscle lying beneath the three primary skin layers. The fat and muscle, each with mechanical properties different from skin, will change the overall compliance when attempting to penetrate the skin using a microneedle device. The compliance will change for people with varying body compositions and for different locations on the body where there may be more or less subcutaneous fat. This will inevitably change the load versus displacement plots that would help determine how much force is needed to penetrate to a certain depth.

The mechanical properties of human skin can have a large impact on penetration load and displacement. Larger values of puncture fracture toughness will necessitate larger loads to initiate penetration. Larger values of elastic modulus will increase the force required to penetrate skin.

**Effect of Friction in Analysis**

Friction has a substantial effect on penetration load for given penetration depths. Friction enters the total penetration force equation at Eq. **7.15** and involves the normal force on the needle and the friction coefficient. Figure **7.98** shows the effects of varying the friction coefficient on the plot for penetration force versus penetration depth. The figure shows the effect on a single steel needle of increasing friction from 0.05 to 1.00 in increments of 0.05.

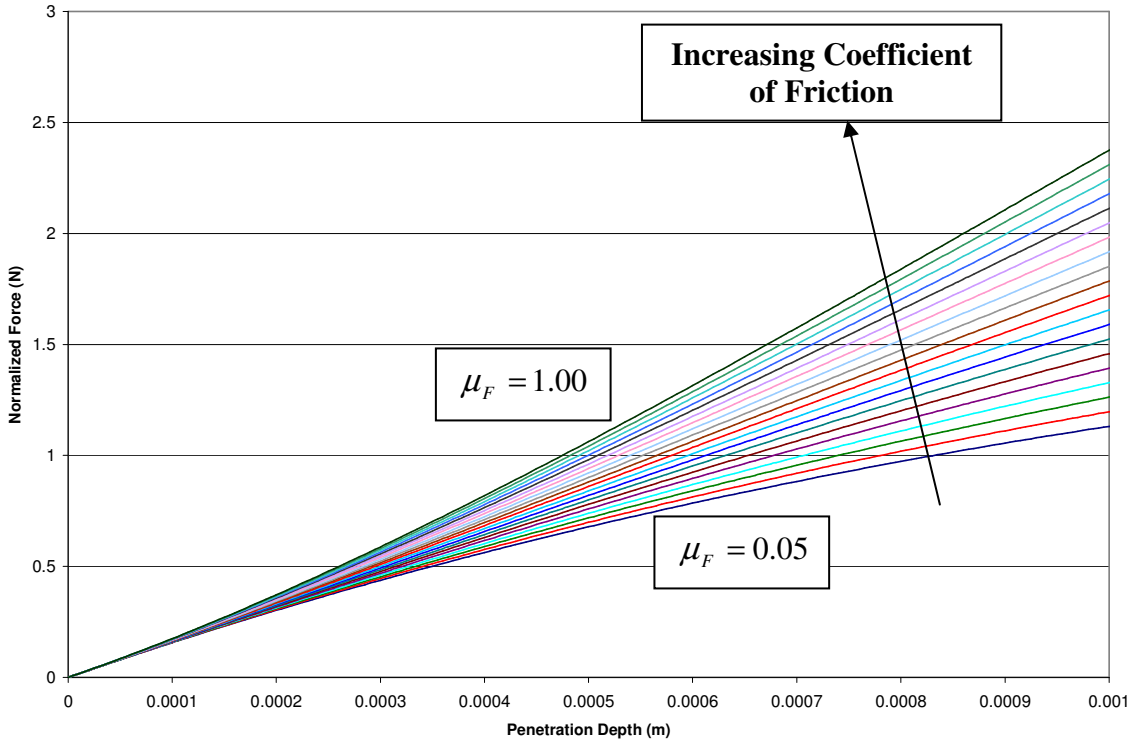


Figure **7.98**: Penetration force versus penetration depth on a single steel needle for an increasing friction coefficient.

The effect of friction widens between the lowest and highest friction coefficients as penetration depth increases. This is best explained by Eq. **7.15** which shows that friction force is directly proportional to both friction coefficient and the needle's average penetrating diameter. A larger penetrating diameter is the result of deeper penetration for a conical shaped needle and will cause a proportionally higher normal force. The friction coefficient translates normal force in the transverse direction to the penetration force. For example, a friction coefficient of one translates all force from the normal direction to the applied force direction. The force required to penetrate the needle to a 1 mm depth is approximately double for a friction coefficient of 1.00 compared to a friction coefficient

of 0.05. This shows that reducing the friction coefficient has a direct impact on reducing the force required for penetration. Various coatings and friction modifiers have been in the field of penetration science to reduce the effects of friction in skin penetration. Testing has suggested that reducing needle friction can be beneficial in decreasing discomfort associated with skin penetration (Stellman, 2009).

**Optimization of Needle Design**

A comparison of several different needle shapes shows that a column with a conical tip will maximize penetration depth and exposed surface area. Using the microneedle penetration analysis developed in this chapter shows that for a theoretical maximum insertion force of 5 N and 1 square cm area, a microneedle device with 49 needles and a conical tip can penetrate to a depth of 120 microns. The ideal needle shape has a tip radius of 10 microns, angle of 15 degrees, and a diameter of 50 microns. These dimensions are considered reasonable, given the demonstrated ability to fabricate molds with such dimensions. A needle length of 420 microns is sufficiently long enough to penetrate to the maximum depth of 120 microns. This is an improvement in the ratio of penetration depth to needle length when compared to the tested device needle lengths of 600 to 750 microns that were able to penetrate to depths of 120 to 185 microns.

A cone-tipped needle is able to penetrate deeper into skin compared to a conical shaped needle with the same tip radius and angle. Figure 7.99 shows a comparison of the two needle shapes. A conical needle of the same shape would penetrate to only 70 microns using the same constraints and would expose only 0.14 square mm of surface

area compared to a cone-tipped needle with the same tip geometry which would expose 0.40 square mm of surface area. This means that the cone-tipped needle would penetrate approximately twice as deep and expose approximately three times the surfaces area to tissue that could absorb the desired drug therapy.

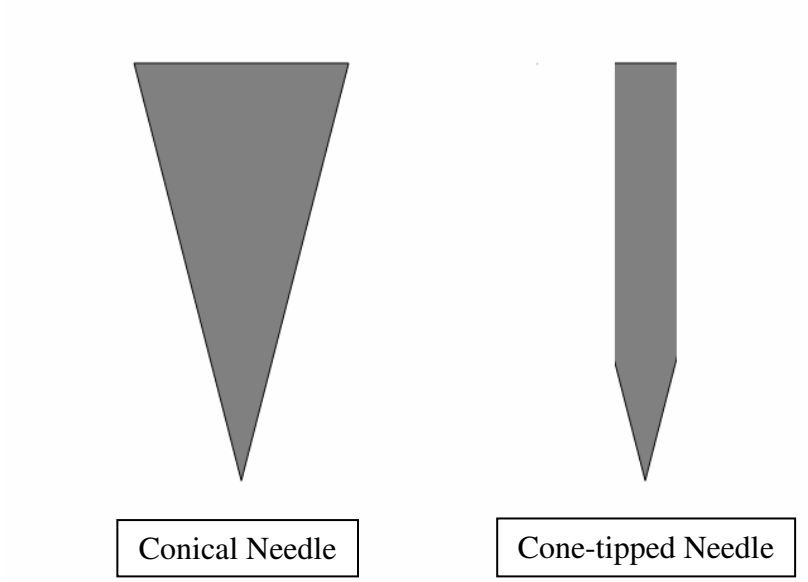


Figure **7.99**: Comparison of needle geometry for conical and cone-tipped needles.

The advantage of the cone-tipped needle over the conical needle comes from the mechanics of penetration that come from changing the needle shape. By fixing the needle's diameter, as in the cone-tipped needle, the penetration force that comes from crack growth is also fixed after opening the crack to the maximum needle diameter. From that point, only the friction force continues to increase which leads to a lower required application of force required to penetrate the skin. The crack initiation force will be the same for both the conical and cone-tipped needle because the tip geometry is exactly the same. Crack initiation force is dependant on only needle geometry and

material properties. The friction force will increase more slowly in the case of the cone-tipped needle because the normal force acting on the needle will only increase linearly due to increases in penetration depth and not increasing diameter. In the case of the conical needle, the normal force also increases as the penetrating diameter increases. This is because the rubber exerts more force on the needle the more the crack is opened. In the case of the cone-tipped needle, the only force that continues to increase after the transition to a fixed diameter is the friction force. This is because the crack growth force component is related only to the needle diameter and the crack initiation force is fixed after penetration begins.

The magnitude of the forces in the case of both the conical and cone-tipped needles is approximately the same. At 5 N of penetration force, the crack growth component is the largest force, followed by the crack initiation force, and the friction force is the smallest component. This is important for explaining why the cone-tipped needles are superior to the conical needles. The largest force component, crack growth force, will always increase in the case of the conical needle whereas it will stop increasing in the case of the cone-tipped needle design. This is because the crack does not need to grow any farther to accommodate the cone-tipped needle after the hole is opened to its full diameter. Only the smallest force, friction force, will continue to increase in the case of the cone-tipped needle. This means that a cone-tipped needle will always experience lower penetration force than a similarly shaped conical needle.

Another theoretical exercise for optimizing microneedle involves doubling the applied penetration force from 5 N to 10 N. The cone-tipped needle remains the best design with an increase in penetration force. Continuing with a fixed area of 1 square

cm, the best design would simply increase the number of needles from 49 to 100 and sacrifice a few microns of penetration depth compared to the 49 needle, 5 N penetration force design. This would also require a slight increase in the needle length from 420 to 430 microns to accommodate the extra multiple needle deflection that would occur. This would effectively double the exposed surface area available for drug delivery from the needles.

A final scenario involves the doubling the length of each side of the array from 1 cm to 2 cm resulting an increase in area from 1 square cm to 4 square cm. In this case, assuming no increase in the allowed penetration force of 5 N, increasing the spacing between needles is the best design change. This case should maintain the cone-tipped needle design discussed and spread the needles over a larger area. This allows the needle length to decrease to 410 microns due to the decrease in multiple needle deflection. These optimal theoretical designs demonstrate that the analysis methods developed in this project can provide guidance to future researchers in the area of microneedle design and optimization.

**Summary**

This chapter has outlined the development of an analytical model summarized in figures **7.17** and **7.18** that is used to predict the behavior of microneedle penetration. These equations incorporate many of the important attributes relating applied force to penetration depth including needle geometry, mechanical properties of skin, friction

effects, and needle spacing. Results from steel needle testing were used to construct missing material properties and refine the model.

The calculated outputs from the analytical model, shown in figures **7.17** and **7.18**, were compared to the measured steel needle test results. Comparisons were made between plots for measured and calculated data for each multiple steel needle pattern and show there is reasonable agreement. There is error in the ability of the analytical model to accurately predict load versus displacement as well as measurement error. Other sources of error include deficiencies in the model to predict other physical events such as the difference in the effect of needles located on the perimeter of a multiple needle pattern versus an interior needle. The analytical model provides a good prediction of the trends of measured data based on needle and skin attributes.

Penetration depths for the polymer microneedle devices were limited by the lengths of the needles. Comparisons of the predicted and measured data for polymer microneedles devices show that there is little difference for the patterns tested due to the minor influence of the needle spacing on total displacement at such shallow penetration depths and relatively large spacing. Yan, in a study that evaluated microneedle length and density in the consideration of optimizing drug delivery, that only microneedle arrays with lengths larger than 600 microns were effective at enhancing drug flux across the skin (Yan *et al*., 2010). Another study notes that for a device with 1 mm length microneedles, penetration of only about 200 microns was observed (Crichton *et al.*, 2010, p. 4563). This seems to agree with the findings of this study that show that needles with lengths of approximately 600-750 microns penetrate only 100-185 microns to create a drug pathway. Needle spacing, pattern type, tip radii, and needle length are the only

differences between different polymer microneedle devices that are included in the analytical model. The analytical model provides good predictions for the general trends based on various needle and skin attributes.

The sensitivity of selected needle and skin properties and friction coefficients were examined using the analytical model shown in figures **7.17** and **7.18**. Needle tip radius and angle were shown to have an influence on the required force and displacement to initiate skin penetration. Larger tip radii and larger angles require more force to start penetration as shown in figure **7.93**. Higher values of puncture fracture toughness are shown to require more force and displacement from to initiate skin penetration. Higher skin elastic modulii were also shown to require higher force levels to start penetration, higher force levels to continue penetration due to friction, and higher force levels to cause single needle deflection.

Friction coefficient greatly impacts penetration force. Higher friction coefficients will cause an increase in the force applied to the needle to continue penetration. Another friction force consideration comes from the effect of closely spaced needles causing higher normal forces. This is due to the higher stretch ratio of multiple needles compared to a single needle. Although this was not specifically included in the model, it will have an effect on the penetration forces that are recorded. Lower friction coefficients are better for decreased pain sensation due to the lower force required for penetration (Busillo, 2008; Stellman, 2009).

Tip sharpness has a definite impact on the predicted behavior of microneedle devices during penetration. Tip sharpness is measured by tip angle and tip radius. Smaller tip angles and radii are preferred to decrease the force required to initiate skin

penetration. This can be seen in Figure **7.93** which shows that smaller tip angles and radii have a large influence on initial penetration force. The effect of tip radius can be seen in measured data when comparing microneedle devices made from different polymers in Figure **7.87**. In that figure, the Makrolon material has an average tip radius of 32 microns versus 15-23 microns for the other materials. The figure shows that the larger tip radii of the Makrolon material increases the force required for penetration for all displacement values.

Sharper needles are more desirable for patient comfort and enhanced drug delivery. This is because a sharper needle requires less force and skin deflection before the start of penetration. Less force will result in less pain sensation for the patient. Sharper needles will also enhance drug delivery by penetrating to the required depth with shorter needles and with less skin deflection. The relationship between lower pain perception due to sharper tips and less skin deflection was observed in two separate studies (Khanna *et al*., 2010; Yan *et al*., 2010).

Needle length will influence the penetration depth of a microneedle device. The force increases quickly after the needle length is reached as seen in the testing of each microneedle device. Once reached, the base of the device will only work to compress the skin simulant and will not penetrate further. This indicates that needle length is critical to predicting needle penetration depth. As seen in Table **7.3**, needle length and sharpness, which reports the required initial penetration force and displacement, are the two main factors in predicting penetration depth. This point is echoed by the literature, which notes that sharp needle tips are critical to overcome the deflection of the skin under load (Khanna *et al*., 2010; Park & Prausnitz, 2010, p. 1223).

Needle length plays a role in both pain felt by the patient and proper drug delivery. Longer needles will increase pain sensation to a patient because of activation of more nerve endings at larger penetration depths. Tissue beyond the first two skin layers contains increasing numbers of nerve endings and the patient will experience more pain with longer needles. For drug delivery, needle length should be selected for the penetration depth required for a specific treatment. Treatments may need to be delivered into varying skin depths depending on the specific application.

Needle spacing is an attribute that has a role in predicting penetration behavior of a microneedle device. The "bed of nails" effect can be seen clearly through examination of the steel needle analysis. The closest needle spacing of 0.75 mm shows that there is a measurable amount of extra material deflection compared to the farthest needle spacing of 2.50 mm. This can be attributed to the array of needles acting like a solid object pressing into the rubber skin simulant and no longer penetrating after a certain point. The 2.50 mm steel needle spacing had very little of this multiple needle effect throughout penetration. This effect was modeled by using the compressive properties of the rubber under a solid object and spacing of the needles to show how the total displacement is affected.

The effect of spacing needles in a pattern will have a definite effect on pain sensation and drug delivery for a patient. Larger distances between needles are preferable on both matters due to the increased skin deflection associated with closely spaced patterns. Patterns with close distances between needles will cause the skin to compress more for a given amount of penetration. The needle spacing will also affect drug delivery due to the decreased penetration possible with more closely spaced

patterns. However, the desire for less skin deflection also would need to be balanced with the desire for a more compact device and the actual depth of penetration desired for the particular drug being delivered.

Both square and hexagonal patterns were tested. Testing showed there was a small but noticeable difference in the amount of total displacement for square and hexagonal patterns. Square patterns were shown to have a larger effective distance between needles than a similarly spaced hexagonal pattern. This effect was modeled by Eq. **7.24** that adjusts the spacing for a square pattern to simulate a hexagonal pattern. A hexagonal pattern has equal spacing between all adjacent needles while a square pattern has differing distances between diagonal and orthogonal needles. The selection of a square needle pattern compared to a hexagonal pattern has no effect on minimizing pain or maximizing drug delivery when adjusted for the spacing effect.

In summary, this chapter has discussed the results of penetration testing presented in Chapter 6. The results were used to develop an analytical model relating penetration forces, penetration depths, and material compression. Comparisons were be made between various attributes including mechanical skin properties, needle features, and friction properties. Chapter 8 will present conclusions of work performed and recommendations for future work.

# Chapter 8

## Conclusions and Recommendations

This chapter presents conclusions of work performed and recommendations for future work.

## Conclusions

- Solid polymer microneedle devices were successfully created using the injection molding process. A total of four different molds were fabricated in patterned arrays that included square and hexagonal patterns and two spacing distances. Four polymers were successfully injection molded including polystyrene, Topas cyclic olefin copolymer, glass reinforced Solvay IXEF polyarylamide, and glass reinforced Ticono Vectra liquid crystal polymer. Molded parts showed that microneedle tip radii below 15 microns can be achieved using this injection molding technique.
- Injection molds were created using a process that utilized the mechanical properties of two different materials and a manufacturing technique that combines drilling and indenting to create sharp-tipped microneedles at low cost. These mold fabrication techniques use simple machining operations that can

performed at most machine shops for little cost to create high quality molds with microneedle tip radii of less than 10 microns.

- An economic analysis showed that solid injection molded polymer microneedle devices can be manufactured for a market acceptable cost of $0.10 – $0.179 per part. The added benefits of low pain perception, improved drug delivery for certain treatments, and the possibly of being recyclable make injection molded microneedle devices more desirable. Testing and analysis show that the microneedle devices can penetrate skin to depths between 120 and 185 microns depending on pattern and certain molded attributes like tip radius and needle length.
- Penetration testing of solid polymer microneedle devices was successfully performed using a grade of silicone rubber with mechanical properties similar to human skin.
- Testing showed that needle spacing in solid needle arrays is a factor in the amount of skin deflection experienced during penetration. A larger distance between adjacent needles in a pattern reduces skin deflection and allows individual needles to act independently. A smaller distance between adjacent solid needles causes the entire pattern of needles to act more like a solid surface and causes more skin deflection than penetration.
- Analysis showed that square and hexagonal needle arrays behave differently because of spacing between adjacent needles. It was shown that a square pattern can be transformed to simulate a hexagonal pattern with more distance between needles.

- Testing and analysis showed that sharper needle tips and a lower friction coefficient will decrease the force and deflection required to penetrate to the desired skin depth and allows for shorter needles to be used. Lower force and less deflection will cause less pain sensation for a patient and presumably allow for better drug delivery.
- Needle length is critical to the determination of penetration depth. Needle length, as measured from the base of a device, can be selected to determine how deep it can penetrate. This has real implications for pain sensation and drug delivery. Longer needles will cause a patient more pain due to more stimulation of nerves deeper in the skin. Needle length can be selected for the drug therapy being delivered to target a specific depth for maximum effectiveness.
- Penetration testing of solid steel needles patterns in a flexible fixture helped to develop the analytical model and clearly showed the relationship between solid needle spacing and skin deflection.
- An analytical model was developed that can be used to predict the effects of various microneedle and skin characteristics. The model was based on a published literature sources and was refined and compared with results from solid steel needle testing. The analytical model accounts for the microneedle properties like coefficient of friction, tip radius, tip angle, and needle spacing. Also explained in the model are the skin or simulant mechanical properties such as elastic modulus, mode I fracture toughness, and puncture fracture toughness. The accuracy of the model is greatly enhanced when considering the variation of needle length, tip radii, and testing inaccuracies. These inaccuracies are

incorporated into the predicted model using a type of Monte Carlo methodology to classify these indefinite errors.

- The analytical model is shown to be a reasonable predictor of penetration behavior for solid needles in a structured pattern. Comparisons were made between predicted data based on the analytical model and actual test results of solid steel and polymer needle patterns and show agreement above 90% when the error is classified for differing levels of needle length variation.

## Recommendations for Future Work

Several variations and improvements can be made to enhance aspects of testing, analysis, and injection molded microneedle devices. One such variation of interest comes from the ability to fabricate hollow microneedles. Hollow microneedles have been created using wafer fabrication techniques, but are not common with polymer microneedles. A hollow microneedle array may give the ability to actively inject drug therapies, rather than the passive absorbance possible with solid microneedles.

Future testing should include more extensive friction testing. This study dealt only with testing friction effects on the solid steel needles due to the ease of testing. Future testing should explore plastic microneedle friction coefficients and the measured effects of friction modifiers. Such testing has been more extensively performed with hypodermic needles using silicone-based lubricants and friction reducers such as Triboglide and MDX (Busillo, 2008; Stellman, 2009). Other studies testing the effects of

friction on successful needle penetration have shown that reducing the amount of force needed to penetrate into skin and may decrease pain sensation.

Further studying the effect of friction in multiple needle arrays would enhance the prediction model that was developed. Normal force will increase from the higher stretch ratio between needles in an array compared to a single needle acting alone. Higher normal forces acting on the needles will increase the amount of force required to penetrate the skin.

Another testing variation would be to add biological samples. Other research groups have evaluated needle penetration using human and animal skin. Such testing is more cumbersome and involves proper cleanliness and disposal practices, but offers more realistic testing compared to using non-biological skin simulants. Pig skin is a good candidate for biological testing due to the similarity of its mechanical properties to human skin. Chicken breasts and other animal sections also could be evaluated. Tests on skin simulants and biological samples must eventually lead to testing in live human subjects. *In vivo* testing is the only true measure of microneedle penetration ability and pain-perception due to the inevitable differences present between skin simulants, animals, and humans.

Utilization of *in vivo* testing would greatly enhance the understanding of the relationship between drug delivery and penetration mechanics. The link between these concepts is important because research has shown that there is a close connection between the size of a drug's molecule and the depth of penetration required for effective delivery to the body (Yan, Warner, Zhang, Sharma, & Gale, 2010). Other studies have shown that needle density is also related to the ability of a microneedle device to achieve

sufficient drug flux across the skin to deliver the proper treatment dosage (Al-Qallaf, Das, & Davidson, 2009). Linking the understanding of penetration mechanics with the biological response of the body to specific drug therapies will help to further the field of microneedle drug delivery research.

Another logical step in the field of injection molded microneedles is to study the efficacy of coating polymer needles with a biocompatible drug suspension. Coating microneedles with a drug suspension has been successfully accomplished using metallic microneedles, but has not been used with polymer needles (Koutsonanos et al., 2009). Drug coated polymer microneedles need to be studied to ensure that the drug suspension adheres to the needles, maintains the ability to puncture the skin, and can successfully deliver the therapy to the body. Demonstration of such drug delivery using coated polymer microneedles would show that such devices are indeed a viable technology with the ability to provide a low cost solution for transdermal drug delivery.

Several sources of error were suggested during the analysis of penetration forces, however, more work needs to be completed to positively identify the source and magnitude of each source of error. These error sources include testing that is non-orthogonal to the surface of the rubber, needle length variation, needle tip radius variation, and inter-needle normal forces that were left unaccounted for in the penetration analysis.

Classifying error sources that were described using the Monte Carlo error analysis method includes the angle that the needles penetrate the rubber skin and the variation in needle length. These sources of error are confounded and further testing is needed to identify the magnitude of each error and its contribution to the penetration analysis in

order to improve future analysis. The most direct way to separate these effects is to measure each effect separately. First, measuring the length of a large number of needles in each microneedle devices and performing penetration testing with those devices will allow for a direct comparison of the actual and theoretical needle length standard deviation. Any residual difference in the results could be properly attributed to the angle of approach of the microneedle devices during testing.

Another way to classify these errors is to improve the fixture that holds the microneedle device and restricts movement to only one direction. This would help to eliminate any error that can be attributed to the microneedle device's testing angle. Such a device can be envisioned having precise linear bearings that allow movement only in the z-direction.

The last identified errors that can be better evaluated are the inter-needle forces that affect normal force acting between multiple needles in an array. This increased normal force will act to increase the friction force during penetration as the needles penetrate deeper into the skin. Measuring this force involves further separation of single needle forces from multiple needle forces. This could be accomplished by first measuring penetration force on a single needle. Next, a second needle with the same length could be added at known distances. This would add the effect of only normal force increase without aliasing other effects. Next, a single square pattern consisting of four needles at set distances could be tested to determine any effects for a single square pattern. Doing this type of experiment for each pattern type would help to further classify sources of error that cause differences between the measured and theoretical

results. Further classification and measurement of the present errors would help to improve understanding of microneedle penetration analysis.

The use of a flexible base may offer advantages over the stiff base used for this project. First, a flexible base would allow a microneedle device to form to the contours of the skin. Very few, if any, locations on the human body are flat. This makes it difficult to effectively penetrate the skin with all needles of a microneedle device with a stiff base. A device with a flexible base would mold to the contours of the skin and could be embodied as a patch using adhesive to stick to the skin.

Another advantage a flexible base may offer is the ability to penetrate the skin with lower localized forces. Because the base is flexible, smaller sections of needles could penetrate with less force than it would take to penetrate the entire patch simultaneously. This would lessen restrictions on overall force because small regions could penetrate the skin separately. This would also allow a higher overall number of needles to be located on the same patch to maximize drug delivery without compromising on insertion force.

The needle shape and needle spacing on a microneedle device with a flexible base may differ slightly from the optimal design depending on the intended use. One idea is to have multiple needle arrays located on the same flexible patch. This would allow the patient to stay below the 5 N insertion force limit, but could deliver larger quantities of medication than a single array. Such a device would allow a user to apply one small array at a time, rather than a large array of needles at once. This would distribute the applied force over many small sites. Needle shape for a flexible base design would not

differ much from the optimal design. A cone-tipped columnar needle with a sharp tip and small diameter offers deep dermal penetration at low force values.

Flexible base microneedle devices offer definite advantages over devices with a stiff base. Producing a flexible base device can likely be accomplished using injection molding. Most non-reinforced polymers are mechanically flexible in thin sections. A thin-base microneedle device would require well designed runners, gates, and ejectors to prevent sticking to the mold and to produce good parts. Also, the mold design would likely need to be heated and cooled to ensure complete mold filling and release due to the large surface area - to - volume ratio. Such technical challenges can be overcome and would result in an improved microneedle design with the low cost benefit of injection molding.

Improvements and alterations of the mold fabrication process could be implemented. One such improvement that could make an immediate impact is to create a single-piece mold without removable inserts. This would remove the gaps between the mold inserts and the larger mold block. The gaps prevent the two mold plates from fully sealing and cause excessive flash.

The molds used in this project can be considered proof-of-concept molds that can be easily modified and are capable of producing only two parts at a time. Several changes can be envisioned that would improve the quality of parts produced. One idea that builds on the existing manufacturing method of drilling and indentation would be to utilize a harder indenter material that can create smaller tip radii than the cobalt-steel tools used in this project. A diamond indenter was special ordered for this project and was used to create tip radii as small as 2 microns. Unfortunately, the diamond became

detached from its shank during one trial and became unusable. Further testing may show that use of a diamond indenter in conjunction with higher quality drilling tools will allow for even smaller mold tip radii. Use of a higher quality high speed milling machine with higher x-y accuracy as well as a CNC-programmable z-axis would help to improve the quality of the part molds by improving the ability to indent the mold directly on top of the drilled cavity and removing the human influence on machining.

Electrical discharge machining is commonly used for mold fabrication. The sinker version of this technology uses a consumable electrode that is usually made from either graphite or bronze. An electrical current is passed from the electrode into the part through a dielectric liquid to liquefy and remove material from the mold. This results in a mold cavity that can be made very precisely with small feature sizes. The nature of the process allows any electrically conductive material to be used for molds and eliminates the need for traditional machining or forming tools. This would allow the molds to be made from hardened steel to improve longevity. The biggest drawback to this method includes the cost, which may be very high for parts that require small geometries like a microneedle tip. EDM would enable a larger variety of needle shapes to be manufactured.

Another potential improvement to the injection molds is reducing the surface roughness of the molds. This would improve the resulting microneedle devices in two ways. The reduced roughness would reduce friction that the polymer will encounter during the injection molding process. This would allow for more complete filling of the molds before the polymer freezes by reducing the obstructing friction forces. The reduced roughness will also result in a smoother finished microneedle tip. The reduction

in surface asperities would reduce friction during skin penetration. This would allow for deeper penetration at lower force levels. Surface roughness can be improved in a variety of ways including changing parameters to machine the small features more slowly, using sharper machining tools, and adding polishing operations.

One last way to improve the microneedle molds includes drilling a through-hole in the needle tip cavities to relieve any air pressure in the mold. This would include drilling a hole at the tip of each cavity smaller than the desired tip radius. Relieving air pressure inside the mold cavity in this way is a similar concept to using a vacuum to draw material into a mold to allow the liquid polymer to completely fill the mold during the filling process. Drilling a small hole in the mold could be accomplished by drilling from the back-side of the mold, although this would be a technical challenge to locate the small features accurately. Improving the molds for manufacturing environments is a challenge. By implementing some of the ideas outlined may help advance the technology to make it technically viable.

Injection molding the plastic microneedle devices presented several challenges where future improvements could be explored. Molded features such as tip radii and length consistency could be improved. The methods used for molding parts could be enhanced using certain well-known techniques that increases part consistency and may increase the range of materials that could be tested. The molds used during for this project could also be improved to enhance the parts that are produced.

There is a large range of injection molding variations that can be employed to improve critical features, reduce part warpage, and improve cycle times on molded parts. One basic technique known to enhance complete filling of a mold cavity is to heat the

mold. Heating molds will allow molten material more time to completely fill the mold cavity. More completely filling a mold would enhance microneedle devices by ensuring that material reached the tip of the mold cavities and make for sharper needle tips. This would also allow for a wider range of materials to be used that would normally freeze prior to reaching the mold tips. Heating a mold is normally accomplished in one of two ways; running a hot fluid through the mold or using electric heaters. Water or oil are normally used in hot fluid mold heating and normally make for an evenly heated mold, but can be more cumbersome to use due to extra maintenance and equipment that is required. More common are electric mold heaters that are easily installed and require little maintenance, but do not create uniform mold temperatures due to their constant on-off cycling.

Mold cooling can be used to enhance injection molded parts. This is accomplished by installing passageways for water through the mold. This allows for the molded parts to be quickly and uniformly cooled. Uniform cooling reduces part warpage by evenly cooling all areas of a part and reducing hot-spots in the part. Hot-spots in the part can cause a part to shrink in localized areas and distort resulting in warpage. Keeping a flat part is ideal for microneedle devices because the needle tips should be uniform in height from the base. Mold cooling also has advantages in improved cycle times because parts are frozen much sooner compared to non-cooled molds. Improved cycle times are important in mass production scenarios.

Another idea to improve the process of injection molding is to utilize a mold filling simulation to optimize the mold design. Software packages such as Autodesk Moldflow(R) help designers improve injection molds and processes using solid 3D

models. This includes improving the gate and runner system for the microneedle device and optimizing the machine settings. This would help to ensure that the mold is filled completely without premature freezing and would improve surface finish and minimize waste.

Finally, adding a vacuum system to the injection molds would allow complete evacuation of air from the mold cavity. This would enable better part filling by eliminating the pressure pockets that build up inside the needle mold tips. The needle mold tips were measured to be as small as 5 microns, however, the smallest tip radii achieved on the microneedle parts was 10 microns. Eliminating the air pocket as well as heating the injection molds would allow the liquid polymer to fill this space during filling and would result in better part quality with sharper microneedle tips.

The ideal material for use in microneedle devices is a biodegradable plastic that would decompose and eliminate all waste products. Such materials would enable a device to deliver drug therapies without the waste produced by hypodermic needles. Ideally a biocompatible polymer could be used that would also eliminate the sharps hazard by dissolving the needle tips into the body as part of the drug delivery process. The feasibility of injection molding biodegradable polymers for microneedle devices has yet to be proven, but some materials exist that may well work in such an application.

Polylactic acid is one polymer that could be tested for use in microneedle devices. Certain grades of PLA can be injection molded and have strength and stiffness comparable to unfilled polystyrene ("Prospector - NATUREPLAST PLI 005," 2010). One big advantage of PLA is that it is already in use in other medical applications. This indicates that regulatory approval for manufacturing and testing microneedle devices

made from this material would happen more quickly than other unproven materials. Other materials that should be considered include polydioxanone and polygylcolic acid which are both commonly used in dissolving sutures (Lai, 2010). Injection molded microneedles that can be made to dissolve after contact with tissue, but are strong enough to withstand penetration forces would be a positive evolution in drug delivery.

Improvements to the analytical model would increase the correlation between predicted data and measured data. Such improvement may include the ability to quantify and include measurement error into the model using statistical enhancements based on measured needle attributes like needle length variations, tip radius variations, and needles that are non-orthogonal to the base of the device. Including testing errors would also enhance the prediction capacity of the model by being able to include angular approach of the needle device to the skin simulant. Another possible improvement comes from including the effects of needles at the edge of a pattern that are different from interior needles. The current model treats all needles as interior needles and ignores differing effects on force and displacement.

Employing certain enhancements to the molding process, improving the molds, and selecting the correct polymers may one day allow microneedles to become a viable drug delivery technology. Drug coating research must also be completed to prove that solid polymer microneedles can be coated to deliver drug therapies. If these steps are taken and human trials prove successful, microneedles may one day help to increase patient comfort and become a dominant drug delivery technology.

## Bibliography


Ai-Qallaf, B., & Das, D. (2008). Optimization of square microneedle arrays for increasing drug permeability in skin. *CHEMICAL ENGINEERING SCIENCE*, *63*(9), 2523-2535.

Allegro Medical Supplies, Inc. (2009). . Retrieved April 9, 2009, from http://www.allegromedical.com/index.html

Aoyagi, S., Izumi, H., Isono, Y., Fukuda, M., & Ogawa, H. (2007). Laser fabrication of high aspect ratio thin holes on biodegradable polymer and its application to a microneedle. *SENSORS AND ACTUATORS A-PHYSICAL*, *139*(1-2), 293-302.

Boothroyd, G., Knight, W., & Dewhurst, P. (2001). *Product Design for Manufacture & Assembly Revised & Expanded* (2nd ed.). CRC.

Briscoe, B., Sebastian, K., & Adams, M. (1994). THE EFFECT OF INDENTER GEOMETRY ON THE ELASTIC RESPONSE TO INDENTATION. *JOURNAL OF PHYSICS D-APPLIED PHYSICS*, *27*(6), 1156-1162.

Burford, R. P., & Potok, A. (1987). The fracture toughness of polybutadiene and other elastomers in cold nitrogen gas. *Journal of Materials Science*, *22*(5), 1651-1656. doi:10.1007/BF01132387

Busillo, E. (2008). *Characterization of Plastic Hypodermic Needles*. Georgia Institute of Technology.

Centers for Disease Control and Prevention. (2007). National Center for Immunization

and Respiratory Diseases. *Estimated Vaccination Coverate with Individual Vaccines and Selected Vaccination Series*. Retrieved October 30, 2007, from http://www.cdc.gov/vaccines/stats-surv/nis/data/tables_2006.htm

Chen, B., Wei, J., Tay, F., Wong, Y., & Iliescu, C. (2008). Silicon microneedle array with biodegradable tips for transdermal drug delivery. *MICROSYSTEM TECHNOLOGIES-MICRO-AND NANOSYSTEMS-INFORMATION STORAGE AND*, *14*(7), 1015-1019.

Cormier, M., Johnson, B., Ameri, M., Nyam, K., Libiran, L., Zhang, D., & Daddona, P. (2004). Transdermal delivery of desmopressin using a coated microneedle array patch system. *JOURNAL OF CONTROLLED RELEASE*, *97*(3), 503-511.

Crichton, M., Ansaldo, A., Chen, X., Prow, T., Fernando, G., & Kendall, M. (2010). The effect of strain rate on the precision of penetration of short densely-packed microprojection array patches coated with vaccine. *BIOMATERIALS*, *31*(16), 4562-4572. doi:10.1016/j.biomaterials.2010.02.022

Datamonitor. (2002). Vaccines Industry Profile: United States.

Davis, S., Landis, B., Adams, Z., Allen, M., & Prausnitz, M. (2004). Insertion of microneedles into skin: measurement and prediction of insertion force and needle fracture force. *JOURNAL OF BIOMECHANICS*, *37*(8), 1155-1163.

Davis, S., Martanto, W., Allen, M., & Prausnitz, M. (2005). Hollow metal microneedles for insulin delivery to diabetic rats. *IEEE TRANSACTIONS ON BIOMEDICAL ENGINEERING*, *52*(5), 909-915.

Dorlands Directories. (1999). Needles and Syringes (and Catheters): The World Markets. *Medical & Healthcare Marketplace Guide: I-830*.

Egekvist, H., Bjerring, P., & Arendt-Nielsen, L. (1999). Pain and mechanical injury of human skin following needle insertions. *EUROPEAN JOURNAL OF PAIN*, *3*(1), 41-49.

Food and Drug Administration. (2003). Food and Drug Administration: Device Advice. Retrieved April 9, 2009, from http://www.fda.gov/cdrh/devadvice/pma/review_process.html#steps

Hendriks, F., Brokken, D., Oomens, C., Baaijens, F., & Horsten, J. (n.d.). Mechanical Properties of Different Layers of Human Skin.

Instron. (2009). 2525 Series Drop-through Load Cells. Retrieved December 10, 2009, from http://www.instron.us/wa/acc_catalog/prod_list.aspx?cid=480&cname=2525%20Series%20Drop-through%20Load%20Cells

Izumi, H., & Aoyagi, S. (2007). Novel fabrication method for long silicon microneedles with three-dimensional sharp tips and complicated shank shapes by isotropic dry etching. *IEEJ TRANSACTIONS ON ELECTRICAL AND ELECTRONIC ENGINEERING*, *2*(3), 328-334.

Kaushik, S., Hord, A., Denson, D., McAllister, D., Smitra, S., Allen, M., & Prausnitz, M. (2001). Lack of pain associated with microfabricated microneedles. *ANESTHESIA AND ANALGESIA*, *92*(2), 502-504.

Khanna, P., Luongo, K., Strom, J., & Bhansali, S. (2010). Sharpening of hollow silicon microneedles to reduce skin penetration force. *JOURNAL OF MICROMECHANICS AND MICROENGINEERING*, *20*(4). doi:10.1088/0960-1317/20/4/045011

Khumpuang, S., Horade, M., Fujioka, K., & Sugiyama, S. (2007). Geometrical strengthening and tip-sharpening of a microneedle array fabricated by X-ray lithography. *MICROSYSTEM TECHNOLOGIES-MICRO-AND NANOSYSTEMS-INFORMATION STORAGE AND*, *13*(3-4), 209-214.

Koutsonanos, D., Martin, M., Zarnitsyn, V., Sullivan, S., Compans, R., Prausnitz, M., & Skountzou, I. (2009). Transdermal Influenza Immunization with Vaccine-Coated Microneedle Arrays. *PLOS ONE*, *4*(3). doi:10.1371/journal.pone.0004773

Kumar, R., & Philip, A. (2007). Modified Transdermal technologies: Breaking the barriers of drug permeation via the skin. *TROPICAL JOURNAL OF PHARMACEUTICAL RESEARCH*, *6*(1), 633-644.

Lee, J., Park, J., & Prausnitz, M. (2008). Dissolving microneedles for transdermal drug delivery. *BIOMATERIALS*, *29*(13), 2113-2124. doi:10.1016/j.biomaterials.2007.12.048

Li, X., Zhao, R., Qin, Z., Zhang, J., Zhai, S., Qiu, Y., Gao, Y., et al. (2010). Microneedle pretreatment improves efficacy of cutaneous topical anesthesia. *The American Journal of Emergency Medicine*, *28*(2), 130-134. doi:10.1016/j.ajem.2008.10.001

Marchal, Y., Oldenhove, B., Daoust, D., Legras, R., & Delannay, F. (1998). Characterization of the fracture toughness of rubber-toughened polypropylene thin plates. *POLYMER ENGINEERING AND SCIENCE*, *38*(12), 2063-2071.

Martanto, W. (2005). *Microinjection into Skin Using Microneedles*. Georgia Institute of Technology.

Matriano, J., Cormier, M., Johnson, J., Young, W., Buttery, M., Nyam, K., & Daddona, P. (2002). Macroflux (R) microprojection array patch technology: A new and

efficient approach for intracutaneous immunization. *PHARMACEUTICAL RESEARCH*, *19*(1), 63-70.

McAllister, D. V. (2000). *Microfabricated Needles for Transdermal Drug Delivery*.

Moh, J., Kim, M., Lee, T., Khang, G., Lee, H., Rhee, J., & Lee, H. (2009). Transdermal Microneedle for Drug Delivery Applications (Retraction of vol 4, pg 174, 2007). *TISSUE ENGINEERING AND REGENERATIVE MEDICINE*, *6*(14), 1446-1446.

Park, J., Allen, M., & Prausnitz, M. (2005). Biodegradable polymer microneedles: Fabrication, mechanics and transdermal drug delivery. *JOURNAL OF CONTROLLED RELEASE*, *104*(1), 51-66.

Park, J., & Prausnitz, M. (2010). Analysis of the Mechanical Failure of Polymer Microneedles by Axial Force. *JOURNAL OF THE KOREAN PHYSICAL SOCIETY*, *56*(4), 1223-1227. doi:10.3938/jkps.56.1223

Park, J., Yoon, Y., Choi, S., Prausnitz, M., & Allen, M. (2007). Tapered conical polymer microneedles fabricated using an integrated lens technique for transdermal drug delivery. *IEEE TRANSACTIONS ON BIOMEDICAL ENGINEERING*, *54*(5), 903-913.

Prausnitz, M., Mitragotri, S., & Langer, R. (2004). Current status and future potential of transdermal drug delivery. *NATURE REVIEWS DRUG DISCOVERY*, *3*(2), 115-124.

Prospector - Ixef® 1022. (2010, February 10). . Retrieved February 24, 2010, from http://prospector.ides.com/DataView.aspx?E=2131

Prospector - Makrolon® 2207. (2010, February 10). . Retrieved February 24, 2010, from http://prospector.ides.com/DataView.aspx?E=64445

Prospector - Makrolon® 2458. (2010, February 10). . Retrieved February 24, 2010, from http://prospector.ides.com/DataView.aspx?E=1133

Prospector - Polystyrol 145 D. (2010, February 10). . Retrieved February 24, 2010, from http://prospector.ides.com/DataView.aspx?E=97477

Prospector - Topas® 5013S-04. (2010, February 10). . Retrieved February 24, 2010, from http://prospector.ides.com/DataView.aspx?E=38791

Prospector - Topas® 8007X10. (2010, February 10). . Retrieved February 24, 2010, from http://prospector.ides.com/DataView.aspx?E=83582

Prospector - Vectra® A130. (2010, February 10). . Retrieved February 24, 2010, from http://prospector.ides.com/DataView.aspx?E=83

Reed, M., & Lye, W. (2004). Microsystems for drug and gene delivery. *PROCEEDINGS OF THE IEEE*, *92*(1), 56-75.

Roxhed, N., Gasser, T., Griss, P., Holzapfel, G., & Stemme, G. (2007). Penetration-enhanced ultrasharp microneedles and prediction on skin interaction for efficient transdermal drug delivery. *JOURNAL OF MICROELECTROMECHANICAL SYSTEMS*, *16*(6), 1429-1440.

Sammoura, F., Kang, J., Heo, Y., Jung, T., & Lin, L. (2007). Polymeric microneedle fabrication using a microinjection molding technique. *MICROSYSTEM TECHNOLOGIES-MICRO-AND NANOSYSTEMS-INFORMATION STORAGE AND*, *13*(5-6), 517-522.

Segal, M. (1991). Patches, pumps, & timed release. *FDA Consumer*, *25*(8), 13. doi:Article

Shergold, O., & Fleck, N. (2004). Mechanisms of deep penetration of soft solids, with

application to the injection and wounding of skin. *PROCEEDINGS OF THE ROYAL SOCIETY OF LONDON SERIES A-MATHEMATICAL*, *460*(2050), 3037-3058. doi:10.1098/rspa.2004.1315

Shergold, O., & Fleck, N. (2005). Experimental investigation into the deep penetration of soft solids by sharp and blunt punches, with application to the piercing of skin. *JOURNAL OF BIOMECHANICAL ENGINEERING-TRANSACTIONS OF THE ASME*, *127*(5), 838-848.

Shikida, M., Hasada, T., & Sato, K. (2006). Fabrication of a hollow needle structure by dicing, wet etching and metal deposition. *JOURNAL OF MICROMECHANICS AND MICROENGINEERING*, *16*(10), 2230-2239.

Stellman, J. T. (2009, May). *Development, Production, and Characterization of Plastic Hypodermic Needles*.

Strong, A. B. (1996). Plastics : materials and processing /.

Subramanyan, K., Misra, M., Mukherjee, S., & Ananthapadmanabhan, K. (2007). Advances in the materials science of skin: A composite structure with multiple functions. *MRS BULLETIN*, *32*(10), 770-778.

Sumitomo. (2009, January 11). SE75DU specs METRIC. *Sumitomo 75 Ton Metric Specs*. Retrieved January 12, 2010, from http://www.sumitomopm.com/pdfs/SE75DUspecsMETRIC.pdf

WHO Press Office. (2002). World Health Organization Fact Sheet: Injection Safety.

Yan, G., Warner, K. S., Zhang, J., Sharma, S., & Gale, B. K. (2010). Evaluation needle length and density of microneedle arrays in the pretreatment of skin for transdermal drug delivery. *International Journal of Pharmaceutics*, *391*(1-2), 7-

12. doi:10.1016/j.ijpharm.2010.02.007

Zhu, Q., Zarnitsyn, V., Ye, L., Wen, Z., Gao, Y., Pan, L., Skountzou, I., et al. (2009). Immunization by vaccine-coated microneedle arrays protects against lethal influenza virus challenge. *PROCEEDINGS OF THE NATIONAL ACADEMY OF SCIENCES OF THE UNITED STATES OF*, *106*(19), 7968-7973. doi:10.1073/pnas.0812652106